

The Cells and Molecules Underlying Mechanosensation

Ruby Minh Lam

B.S. Emory University, 2014

A dissertation submitted in partial fulfillment of the requirements for the degree of

Doctor of Philosophy in the Department of Neuroscience at Brown University

Providence, Rhode Island

2024

© Copyright 2024 by Ruby Minh Lam

This dissertation by Ruby Minh Lam is accepted in its present form
by the Department of Neuroscience as satisfying the
dissertation requirement for degree of Doctor of Philosophy

Date _____

Alexander T Chesler, PhD Advisor

Recommended to the Graduate Council

Date _____

Nicholas J Ryba, PhD Reader

Date _____

Alexander Fleischmann, PhD Reader

Date _____

Valeria Vasquez, PhD Outside Reader

Approved by the Graduate Council

Date _____

Thomas A. Lewis , Dean of Graduate School

Ruby M. Lam

Education:

Brown University Providence, RI PhD. <u>Brown-NIH Neuroscience Graduate Partnership Program</u>	2016-Present
Emory University Atlanta, GA B.S. Neuroscience and Behavior Biology, Minor. Predictive Health	2014
Oxford College , Emory University Atlanta, GA <i>A.A. Oxford Academic Merit List</i>	2012

Research Experience:

Thesis Lab Brown-NIH GPP National Center for Complementary and Integrative Health Sensory Cells and Circuits Section PI: Alexander Chesler, Ph.D.	2017-present
Brown GPP Rotation Brown University Department of Neuroscience PI: Gilad Barnea Ph.D.	2016-2017
NIH GPP Rotation National Institute of Mental Health- Unit on Neural Computation and Behavior PI: Mark Histed, Ph.D.	Summer 2017
NIH Intramural Postbac National Institute of Aging -Laboratory of Behavioral Neuroscience Neural Circuits and Cognition Unit PI: Shih-Chieh Lin, M.D., Ph.D.	2014-2016
NET/Work -NIH Blueprint ENDURE-Undergraduate RA Physiology Department Emory School of Medicine, Atlanta GA PI: Shawn Hochman, PhD	2012-2014
Summer Training Academy for Research in the Sciences Anesthesiology Department University of California San Diego PI: Wendy Campana, PhD	Summer 2013
Behavioral Research Advancement in Neuroscience Fellowship, Center of Behavioral Neuroscience Georgia State University, Atlanta, GA PI: Michael Black, PhD	Summer 2012

Publications:

Lam, R. M., von Buchholtz, L. J., Falgairolle, M., Osborne, J., Frangos, E., Servin-Vences, M. R., ... & Chesler, A. T. (2023). PIEZO2 and perineal mechanosensation are essential for sexual function. *Science*, *381*(6660),906-910.

<https://doi.org/10.1126/science.adg0144>

Servin-Vences, M. R., **Lam, R. M.**, Koolen, A., Wang, Y., Saade, D. N., Loud, M., ... Chesler, A.T., & Patapoutian, A. (2023). PIEZO2 in somatosensory neurons controls gastrointestinal transit. *Cell*, *186*(16),3386-3399

<https://doi.org/10.1016/j.cell.2023.07.006>

Schrenk-Siemens, K., Pohle, J., Rostock, C., Abd El Hay, M., **Lam, R. M.**, Szczot, M., ... & Siemens, J. (2022). Human Stem Cell-Derived TRPV1-Positive Sensory Neurons: A New Tool to Study Mechanisms of Sensitization. *Cells*, *11*(18), 2905.

Szczot, M., Nickolls, A. R., **Lam, R. M.**, & Chesler, A. (2021) The Form and Function of Piezo2. *Annu Rev Biochem.* 2021 Jun 20;90:507-534. doi: 10.1146/annurev-biochem-081720-023244. PMID: 34153212. <https://doi.org/10.1146/annurev-biochem-081720-023244>

von Buchholtz, L. J., Ghitani, N., **Lam, R. M.**, Licholai, J. A., Chesler, A. T., & Ryba, N. J. (2021). Decoding cellular mechanisms for mechanosensory discrimination. *Neuron*, *109*(2), 285-298. PMID: 33186546 <https://doi.org/10.1016/j.neuron.2020.10.028>

von Buchholtz, L. J. , **Lam, R. M.**, Joshua J. Emrick, Chesler, A. T., and Ryba, N.J.P.(2020). Assigning transcriptomic class in the trigeminal ganglion using multiplex in situ hybridization and machine learning . *Pain.* 2020 Jun 3.PMID: 32379225

<https://journals.lww.com/pain/toc/2020/09000>

Nickolls, A. R., Lee, M. M., Espinoza, D. F., Szczot, M., **Lam, R. M.**, Wang, Q., ... & AlJanahi, A. A. (2020). Transcriptional Programming of Human Mechanosensory Neuron Subtypes from Pluripotent Stem Cells. *Cell Reports*, *30*(3), 932-946. PMID: 31968264 <https://doi.org/10.1016/j.celrep.2019.12.062>

Szczot, M., Liljencrantz, J., Ghitani, N., Barik, A., **Lam, R.**, Thompson, J. H., ... & Foley, A. R. (2018). PIEZO2 mediates injury-induced tactile pain in mice and humans. *Science translational medicine* *10*,10(462)

PMID: [30305456 https://doi.org/10.1126/scitranslmed.aat9892](https://doi.org/10.1126/scitranslmed.aat9892)

Lam, R. M., & Chesler, A. T. (2018). Shear elegance: A novel screen uncovers a mechanosensitive GPCR. *The Journal of General Physiology*, jgp.201812101. PMID: 29903977 <https://doi.org/10.1085/jgp.201812101>

Collaborating Journal Reviewer:

Journal of Neuroscience - ELIFE - Nature - Nature Neuroscience - Science

Awards:

NIH Fellows Award for Research Excellence 2023 Awarded from Study Section :Neuroscience -Sensory "Piezo2 channels provide essential input for genital sensation and sexual behaviors"	2022
NCCIH Annual Director's Merit Award: Fellow Award <i>for contributions that have helped uncover the molecular and cellular basis of mechanosensation</i>	2021
Nu Rho Psi, The National Honor Society in Neuroscience	2013-2014
Who's Who in America,	2012
Oxford Academic Merit List	2010-2012

Leadership and Extracurricular:

Program for Advancing the Health Sciences(PATHS) in Health and Biosciences <i>Prince George's County Public School Committee</i> <i>Development Workshop Coordinator and mentor to PATHS students</i>	2019-present
Philosociencing twitch stream science outreach and podcast <i>Interactive science chat on Twitter:@PhilScienceing and twitch:@philososcienceing</i>	2020-present
Skype a scientist - Virtual science instructor	2020-present
Brown-GPP Student representative and Recruitment	2018-2022
NIH Graduate Student Council	2017-2019
NIH Graduate Student Symposium Committee	2017-2018
Rhode Island Brain Week - Volunteer Classroom instructor	2016-2017
SFN Brain Bee , Brown and Baltimore chapters	2015-2017
Refugee Youth Project -Volunteer Academic Tutor	2014-2016
Orientation Leader,- Emory College of Arts and Sciences	2012- 2014
AP Biology Tutor- Supplementary Instructor	2011-2012
Peer Assistant Leader (PALs), Seminar instructor Oxford College	2011-2012
Student Admissions Association, Oxford College	2010-2012

Additional Relevant Experience:

2020	Conference Assistant Keystone Symposia- Somatosensation J8	Keystone, Co
2014	TA for NBB361W Project Lab in neurophysiology	Emory University, GA
2010-2012	Biology Lab Technician	Oxford College Emory, GA
2008-2011	Orthopedic Surgery/Play-Safe Sports Medicine Intern	UCSF, CA
2010	Chevron Oronite Project Seed Intern	American Chemical Society, CA
2008-2010	Ornithology Naturalist	San Francisco Nature Ed., CA
2009	United States Department of Agriculture (USDA-ARS),	American Chemical Society, CA

Selected Conference Presentations:

Lam, R.M., Osborne, J., Servin-Vences, MR., Frangos, E. , Saade,D., Patapoutian, A., Bönnemann C. G., & Chesler, A.T. "PIEZO2 activation links mechanosensation to sexual function" Keystone Symposia Vertebrate sensory systems. Lake Tahoe, CA 2022

Servin-Vences, MR., **Lam, R.M.**, Marshall, K., Wang, Y., Koolen, A., Loud, M., Bönnemann C. G. Chesler, A.T & Patapoutian, A. "PIEZO2 in sensory neurons coordinates gastrointestinal motility." Lake Tahoe, CA 2022

Lam, R.M and Chesler, A.T., "PIEZO2 Channels provide essential input for Genital sensation and Sexual Behaviors" 17th Annual NIH Graduate Student Research Symposium, Natcher Conference Center, Bethesda, MD 2021.

Lam, R.M. and Chesler, A.T., "Investigating Molecular Mechanisms of Touch and Pain " 16th Annual NIH Graduate Student Research Symposium, Natcher Conference Center, Bethesda, MD 2020.

Lam, R.M. , Bucholtz, L.V. , Ryba, N., and Chesler, A.T., "Genetic Identification of Meningeal Afferents and Their Targets in the Brain " 14th Annual NIH Graduate Student Research Symposium, Natcher Conference Center, Bethesda, MD 2017.

Lam, R.M. , Scaglione, A., Liang, J., and Lin, S.C., "Optogenetic Dissection of Basal Forebrain neuronal Circuitry reveals GABAergic Identity of Salience-Encoding Neurons " Society for Neuroscience, San Diego, CA 2016.

Lam, R.M. and Lin, S.C., "An Anatomical Study of Rodent Basal Forebrain Circuitry using Multiple Tracing Paradigms and Immunohistological Techniques" NIH- OITE postbac Poster day, Bethesda MD, 2016

Lam, R. M., Sawchuk, M. and Hochman, S. "Limited incidence of tyrosine hydroxylase-expressing C-fiber low-threshold mechanoreceptors in the first two weeks of postnatal development of mouse." Society for Neuroscience, Washington D.C., 2014.

Lam, R.M. "Developmental organization of C-fiber Low-Threshold Mechanoreceptors: A study of TH positive afferents implicated in affective touch in a rodent model." NET/work 2014 Spring Symposium, Georgia State and Emory University, Atlanta GA, 2014.

Lam, R.M. "The Role of Schwann Cell Low Density Lipoprotein Receptor- Related Protein 1(LRP1) in Inflammation and Regeneration Following Peripheral Nerve Injury." UCSD Summer 2013 Research Conference, University of California San Diego, La Jolla, CA, 2013.

Lam, R.M. "Developmental Organization of a Unique Class of Cutaneous Afferents Implicated in Social Touch." NET/work 2013 Spring Symposium, Georgia State and Emory University, Atlanta GA, 2013.

Lam, R. M., Butkovich, L. M., Herzig, E., and Singleton, K. "Effects of Acute and Repeated Cocaine on Locomotion and Monoamine Receptor Expression in *Procambarus clarkii*." Georgia State University Poster Symposium ,Georgia State and Society for Neuroscience, New Orleans, 2012.

***I dedicate this dissertation to my family,
who have inspired it and will probably not read it***

To my Mom, who instilled a love for books and encouraged freedom of thought.

To my Dad, who instilled a firm belief in “where there's a will there's a way”. Inheriting your proclivity for tinkering has been clutch in more situations than you will ever know.

To my Grandparents, who were my first teachers, and instilled an appreciation for well crafted storytelling. Hope this makes up for barely learning Chinese after all these years.

To my sister, Reena, Thanks for holding down the fort with the unit and grand unit during the global pandemic. Next vacation adventure is on me.

To my partner, Jason, thank you for filling my days with endless laughter and support.

Acknowledgements

When I dreamt about becoming a scientist when I grew up, I imagined discovering something truly meaningful. These humans have made this scientific journey more meaningful than I could have ever dreamed.

I am profoundly grateful to my advisor Alex Chesler, for creating a stimulating and supportive environment, encouraging exploration by greenlighting many side quests and for being the ultimate cheerleader.

I would like to thank Nick Ryba for his immense generosity with his time and for being the most stable person I know. Thank you for the regular masterclasses in all aspects of science from experimental design, data interpretation, writing, and data presentation.

I would like to thank the other members of my committee, Alexander Fleishman, for the pointed comments and career guidance. And Valeria Vasquez for agreeing to serve as my outside reader.

I would also like to thank many of the past and present members of the Chesler group:

Marcin Szczot, Nima Ghitani, Arnab Barik and Melanie Falgairolle thanks for showing me the ropes, sharing your rigs, advising, mentoring, coffees and putting up with all my showtunes. Jennifer Osborne, thanks for being an outstanding postbac even in the face of many challenging and strange experiments. Alec Nickolls, Donald MacDonald, Max Nagel, Jonathan Seaman, Raiza Hardy, Caroline Pierotti, Monesha Jayabalan and James Thompson. Thanks for all the awesome chats in our bays. Y'all have been awesome. I hope to "DATA" with you all someday

Thank you to many members of the NIH community for making it such an amazing place to learn and collaborate. Especially, Lars von Buchholtz, Minh Nguyen, Anu Sathyamurthy, Mark Hoon, Kevin Liu, Doris Wu, Mark Histed, Katherine Roche and Mark Stopfer.

I've also been lucky to have awesome non-NIH collaborators too, Ardem Patapoutian, Rocio Servin, Kara Marshall, I will miss our bi-monthly poop Zooms.

I would like to thank all of my science mentors and teachers especially Gilad Barnea, Shih-Chieh Lin, Shawn Hochman, Steve Baker, Nitya Jacob, Jennifer Bragg, and Jennifer Barbarow, thanks for hiring and/or teaching me. I must have been a handful.

Finally, I want to thank all my supportive friends. Especially Jonathan Lee, Jenny Huynh, Erin Brown, Nathan Whitmore, Nadira Yusif, Tanesha Singletary, Mor Alkaslasi, Kathleen Huntzicker Thanks for all the long chats at strange hours. Kaitlin Wilcoxon, Jessica Noss, Adriana Rizzo, Arty Zhang, Kat Daly, Frances Fan, Kaya Matson, Julia Licholai, Rebekah Lim, Althea Roy, Jing Liang, Roberto Aponte Rivera, Vannida Ket, Amanda Wong, Megan Wong, Leanna Chan, Karina Mark and my entire trauma bonded 2016 NSGP-GPP cohort you've been awesome thanks for all the adventures.

y'all it's been real

Table of Contents

Chapter 1-Introduction and review	1
Background	2
Part 1- The Cells	5
Part2 The Molecules	20
Part3- Piezos!	26
Conclusion- Questions I will address in this thesis	58
Chapter 2- Piezo2 and perineal mechanosensation are essential for sexual function	64
Supplementary materials	71
Chapter 3-PIEZO2 in somatosensory neurons controls gastrointestinal transit	90
Star Methods.....	106
Supplementary materials	112
Chapter 4-Functional characterization of molecules and cells that shape somatosensory responses	121
Part1- Redefining sensory neuron classes using their transcriptomic profiles.....	123
Supplementary materials	137
Part 2-Mapping functional cellular responses to transcriptomic class	145
Supplementary materials	166
Chapter 5- Discussion and end of thesis	177
Acknowledgements Take Two and Behind the Scenes.....	181

Chapter 1

The Cells and Molecules Underlying Mechanosensation Introduction and Review

*Chapter1 Part 3 - Piezos! is presented in the form it was published in the Annual review of Biochemistry with the following citation:

“Szczot, M., Nickolls, A. R., Lam, R. M., & Chesler, A. T. (2021). The form and function of *PIEZO2*. Annual review of biochemistry, 90, 507-534. <https://doi.org/10.1146/annurev-biochem-081720-023244>”

Background and significance

Embracing the understudies of senses: the importance of studying the somatosensory System

盲人摸象 is a buddhist proverb I was taught as a child to discuss the limits of subjective experiences and why it is important not to jump to conclusions. It literally translates to “blind people touch elephant” and it tells a story of several blind people who meet an elephant for the first time. They each examine the elephant on their own and then describe what they thought an elephant was to each other. Because each only appraised a single part of the elephant (the trunk, tusk, tail, ear or leg) they all inevitably disagreed on what an elephant was. Aside from the obvious lesson, this proverb also nicely demonstrates how different types of information can be used to build an ultimate picture of the world... In this case, each blind person is a sensory system (vision, hearing, smell, taste, or touch) and the elephant is the world.

Sensory systems play a crucial role in encoding external features of the environment that the brain integrates to create an internal representation of the world. By tapping into the senses, every creature has evolved a unique combination of sensory modalities that have been optimized for their survival. While every sensory system has its own strengths and provides fundamental building blocks of every creature's umwelt, the somatosensory system often assumes a supportive role that backs up the reality of all the other senses. Yet, much like the versatile ensembles of theater understudies ready to jump into any main role at a moment's notice, the true strength of somatosensation lies in the breadth of submodalities it encompasses.

Somatosensation includes a hodgepodge of everything else excluding vision, audition, taste and smell. In particular, the somatosensory system provides our brain with a window into the physical parts of the world, including touch, temperature, chemicals, and pressure. Tactile touch uses the largest sensory organ, the skin, to interface with the external environment and allows us to sense physical contact, irritants and temperature. Interoception enables us to monitor the condition of many of our internal organs including our heart rate and gastrointestinal

distress. Proprioception helps us stay upright and track the position and movement of our limbs in space. Bone, tendon and muscle sensations as well as other unique animal adaptations like infrared thermal radiation sensing or magnetoreception can all be encompassed by somatosensation. Once we embrace the ever presence of our somatosensory system, we can truly appreciate their supportive roles in our experience of the world. For what is tasting food without texture or temperature, and what is seeing or hearing a scary movie without feeling your heart palpitate?

All the submodalities of our somatosensory systems are constantly engaged and intricately entwined with our attention and motor feedback. Every moment we are awake and conscious, we are likely monitoring and evaluating some kind of somatosensation. Is the temperature of the room a bit cold? Is there an itch under my collar? Does this stomach rumble mean I'm hungry? We can also completely shift our attention away from these sensations, to perform more important things like writing this thesis. By studying the intricacies of the somatosensory system, we can better understand how organisms gate the constant flood of sensory information from the external world and generate appropriate behaviors, including the behaviors that prompt us to put on sweaters, scratch that itch, and eat that sandwich.

The 21st century presents an exciting era for sensory neuroscience. The field has inherited a wealth of detailed anatomical knowledge and gained access to powerful molecular tools and genetic techniques. This allows us to address long-standing questions and fill gaps in our understanding. However, studies that comprehensively span multiple levels of neuroscience investigation in the somatosensory domain remain scarce. In this thesis, I will demonstrate how a cohesive approach, integrating molecules, cells, circuits, and behavior investigations can provide profound insights into the organization of our somatosensory system. For example, in chapters two and three, I will investigate the roles of a molecule, Piezo2, in neurons innervating the gastrointestinal or perigenital area of the mouse to better understand the importance of mechanosensation in bowel motility and sexual reproduction. By connecting the role of key

molecules and their specific expression pattern to functional roles that result in specific behaviors and phenotypes, we can uncover the relationships between the organization of our somatosensory system and our perception that shapes our daily lives.

Anatomy and organization of the somatosensory system

“All our knowledge begins with the senses, proceeds then to the understanding, and ends with reason. There is nothing higher than reason.”- Immanuel Kant

The ability of humans to perceive the slightest deformation in the skin when an insect lands on us is nothing short of remarkable. Primary sensory neurons bridge the gap between the external world and the black box that is our central nervous system (CNS) with some of the longest axons in the body. Primary sensory neurons comprise a remarkably heterogeneous population of neurons responsible for relaying information about both external environmental cues and internal bodily conditions. As such, they play a pivotal role in facilitating our perception of the world around us (exteroception), monitoring our internal physiological state (interoception) and ourselves (proprioception). The neuron bodies reside in a chain of sensory ganglia found in the intervertebral foramen immediately lateral to each side of the spinal cord and brainstem called dorsal root ganglia (DRGs) or at the base of the skull called trigeminal ganglia (TG) and send a bifurcating axon to both the periphery and the CNS. At the periphery, the axon tip of a primary sensory neuron embedded in the patch of skin the insect landed on must transduce that mechanical disturbance into an electrical/chemical signal. That signal travels all the way to the soma body in the DRG. The neurochemical impulse must then travel to the spinal cord or brainstem where second order neurons take the sensory information into places like the thalamus and cortex and will eventually induce the appropriate behavior of swatting the insect away. Each ganglion consists of neurons that densely innervate specific patches of skin called dermatomes that consecutively cover the entire surface of the body in a partially overlapping manner. The neurons in each ganglion are physiologically distinct and diverse enough to

transduce the entire range of features from the external world including thermal, tactile, chemical, interoceptive and pain sensations. Thus, taxonomizing and categorizing sensory neurons to better understand the sensory experience has occupied many investigators throughout the years.

Part 1- The Cells

Organizing primary sensory neurons into functional classes

“Unfortunately nature seems unaware of our intellectual need for convenience and unity, and very often takes delight in complication and diversity” - Ramón y Cajal

Somatosensory neurons exhibit diverse conduction velocities, cell soma diameters, receptor expression profiles, ion-channel compositions, and neuropeptide patterns. They selectively target both peripheral and central areas and display varied functional response profiles¹⁻⁵. The incredible diversity of somatosensory neurons allows us to interpret a wide range of sensory information. However, this diversity poses a challenge when it comes to categorizing these neurons into distinct groups. Despite over a century of scientific inquiry, attempts to classify sensory neurons have been confined by the technological limitations of the era, resulting in useful, but unsatisfying categorization. In the following sections I will walk through some of the more significant and useful organizational schemes proposed and used between the 19th and the present day.

Classical organization schemes

The idea of specific sense energies, or a labeled line principle, where the perception of our senses is transmitted by morphologically distinct receptors that transduce particular forms of energy and transmit this information to the brain through nerve fibers dedicated to that modality, was first introduced by Charles Bell and Johannes Muller in the early 1800s⁶⁻¹⁰. Thomas Young proposed an even more specific nerve energy principle, where qualities of sensation within the same sensory system followed the same pattern, when he described the three receptors

underlying color vision^{11,12}. Ludwig Natanson, similarly, observed that during paresthesia, when a limb “falls asleep” from sustained pressure compressing a nerve, three qualities of sensation, (1)temperature, (2)pressure and (3)touch/tickle would fall away and return in a reproducible order¹⁰. As a result, he proposed that three independent organs were responsible for each sensation and pain was the product of activating all three classes of skin nerves at the same time. The specific nerve energy theory was then tested in the late 1880s by several scientists, including Magnus Blix¹³, who performed a series of experiments on himself. In these experiments, he used electrodes, thermodes and pins to stimulate patches of skin on his hands and face, and discovered that adjacent spots of skin would evoke different sensations; stimulation in some spots would evoke sensations of touch and some spots would evoke cooling. By stimulating the skin surface or subcutaneously, Alfred Goldscheider showed that the same tactile sensation could be evoked whether the stimulation was applied to the skin or anywhere along the length of the same nerve fiber¹⁰. These experiments relied on the test subjects, often the researchers themselves,¹⁴ to report the sensations they experienced. Mapping the sensation spots on the surface of the skin was variable across subjects, and created several controversies about the sensations, especially in regards to nerves that could simultaneously sense tactile and temperature sensations. Thus more information was needed to further organize sensory neurons.

Organizing by electrical properties

Predating electrical recordings, von Frey proposed that four different sensations that could be associated with a receptor type were touch, pain, warmth, and cooling and that the skin consisted of a mosaic of spots tuned for each sensation¹⁰. The invention and advancements in cathode-ray oscilloscope designs like those by Erlanger and Gasser in the late 19th century allowed for long stable recordings of electrical signals from nerve fibers¹⁵. The ability of these recording tools to capture the waveforms of nerve fibers immediately led to experiments that combined stimulation and recording of the rapid impulses in nerves. This

became a new opportunity to categorize sensory neurons and test if indeed there were just four different sensations mosaically organized across the skin.

Physiologists, beginning with Charles Sherrington¹⁶, followed by pioneering studies from Zotterman¹⁷, Loewenstein¹⁸, Iggo¹⁹, Perl²⁰, Burgess²¹, and others²², used electrical recordings to characterize peripheral neuron responses and the signals they send to the central nervous system. In addition to allowing them to record different kinds of action potentials in nerve bundles, these electrical recordings allowed a snapshot into the different types of neurons that existed. They could be categorized in three major ways: 1-conduction velocities, 2-tuning the type of stimulus that best created action potentials, and 3-the adaptive rate of the neurons.

The conduction velocity, or axon conduction speed, is a property of the primary afferent fiber. The speed is directly correlated to the amount of myelination, and fiber diameter of the neurons. In humans, A α fibers are the most heavily myelinated, with fiber diameters of 12-20 μ m and have very fast conduction velocities of 80-120 m/s. A β fibers are highly myelinated neurons, with fiber diameters of 6-12 μ m and have fast conduction velocities of 30-80 m/s. A δ are lightly myelinated with fiber diameters of 1-6 μ m and have medium conduction velocities of 2.5-30 m/s, and C- fibers have little to no myelination, fiber diameters of smaller than 2 μ m and by far the slowest conduction velocities of slower than 2.5m/s^{23,24}. This categorization of sensory neurons by their conduction speeds categories may seem like an unbiased way to organize neurons; however, there is a large continuous range of velocities even within the same category. Furthermore, the diameter of the soma body itself, fails to correlate nicely to the conduction velocity of the axons, which likely means each of these categories are still quite heterogeneous^{25,26}.

Another way to organize sensory neurons is by what they are tuned to, or what types of stimuli will produce the most reliable action potentials. Cutaneous primary sensory neurons can be tuned to low, medium and high mechanical forces. Neurons could be specifically activated by how the stimulus is applied to the skin– like rate, duration and direction of the mechanical

force²⁷. Some sensory neurons can also be tuned for temperatures, like cooling and warming, or just the change of temperatures. There are also neurons specifically tuned to chemicals and can be further divided by what kind of chemicals they respond to, such as plant extracts like menthol, AITC, capsaicin, or endogenous chemicals like Glutamate and ATP, or even chemicals and toxins from insects and bacteria^{24,28}. This type of classification on its own is also unsatisfactory as there are large portions of neurons that are polymodal, and will respond to multiple stimuli. In fact, should any of these neurons be challenged with the most extreme versions of any of these stimuli, it could result in the transduction of a membrane damage signal as extracellular ions leak into the cell.

The third canonical way of organizing sensory neurons is their responses to continual stimulus application. Neurons can be separated into either rapidly or slowly adapting categories²⁷. Rapidly adapting neurons will respond briefly at the onset of a stimulus and at the end of the stimuli presentation whereas a slowly adapting neuron will begin responding at the onset of the stimuli and continue generating action potentials until the stimuli is removed. Slowly adapting neurons can further be split into groups of regularly responding (SAtype1) or irregularly responding (SAtype2) neurons.

Modern single unit axon recordings (microneurography) in awake humans and primates has further allowed researchers to connect reports of mechanical sensations to specific nerve fibers with these different electrical profiles²⁹. An organizational principle where there is a fast system and a slow system that deals with interpreting different sensory information can be made since humans with neuropathies of their A β have altered gentle and discriminate touch; and patients with neuropathies in their A δ and C-fibers are insensitive to temperature, pain and affective touch. But this is a deceiving simplification of the true diversity of sensory neurons, for example high frequency electrical stimulation of A β will also generate a painful response. Furthermore, reflexive pain responses happen rapidly, which alludes to a role for myelinated

sensory neurons. Consequently, organizing by electrical properties itself, was not enough to effectively and satisfactorily categorize sensory neurons.

Organizing by receptor morphology

We often prioritize understanding how the intrinsic properties of sensory neurons shape their diverse tuning properties. However, it is equally important to recognize the significant roles played by the anatomical location and ultrastructures of the end organs in shaping the responses. Whether through structural filtering, physical tethering, or the active propagation and modulation of force sensation, the non-neuronal components of end organs contribute significantly to the communication between the skin and the brain.

In the late 19th century, significant scientific advancements revolutionized the study of neurons and the anatomical structures with which they interacted. Beginning with Otto Friedrich Karl Deiter's³⁰ Carmine dye and potassium dichromate³¹ was used on tissue to visualize individual neurons(fig1). This was further improved by Camillo Golgi's silver nitrate staining method, which allowed sparse labeling revealing the detailed processes of neurons. Around the same time, Ernst Abbe's optical innovations, such as apochromatic lenses, condensers, refractometers, and an optical formula for lenses resulted in reliable manufacturing of light microscopes. By improving the resolution of microscopic images, anatomists Ramon y Caja, von Frey, Pacini, Meissner, Ruffini, and Merkel³² could describe structural specializations at peripheral axonal endings and guided the formulation of theories describing how morphology of peripheral endings contributes to specific sensory functions. These detailed observations facilitated the organizational categorization of sensory neurons based on morphological endings. The anatomical locations with these specialized endings were then correlated with specific functions. Modern electron microscopy, immunohistochemistry and genetic techniques have largely confirmed these initial observations in fine 3D detail. The following is a brief summary of sensory neurons organized from most morphologically complex to least.

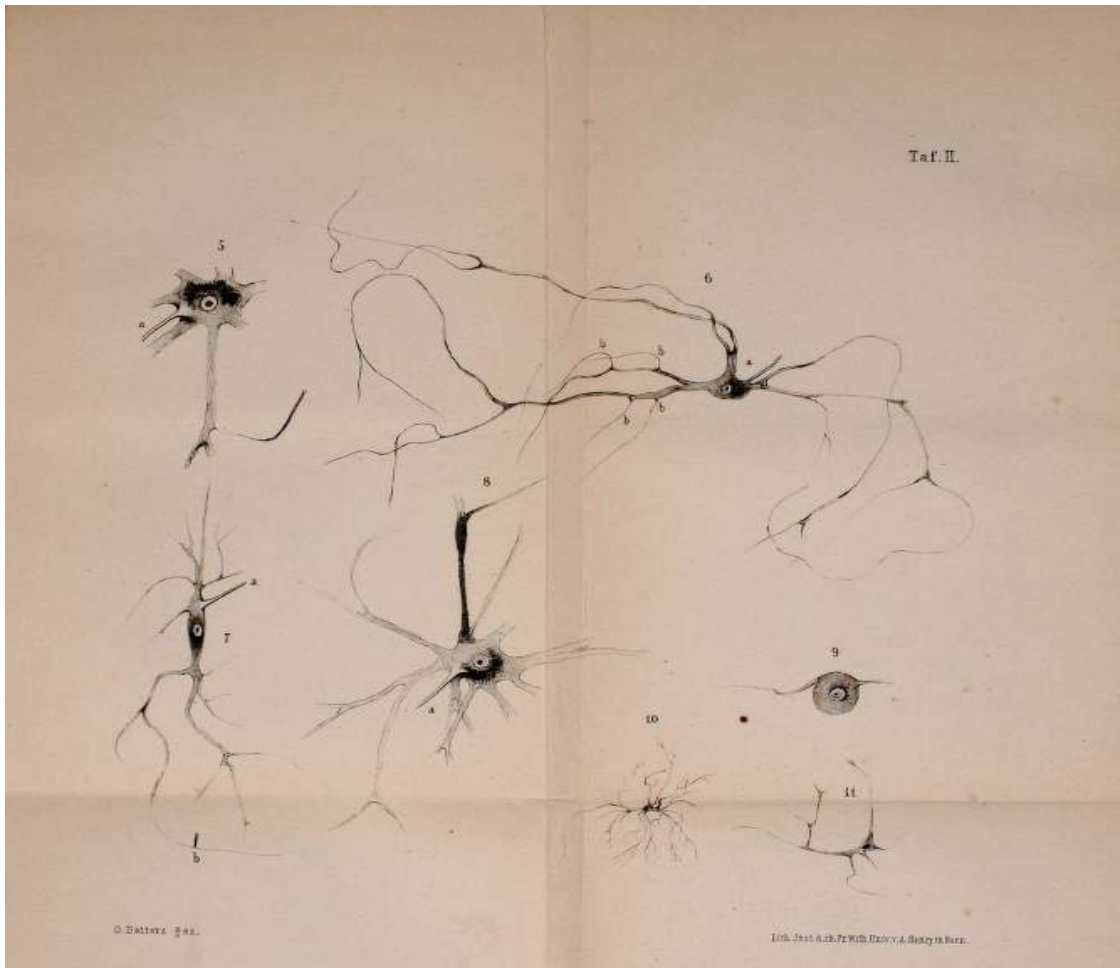


Fig. 1. Otto Karl Deiter's first drawing of neurons. Adapted from Reference³³

The structural specializations of receptors

Complexed-Encapsulated corpuscles

Vater-Pacian and Golgi-Mazzoni

Vater-Pacian corpuscles are the largest end structures, and can even be seen with the naked eye; thus they were the first to be discovered. They were first observed by Abraham Vater and then rediscovered by Fillippo Pacini in 1835^{34,35}. These corpuscles, measuring between 0.5-5 mm in length and 1-2 mm in width, are situated deep in the dermis and possess large receptive fields without direction sensitivity. While they may be sparser compared to other sensory neurons, they exhibit higher density in the fingertips. Each sensory neuron axon ending terminates at the center of the corpuscle with a blunt-ended knob, interacting with a non-

myelinating terminal Schwann cell that forms concentric layers of fluid-filled laminae shaped like an onion that is enveloped by a dense external capsule. A similar structure, called the Golgi-Mazzoni, has several elongated axon processes that terminate into the center of the onion shaped corpuscle. Golgi-Mazzoni corpuscles are commonly found in close association with the digital arteries, particularly concentrated around the joints and nail/claw attachments of the digits, and are also present in the mesenteries of the intestines^{14,24}.

The onion-shaped terminal Schwann cell functions as a high-pass filter, allowing high-frequency mechanical stimuli to pass through; as a result, these corpuscles are ultra-sensitive to dynamic stimuli such as vibrations or textures, with maximum sensitivity ranging between 400-800 Hz. Electron microscopy reconstruction of these corpuscles reveals the blunt ends and elongated axon processes are protrusions the neuron uses to interface with the non-neuronal lamellar schwann cell. Notably, Vater-Pacinian are supplied by the largest caliber A β -fibers^{3,4,36,37}.

Meissner corpuscles

Initially described by Wagner and Meissner in 1852, Meissner corpuscles are the next most complex group of sensory neuron endings. They are incompletely encapsulated endings measuring 40-150 μ m in length and 60 μ m wide, found most abundantly in the hairless glabrous skin^{32,38}. They are usually found densely packed together, like on fingertips in the dermal papillae along the sides of the primary epidermal ridges, which allow them to detect direction and low frequency vibrations as we move fingertips across different textured objects^{3,24}. Gold chloride technique showed that Meissner corpuscles consist of an axon with a zig-zagging horizontal course between stacks of bouton disks, spiraling between terminal Schwann cells. They are primarily supplied by A β -fibers, although sometimes multiple fibers contribute to their sensory input^{4,39,40}.

Krause endings

Krause endings in primates, first described by Krause in 1860, are globular or spherical end bulbs with an average diameter of 100 μm . They possess a distinct capsule comprising 2-6 layers and are referred to by various names, including "small Paciniform corpuscles," "simple encapsulated end organs," and "innominate corpuscles"^{24,32}. These specialized sensory receptors are found in various locations, such as the conjunctiva, nasal and oral mucosa, the glabrous skin of the hands and feet, and notably, genitalia⁴¹.

Medium anatomically complexed end organs

In addition to terminal Schwann cells association, sensory neurons are known to have complex relationships with other cells and structures such as epithelial cells, hair, and blood vessels.

Merkel cell neuron disk complex touch domes

The Merkel cell and nerve terminal disk complex, or touch dome, was first described by Merkel 1875. But the first cell and nerve terminal was first described in detail using electron microscopy in 1962 by Cauna. It revealed an axon terminal which was flattened into a 7 μm by 1 μm thick disk with a high density of mitochondria which has an intimate relationship with a Merkel cell. Clusters of Merkel touch domes are highly localized in the hairy epidermis at the level of the sebaceous glands of guard hair follicles³². In primates including humans, Merkel complexes are highly prevalent on the ridges of fingerprints. Merkel nerve endings are typically described as A β SA1- low-threshold mechanoreceptors (LTMRs) and convey information about texture, curvature, and object shape with high spatial acuity. Merkel cell-associated neurons respond to skin compression and hair deflections with firing properties that increase proportionally to the intensity of the stimuli. The nerve supply to Merkel cell complexes tend to have larger diameters, and better individual resolving power compared the Meissners⁴.

Ruffini corpuscles

Ruffini endings are encapsulated spindle shaped corpuscles which was classically considered one of the major types of skin innervation. It was first described by Ruffini in 1894 in gold chloride stains of cat hairy skin. Initially they were proposed to be terminal endings of A β SA2-LTMRs which were particularly sensitive to skin stretch and found oriented along stretch lines. While Ruffini corpuscles exist in the hairy paw skin of cats, recent investigations of glabrous skin in humans and monkeys, where SA2 fibers were previously detected, have not definitively demonstrated the presence of Ruffini corpuscles. The identity of these corpuscles are currently in question, as the spindle-like Ruffini formations described could potentially represent diffuse Merkel cells, A δ -fibers, or even sympathetic C-fibers, which innervate and detect tension in the walls of blood vessels^{24,42}.

Hair follicle innervating endings

While all hair follicles are innervated, different types of hair follicles have varying amounts of innervation that reflect their importance for function. For example, vibrissa hair follicles of the whiskers have the most dense and elaborate endings and can generate a large range of differential patterns of neural activity in response to orientation, direction, velocity, texture, duration, and intensity of stimuli. In rodents, the guard hairs in the overcoat have the next most innervation whereas the zigzag hairs of the undercoat are the least innervated. These differences indicate important functional roles for these endings in detecting mechanosensation related to hair deflection²⁴.

Lanceolate complex

Lanceolate endings terminate in the dermis and are highly associated with the hair follicles. These endings consist of combinations of several LTMRs and terminal Schwann cells which create a crown around the base of hair follicles, lined with flattened blade structures

which run parallel to the hairs. Each hair follicle can be innervated by several different axon endings. To create this crown of innervation, the blades for each individual axon are distributed around the perimeter of the hair follicle and alternate with blades from other axon endings. Some will innervate just one side of the base of the shaft⁴³ and be used to differentiate the direction of a brush stimulus²⁴.

Circumferential Endings

Like lanceolate endings, circumferential endings are also closely associated with the hair follicles. These endings lasso around the base of hair follicles, interlacing and surrounding the lanceolate endings. Some neurons will have axon endings which innervate entire patches of skin including multiple hairs. Circumferential endings can be important components of the piloneural complex and can be found at terminal endings around hair follicles supplied by all different diameters of nerve fibers. Notably, the A δ -HTMRs that respond to noxious hair pulling have circumferential endings^{24,44}.

Least complex endings

Free nerve endings

Free nerve endings are, as they are named, free with non-descript endings. They are the most abundant kind of sensory ending and terminate in all levels of the epidermis in both hairy and glabrous skin. They are the only endings found in highly sensitive areas, like the cornea, where they terminate in beautiful spiral patterns. While free nerve endings may seem like the category of all the leftover sensory endings without any specialized structures, it can be argued that these are actually the sensory neurons which have reached their true full potential; whereas all the other specialized endings I've mentioned above, are the result of sensory neurons which have encountered obstacles enroute to innervating them during their developmental sprouting phase and instead spent the rest of the time in a misdirected waylay⁴⁵. Notably, many nociceptors, which transduce painful stimuli, have free nerve endings^{4,46}.

The Cells conclusion

So how many somatosensory neuron subtypes are there?



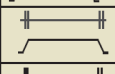
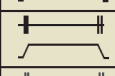
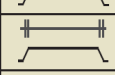
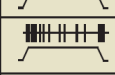

Overall, I have just highlighted a few of the more heavily studied groups of sensory organs anatomists have taxonomized. As scientists began incorporating new techniques like gold/silver staining, methylene blue, perfusion fixation, immunohistological and added information gained from microscopy advances from light, confocal and electron microscopy, it became clear that the different techniques were underlying the “discoveries”. In their zeal to make new discoveries, at some point, anatomists named over 30 different types of sensory organs with special terminations in specific tissues. Since many sensory neuron characteristics vary on a continuum, classifying sensory neurons in a discreet and unbiased way is difficult. Often, binning neurons into discrete categories requires creating arbitrary cutoffs. Perhaps all sensory neurons are not distinct populations at all and instead reflect a spectrum and can be placed along a line from high, medium to low complexity. Whether we are in the splitter or lumping camp, it is clear that sensory endings are complicated and that their diversity is evolutionarily conserved because it is important to have a range of sensations and a breadth of tools to interact with the external world with.

Taken together, these basic categorization systems gave us a common vocabulary to discuss different types of nerve fibers, and allowed physiologists a framework to compare their functions. Currently combinations of all of these organizational schemes are used when describing sensory neurons. These shorthands may seem like a letter salad to those who have not been entrenched in the field, but they are simply describing neurons intersectionally by their morphological endings, conduction velocity, response properties, and location of termination. For example a neuron that innervates hairy skin, has rapidly adapting dynamics in response to mechanical stimuli, is heavily myelinated and is sensitive to low forces could be called cutaneous RA A β -LTMR While a neuron that wraps around a hair shaft, and responds to

noxious mechanical stimuli could be called a C-HTMR. This table summarizes the breadth of sensory neurons using these classical organization principles (Table 1)⁴.

Table 1. A comparison of Cutaneous Mechanoreceptors⁴

*Adapted from reference 4

Physiological subtype	Associated fiber (conduction velocity ¹)	Skin type	End organ/ending type	Location	Optimal Stimulus ⁴	Response properties
SAI-LTMR	A β (16-96m/s)	Glabrous Hairy	Merkel cell Merkel cell (touch dome)	Basal Layer of epidermis Around Guard hair follicles	Indentation	
SAII-LTMR	A β (20-100m/s)	Glabrous Hairy	Ruffini ² unclear	Dermis ³ unclear	Stretch	
RAI-LTMR	A β (26-91m/s)	Glabrous Hairy	Meissner corpuscle Longitudinal lanceolate ending	Dermal papillae Guard/Awl-Auchene hair follicles	Skin movement Hair follicle deflection	
RAII-LTMR	A β (30-90m/s)	Glabrous	Pacinian corpuscle	Deep dermis	Vibration	
A δ -LTMR	A δ (5-30m/s)	Hairy	Longitudinal lanceolate ending	Awl-Auchene/ Zigzag hair follicles	Hair follicle deflection	
C-LTMR	C (0.2-2m/s)	Hairy	Longitudinal lanceolate ending	Awl-Auchene/ Zigzag hair follicles	Hair follicle deflection	
HTMR	A β /A δ /C (0.5-100m/s)	Glabrous Hairy	Free nerve ending	Epidermis/Dermis	Noxious mechanical	

The Cells to the Molecules

A modern reorganization - emergence of transcriptomic identities

In the last 15 years, there has been a meteoric advance in the development of single cell RNA sequencing technology; It began with sequencing single cells manually in 2009, followed by 100 cells in microfluidic circuits, then 100,000 cells in nanodroplets, and now more than a million cells using *in situ* barcoding^{47,48}. Once again, a new technology has offered scientists an opportunity to categorize sensory neurons and re-evaluate previous organizational principles.

With these new sequencing technologies, we can now explore the genetic differences between individual sensory neurons and determine if they form a continuum or discrete populations⁴⁹. Using large data sets of neuron transcriptome profiles, unbiased clustering and dimensional reduction analysis revealed 13-16 distinct classes of sensory neurons^{5,50-54}. This evidence supports the idea that sensory neurons can truly be categorized into discrete and distinct populations of neurons at the molecular level, and the existence of organizational principles beyond placing all neurons on a spectrum of complexity. These sequencing experiments revealed that transcriptomically distinct subtypes of sensory neurons are well conserved amongst different sensory ganglia and could accurately predict non-

overlapping populations of neurons with specific markers that can be verified with *in situ* hybridizations.

After establishing that sensory neurons are transcriptomically distinct populations in adult animals, new questions can be asked. For instance: how do sensory neurons attain their terminally differentiated identities? When and how do they emerge throughout development? Are animals born with already segregated populations, or do these populations diversify later as the animals are exposed to somatosensory inputs?

We have yet to all agree on a unified nomenclature for these newly defined groups. Overall, the addition of sequencing information greatly expands the molecular taxonomy of sensory neurons and helps predict molecular targets that may give genetic access to these distinct groups of sensory neurons. Sequencing information also complements the efforts to link gene expression with functional roles of sensory neurons. However, there are several problems in directly linking transcriptomic data to functioning sensory neurons in intact animals. First, sequencing sensory neurons is methodologically difficult and even the best preparations lose information from cells at every step of the process and result in only a sample of neurons, biased towards those that can survive the dissociation and sorting steps. Second, the most highly expressed transcripts are rarely also the transcripts which help differentiate populations of neurons from each other. Frequently complex transcriptional patterns are necessary to define many of the classes. Furthermore, because these class-separating diagnostic transcripts have no clear functional relevance, without already knowing sensory molecules of interest such as ion channels, GPCRs, Trp channels, peptide, purigen/ATP, or opioid receptors, it is hard to assign a functional role to transcriptomic classes. We have attempted to connect these transcriptomically defined populations with function in a series of experiments (See Chapter 4).

distress. Proprioception helps us stay upright and track the position and movement of our limbs in space. Bone, tendon and muscle sensations as well as other unique animal adaptations like infrared thermal radiation sensing or magnetoreception can all be encompassed by somatosensation. Once we embrace the ever presence of our somatosensory system, we can truly appreciate their supportive roles in our experience of the world. For what is tasting food without texture or temperature, and what is seeing or hearing a scary movie without feeling your heart palpitate?

All the submodalities of our somatosensory systems are constantly engaged and intricately entwined with our attention and motor feedback. Every moment we are awake and conscious, we are likely monitoring and evaluating some kind of somatosensation. Is the temperature of the room a bit cold? Is there an itch under my collar? Does this stomach rumble mean I'm hungry? We can also completely shift our attention away from these sensations, to perform more important things like writing this thesis. By studying the intricacies of the somatosensory system, we can better understand how organisms gate the constant flood of sensory information from the external world and generate appropriate behaviors, including the behaviors that prompt us to put on sweaters, scratch that itch, and eat that sandwich.

The 21st century presents an exciting era for sensory neuroscience. The field has inherited a wealth of detailed anatomical knowledge and gained access to powerful molecular tools and genetic techniques. This allows us to address long-standing questions and fill gaps in our understanding. However, studies that comprehensively span multiple levels of neuroscience investigation in the somatosensory domain remain scarce. In this thesis, I will demonstrate how a cohesive approach, integrating molecules, cells, circuits, and behavior investigations can provide profound insights into the organization of our somatosensory system. For example, in chapters two and three, I will investigate the roles of a molecule, Piezo2, in neurons innervating the gastrointestinal or perigenital area of the mouse to better understand the importance of mechanosensation in bowel motility and sexual reproduction. By connecting

the role of key molecules and their specific expression pattern to functional roles that result in specific behaviors and phenotypes, we can uncover the relationships between the organization of our somatosensory system and our perception that shapes our daily lives.

Anatomy and organization of the somatosensory system

“All our knowledge begins with the senses, proceeds then to the understanding, and ends with reason. There is nothing higher than reason.”- Immanuel Kant

The ability of humans to perceive the slightest deformation in the skin when an insect lands on us is nothing short of remarkable. Primary sensory neurons bridge the gap between the external world and the black box that is our central nervous system (CNS) with some of the longest axons in the body. Primary sensory neurons comprise a remarkably heterogeneous population of neurons responsible for relaying information about both external environmental cues and internal bodily conditions. As such, they play a pivotal role in facilitating our perception of the world around us (exteroception), monitoring our internal physiological state (interoception) and ourselves (proprioception). The neuron bodies reside in a chain of sensory ganglia found in the intervertebral foramen immediately lateral to each side of the spinal cord and brainstem called dorsal root ganglia (DRGs) or at the base of the skull called trigeminal ganglia (TG) and send a bifurcating axon to both the periphery and the CNS. At the periphery, the axon tip of a primary sensory neuron embedded in the patch of skin the insect landed on must transduce that mechanical disturbance into an electrical/chemical signal. That signal travels all the way to the soma body in the DRG. The neurochemical impulse must then travel to the spinal cord or brainstem where second order neurons take the sensory information into places like the thalamus and cortex and will eventually induce the appropriate behavior of swatting the insect away. Each ganglion consists of neurons that densely innervate specific patches of skin called dermatomes that consecutively cover the entire surface of the body in a partially overlapping manner. The neurons in each ganglion are physiologically distinct and diverse enough to

Part 2 - The Molecules

Organizing by transduction molecules

Connecting molecules and function

While classifying sensory neurons using their anatomical, neurochemical, electrophysiological, and tuning features was useful in providing a nomenclature, neurons in the same class remain very heterogeneous and functionally diverse. In recent years, the diverse functional roles of anatomically similar sensory neurons could be elucidated with the addition of information about the molecules they express⁵⁵.

The fusion of classical electrophysiological and morphological studies with more recent identification of receptors mediating certain kinds of sensations has elevated our collective understanding of sensory neurons. Certain populations of sensory neurons express molecules that are necessary for specific types of sensations.

Identification of transduction molecules

The late 1990s and early 2000s witnessed significant breakthroughs in the identification of transduction molecules in the somatosensory system. The advent of genetic tools facilitated comprehensive screening of genes for these kinds of molecules. For example, thermosensitive TRP channels were discovered by using expression cloning to identify TRPV1, a capsaicin and heat activated ion channel⁵⁶. The discovery of other Transient Receptor Potential (TRP) ion channels soon followed, including the menthol and cooling gated TRPM8⁵⁷ and Wasabi receptor TRPA1⁵⁸⁻⁶⁰. These transduction molecules convert temperature and natural products exposed in the periphery, into nerve impulses centrally, which elicit very specific sensory experiences. These discoveries clearly connect the molecules particular sensory neurons expressed with their functional role and ultimately the sensory percept.

Finding the Mechanotransduction molecule

Since the twentieth century, neurophysiologists have been on the question to uncover the molecular mechanism for mechanotransduction when their electrical recordings indicated that force sensing might be an intrinsic feature of touch fibers³⁷. However, identifying the specific molecule(s) responsible for mechanical transduction presented several challenges. Unlike thermoreceptors or chemoreceptors, mechanotransduction lacked easily identifiable natural compound agonists, like capsaicin for heat sensation or menthol for cooling, that could be used for a pharmacological screening. In many cases, the mechanotransduction site, such as the skin, muscle, or organs, is located within thick protective tissues, making them inaccessible to direct physical manipulation. Additionally, developing reliable and quantitative assays to apply forces to cell membranes, and simultaneously recording from them was challenging. Finally, the lingering doubt that impeded the discovery of the touch receptor molecule was the question of whether a single transducing molecule existed at all. The prevailing hypothesis was that the entire specialized structure of sensory endings or cell itself was the mechanotransducer. For example, slowly oscillating strains on cellular attachments with the surrounding extracellular environment or neighboring cells are sensed by adhesion receptors⁶¹. Integrins and cadherins interacting with the extracellular matrix and intracellular cytoskeletal elements are critical components of force-dependent remodeling during development⁶²⁻⁶⁴.

A crucial breakthrough in the search for the molecular basis of mechanotransduction emerged in 1979. During this time, Corey and Hudspeth⁶⁵ showed that mechanotransduction in the hair cells of the bullfrog sacculus worked at an astonishingly fast time scale (<40 μ s). Mechanically induced responses with millisecond kinetics were also recorded from *C. elegans* and *Drosophila* in the early 2000s^{66,67}. Because a unifying feature of ionotropic channel gating is extremely fast ion flux, this speed implicated an ion channel as the putative receptor directly activated by mechanical force. Mechanosensitive ion channels have been proposed to function

as receptors in a diverse array of cells, tissues, and sensory systems from many organisms. Over the years, a number of candidate molecules have been proposed to mediate aspects of mechanosensation. Electrophysiological, biochemical approaches as well as genetic screens identified candidate molecules in bacteria⁶⁸⁻⁷¹, in yeast⁶⁸, in invertebrates like *C. elegans*^{67,72} and *Drosophila melanogaster*^{66,73,74}. Many of these molecules are part of ion channel families, these include, but are not limited to, the bacterial nonselective large conductance MscL channel⁶⁹, the epithelial amiloride-sensitive Na⁺ channel (DEG/ENac) family⁷⁵, the two-pore K channels⁷⁶, the cation-selective Transient Receptor Potential (TRP) channel family^{74,77,78}. Disappointingly, vertebrate orthologs for these ion channels either did not exist or were not mechanosensitive. More promisingly, candidate molecules in hearing were identified during this period by mapping the genes involved in hereditary deafness⁷⁹. While candidate approaches turned up several potential mechanosensitive ion channels⁸⁰, none of the proposed molecules proved to be essential for touch responses. At this point in time, human patients with hereditary mutations which specifically affected touch sensation had yet to be identified, and as such, the transduction mechanisms for touch remained elusive.

Despite these discouraging results, new methods like pressure clamp recording, patch clamp and poking solidified the hypothesis that indicated the existence of a force gated ion channel. The pressure-clamp technique involves applying positive or negative pressure to a membrane patch while simultaneously recording electrical activity⁸¹. This technique screened candidate molecules quickly and accurately. Another robust method for testing mechanical sensitivity of neurons is by making whole cell patch clamp recordings while simultaneously poking the cell with a blunt glass probe⁸²). By driving the poking stimulus with a piezo actuator, membrane indentations to be triggered at millisecond speeds, with micrometer resolutions, and in a reproducible manner. For example, poking primary sensory neurons dissociated from mouse DRGs evokes large and distinctive currents with biophysical properties that could be rigorously characterized^{83,84}.

The transduction of force into mechanically evoked current at the cell membrane of many vertebrate species is an evolutionarily conserved feature that has led to adaptations ranging from vibration sensing to highly tuned auditory systems. The conservation of this mechanism across species aided its discovery. In the landmark study by Coste and colleagues in 2010⁸⁵, the authors correctly reasoned that a loss of function screen performed in a cell line with robust electrical responses to membrane stretching, recorded using patch clamp electrophysiology, could be employed to identify this evolutionarily conserved mechanotransducer at the membrane. This insight led to their success in identifying the mechanosensitive ion channels Piezo1 and 2.

Coste and colleagues recorded cells using whole-cell patch clamp while simultaneously poking the cell surface with a piezo-electrically driven blunted glass probe. They screened several cell lines including (C2C12, NIH/3T3, Min-6, 50B11, F11, N2a and PC12) and identified the mouse neuroblastoma cell line (N2a), derived from neural crest cells of the tumor, as having distinctive and consistent mechanical responses. In the whole cell configuration, they found that the N2a line had the fastest adaptation kinetics. In cell attached recording configuration, they were able to characterize the current-pressure relationship, which was similar to properties of reported stretch-activated channels. Once they determined that N2a cells were reliably mechanically activatable, they performed a loss of function screen.

To generate a list of candidate genes, Coste and colleagues looked for transcripts that were highly enriched using microarray gene expression profiling of the N2a cell line. They further focused their list on proteins which were predicted to have multiple transmembrane domains (a shared characteristic of ion channels), previously identified cation channels, and orphan proteins with no known functions. The necessity of each of these candidate genes for the observed mechanically activated current was then laboriously tested by knocking-down gene expression, one at a time, using siRNAs in the N2a cells and performing whole cell patch recordings while poking the cell. Using this screening method, the gene family with sequence

similarity 38 (Fam38a) was identified. Knocking down Fam38a with various siRNAs resulted in significantly reduced mechanical responses. Because of its mechanosensitive nature, Fam38a was named Piezo1, from the Greek "πιεση"(píesi). Interestingly, Piezo1 had one other homologous family member in the mouse and human genome, Fam38b, or Piezo2. Importantly, examining the expression patterns of these genes revealed that while Piezo1 was expressed broadly in all types of tissues Piezo2 was found mostly in sensory neurons.

Piezos are bona fide mechanotransducers

As outlined by Martin Chalfie in his influential review just a year before the discovery of Piezos⁸⁶, there are four requirements for a bona fide mechanotransducer. First, the molecule needs to be localized to the correct cells and to the correct position for mechanosensing. Most researchers assume this means the molecule should be expressed in sensory neurons and localized at the sensory endings. On this requirement, Piezo2 passes. Not only is Piezo2 found in sensory neurons, and at the axon endings, it is also found in places where the axons interact with other specialized organs. For example, Piezo2 can be found all over the merkel cell/axon disk complex and in the tips of the axon where it interacts with the lamellar cells in pacinian corpuscles.

The second criteria is that the molecule must be necessary for the electrical response of the sensory cell to the mechanical stimulus and not for subsequent activity of the cell. The best evidence for an unknown molecule expressed in sensory neurons comes from *in vitro* experiments. Primary cultures of somatosensory neurons are acutely mechanosensitive, but are generally quiet without any stimulation. Mechanical indentation of the plasma membrane directly evokes currents from sensory neurons that presumably arise from the gating of stretch-gated ion channel like Piezo⁸⁷. All currents recorded from primary cultures bear characteristics of non-selective cation channels with a range of inactivation kinetics (rapidly adapting or RA, intermediately adapting or IA and slowly/non-adapting or SA).

The third criterion is that mechanical forces must gate this molecule in a heterologous cell line or lipid bilayer. Therefore, when a putative mechanotransducing molecule is expressed into mechano-insensitive cell lines, these cells should be rendered mechanosensitive. Again, Piezo2 clearly meets this requirement. Heterologous expression of cDNA from Piezo2 endows mechanically insensitive HEK293 cells with stretch-evoked responses. However, although Piezo2 meets this criterion, other putative mechanosensitive ion channels have yet to be reconstituted in heterologous systems. Notably, neither the MEC channel complex from worms nor the TMC1/2 complex from vertebrate hair cells have been successfully expressed outside of their native cell types.

The fourth and final criteria is that gating should recapitulate the mechanically gated current observed in its natural environment where alterations of the properties of the channel protein should also alter the mechanical response properties. In this case, the mechanically sensitive activity should look and perform like it does in the context of a whole intact, and alive animal. Again, Piezo2 meets this criterion. The biophysical properties (permeability, sensitivity and kinetics) recorded from heterologously expressed Piezo2 closely match the rapidly adapting current characterized in sensory neurons. Whether this would hold true for other mechanosensitive ion channels is unclear. Many ion channels have subunits that are not required for trafficking and assembly but also dramatically impact their functional properties⁸⁸. Because Piezo2 fulfills all of these requirements, it unequivocally establishes itself as a bona fide mechanoreceptor.

Part 3- Piezos!

*this section is presented in the form it was published with the following citation

“Szczoł, M., Nickolls, A. R., Lam, R. M., & Chesler, A. T. (2021). The form and function of *PIEZO2*. Annual review of biochemistry, 90, 507-534. <https://doi.org/10.1146/annurev-biochem-081720-023244>”

Contributions: This review on the form and function of Piezo2 was written in collaboration between all the authors. Specifically, R.M.L. generated Figure1, drafted and edited sections 1.1,1.2,2.1, 3.1,3.2,3.3,3.4,3.5,3.6,3.7,3.8,3.9,3.10,3.11, 5 and the associated citations. This review replaces Part 3 of the introductory chapter after discussion during the thesis defense examination.

*Annual Review of Biochemistry***The Form and Function
of PIEZO2****Marcin Szczot,^{1,2,*} Alec R. Nickolls,^{1,*} Ruby M. Lam,^{1,3}
and Alexander T. Chesler^{1,4}**

¹National Center for Complementary and Integrative Health, National Institutes of Health, Bethesda, Maryland 20892, USA; email: alexander.chesler@nih.gov

²Center for Social and Affective Neuroscience, Department of Clinical and Experimental Medicine, Linköping University, 583 30 Linköping, Sweden

³NIH–Brown University Graduate Program in Neuroscience, Providence, Rhode Island 02912, USA

⁴National Institute of Neurological Disorders and Stroke, National Institutes of Health, Bethesda, Maryland 20892, USA

Annu. Rev. Biochem. 2021. 90:507–34

The *Annual Review of Biochemistry* is online at
biochem.annualreviews.org

<https://doi.org/10.1146/annurev-biochem-081720-023244>

This is a work of the US Government and is not
subject to copyright protection in the United States

*These authors contributed equally to this article

Keywords

PIEZO2, mechanosensation, mechanotransduction, somatosensation,
touch, proprioception, ion channel

Abstract

Mechanosensation is the ability to detect dynamic mechanical stimuli (e.g., pressure, stretch, and shear stress) and is essential for a wide variety of processes, including our sense of touch on the skin. How touch is detected and transduced at the molecular level has proved to be one of the great mysteries of sensory biology. A major breakthrough occurred in 2010 with the discovery of a family of mechanically gated ion channels that were coined PIEZO2. The last 10 years of investigation have provided a wealth of information about the functional roles and mechanisms of these molecules. Here we focus on PIEZO2, one of the two PIEZO proteins found in humans and other mammals. We review how work at the molecular, cellular, and systems levels over the past decade has transformed our understanding of touch and led to unexpected insights into other types of mechanosensation beyond the skin.

**ANNUAL
REVIEWS CONNECT**

www.annualreviews.org

- Download figures
- Navigate cited references
- Keyword search
- Explore related articles
- Share via email or social media

Contents

1. DISCOVERY OF PIEZO2	508
1.1. The Search for the Touch Receptor	508
1.2. The Identification of PIEZO2	510
2. MECHANOTRANSDUCTION BY PIEZO2 CHANNELS	511
2.1. Channel Structure and Mechanogating	511
2.2. Lipid and Protein Interactome	513
2.3. Intracellular Signaling and Regulation	514
3. PIEZO2 IN MECHANOSENSATION	515
3.1. PIEZO2 Clinical Significance	515
3.2. Expression	516
3.3. Touch	518
3.4. Mechanical Pain	520
3.5. Itch	521
3.6. Proprioception	521
3.7. Breathing	522
3.8. Gastrointestinal Tract	522
3.9. Bladder	523
3.10. Baroreflex	523
3.11. Additional Biological Roles	524
4. NEW MODEL SYSTEMS AND PHARMACOLOGICAL INTERVENTIONS	524
4.1. Human Stem Cell–Based Models	524
4.2. PIEZO2 Drug Discovery	525
5. CONCLUDING REMARKS AND FUTURE PERSPECTIVES	527

1. DISCOVERY OF PIEZO2

1.1. The Search for the Touch Receptor

As we move through the world, we sense, respond, and adapt to many types of mechanical forces. These processes, broadly referred to as mechanosensation, include the conscious perception of touch (an aspect of somatosensation), the effortless control of our posture (proprioception), and the unconscious regulation of physiological functions such as breathing and heart rate (interoception). In each of these cases, force activates specialized cells called mechanoreceptors that generate and transmit signals to the nervous system and body. At the mechanistic level, the key step in mechanosensation is the conformational change of molecules expressed in mechanoreceptors. Conformational changes of these molecules are caused by stress, shear stress, pressure, and/or tension and convert force into electrochemical signals, a process called mechanotransduction.

Of the many types of mechanosensation, touch is perhaps the most integral to our daily activities and therefore the most relatable. This sensory system is exquisitely sensitive, remarkably accurate, and extremely fast, allowing us to localize miniscule forces such as the movement of a single hair within a fraction of a second. Uncovering the mechanisms by which the touch system achieves these feats has been a major effort of scientists for over a century. But it is really in only the past decade that we have begun to understand how this type of mechanosensation functions at the molecular level.

Research dating back to the mid-to-late-1800s revealed beautiful details about the structural basis for mechanosensation in the skin. In the nineteenth century, anatomists such as von Frey, Pacini, and Merkel described the structural specializations of mechanoreceptors and developed theories describing how their physical forms influence sensory function (1). Physiologists, beginning with Sherrington (2), followed by pioneering studies from Iggo, Burgess, Perl, Loewenstein (3–6) and others, used electrical recordings to characterize peripheral neuron responses and the signals they send to the central nervous system. These studies laid out principles for the organization of the somatosensory system that serve as the foundation of our understanding of touch today. However, the question remained as to how forces activate these specialized cells in the first place.

The search for mechanotransduction mechanisms can be traced back to the mid-twentieth century, when neurophysiological observations indicated that force sensing might be an intrinsic feature of touch fibers (7). A turning point in the search for the molecular basis of mechanotransduction came in 1979, when Corey and Hudspeth (8) showed that mechanotransduction in hair cells, the principal mechanoreceptors for hearing, is extremely fast ($<40 \mu\text{s}$). They concluded that only the physical opening, or gating, of ion channels could convert force to electrical current with that temporal resolution. However, it was not until the invention of the patch-clamp recording technique in the early 1980s (9) that direct evidence for mechanotransduction involving ion channels could be demonstrated (10, 11). Since then, mechanosensitive ion channels have been proposed to function as receptors in a diverse array of cells, tissues, and sensory systems from many organisms (12). However, these hypotheses proved difficult to test. In many cases, the site of mechanotransduction (e.g., skin, muscle, or organs) is embedded in thick protective tissue, making it inaccessible to direct physical characterization. Assays that reliably and quantitatively apply force to cell membranes have also proved difficult to implement. But, perhaps the biggest challenge of all has been uncovering the identity of the molecules involved.

Major advances in identifying transduction molecules in the somatosensory system came in the late 1990s and early 2000s with the cloning of the capsaicin receptor TRPV1 (which also responds to heat, protons, toxins, and irritants) (13), followed by those of other TRP channels that sense temperature and chemical irritants (14, 15). At the same time, mechanosensitive ion channels were identified in bacteria using electrophysiological and biochemical approaches (16–19) and in invertebrates using genetic screens [notably in *Caenorhabditis elegans* (20, 21) and *Drosophila melanogaster* (22)]. Disappointingly, however, orthologs for these ion channels in vertebrates were either not found or had seemingly nonmechanosensory functions. More promisingly, candidate molecules in hearing were identified during this period by mapping the genes involved in hereditary deafness (23). Unfortunately, hereditary mutations selectively affecting touch had not yet been observed (24), and consequently, the transduction mechanisms for touch remained a mystery. While candidate approaches turned up several potential mechanosensitive ion channels (25), none of the proposed molecules proved to be essential for touch responses.

Despite these discouraging results, by the early 2000s, enough evidence had accumulated from new methods to indicate that the touch receptor was a force-gated ion channel. One method, the pressure-clamp technique, allowed screening to be performed both quickly and accurately. In this approach, positive or negative pressure can be applied to a membrane patch while simultaneously recording electrical activity (26). Another approach poked cells with a blunt glass probe using a piezo actuator during whole-cell recording (27). The use of piezo positioning allowed membrane indentation to be triggered at millisecond speeds, with micrometer resolutions, and in a reproducible manner. Notably, using a piezo-driven probe to mechanically stimulate sensory neuron cultures isolated from the sensory ganglia of rodents evoked large and distinctive currents whose biophysical properties could be rigorously characterized (28, 29). Together, these data provided

key signatures of mechanosensitive ion channels in sensory neurons and the technical means to uncover their identity.

1.2. The Identification of PIEZO2

The challenges of finding the touch receptor gene(s) were several-fold. Unlike with thermosensation, there were no natural products like capsaicin or menthol that could be used as pharmacological probes. As candidate approaches continued to fail, the best guess was that the touch receptor would be a molecule with multiple membrane-spanning domains that would be enriched in sensory neurons. The prevailing view from the touch system in *C. elegans* and vertebrate hair cells was that mechanotransduction involved the assembly of multimeric complexes, making the prospect of expression cloning daunting. As it turned out, instead of a direct approach using sensory neurons, the touch receptor was ultimately found by screening a neural crest cell-derived cancer cell line (N2a cells).

In their landmark study, Coste et al. (30) reasoned that if they identified immortalized cell lines that had robust responses to membrane stretch measured using patch-clamp recording, they could perform a loss-of-function screen to discover mechanotransducers. Sure enough, while many cell lines had no mechanically evoked currents, mouse neuroblastoma N2a cells exhibited characteristic responses in the pressure-clamp and poking assays. Microarray gene expression profiling was used to create a list of genes with transmembrane domains found in N2a cells but not in nonresponsive cell lines. The necessity of each candidate molecule for the observed pressure-clamp responses was then laboriously tested one at a time using a loss-of-function knockdown strategy. Screening this way revealed that knockdown of a gene called *Fam38a* significantly reduced pressure-clamp responses. It turned out that *Fam38a* was a very unusual molecule that did not resemble anything previously studied in the context of mechanosensation (31). The gene had an enormous open reading frame (over 9 kb) that encoded a molecule predicted to span the membrane dozens of times. As predicted for a bona fide mechanotransducer, expression of the *Fam38a* cDNA in a nonresponsive cell line endowed those cells with large mechanically evoked currents that matched the kinetics of the endogenous responses seen in N2a cells. Intriguingly, a homology search found that *Fam38a* had a single homologous family member in the mouse and human genomes, called *Fam38b*, that also made normally nonresponsive cells mechanosensitive when it was expressed heterologously. Examining the expression patterns of these genes revealed that while *Fam38a* transcripts were found in many tissues, *Fam38b* appeared to be more selectively expressed and particularly enriched in somatosensory neurons. Importantly, siRNA knockdown of *Fam38b* reduced mechanically evoked currents in somatosensory neurons cultured from mouse tissue.

Based on their ability to respond to force, the mouse proteins *Fam38a* and *Fam38b* were renamed *Piezo1* and *Piezo2* respectively, after the Greek word for pressure. The human homologs are highly similar at the amino acid level (95% for *PIEZO2*) (24). Correspondingly, the human versions of these proteins are termed *PIEZO1* and *PIEZO2*. In the decade since their discovery, *PIEZO*s have been shown to be evolutionarily conserved force-gated ion channels present in plants, protists and worms (30), insects (32), and multiple vertebrate species including fish (33), birds (34), rodents (35), and humans (24, 36). In vertebrates, *PIEZO2* has a specialized sensory role. Knockout studies in mice (35, 37–40) and the study of human individuals with rare loss-of-function mutations (24, 38) have revealed that *PIEZO2* is indeed an essential mechanotransducer for touch, proprioception, and interoception. In the following sections, we summarize what we have learned in the past 10 years about the structure and function of *PIEZO2*, with an emphasis on its role as a mechanotransducer in vertebrate sensory systems, and we highlight some of the key questions that remain unanswered.

2. MECHANOTRANSDUCTION BY PIEZO2 CHANNELS

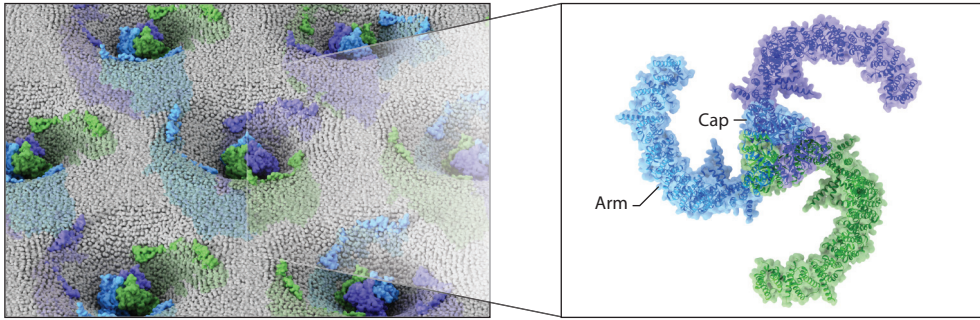
2.1. Channel Structure and Mechanogating

Initially, mutagenesis and epitope mapping (41, 42) were used to investigate the transmembrane topology of PIEZO1 and PIEZO2. From these and other studies, it was clear that the ion permeation pathway is localized to the C-terminal region and that the channels contain a very large intracellular loop of likely functional significance (43). A major advance came with the development of cryo-electron microscopy as a tool to study ion-channel structure (44). First, three research groups were able to obtain high-resolution structures of mouse PIEZO1, showing that the functional ion channel is a trimer assembled from three PIEZO1 monomers and arrayed in an unusual triple-bladed propeller conformation (45–47). Recently, this arrangement was confirmed for mouse PIEZO2, whose structure further revealed that each monomer contains an unprecedented 38 transmembrane segments, the most of any known membrane protein (48). The pore of the channel, which conducts an excitatory nonselective cation current that slightly favors Ca^{2+} (30), is located at the center of the propeller shape, where the three monomers meet, and spans the plasma membrane (48). Several additional structural elements—such as the beam and clasp—lie below the plane of the membrane in the cytoplasm, and another component—the cap—lies above the pore in the extracellular space (**Figure 1a–c**). Based on structure–function studies, these modules were shown to critically regulate or directly facilitate channel opening in response to mechanical force (42, 48–50).

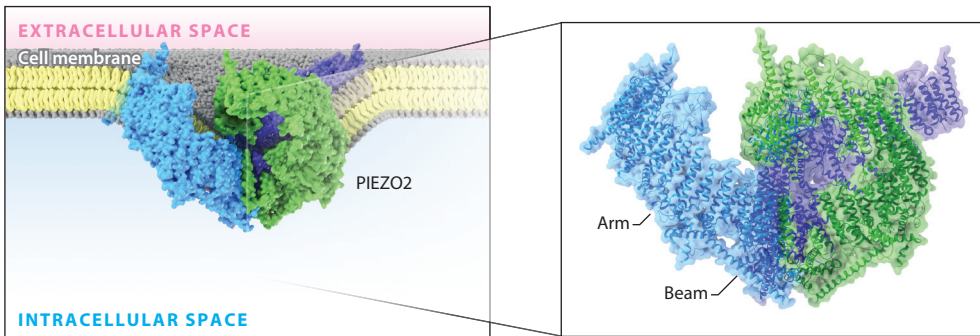
A potential clue to the mechanogating mechanism of PIEZO2 comes from an unexpected structural feature: When viewed from the side, the channel's propeller blades are curved upward and away from the plane of the plasma membrane in a convex arrangement (**Figure 1b**) (48). A similar conformation is found in PIEZO1 when reconstituted in synthetic liposomes, and this arrangement has been proposed to deform the local membrane into a cup shape while the channel is in the closed state (45–47, 51). If a mechanical stimulus were to laterally stretch the channel, the cup shape could hypothetically be pulled flat; the propeller blades would consequently straighten, providing the energy needed for channel opening (51). It remains unknown whether this mechanogating mechanism occurs in native plasma membranes, as the aforementioned experiments were conducted in cell-free systems (52). Nonetheless, such detailed views of mouse PIEZO2 architecture enable a mechanistic understanding of how RNA alternative splicing could alter channel structure (42, 53), and they explain how clinically relevant mutations in human *PIEZO2* might affect channel function (**Figure 1c**). For a comprehensive review on PIEZO structures, refer to a recent article by Xiao (43).

The full repertoire of mechanical stimuli that PIEZO2 can transduce, as well as the means by which force is coupled to channel gating, remains unclear. One of the most prominent ideas for how mechanogating might occur is the force-from-lipid model (54). If the gating of PIEZO2 conforms to this model, a sudden increase in lipid bilayer tension would be sufficient to open the channel without any auxiliary proteins present. The force-from-lipid hypothesis can be tested by mechanically stretching the membrane of liposomes that contain purified PIEZO2 while recording the channel's conductance. Although this result has not yet been achieved for PIEZO2, data from other mechanosensitive ion channels—including mouse PIEZO1—indicate they can be gated in response to membrane stretch alone (55, 56). Based on the high degree of structural relatedness between PIEZO1 and PIEZO2 (46–48), it seems likely that PIEZO2 would be similarly receptive to membrane stretch. However, some studies have indicated that PIEZO2 might preferentially respond to indentation of the plasma membrane, while PIEZO1 is sensitive to all forms of mechanical perturbation (57, 58). Furthermore, lipid bilayer stiffness has a lesser effect on the mechanosensitivity of PIEZO2 compared to PIEZO1 (50, 59). Interestingly, chemical

a Extracellular view



b Side view



c

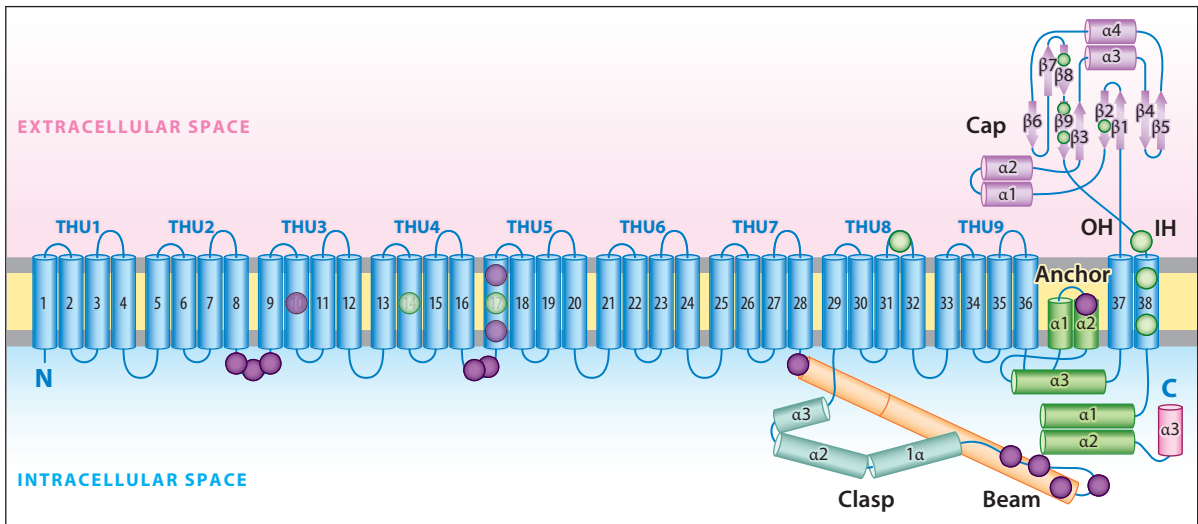


Figure 1

The structure of mouse PIEZO2. (a) A top-down illustration of mouse PIEZO2 channels in the membrane as viewed from outside the cell. (b) A side-view illustration of a PIEZO2 channel curving the plasma membrane. (c) Ribbon diagram of one blade of PIEZO2 highlighting key functional domains. Lavender and green circles indicate approximate reported locations of human loss-of-function and gain-of-function variants, respectively. Structure adapted with permission from Reference 48. Abbreviations: α , α -helix; β , β -pleated sheet; IH, inner helix of the ion-conducting pore; OH, outer helix of the ion-conducting pore; THU, transmembrane helical unit.

destruction of the cytoskeleton impairs PIEZO2 mechanogating more than PIEZO1 (50, 59, 60), and enzymatic digestion of the extracellular matrix also putatively interferes with PIEZO2 transduction (61). These data indicate that PIEZO2 may be influenced by both intra- and extracellular protein tethers as well as lipid bilayer curvature. Future studies are needed to address the specific lipid, water, and protein interactions that underlie PIEZO2 mechanogating. For a more detailed discussion of mechanogating mechanisms, see the review by Grandl and colleagues (62).

2.2. Lipid and Protein Interactome

In addition to the factors discussed in Section 2.1, the fatty acid composition of the lipid bilayer may affect PIEZO2 function directly, through lipid-protein binding, or indirectly, through changes to membrane fluidity and lipid raft organization (63, 64). Recent discoveries indicate that PIEZO2 mechanogating is modulated by several classes of membrane lipids. Margaric acid, a dietary saturated fatty acid, incorporates into cell membranes and increases their structural order and stiffness at micromolar concentrations in vitro (59). Margaric acid treatment inhibits PIEZO2 currents in a concentration-dependent manner, indicating that PIEZO2 mechanosensitivity is influenced by lipid bilayer rigidity (50). PIEZO2 function has also been shown to be potentiated by the presence of cholesterol-rich lipid rafts and the cholesterol-binding protein *Stoml3* (stomatolike 3) (65, 66). In addition, phosphoinositides—specifically phosphatidylinositol 3,5-bisphosphate [PI(3,5)P₂], as well as PI(4,5)P₂ and perhaps PI(4)P₂—can bind directly to PIEZO2 and facilitate mechanotransduction (67, 68). The importance of phosphoinositides was further suggested by studies showing that PIEZO2 function can be modulated by expression of the proteins *Mtmr2* and *Tentonin3*, which are proposed to be involved in phospholipid homeostasis (68, 69). Overall, the mechanisms for lipid-based control of PIEZO2 are not fully understood, and it is still unknown whether many of these lipids act directly or indirectly on the channel. In the future, it will be interesting to examine whether PIEZO2 localizes to specific membrane microdomains, similar to other sensory channels such as *Trpa1* (70), where its function may be dynamically modified based on the local lipid environment.

The extracellular matrix and intracellular cytoskeleton have also been implicated in affecting PIEZO2 function. They are essential anchors for tissue and cell structures that could transmit mechanical force to PIEZO2, either by indirect linkage to the plasma membrane or by a direct tether to PIEZO2. A tether mechanism has already been demonstrated for the NOMPC mechanotransduction channel, which mediates touch sensation in *Drosophila* (71–73). Although some evidence suggests that an extracellular matrix linker can mediate force transfer in mammalian mechanosensory neurons (61, 74), a direct interaction between PIEZO2 and the extracellular matrix has not yet been found. So far, there is also no biochemical proof of a direct linkage between PIEZO2 and the cytoskeleton, despite several lines of functional evidence. Treatment with latrunculin A, an actin-depolymerizing toxin, strongly blunts PIEZO2 mechanosensitivity in vitro (60). By contrast, the mechanogating function of PIEZO1 is much less affected by latrunculin A treatment (59). Interestingly, a chimeric PIEZO2 in which the intracellular beam domain is replaced by the PIEZO1 version of the same structure loses much of its sensitivity to latrunculin A actin disruption (50). This points to a functional link between the PIEZO2 beam domain and the cytoskeleton that may mediate a form of mechanogating distinct from that of PIEZO1.

Immunoaffinity purification followed by mass spectrometry has been used as an exploratory method to identify proteins that potentially interact with PIEZO2 in mouse sensory ganglia. So far, this approach has uncovered pericentrin, SERCA, and *Mtmr2*, among others (68, 75, 76). Interestingly, expression of each of these proteins is correlated with suppression of PIEZO2 mechanogating. *Mtmr2*, as mentioned briefly above, functions as a negative regulator of the PIEZO2-potentiating lipid PI(3,5)P₂ (68). The biochemical mechanisms by which PIEZO2 is

regulated by pericentrin and SERCA, as well as by other proteins identified by mass spectrometry, remain to be determined. Future work is needed to explore whether PIEZO2 can respond to mechanical stimuli when reconstituted in lipid bilayers in the absence of other proteins.

2.3. Intracellular Signaling and Regulation

As a sensory transduction channel, PIEZO2 represents the first step in a bioelectrical cascade that translates mechanical inputs into cellular responses. Mechanical force on the cell membrane permits the passage of cations through the PIEZO2 channel (30). For neurons, this influx of cations to the cytosol is excitatory, acting to depolarize the membrane and trigger the firing of action potentials. Several studies have shown that genetic deletion of *PIEZO2* in certain skin cells and mechanosensory neurons ablates all mechanically evoked electrical activity in those cells, leading to profound deficits in mechanosensation (39, 77–79). These results, combined with sensory testing of human patients with PIEZO2 loss of function, demonstrate the importance of this receptor for initiating the electrochemical relays underlying our perception of various mechanical stimuli (24, 38). The physiological roles of PIEZO2 in human and animal models are covered in Section 3.

Ca²⁺ entry into cells is the starting point for many biochemical signals, including regulation of gene expression, cytoskeletal remodeling, and protein trafficking (80). Thus far, the Ca²⁺ permeability of PIEZO2 has been implicated in the mechanical regulation of axon pathfinding, cell motility, differentiation, and cancer metastasis (74, 81–83). PIEZO2 is also thought to interact with various intracellular Ca²⁺-response proteins (76), which can drive specific outcomes including actin polymerization or the activation of the NFAT, Yap1, and β -catenin transcription factors (81–83). In tissues that express both PIEZO1 and PIEZO2, it is still unclear how both channels are used and whether there are distinct intracellular pathways linked to each channel (40, 83).

In addition to regulating various signal cascades, PIEZO2 itself is regulated. There are at least two broad intracellular mechanisms that either suppress or potentiate PIEZO2 activity; they involve phosphoinositide or cyclic adenosine monophosphate (cAMP) second messengers, respectively. As discussed in Section 2.2, depletion of plasma membrane phosphoinositides such as PI(3,5)P₂, PI(4,5)P₂, and PI(5)P₂ inhibits PIEZO2 mechanotransduction (67, 68). The major known mechanism involves Ca²⁺ influx through either the heat-sensing channel Trpv1 or the electrophile-sensing channel Trpa1; this activates phospholipase C, which in turn enzymatically depletes PI(4,5)P₂, leading to blockade of PIEZO2 activity (67). In contrast, the cAMP pathway can boost PIEZO2 mechanosensitivity via activation of PKA and PKC—a process that can be initiated by the inflammatory peptide bradykinin, which signals through G α q-coupled receptors on the surface of sensory neurons (84). Similarly, expression of Epac1 potentiates PIEZO2 sensitivity and is linked to the development of inflammatory pain, perhaps through G α s-coupled prostaglandin receptors (60, 85). Distinct from these G α q and G α s pathways, PIEZO2 is also potentiated by activation of G β γ -coupled receptors, which can include γ -aminobutyric acid, serotonin, or opioid receptors (86). Many of these signaling molecules, including PKA, PKC, and Epac1, are targets of cAMP signaling in pain-sensing neurons (87), suggesting a concerted inflammatory pathway that impinges on PIEZO2.

Another source of intracellular regulation of PIEZO2 is through alternative RNA splicing. In the somatosensory system of mice, *PIEZO2* can exist in as many as 12 mRNA isoforms (42). The resulting structural diversity affects functional properties of the protein. Isoforms differ in deactivation kinetics and their relative permeability to Ca²⁺, which may be a mechanism for regulating downstream signaling cascades, as described above. The mechanical sensitivity of PIEZO2 splice variants can also be differentially modulated by intracellular Ca²⁺, indicating a potential for self-regulation during prolonged or repeated activity.

At present, many elements of PIEZO2 biochemistry are still unknown, including the exact inflammatory molecules, intracellular signaling networks, and posttranslational modifications that influence PIEZO2 mechanotransduction. Identifying these factors may have particular clinical relevance for understanding and treating mechanical allodynia and hyperalgesia—conditions thought to be caused in part by injury-induced enhancement of mechanotransduction (37, 38, 88). For a more in-depth discussion, Borbiri and Rohacs (89) have recently reviewed PIEZO2 regulatory pathways.

3. PIEZO2 IN MECHANOSENSATION

3.1. PIEZO2 Clinical Significance

Several years ago, the Chesler and Bönemann labs identified two unrelated individuals with an unusual constellation of symptoms, including severe motor and skeletal phenotypes such as hip dysplasia, finger contractures, progressive scoliosis, and hypotonia (24). Family reports indicated that both subjects were born by cesarean section due to being in a breech position and required immediate oxygen support and food supplementation as infants. Both individuals were delayed in reaching motor milestones, learning to crawl only by age four and walk (with assistance) by age eight. These subjects have ongoing difficulties with routine activities, such as dressing and eating, that significantly affect their daily lives. In addition, they display abnormal interoceptive phenotypes, including lack of breath support (i.e., shallow breathing), urinary urgency, and nocturnal enuresis.

Exome sequencing revealed that each subject carried two inactivating mutations in the *PIEZO2* gene in compound heterozygosity. Complete loss of PIEZO2 function was confirmed using heterologous in vitro models (24) and later with patient-derived sensory neurons generated using stem cell technologies (for details, see Section 4) (90). The parents of both individuals were healthy carriers, indicating that PIEZO2 haploinsufficiency is apparently asymptomatic. Medical and quantitative sensory assessment showed that loss of function of PIEZO2 results in a profound lack of the sense of proprioception: Patients exhibited pseudoathetosis (involuntary limb movements) when closing their eyes, a lack of awareness of limb and joint positions, and an absence of tendon reflexes. Both subjects also had severe hyposensitivity to gentle touch, including an inability to perform simple touch discrimination tasks and a complete loss of vibration sensation. These deficits were highly selective, with temperature detection and pain thresholds in these individuals matching those of healthy volunteers. Notably, since the discovery of the first patients with *PIEZO2* null mutations, several other groups have identified individuals that lack functional *PIEZO2* genes, and subjects across the studies share highly conserved motor and skeletal phenotypes (91–94). In each new case, both *PIEZO2* alleles have base changes that cause premature stop mutations, truncating protein translation such that the ion channel permeation pathway found in the protein's C terminus is missing (**Figure 1c**). Together, these studies form the foundation for the diagnosis of the rare disease we now call PIEZO2 deficiency syndrome.

In parallel studies, the Patapoutian group described distinct *PIEZO2* mutations linked to a condition called distal arthrogyriposis type 5 (DA5). Similar to people with PIEZO2 deficiency syndrome, individuals with DA5 also have joint contractures and skeletal abnormalities, including short stature (36). However, detailed sensory evaluations have not yet been carried out for individuals with DA5, and the phenotypes of these patients include ophthalmoplegia (restriction of eye movement) and hypomimia (reduced facial expression) not seen with loss of PIEZO2 function. Notably, in vitro characterization of the biophysical properties of PIEZO2 channels affected by the point mutations seen in DA5 patients showed that these channels are slower to inactivate, likely leading to hyperexcitability or aberrant signaling of PIEZO2-expressing cells. These findings

indicate that at least one cause of DA5 may be *PIEZO2* gain of function. Interestingly, whole-exome sequencing has found potential gain-of-function mutations in *PIEZO2* linked to other types of distal arthrogryposis (type 3 or DA3) (95–97). As of today, dozens of potential disease-causing, gain-of-function mutations in *PIEZO2* have been identified (**Figure 1c**).

One of the most remarkable aspects of the human studies described above is how well they match conclusions drawn from animal studies, particularly those from mouse models. When considered together, a compelling picture has emerged of a conserved and essential role for *PIEZO2* as a principal mechanotransduction channel governing several key aspects of mechanosensation including touch, proprioception, and interoception. Next, we examine each sensory modality where *PIEZO2* function has been demonstrated to play an important role in mouse models and compare those results to the known clinical data.

3.2. Expression

Although a comprehensive survey has not been completed, it is clear that *PIEZO2* is predominantly expressed in sensory ganglia and limited types of epithelial cells. In mice, high levels of *PIEZO2* transcripts are found in the dorsal root and trigeminal ganglia (DRG and TG, respectively). These ganglia are comprised of the cell bodies of a heterogeneous group of peripheral sensory neurons that include multiple types of touch neurons, proprioceptors, thermoreceptors, and nociceptors (**Figure 2a,b**). Each type of sensory neuron has a unique transcriptomic profile, and often the expression of one or a few genes is enough to genetically identify them. This type of genetic classification has been useful in outlining which functional subtypes of sensory neurons express *PIEZO2*. Multicolor fluorescent in situ RNA hybridization and single-cell RNA sequencing experiments have demonstrated that within the DRG and TG, *PIEZO2* is detectable in all known types of low-threshold mechanoreceptors (LTMRs), consistent with a broad role in touch (see Section 3.3) (42, 98–101). These touch neurons can be differentiated by their physiological properties: fast-conducting, thickly myelinated, slowly adapting A β fibers (SA-LTMRs); fast-conducting, thickly myelinated, rapidly adapting A β fibers (RA-LTMRs); medium-conducting, thinly myelinated A δ fibers (A δ -LTMRs); and slow-conducting, unmyelinated C fibers (c-LTMRs) (102). *PIEZO2* is also found in select types of nociceptors including fast conducting A δ nociceptors and slowly conducting nonpeptidergic C nociceptors, indicating a potential role in pain. Notably, however, *PIEZO2* expression is not found in thermoreceptors or neurons believed to detect itch, consistent with the highly selective touch deficits seen in individuals with *PIEZO2* deficiency syndrome (however, for more details, see Section 3.5). Also, as expected from the clinical phenotypes, *PIEZO2* transcripts are particularly abundant in proprioceptors (see Section 3.6).

It is becoming increasingly clear that *PIEZO2* is very important for interoception as well as somatosensation (103–105). Single-cell sequencing of the mouse vagal complex revealed selective expression of *PIEZO2* in several classes of jugular and nodose ganglia neurons (JG and NG, respectively) (105). The JG contains the cell bodies of neurons that innervate somatic and visceral structures in the cranial and cervical regions. Transcriptomically, JG neurons closely resemble those found in other neural crest-derived ganglia (the DRG and TG) and likely perform analogous functions (**Figure 2c**). On the other hand, placode-derived NG neurons are quite distinct in terms of transcriptomic profile (**Figure 2d**) and functional roles. Deciphering the distinct functions of the different types of NG neurons remains an ongoing effort, but interestingly, *PIEZO2* is very selectively expressed in approximately half a dozen of these cell classes. Since many NG neurons innervate organs that contain tissues in highly dynamic mechanical environments (e.g., lungs, stomach, intestines, and bladder), it is not surprising that mechanotransduction through

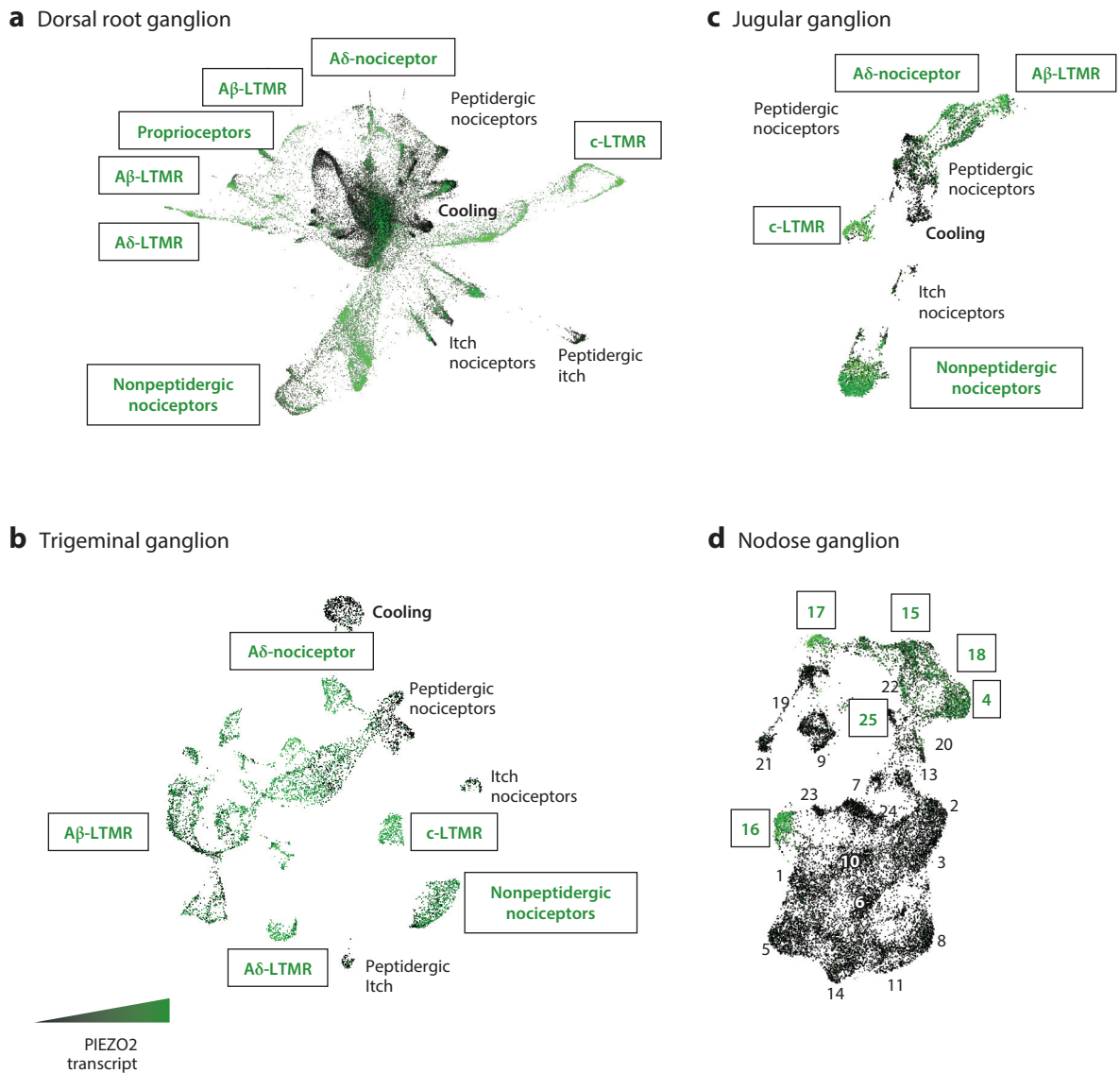


Figure 2

The expression of *PIEZO2* in mouse sensory neuron classes. Single-cell RNA sequencing data from four distinct peripheral ganglia are shown: dorsal root, trigeminal, jugular, and nodose. For each ganglion, transcriptomic cell classes are given in the UMAP plots with *PIEZO2* expression level visualized and color coded by high expression (*green*) or no expression (*black*). (a) Single-cell sequencing from isolated dorsal root ganglia neurons across development, with the earliest embryonic time points at the center of the UMAP and adult neurons at the outer edges (100). (b) Single-nucleus sequencing of trigeminal ganglia. Note that the more prominent representation of A β -LTMRs is likely to be the result of the nuclear isolation method (106), which better captures large-diameter neuron subtypes that are normally lost during single-cell isolation. (c) Single-cell sequencing of the vagal complex shows that cell classes in the jugular ganglia are transcriptomically analogous to those found in the dorsal root and trigeminal ganglia. (d) The nodose ganglion, on the other hand, is comprised of transcriptomically and functionally unique sensory neurons (105). The labels for classes of neurons with high *PIEZO2* expression are boxed, while those with low or no expression are in italics. Panel *a* adapted with permission from Reference 100, panels *b* and *d* adapted with permission from Reference 105, and panel *c* adapted from Reference 106. Abbreviations: LTMR, low-threshold mechanoreceptor; UMAP, uniform manifold approximation and projection.

PIEZO2 is important for aspects of breathing (see Section 3.7), bladder control (see Section 3.9), blood pressure regulation (see Section 3.10), and likely many other interoceptive processes.

3.3. Touch

Complete loss of function of PIEZO2 in mice results in mortality within hours after birth due to a breathing deficit (107, 108). Therefore, strategies to examine PIEZO2 function have relied on conditional gene knockout ($PIEZO2^{fl/-}$), whereby cell-type-specific promoters driving Cre recombinase allow for the elimination of $PIEZO2$ in subsets of cells. Early studies used the *Advillin* gene (*Adv*) to drive a drug-inducible version of Cre (CreERT2) that allowed for postnatal $PIEZO2$ knockout in peripheral neurons (109). $Adv^{CreERT2};PIEZO2^{fl/-}$ mice treated with tamoxifen as adults were found to have reduced brush sensitivity, elevated withdrawal thresholds to punctate touch (von Frey assay), and several touch-related behavioral defects (i.e., failed to remove small pieces of adhesive tape from their backs or avoid mildly aversive vibrating floors) (35). While these phenotypes were consistent with PIEZO2 having a broad role in gentle touch sensation, the animals still responded to many types of mechanical stimuli, albeit with reduced sensitivity. Moreover, electrical recordings from an ex vivo preparation revealed a reduction in evoked action potentials to mechanical stimuli in only a portion of neurons. Notably, the touch deficits of $Adv^{CreERT2};PIEZO2^{fl/-}$ mice were less severe than those that were subsequently reported for human subjects with PIEZO2 loss of function. PIEZO2 deficiency syndrome patients required orders of magnitude more force compared to healthy volunteers before detecting a von Frey filament and were unable to feel brushing on the palm of the hand or detect a vibrating probe (24, 38).

Recently developed approaches to knock out murine PIEZO2 expression cause more severe mechanosensory phenotypes in mice that better match those reported for humans, suggesting that the prior conditional strategy was incompletely effective. Crossing $PIEZO2^{fl/-}$ mice with $HoxB8^{Cre}$ animals results in loss of expression of PIEZO2 in the majority of sensory neurons from the cervical region of the spinal cord and more caudal regions (37). These mice survive to adulthood, presumably because neurons including those in the jugular complex and rostral DRG do not lose PIEZO2 expression (see Section 3.7), allowing for behavioral and functional characterization. $HoxB8^{Cre};PIEZO2^{fl/-}$ mice are completely insensitive to von Frey stimulation of their paws. Additionally, skin-nerve recordings from these mutant mice show that the majority of A β and A δ fibers require PIEZO2 for mechanosensitivity to touch stimuli, whereas C fibers were less affected (37). $PIEZO2$ can also be knocked out through systemic injection of viral vectors (38). Injection of AAV vectors encoding Cre into newborn $PIEZO2^{fl/fl}$ mice results in recombination in peripheral neurons throughout the body with 50–90% efficiency. As seen in the $HoxB8^{Cre}$ animals, high-efficiency knockout of $PIEZO2$ using viral vectors (>80% of sensory neurons) results in profound behavioral deficits to punctate and dynamic touch stimuli. Importantly, in vivo Ca^{2+} imaging revealed that PIEZO2 is absolutely required for responses to gentle brush and vibration across a range of frequencies (38, 79); responses to high-intensity mechanical stimuli such as pinch, however, remain intact. Together these studies show that PIEZO2 is the principal touch receptor for many types of dynamic, punctate, and repetitive mechanical stimuli in the innocuous range (Figure 3).

It has become well appreciated that some nonneuronal cells in the skin can express PIEZO2 and play important roles in touch. Particularly important are the interactions between slowly adapting type I A β neurons (SA1-LTMRs) and specialized epithelial (Merkel) cells. The function of Merkel cells in touch was debated (110–113), but studies from the Lumpkin group and others have provided clear evidence that they have a primary sensory role by showing that these cells are required for normal touch responses (114, 115). Mouse Merkel cells were demonstrated to be intrinsically mechanosensitive, relying on PIEZO2 for mechanotransduction; additionally, PIEZO2














		 PIEZO2-deficiency syndrome	 Cellular function and molecular mechanism
	Proprioception	Difficulty walking Pseudoathetosis Loss of coordination ^(23, 90–92)	Loss of mechanosensitivity in proprioceptive neurons ^(39, 125)
	Touch	Severe loss of touch sensitivity in glabrous skin Partial loss of touch sensitivity in hairy skin Loss of sensitivity to vibration ^(24, 38)	Severe loss of A β - and A δ -LTMR mechanosensitivity ^(35, 77, 78) Loss of DRG neuron responses to brushing on the skin ⁽³⁸⁾
	Pain	Severe loss of perception of neurogenic mechanical allodynia ⁽³⁸⁾	Loss of LTMR response in mechanical neurogenic and immunogenic allodynia ^(37, 38, 60)
	Itch	Not reported	Change in firing rates of SAI-LTMR afferents due to loss of Merkel cell response component ⁽¹²²⁾
	Breathing	Difficulty breathing in infancy No deficits described in adult patients ^(24, 38)	Loss of DRG neuron and urothelial cell mechanosensitivity disrupts neonatal breathing pattern development and Heuring-Bauer reflex, respectively ⁽¹⁰⁷⁾
	Bladder	Diminished perception of urinary urgency Other urinary dysfunctions ⁽¹⁴⁰⁾	Loss of DRG neuron and urothelial cell mechanosensitivity impairs detection of low-pressure bladder filling and synchronous voiding ⁽¹⁴⁰⁾
	Baroreflex	Not reported	Baroreflex requires PIEZO1- and PIEZO2-dependent mechanosensitivity of vagal neurons ⁽⁴⁰⁾
	Gut	Not reported	PIEZO2 is required for mechanically induced serotonin release in enterochromaffin cells ⁽¹³³⁾ Colon-projecting DRG neurons express PIEZO2 ^(130–139)
	Hearing	Normal	Reverse polarity response in hair cells of the mammalian auditory system ^(150, 151)
	Cartilage	Not reported	PIEZO2 and PIEZO1 expressed in chondrocytes and are needed for in vitro response to high-level strain ⁽¹⁴⁷⁾
	Bone	Hip dysplasia Progressive scoliosis symptoms likely due to diminished proprioceptive input ^(24, 90–92)	PIEZO1 and 2 mechanotransduction needed for synchronization of bone formation ⁽⁸²⁾ Skeletal malformations due to diminished proprioceptive input ⁽¹⁴⁹⁾

Figure 3

Biological systems in which PIEZO2 transduction is involved. The left column summarizes the clinical phenotypes reported in PIEZO2 deficiency syndrome. The right column describes the physiological roles of PIEZO2 in mouse models that may underlie each phenotype. Abbreviations: DRG, dorsal root ganglion; LTMR, low-threshold mechanoreceptor; SAI-LTMR, slowly adapting type I A β -LTMR.

expression in these cells was shown to be necessary for normal A β SAI-LTMR responses (77, 116). A two-part mechanism for how the Merkel cell–neurite complex transduces touch stimuli has been proposed, whereby both the primary sensory neuron and Merkel cells use PIEZO2 for mechanotransduction and contribute to the responses generated by different phases of sustained touch (117).

While it is clear that PIEZO2 is broadly required for touch transduction, many questions remain to be answered. Sensory neurons are functionally and anatomically heterogeneous, and the exact contribution of PIEZO2 to each class has yet to be determined. At the subcellular level, knowing where PIEZO2 molecules localize within afferent terminals in skin is important for determining how force is transmitted through tissue and gates these molecules with such exquisite sensitivity.

3.4. Mechanical Pain

In addition to being expressed in LTMRs, PIEZO2 is also present in several classes of pain-sensing somatosensory neurons defined as nociceptors (**Figure 2a,b**), raising the possibility that this receptor plays a role in the sensation of mechanical pain. Optogenetic activation of all *PIEZO2*-expressing neurons in mice evokes nocifensive behaviors such as flinching, guarding, and licking (37). *HoxB8^{Cre};PIEZO2^{fl/-}* mice also need over four times the mechanical force as wild type controls to induce paw withdrawal and fail to properly respond to punctate touch stimulation using forces in the noxious range (37). However, cells lacking *PIEZO2* still exhibit robust Ca^{2+} responses in vivo to pinching during functional imaging studies (38). Individuals with PIEZO2 deficiency syndrome also display normal perceptual thresholds to acute mechanical nociceptive stimuli (38). Therefore, from both studies, it appears PIEZO2 may be important for some aspects of acute mechanical pain detection, but it is not the primary mechanotransducer for this modality. As-yet-undiscovered and recently identified ion channels such as Tmem63 (118) or TACAN (119) are potential candidate high-threshold mechanotransducers. Furthermore, nonneuronal cells, notably terminal Schwann cells (120), have been implicated as having an important role in the transduction of noxious stimuli.

Following tissue injury and inflammation, normally innocuous mechanical stimuli, such as gentle touch, become painful. This sensory transformation, called mechanical allodynia, is a leading symptom in clinical pain and is often therapeutically intractable. Notably, mice lacking *PIEZO2* and human individuals with PIEZO2 deficiency syndrome do not become oversensitive to touch stimuli, showing that PIEZO2 is essential for mechanical allodynia. Specifically, in vivo Ca^{2+} imaging showed that neural responses to gentle touch and vibration required PIEZO2 expression, even during conditions known to produce profound touch hypersensitivity (38). Furthermore, behavioral responses to gentle mechanical stimuli are not sensitized by tissue inflammation or nerve injury in *HoxB8^{Cre};PIEZO2^{fl/-}* mice (37). Most importantly, tactile allodynia was evaluated in human subjects experimentally using a capsaicin neurogenic inflammation model. Healthy volunteers invariably found the area surrounding inflammation to be more painful to touch than reference sites, whereas individuals with PIEZO2 deficiency syndrome failed to report altered touch-evoked sensations, painful or otherwise (38). Together, these studies provided compelling evidence that mechanical allodynia is mediated by mechanotransduction through PIEZO2 (**Figure 3**).

The detailed mechanisms through which PIEZO2 contributes to mechanical allodynia remain uncertain. In the periphery, PIEZO2 channels have been shown to be potentiated downstream of proinflammatory compounds like bradykinin (84) and second messenger proteins such as Epac1 (60). These biophysical changes can sensitize sensory neurons, making them easier to activate or making their responses to mechanical stimuli last longer. In the central nervous system, tissue damage and inflammation cause alterations in information processing in the dorsal spinal cord. Under normal conditions, touch and pain sensations result from activation of distinct ascending pathways. The prevalent gate-control model states that mechanical allodynia arises when neurons carrying information about gentle mechanical stimulation of skin gain access to the ascending nociceptive pathways. In this scenario, the absence of PIEZO2 blocks LTMR touch responses;

consequently, mechanical allodynia simply cannot occur. Recently, a specific A δ -LTMR subtype that expresses high levels of PIEZO2 has been proposed to be particularly important for driving mechanical allodynia (121). Together these findings indicate that PIEZO2 may prove an advantageous pharmacological target with widespread clinical relevance, as its loss of function does not impair biologically useful acute pain sensing but instead abolishes hypersensitivity and aberrant pain perception.

3.5. Itch

Itch is yet another complex human experience where advances have been made in recent years by correlating human clinical experiences with experiments in animal models (122). A recent rodent study has linked PIEZO2 to a pathological form of mechanical itch known as alloknesis, or excessive itching evoked by light touch, through an indirect pathway (123). The authors found that in aged mice, where the activity of A β SA1-LTMRs decreases because of Merkel-cell loss, alloknesis is much more prominent. Further experiments revealed that loss of Merkel cell activity is necessary and sufficient for alloknesis. Interestingly, the same result can be achieved by knocking out PIEZO2 expression only in Merkel cells. Together, these findings indicate that PIEZO2 in the Merkel cell afferent pathway may not only act as a touch detector but also help maintain the tone of A β SA1-LTMRs and suppress itch circuitry in the spinal cord (**Figure 3**) (124).

To date, no differences in itch sensitivity have been reported in PIEZO2 deficiency syndrome. This may be a result of the relatively young patient demographic, as alloknesis is a typically late-onset condition. Alternatively, the global absence of PIEZO2 in both sensory neurons and Merkel cells in these individuals may result in much more dramatic silencing of A β SA1-LTMRs such that itch is less likely to occur. Further clinical assays focused on addressing the role of PIEZO2 in itch and potential translational implications of the findings in mice are important.

3.6. Proprioception

Based on clinical data, perhaps one of the most profound phenotypes seen in the absence of PIEZO2 function is the complete lack of proprioception. This underappreciated and poorly understood sense provides the brain with feedback about body position and posture (125) through proprioceptive neurons that innervate muscle spindles (which signal change in the length of muscles) and Golgi tendon organs (GTOs; which react to muscle tone). Individuals with PIEZO2 deficiency syndrome are uncoordinated, unable to sense joint positions, lack tendon reflexes, display pseudoathetosis, and have difficulty performing even simple motor tasks when deprived of visual inputs (24). Experiments in mice demonstrate that these phenotypes almost certainly arise from a failure of proprioceptive neurons to be activated by changing mechanical forces. Conditional deletion of *PIEZO2* in mouse proprioceptors (39) or across many classes of sensory neurons (37, 38) results in mice with severe ataxia, irregular gait, and atypical posture. Anatomical examination of muscle spindles and GTOs confirmed that loss of *PIEZO2* does not cause morphological changes to these end structures. Physiologically, however, PIEZO2 expression was required for stretch-evoked nerve responses from muscles *ex vivo* as well as mechanical responses from isolated proprioceptive neurons in culture (39). Interestingly, PIEZO2 is also functionally expressed in a small group of sensory neurons, located within the mesencephalic trigeminal nucleus in the brainstem, that are thought to perform proprioceptive functions for the head and require this receptor for mechanosensitivity (126). Collectively, these experiments demonstrate an essential function of PIEZO2 for proprioception in both mice and humans (**Figure 3**).

Although the identification of PIEZO2 as the primary transducer of proprioception provided a molecular understanding of the sense, many questions about PIEZO2's functional and temporal

roles remain unanswered. For example, all mouse proprioceptive fibers fire slowly adapting action potentials that persist over the course of seconds; however, the vast majority of PIEZO2 responses recorded in proprioceptive neurons adapt rapidly on the order of milliseconds (39). How PIEZO2 mediates sustained firing in these cells remains unknown. An even more intriguing question stems from clinical observations showing that, despite significant impairments, individuals with PIEZO2 deficiency syndrome develop a number of compensatory strategies to perform motor tasks. The central mechanisms underlying these adaptations may reveal new features governing plasticity and flexibility of the neural circuits controlling proprioception.

3.7. Breathing

Breathing is an essential physiological process that requires interoceptive sensing of pressure in the upper and lower respiratory tract. When PIEZO2 is globally ablated in mice, newborn pups suffer respiratory distress and die within a day of birth (108). Similarly, human infants born with PIEZO2 deficiency syndrome require emergency oxygen support at birth and continue to exhibit diminished breath support with shallow breathing throughout life (24). Together, these results indicate that PIEZO2 is required for newborn mammals to make the transition from umbilical oxygen supply to air breathing.

The lungs are exposed to continuous mechanical stresses and need to sequentially compress and decompress; not surprisingly, many of the sensory neurons innervating them are mechanosensitive (127, 128). *PIEZO2* is prevalently expressed in several classes of lung-innervating NG, TG, and DRG neurons (**Figure 2a–d**) (105, 129, 130). Lung neuroepithelial cells also express *PIEZO2* (42, 108). *PIEZO2* knockout from all of the JG, TG, and DRG results in similar lethality from respiratory distress as seen in germline *PIEZO2* knockouts. By contrast, mice lacking *PIEZO2* expression only in lung epithelial cells have normal breathing, and mice with selective loss of *PIEZO2* in NG neurons survive but inhale more air per breath and exhibit a diminished Hering–Breuer reflex. The phenotype of mice subjected to *PIEZO2* knockout induced during adulthood is also less severe, involving lower vagal nerve firing and increased respiration activity during lung inflation. Together, these results indicate that mechanosensory neurons in the vagal complex and DRG use *PIEZO2* to sense and control respiration throughout development and into adulthood (**Figure 3**) (108).

3.8. Gastrointestinal Tract

Another organ system in which mechanosensation is critically important is the gut. Many of the tasks for which the gastrointestinal (GI) tract is responsible require mechanosensory information, including peristalsis, digestion, hunger, and satiety signaling. Innervation of the GI tract is correspondingly complex, and *PIEZO2* is expressed in endothelial cells of the gut as well as various myenteric and sensory neurons (131, 132). Therefore, recent studies have sought to define the role of *PIEZO2* in the gut, since discoveries in this area may have relevance to several GI pathologies.

Enteroendocrine cells (ECs) within the gut can autonomously regulate aspects of GI function via sensory-stimulated hormone and neurotransmitter release (133). Recently, *PIEZO2* was shown to be expressed in ECs; these cells respond to mechanical stimulation *in vitro* and signal slow intestinal stretch *in vivo* (109). In a subset of ECs known as enterochromaffin cells, *PIEZO2* activity is partly responsible for neurotransmitter release (134), a process thought to contribute to a host of symptoms in inflammatory bowel diseases when disrupted (135). A series of parallel and elegant tracing studies showed that another subpopulation of ECs participates in volume sensing in the gut and forms a glutamatergic synapse with sensory neurons (136, 137). Through this mechanism,

ECs can send fast signals to vagal afferents about intestinal content (138). While PIEZO2 expression was not evaluated in these tracing studies, it is tempting to speculate that mechanical stimuli may also trigger these important physiological responses in a PIEZO2-dependent mechanism.

Compared to that in ECs, the role of PIEZO2 in sensory neurons targeting the gut is less well studied. In mice, transcriptomic profiling of colon-projecting DRG neurons has revealed that *PIEZO2* is widely expressed among the diverse sensory neuron populations targeting the lower intestine, but the specific functions of each remain to be tested (132). Additionally, the function of PIEZO2 in the NG neurons that innervate the upper intestine is currently unknown. Recent evidence suggests that one subset of these neurons is likely to be a class of silent nociceptors previously shown to prevalently innervate internal organs (139). These nociceptors express PIEZO2 but have very limited mechanical sensitivity, except after exposure to proinflammatory molecules (140). Future studies should clarify whether this mechanism is clinically relevant in humans (**Figure 3**).

3.9. Bladder

Early transcriptomic data in mice pointed to the bladder as an organ outside of the peripheral nervous system that contains *PIEZO2*-expressing cells (30, 38), but it was completely unknown how PIEZO2 influences bladder physiology. Recently, PIEZO2 was demonstrated to be required for normal urinary system function (141). When patients with PIEZO2 deficiency syndrome are questioned about urinary routines and deficiencies, multiple manifestations of bladder dysfunction are evident (24, 141). Their symptoms include decreased voiding frequency, difficulty urinating, and urinal urgency.

Genetic mouse models reveal that PIEZO2 is the principal mechanotransduction channel for low-pressure mechanical activation of bladder-innervating neurons, but high-pressure sensing by a subset of DRG neurons is PIEZO2 independent (141). Careful investigation demonstrated that PIEZO2 is required for synchronization and triggering of micturition reflexes, and *PIEZO2* knockout animals show signs of bladder pathology (bladder wall hypertrophy). Interestingly, it appears that *PIEZO2* expression in both urothelial cells and bladder afferent neurons is required for proper micturition (141). These findings open a new field of study investigating the role of PIEZOs in bladder function (*PIEZO1* is also expressed in bladder tissue). Future work is needed for the molecular identification of specific mechanosensitive neurons and epithelial cells in the bladder, with a goal of elucidating their exact roles in precisely tuning pressure detection in the urinary system.

3.10. Baroreflex

The baroreflex plays a vital role in maintaining homeostasis of blood pressure. For instance, when blood pressure increases, the baroreflex causes heart rate to drop and return pressure to baseline levels. Specific sensory neurons (baroreceptors) innervate the carotid sinus and aortic arch, which are stretch-susceptible tissues that may facilitate this pressure sensing (142). In 2018, Zeng et al. (40) provided evidence that baroreceptors rely on both *PIEZO1* and *PIEZO2* for mechanotransduction (143). The double conditional knockout of *PIEZO1* and *PIEZO2* from the vagal sensory neurons abolishes the baroreflex, with the resulting mutant mice exhibiting unstable blood pressure. Additionally, when *PIEZO2*-expressing carotid sinus and superior laryngeal nerves were optogenetically stimulated, the heart rate and blood pressure of mice fluctuated by over 50%. While some vagal neurons express both *PIEZO1* and *PIEZO2*, most neurons express only one of these channels, suggesting diversity within the baroreceptor population (40).

Recently, Min et al. (104) provided further structural insight into the organization of the baroreceptor by showing that *PIEZO2*-expressing neurons form a distinct macroscopic claw-like

terminal in the walls of the aorta. When these neurons were ablated from the vagus and glossopharyngeal nerves, heart rate was severely affected. These results further underscore the fact that PIEZO2 is involved with interoceptive processes as well as somatosensation (**Figure 3**).

3.11. Additional Biological Roles

In addition to the mechanosensory functions described in Sections 3.1–3.10, PIEZO2 may have clinically relevant roles in additional tissues. For example, PIEZO2 is found in neurons innervating the dental pulp and tongue of mice (144–146) and may contribute to mouthfeel or toothache. *PIEZO2* is also expressed in mouse bone stem cells, where it may be involved in mechanical signaling during bone formation and growth (83), as well as in chondrocytes, a component of cartilage that undergoes constant mechanical stress (147–149). The presence of PIEZO2 in cells related to bone development may explain the abnormal skeletal phenotypes found in individuals with PIEZO2 deficiency syndrome, although recent evidence supports the hypothesis that many of these deficits arise from lack of proprioception (150). *PIEZO2* is also functionally expressed in hair cells of the mouse auditory system. While the bulk of mechanotransduction in the ear is carried out by other channels, the reverse-polarity current resulting from nonphysiological bending of stereocilia is dependent on PIEZO2 (151, 152). It is apparent from these studies that our knowledge of PIEZO2 in various aspects of mechanosensation is still far from complete.

4. NEW MODEL SYSTEMS AND PHARMACOLOGICAL INTERVENTIONS

4.1. Human Stem Cell–Based Models

PIEZO2 has been difficult to study in humans due to the limited accessibility of the tissues in which it resides and the rarity of PIEZO2 deficiency syndrome. To circumvent this problem, induced pluripotent stem cells (iPSCs) can be developed from patients and healthy subjects; iPSCs can theoretically produce any human cell type in vitro, providing an exciting new platform to examine PIEZO2 function in human cells. In this section, we focus on the use of iPSC technology to study human peripheral sensory neurons, since these are cells in which PIEZO2 exerts many of its physiological effects.

When exposed to a specific and empirically determined cocktail of five small molecules, iPSCs can be directed to differentiate into peripheral sensory neurons over the course of a few weeks (153). Neurons produced via this method express PIEZO2 (154); however, several research groups have reported different results with the protocol, ranging from the exclusive generation of nociceptors to a mixture of sensory neuron subtypes with uncertain identities (153, 155–158). To study PIEZO2 in individual cellular subtypes, iPSCs can be more selectively differentiated into just a single category of sensory neuron by forcing overexpression of transcription factors that specify distinct sensory neuron subtypes. A brief pulse of NGN2 expression in iPSC-derived neural crest cells produces large-diameter, PIEZO2-positive touch neurons (78). The yield of this neuronal subtype can be greatly enhanced by additionally expressing the prosensory neuron factor BRN3A (90). Long-term coexpression of NGN2 and BRN3A converts iPSCs into a subtype of cold-sensing mechanoreceptor that also relies on PIEZO2 for mechanosensitivity (90). Overexpression of NGN1 instead generates various populations of heat-sensing nociceptors (159).

Moving forward, the creation of a single-cell RNA sequencing atlas of human sensory ganglia should be an urgent goal (160). Such a resource would reveal key differences between humans and commonly used animal models and also identify which human sensory neuron subtypes express

PIEZO2 and other markers. The sequencing atlas could then be used as a template for determining how closely iPSC-derived sensory neurons generated through different protocols mimic in vivo sensory neurons—this is a crucial step toward developing naturalistic in vitro models to examine PIEZO2 structure, biochemistry, physiology, and pharmacology in specific human cell types.

4.2. PIEZO2 Drug Discovery

Exploring the pharmacology of PIEZO2 represents a new and exciting avenue of research, since the ability to chemically control PIEZO2 could have a profound impact on basic research and treatment for diseases of mechanosensation. There are currently no known drugs or endogenous ligands that specifically bind PIEZO2. However, high-throughput screens on PIEZO1 have already identified several small-molecule agonists, indicating that this family of ion channels can be chemically modulated (161, 162). In this section, we discuss potential strategies for PIEZO2 drug discovery in light of prior studies on PIEZO1 and other mechanosensitive proteins.

PIEZO2 agonists would undoubtedly serve as useful research tools. Currently, to study PIEZO2 transduction, a physical stimulus must be used to deflect the cell body or neurite membrane (58, 66), and this greatly constrains the types of experiments that can be used to investigate PIEZO2-related physiology. Chemical activation of PIEZO2 presents a more selective and less invasive way to trigger channel gating, which would be amenable to bulk or high-throughput in vitro transduction assays, as well as in vivo applications. PIEZO2 agonists could also have clinical utility in treating mechanosensory disorders. For example, certain forms of chronic itch have been linked to a reduction of PIEZO2-expressing cells in the skin (163). In such conditions, drug-induced activation of PIEZO2 might suppress pathological itch signals.

In the case of PIEZO1, agonists were found by high-throughput chemical screening on HEK293T cells overexpressing mouse PIEZO1 (160, 162). Taking advantage of the Ca^{2+} current mediated by PIEZO1 activation, intracellular Ca^{2+} levels were imaged in a fluorescent imaging plate reader (FLIPR). This approach identified the validated PIEZO1 agonists Yoda1, Jedi1, and Jedi2. The same strategy was used in an attempt to identify PIEZO2 agonists, but no agonists were found (160, 162). One possible explanation for this failure is that, because PIEZO2 currents inactivate more rapidly than PIEZO1 (30), the Ca^{2+} influx and fluorescent signal are below the thresholds required by the FLIPR to detect channel opening.

In contrast to agonists, there are no known antagonists that are specific to either PIEZO1 or PIEZO2. Existing molecules such as GsMTx4 and margaric acid nonspecifically affect mechanotransduction by changing the properties of the plasma membrane (50, 59, 164). A PIEZO2-selective antagonist would be a valuable substitute for using genetic knockout approaches to decipher the causal physiological effects of PIEZO2. Also, given that PIEZO2 loss of function prevents mechanical allodynia, PIEZO2 antagonists have been suggested as a treatment for this painful skin condition (37, 38).

Screening for antagonists of PIEZO2 will likely be even more challenging than the search for agonists. Such a screen would presumably require a mechanical stimulus to activate PIEZO2 in a high-throughput cell culture format, and antagonists would be identified based on their ability to block the mechanically evoked PIEZO2 current (**Figure 4**). Membrane stretch, pull, indentation, fluid shear stress, and substrate deformation are examples of stimuli that have been classically applied in a low-throughput setting (30, 42, 66, 165, 166). However, some of these techniques are now being scaled up and may be amenable for mechanical screening of PIEZO2 (167–172).

Given that PIEZO2 has several physiological roles, even if selective agonists and/or antagonists are identified, systemic drug delivery methods may not safely treat a single function in isolation. Incorporation of PIEZO2 drugs into a topical ointment is one strategy for targeting

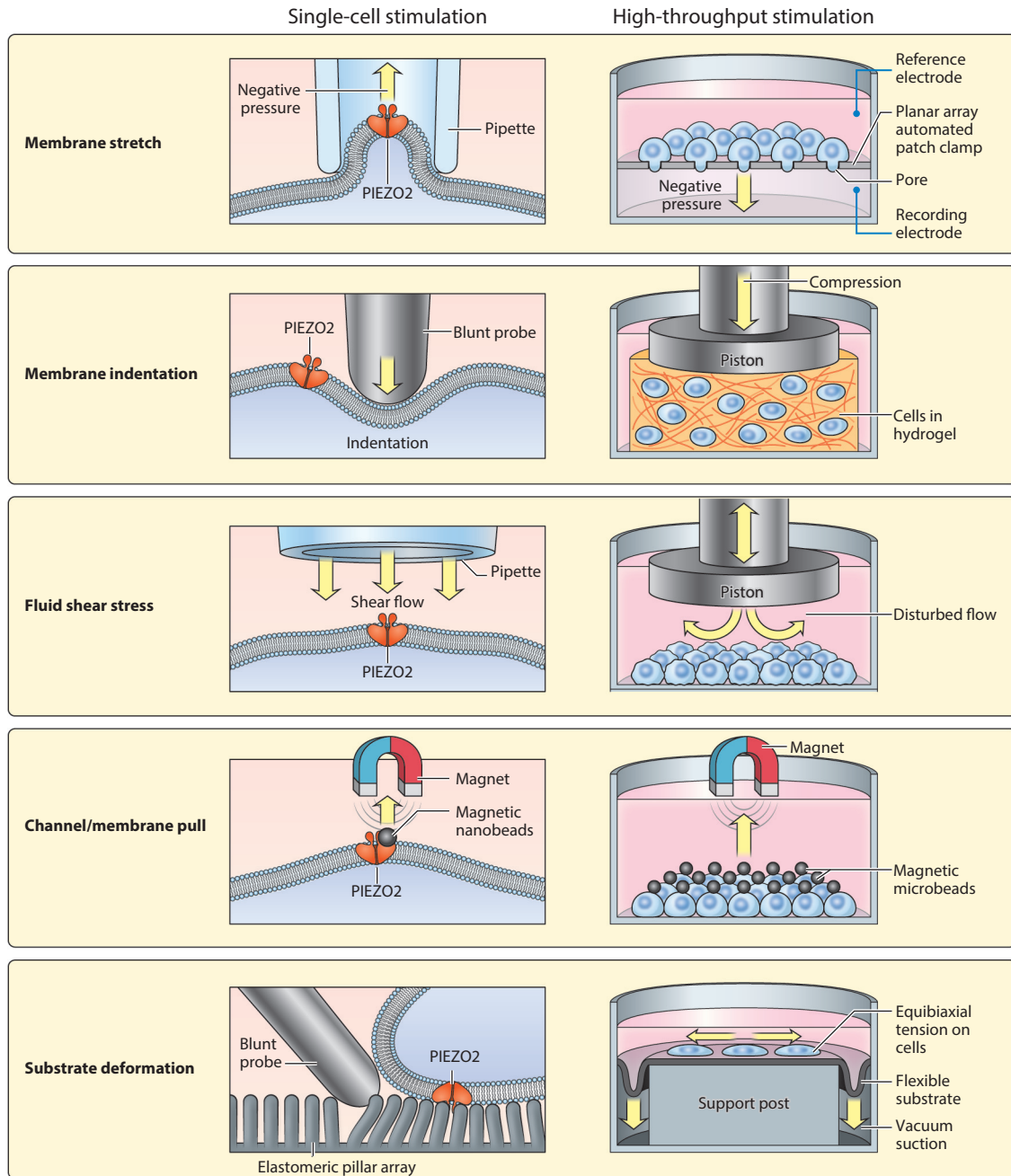


Figure 4

Adapting single-cell mechanical stimulation methods to high-throughput formats. (*Left*) Existing methods for applying mechanical force to the cell membrane. For reference, a graphic depiction of a single PIEZO2 channel is shown in dark orange spanning the cell membrane. (*Right*) Potential strategies for adapting each method for use in high-throughput screening platforms. Yellow arrows indicate the direction of mechanical force in each assay.

channel function in the skin without affecting internal organs, as has been suggested for treating mechanical allodynia (37, 38). It is important to test various drug vehicles and delivery routes to ensure that essential PIEZO2 functions, such as respiration and proprioception, are not affected.

5. CONCLUDING REMARKS AND FUTURE PERSPECTIVES

The year 2020 marked a decade since the discovery of PIEZO2. Thanks to mechanistic studies in animal models and humans, multiple milestones have been achieved in the last decade: PIEZO2 is now established as the principal mechanotransducer in several organ systems, a structural basis for PIEZO2 mechanosensitivity has been outlined, and clinically relevant roles for PIEZO2 have been identified in humans. Now, the journey to pinpoint the cellular and molecular underpinnings of PIEZO2 mechanotransduction is entering a new phase with different challenges and opportunities ahead.

Pioneering studies have demonstrated that PIEZO2 is evolutionarily repurposed across multiple seemingly unrelated mechanical senses, ranging from touch and proprioception to respiration. One of the major efforts at hand is to elucidate PIEZO2 function in all sensory cell types that express it. Very little is known about the physiological tuning, modulation, and molecular anatomy of PIEZO2 in various cells in the peripheral nervous system. Progress in sophisticated mechanical stimulation assays and loss-of-function behavioral models offers new tools to investigate these topics (166, 173, 174).

Another subject of great interest centers around the molecular basis of PIEZO2-independent mechanotransduction. Several mechanosensory processes, notably mechanical pain, persist in the absence of PIEZO2 (24, 37, 38). Definitively identifying the proteins that mediate these specific modalities remains an area of active research (118, 119). Given the broad expression of PIEZO2 in sensory ganglia (**Figure 2**), further work is needed to understand the specific roles that different mechanotransducer proteins play with respect to one another.

The discovery of PIEZO2 deficiency syndrome was a defining moment for translational research on mechanosensation. Being able to talk with these patients has added a dimension simply unachievable in animal studies. Most importantly, the mouse and human data complement each other to provide a broad and consistent view of PIEZO2 function. Together, these data have put a spotlight on how targeting this molecule pharmacologically may be useful for treating a range of clinical conditions involving mechanotransduction. In just 10 years since the discovery of PIEZO2, we have gone from not even knowing what the touch receptor was to having an extensive understanding of its form and function as well as its clinical relevance. This review set out to highlight how much we have learned and, in doing so, has hopefully also made clear that there are many exciting things left to learn about this remarkable protein.

DISCLOSURE STATEMENT

The authors are not aware of any affiliations, memberships, funding, or financial holdings that might be perceived as affecting the objectivity of this review.

ACKNOWLEDGMENTS

We would like to thank Mark Hoon, Claire Le Pichon, Valeria Vasquez, Ardem Patapoutian, Kara Marshall, Jennifer Osborne, and Sarah Shnyder for feedback on the manuscript. We would like to thank David Ginty, Stephen Liberles, Nicholas Ryba and Bailong Xiao for generously providing data and permission to adapt their data into **Figures 1** and **2**. This research was supported by

the National Center for Complementary and Integrative Health Intramural Research Program and the National Center for Advancing Translational Sciences through the National Institutes of Health Helping to End Addiction Long-termSM (HEAL) Initiative. The content is solely the responsibility of the authors and does not necessarily represent the official views of the National Institutes of Health or its HEAL Initiative.

LITERATURE CITED

1. Iggo A, Andres KH. 1982. Morphology of cutaneous receptors. *Annu. Rev. Neurosci.* 5:1–31
2. Sherrington C. 1906. *The Integrative Action of the Nervous System*. New Haven: Yale Univ. Press
3. Perl E. 1968. Myelinated afferent fibres innervating the primate skin and their response to noxious stimuli. *J. Physiol.* 197:593–615
4. Burgess P, Petit D, Warren RM. 1968. Receptor types in cat hairy skin supplied by myelinated fibers. *J. Neurophysiol.* 31:833–48
5. Brown A, Iggo A. 1967. A quantitative study of cutaneous receptors and afferent fibres in the cat and rabbit. *J. Physiol.* 193:707–33
6. Loewenstein WR, Rathkamp R. 1958. Localization of generator structures of electric activity in a Pacinian corpuscle. *Science* 127:341
7. Alvarez-Buylla R, De Arellano JR. 1952. Local responses in Pacinian corpuscles. *Am. J. Physiol.* 172:237–44
8. Corey D, Hudspeth A. 1979. Ionic basis of the receptor potential in a vertebrate hair cell. *Nature* 281:675–77
9. Neher E, Sakmann B. 1976. Single-channel currents recorded from membrane of denervated frog muscle fibres. *Nature* 260:799–802
10. Guharay F, Sachs F. 1984. Stretch-activated single ion channel currents in tissue-cultured embryonic chick skeletal muscle. *J. Physiol.* 352:685–701
11. Sakmann B, Bormann J, Hamill OP. 1983. Ion transport by single receptor channels. *Cold Spring Harb. Symp. Quant. Biol.* 48(Part 1):247–57
12. Chalfie M. 2009. Neurosensory mechanotransduction. *Nat. Rev. Mol. Cell Biol.* 10:44–52
13. Caterina MJ, Schumacher MA, Tominaga M, Rosen TA, Levine JD, Julius D. 1997. The capsaicin receptor: a heat-activated ion channel in the pain pathway. *Nature* 389:816–24
14. Julius D. 2013. TRP channels and pain. *Annu. Rev. Cell Dev. Biol.* 29:355–84
15. Dhaka A, Viswanath V, Patapoutian A. 2006. Trp ion channels and temperature sensation. *Annu. Rev. Neurosci.* 29:135–61
16. Martinac B, Buechner M, Delcour AH, Adler J, Kung C. 1987. Pressure-sensitive ion channel in *Escherichia coli*. *PNAS* 84:2297–301
17. Sukharev SI, Blount P, Martinac B, Blattner FR, Kung C. 1994. A large-conductance mechanosensitive channel in *E. coli* encoded by mscL alone. *Nature* 368:265–68
18. Gustin MC, Zhou X-L, Martinac B, Kung C. 1988. A mechanosensitive ion channel in the yeast plasma membrane. *Science* 242:762–65
19. Martinac B, Adler J, Kung C. 1990. Mechanosensitive ion channels of *E. coli* activated by amphipaths. *Nature* 348:261–63
20. Chalfie M, Au M. 1989. Genetic control of differentiation of the *Caenorhabditis elegans* touch receptor neurons. *Science* 243:1027–33
21. O'Hagan R, Chalfie M, Goodman MB. 2005. The MEC-4 DEG/ENaC channel of *Caenorhabditis elegans* touch receptor neurons transduces mechanical signals. *Nat. Neurosci.* 8:43–50
22. Walker RG, Willingham AT, Zuker CS. 2000. A *Drosophila* mechanosensory transduction channel. *Science* 287:2229–34
23. Petit C. 2006. From deafness genes to hearing mechanisms: harmony and counterpoint. *Trends Mol. Med.* 12:57–64
24. Chesler AT, Szczot M, Bharucha-Goebel D, Čeko M, Donkervoort S, et al. 2016. The role of PIEZO2 in human mechanosensation. *N. Engl. J. Med.* 375:1355–64

25. Lumpkin EA, Bautista DM. 2005. Feeling the pressure in mammalian somatosensation. *Curr. Opin. Neurobiol.* 15:382–88
26. McBride DW Jr., Hamill OP. 1993. Pressure-clamp technique for measurement of the relaxation kinetics of mechanosensitive channels. *Trends Neurosci.* 16:341–45
27. McCarter GC, Reichling DB, Levine JD. 1999. Mechanical transduction by rat dorsal root ganglion neurons in vitro. *Neurosci. Lett.* 273:179–82
28. Delmas P, Hao J, Rodat-Despoix L. 2011. Molecular mechanisms of mechanotransduction in mammalian sensory neurons. *Nat. Rev. Neurosci.* 12:139–53
29. Drew LJ, Wood JN, Cesare P. 2002. Distinct mechanosensitive properties of capsaicin-sensitive and -insensitive sensory neurons. *J. Neurosci.* 22:Rc228
30. Coste B, Mathur J, Schmidt M, Earley TJ, Ranade S, et al. 2010. Piezo1 and Piezo2 are essential components of distinct mechanically activated cation channels. *Science* 330:55–60
31. McHugh BJ, Buttery R, Lad Y, Banks S, Haslett C, Sethi T. 2010. Integrin activation by Fam38A uses a novel mechanism of R-Ras targeting to the endoplasmic reticulum. *J. Cell Sci.* 123:51–61
32. Kim SE, Coste B, Chadha A, Cook B, Patapoutian A. 2012. The role of *Drosophila* Piezo in mechanical nociception. *Nature* 483:209–12
33. Faucherre A, Nargeot J, Mangoni ME, Jopling C. 2013. *piezo2b* regulates vertebrate light touch response. *J. Neurosci.* 33:17089–94
34. Schneider ER, Mastrotto M, Laursen WJ, Schulz VP, Goodman JB, et al. 2014. Neuronal mechanism for acute mechanosensitivity in tactile-foraging waterfowl. *PNAS* 111:14941–46
35. Ranade SS, Woo S-H, Dubin AE, Moshourab RA, Wetzel C, et al. 2014. Piezo2 is the major transducer of mechanical forces for touch sensation in mice. *Nature* 516:121–25
36. Coste B, Houge G, Murray MF, Stitzel N, Bandell M, et al. 2013. Gain-of-function mutations in the mechanically activated ion channel PIEZO2 cause a subtype of Distal Arthrogyposis. *PNAS* 110:4667–72
37. Murthy SE, Loud MC, Daou I, Marshall KL, Schwaller F, et al. 2018. The mechanosensitive ion channel Piezo2 mediates sensitivity to mechanical pain in mice. *Sci. Transl. Med.* 10: eaat9897
38. Szczot M, Liljencrantz J, Ghitani N, Barik A, Lam R, et al. 2018. PIEZO2 mediates injury-induced tactile pain in mice and humans. *Sci. Transl. Med.* 10: eaat9892
39. Woo S-H, Lukacs V, De Nooij JC, Zaytseva D, Criddle CR, et al. 2015. Piezo2 is the principal mechanotransduction channel for proprioception. *Nat. Neurosci.* 18:1756–62
40. Zeng WZ, Marshall KL, Min S, Daou I, Chapleau MW, et al. 2018. PIEZO2s mediate neuronal sensing of blood pressure and the baroreceptor reflex. *Science* 362:464–67
41. Coste B, Murthy SE, Mathur J, Schmidt M, Mechoukhi Y, et al. 2015. Piezo1 ion channel pore properties are dictated by C-terminal region. *Nat. Commun.* 6:7223
42. Szczot M, Pogorzala LA, Solinski HJ, Young L, Yee P, et al. 2017. Cell-type-specific splicing of Piezo2 regulates mechanotransduction. *Cell Rep.* 21:2760–71
43. Xiao B. 2020. Levering mechanically activated Piezo channels for potential pharmacological intervention. *Annu. Rev. Pharmacol. Toxicol.* 60:195–218
44. Liao M, Cao E, Julius D, Cheng Y. 2013. Structure of the TRPV1 ion channel determined by electron cryo-microscopy. *Nature* 504:107–12
45. Guo YR, MacKinnon R. 2017. Structure-based membrane dome mechanism for Piezo mechanosensitivity. *eLife* 6:e33660
46. Saotome K, Murthy SE, Kefauver JM, Whitwam T, Patapoutian A, Ward AB. 2018. Structure of the mechanically activated ion channel Piezo1. *Nature* 554:481–86
47. Zhao Q, Zhou H, Chi S, Wang Y, Wang J, et al. 2018. Structure and mechanogating mechanism of the Piezo1 channel. *Nature* 554:487–92
48. Wang L, Zhou H, Zhang M, Liu W, Deng T, et al. 2019. Structure and mechanogating of the mammalian tactile channel PIEZO2. *Nature* 573:225–29
49. Taberner FJ, Prato V, Schaefer I, Schrenk-Siemens K, Heppenstall PA, Lechner SG. 2019. Structure-guided examination of the mechanogating mechanism of PIEZO2. *PNAS* 116:14260–69
50. Romero LO, Caires R, Nickolls AR, Chesler AT, Cordero-Morales JF, Vásquez V. 2020. A dietary fatty acid counteracts neuronal mechanical sensitization. *Nat. Commun.* 11:2997

51. Lin Y-C, Guo YR, Miyagi A, Levring J, MacKinnon R, Scheuring S. 2019. Force-induced conformational changes in PIEZO1. *Nature* 573:230–34
52. Chesler AT, Szczot M. 2018. Piezo ion channels: portraits of a pressure sensor. *eLife* 7:e34396
53. Geng J, Liu W, Zhou H, Zhang T, Wang L, et al. 2020. A plug-and-latch mechanism for gating the mechanosensitive Piezo channel. *Neuron* 106:438–51.e6
54. Kung C. 2005. A possible unifying principle for mechanosensation. *Nature* 436:647–54
55. Cox CD, Bae C, Ziegler L, Hartley S, Nikolova-Krstevska V, et al. 2016. Removal of the mechanoprotective influence of the cytoskeleton reveals PIEZO1 is gated by bilayer tension. *Nat. Commun.* 7:10366
56. Syeda R, Florendo MN, Cox CD, Kefauver JM, Santos JS, et al. 2016. Piezo1 channels are inherently mechanosensitive. *Cell Rep.* 17:1739–46
57. Moroni M, Servin-Vences MR, Fleischer R, Sánchez-Carranza O, Lewin GR. 2018. Voltage gating of mechanosensitive PIEZO channels. *Nat. Commun.* 9:1096
58. Shin KC, Park HJ, Kim JG, Lee IH, Cho H, et al. 2019. The Piezo2 ion channel is mechanically activated by low-threshold positive pressure. *Sci. Rep.* 9:6446
59. Romero LO, Massey AE, Mata-Daboin AD, Sierra-Valdez FJ, Chauhan SC, et al. 2019. Dietary fatty acids fine-tune Piezo1 mechanical response. *Nat. Commun.* 10:1200
60. Eijkelkamp N, Linley J, Torres J, Bee L, Dickenson A, et al. 2013. A role for Piezo2 in EPAC1-dependent mechanical allodynia. *Nat. Commun.* 4:1682
61. Hu J, Chiang LY, Koch M, Lewin GR. 2010. Evidence for a protein tether involved in somatic touch. *EMBO J.* 29:855–67
62. Wu J, Lewis AH, Grand J. 2017. Touch, tension, and transduction—the function and regulation of Piezo ion channels. *Trends Biochem. Sci.* 42:57–71
63. Cordero-Morales JF, Vásquez V. 2018. How lipids contribute to ion channel function, a fat perspective on direct and indirect interactions. *Curr. Opin. Struct. Biol.* 51:92–98
64. Weinrich M, Worcester DL, Bezrukov SM. 2017. Lipid nanodomains change ion channel function. *Nanoscale* 9:13291–97
65. Qi Y, Andolfi L, Frattini F, Mayer F, Lazzarino M, Hu J. 2015. Membrane stiffening by STOML3 facilitates mechanosensation in sensory neurons. *Nat. Commun.* 6:8512
66. Poole K, Herget R, Lapatsina L, Ngo HD, Lewin GR. 2014. Tuning Piezo ion channels to detect molecular-scale movements relevant for fine touch. *Nat. Commun.* 5:3520
67. Borbiri I, Badheka D, Rohacs T. 2015. Activation of TRPV1 channels inhibits mechanosensitive Piezo channel activity by depleting membrane phosphoinositides. *Sci. Signal.* 8:ra15
68. Narayanan P, Hütte M, Kudryasheva G, Taberner FJ, Lechner SG, et al. 2018. Myotubularin related protein-2 and its phospholipid substrate PIP₂ control Piezo2-mediated mechanotransduction in peripheral sensory neurons. *eLife* 7:e32346
69. Anderson EO, Schneider ER, Matson JD, Gracheva EO, Bagriantsev SN. 2018. TMEM150C/Tentonin3 is a regulator of mechano-gated ion channels. *Cell Rep.* 23:701–8
70. Startek JB, Boonen B, López-Requena A, Talavera A, Alpizar YA, et al. 2019. Mouse TRPA1 function and membrane localization are modulated by direct interactions with cholesterol. *eLife* 8:e46084
71. Zhang W, Cheng LE, Kittelmann M, Li J, Petkovic M, et al. 2015. Ankyrin repeats convey force to gate the NOMPC mechanotransduction channel. *Cell* 162:1391–403
72. Yan Z, Zhang W, He Y, Gorczyca D, Xiang Y, et al. 2013. *Drosophila* NOMPC is a mechanotransduction channel subunit for gentle-touch sensation. *Nature* 493:221–25
73. Walker RG, Willingham AT, Zuker CS. 2000. A *Drosophila* mechanosensory transduction channel. *Science* 287:2229–34
74. Chiang L-Y, Poole K, Oliveira BE, Duarte N, Sierra YAB, et al. 2011. Laminin-332 coordinates mechanotransduction and growth cone bifurcation in sensory neurons. *Nat. Neurosci.* 14:993–1000
75. Zhang T, Chi S, Jiang F, Zhao Q, Xiao B. 2017. A protein interaction mechanism for suppressing the mechanosensitive Piezo channels. *Nat. Commun.* 8:1797
76. Narayanan P, Sondermann J, Rouwette T, Karaca S, Urlaub H, et al. 2016. Native Piezo2 interactomics identifies pericentrin as a novel regulator of Piezo2 in somatosensory neurons. *J. Proteome Res.* 15:2676–87

77. Woo S-H, Ranade S, Weyer AD, Dubin AE, Baba Y, et al. 2014. Piezo2 is required for Merkel-cell mechanotransduction. *Nature* 509:622–26
78. Schrenk-Siemens K, Wende H, Prato V, Song K, Rostock C, et al. 2015. PIEZO2 is required for mechanotransduction in human stem cell-derived touch receptors. *Nat. Neurosci.* 18:10–16
79. von Buchholtz LJ, Ghitani N, Lam RM, Licholai JA, Chesler AT, Ryba NJ. 2021. Decoding cellular mechanisms for mechanosensory discrimination. *Neuron* 109:285–98.e5
80. Hook SS, Means AR. 2001. Ca²⁺/CaM-dependent kinases: from activation to function. *Annu. Rev. Pharmacol. Toxicol.* 41:471–505
81. Song Y, Li D, Farrelly O, Miles L, Li F, et al. 2019. The mechanosensitive ion channel piezo inhibits axon regeneration. *Neuron* 102:373–89.e6
82. Pardo-Pastor C, Rubio-Moscardo F, Vogel-González M, Serra SA, Afthinos A, et al. 2018. Piezo2 channel regulates RhoA and actin cytoskeleton to promote cell mechanobiological responses. *PNAS* 115:1925–30
83. Zhou T, Gao B, Fan Y, Liu Y, Feng S, et al. 2020. Piezo1/2 mediate mechanotransduction essential for bone formation through concerted activation of NFAT-YAP1-β-catenin. *eLife* 9:e52779
84. Dubin AE, Schmidt M, Mathur J, Petrus MJ, Xiao B, et al. 2012. Inflammatory signals enhance piezo2-mediated mechanosensitive currents. *Cell Rep.* 2:511–17
85. Singhmar P, Huo X, Eijkelkamp N, Berciano SR, Baameur F, et al. 2016. Critical role for Epac1 in inflammatory pain controlled by GRK2-mediated phosphorylation of Epac1. *PNAS* 113:3036–41
86. Del Rosario JS, Yudin Y, Su S, Hartle CM, Mirshahi T, Rohacs T. 2020. Gi-coupled receptor activation potentiates Piezo2 currents via Gβγ. *EMBO Rep.* 21:e49124
87. Hucho TB, Dina OA, Levine JD. 2005. Epac mediates a cAMP-to-PKC signaling in inflammatory pain: an isolectin B4(+) neuron-specific mechanism. *J. Neurosci.* 25:6119–26
88. Lechner SG, Lewin GR. 2009. Peripheral sensitisation of nociceptors via G-protein-dependent potentiation of mechanotransduction currents. *J. Physiol.* 587:3493–503
89. Borbiri I, Rohacs T. 2017. Regulation of Piezo channels by cellular signaling pathways. *Curr. Top. Membr.* 79:245–61
90. Nickolls AR, Lee MM, Espinoza DF, Szczot M, Lam RM, et al. 2020. Transcriptional programming of human mechanosensory neuron subtypes from pluripotent stem cells. *Cell Rep.* 30:932–46.e7
91. Delle Vedove A, Storbeck M, Heller R, Hölker I, Hebbbar M, et al. 2016. Biallelic loss of proprioception-related PIEZO2 causes muscular atrophy with perinatal respiratory distress, arthrogryposis, and scoliosis. *Am. J. Hum. Genet.* 99:1206–16
92. Haliloglu G, Becker K, Temucin C, Talim B, Küçükşahin N, et al. 2017. Recessive PIEZO2 stop mutation causes distal arthrogryposis with distal muscle weakness, scoliosis and proprioception defects. *J. Hum. Genet.* 62:497–501
93. Mahmud A, Nahid N, Nassif C, Sayeed M, Ahmed M, et al. 2017. Loss of the proprioception and touch sensation channel PIEZO2 in siblings with a progressive form of contractures. *Clin. Genet.* 91:470–75
94. Case LK, Liljencrantz J, Madian N, Necaie A, Tubbs J, et al. 2021. Innocuous pressure sensation requires A-type afferents but not functional PIEZO2 channels in humans. *Nat. Commun.* 12(1):657
95. McMillin MJ, Beck AE, Chong JX, Shively KM, Buckingham KJ, et al. 2014. Mutations in PIEZO2 cause Gordon syndrome, Marden-Walker syndrome, and distal arthrogryposis type 5. *Am. J. Hum. Genet.* 94:734–44
96. Okubo M, Fujita A, Saito Y, Komaki H, Ishiyama A, et al. 2015. A family of distal arthrogryposis type 5 due to a novel PIEZO2 mutation. *Am. J. Med. Genet. Part A* 167:1100–6
97. Alisch F, Weichert A, Kalache K, Paradiso V, Longardt AC, et al. 2017. Familial Gordon syndrome associated with a PIEZO2 mutation. *Am. J. Med. Genet. Part A* 173:254–59
98. Nguyen MQ, Wu Y, Bonilla LS, von Buchholtz LJ, Ryba NJ. 2017. Diversity amongst trigeminal neurons revealed by high throughput single cell sequencing. *PLOS ONE* 12:e0185543
99. Zheng Y, Liu P, Bai L, Trimmer JS, Bean BP, Ginty DD. 2019. Deep sequencing of somatosensory neurons reveals molecular determinants of intrinsic physiological properties. *Neuron* 103:598–616.e7
100. Sharma N, Flaherty K, Lezgiyeva K, Wagner DE, Klein AM, Ginty DD. 2020. The emergence of transcriptional identity in somatosensory neurons. *Nature* 577:392–98

101. von Buchholtz LJ, Lam RM, Emrick JJ, Chesler AT, Ryba NJ. 2020. Assigning transcriptomic class in the trigeminal ganglion using multiplex in situ hybridization and machine learning. *Pain* 161:2212–24
102. Kandel ER, Jessell TM, Schwartz JH, Siegelbaum SA, Hudspeth AJ, Mack S. 2013. *Principles of Neural Science*. New York: McGraw-Hill Educ. 5th ed.
103. Umans BD, Liberles SD. 2018. Neural sensing of organ volume. *Trends Neurosci.* 41:911–24
104. Min S, Chang RB, Prescott SL, Beeler B, Joshi NR, et al. 2019. Arterial baroreceptors sense blood pressure through decorated aortic claws. *Cell Rep.* 29:2192–201.e3
105. Prescott SL, Umans BD, Williams EK, Brust RD, Liberles SD. 2020. An airway protection program revealed by sweeping genetic control of vagal afferents. *Cell* 181:574–89
106. Nguyen MQ, Le Pichon CE, Ryba N. 2019. Stereotyped transcriptomic transformation of somatosensory neurons in response to injury. *eLife* 8:e49679
107. Chang R, Strohlic D, Nonomura K, Patapoutian A, Liberles S. 2018. Airway mechanoreceptors that control breathing. *FASEB J.* 32:893.3
108. Nonomura K, Woo SH, Chang RB, Gillich A, Qiu Z, et al. 2017. Piezo2 senses airway stretch and mediates lung inflation-induced apnoea. *Nature* 541:176–81
109. Wang F, Knutson K, Alcaïno C, Linden DR, Gibbons SJ, et al. 2017. Mechanosensitive ion channel Piezo2 is important for enterochromaffin cell response to mechanical forces. *J. Physiol.* 595:79–91
110. Iggo A, Muir AR. 1969. The structure and function of a slowly adapting touch corpuscle in hairy skin. *J. Physiol.* 200:763–796.4
111. Diamond J, Mills L, Mearow K. 1988. Evidence that the Merkel cell is not the transducer in the mechanosensory Merkel cell–neurite complex. *Prog. Brain Res.* 74:51–56
112. Mills L, Diamond J. 1995. Merkel cells are not the mechanosensory transducers in the touch dome of the rat. *J. Neurocytol.* 24:117–34
113. Anand A, Iggo A, Paintal AS. 1979. Lability of granular vesicles in Merkel cells of the type I slowly-adapting cutaneous receptors of the cat [proceedings]. *J. Physiol.* 296:19P–20P
114. Maksimovic S, Baba Y, Lumpkin EA. 2013. Neurotransmitters and synaptic components in the Merkel cell–neurite complex, a gentle touch receptor. *Ann. N. Y. Acad. Sci.* 1279:13–21
115. Maricich SM, Wellnitz SA, Nelson AM, Lesniak DR, Gerling GJ, et al. 2009. Merkel cells are essential for light-touch responses. *Science* 324:1580–82
116. Maksimovic S, Nakatani M, Baba Y, Nelson AM, Marshall KL, et al. 2014. Epidermal Merkel cells are mechanosensory cells that tune mammalian touch receptors. *Nature* 509:617–21
117. Woo S-H, Lumpkin EA, Patapoutian A. 2015. Merkel cells and neurons keep in touch. *Trends Cell Biol.* 25:74–81
118. Murthy SE, Dubin AE, Whitwam T, Jojoa-Cruz S, Cahalan SM, et al. 2018. OSCA/TMEM63 are an evolutionarily conserved family of mechanically activated ion channels. *eLife* 7:e41844
119. Beaulieu-Laroche L, Christin M, Donoghue A, Agosti F, Yousefpour N, et al. 2020. TACAN is an ion channel involved in sensing mechanical pain. *Cell* 180:956–67.e17
120. Abdo H, Calvo-Enrique L, Lopez JM, Song J, Zhang M-D, et al. 2019. Specialized cutaneous Schwann cells initiate pain sensation. *Science* 365:695–99
121. Dhandapani R, Arokiaraj CM, Taberner FJ, Pacifico P, Raja S, et al. 2018. Control of mechanical pain hypersensitivity in mice through ligand-targeted photoablation of TrkB-positive sensory neurons. *Nat. Commun.* 9:1640
122. Bautista DM, Wilson SR, Hoon MA. 2014. Why we scratch an itch: the molecules, cells and circuits of itch. *Nat. Neurosci.* 17:175–82
123. Feng J, Luo J, Yang P, Du J, Kim BS, Hu H. 2018. Piezo2 channel–Merkel cell signaling modulates the conversion of touch to itch. *Science* 360:530–33
124. Feng J, Hu H. 2019. A novel player in the field: Merkel disc in touch, itch and pain. *Exp. Dermatol.* 28:1412–15
125. Sherrington CS. 1907. On the proprioceptive system, especially in its reflex aspect. *Brain* 29:467–82
126. Florez-Paz D, Bali KK, Kuner R, Gomis A. 2016. A critical role for Piezo2 channels in the mechanotransduction of mouse proprioceptive neurons. *Sci. Rep.* 6:25923
127. Zhang J, Walker JF, Guardiola J, Yu J. 2006. Pulmonary sensory and reflex responses in the mouse. *J. Appl. Physiol.* 101:986–92

128. Schelegle ES, Green JF. 2001. An overview of the anatomy and physiology of slowly adapting pulmonary stretch receptors. *Respir. Physiol.* 125:17–31
129. Bai L, Mesgarzadeh S, Ramesh KS, Huey EL, Liu Y, et al. 2019. Genetic identification of vagal sensory neurons that control feeding. *Cell* 179:1129–43.e23
130. Chang RB, Strohlic DE, Williams EK, Umans BD, Liberles SD. 2015. Vagal sensory neuron subtypes that differentially control breathing. *Cell* 161:622–33
131. Kupari J, Häring M, Agirre E, Castelo-Branco G, Ernfors P. 2019. An atlas of vagal sensory neurons and their molecular specialization. *Cell Rep.* 27:2508–23.e4
132. Hockley JR, Taylor TS, Callejo G, Willbrey AL, Gutteridge A, et al. 2019. Single-cell RNaseq reveals seven classes of colonic sensory neuron. *Gut* 68:633–44
133. Bühlbring E, Crema A. 1959. The action of 5-hydroxytryptamine, 5-hydroxytryptophan and reserpine on intestinal peristalsis in anaesthetized guinea-pigs. *J. Physiol.* 146:29–53
134. Alcaino C, Knutson KR, Treichel AJ, Yildiz G, Stregge PR, et al. 2018. A population of gut epithelial enterochromaffin cells is mechanosensitive and requires Piezo2 to convert force into serotonin release. *PNAS* 115:E7632–41
135. Najjar SA, Davis BM, Albers KM. 2020. Epithelial-neuronal communication in the colon: implications for visceral pain. *Trends Neurosci.* 43:170–81
136. Bohórquez DV, Shahid RA, Erdmann A, Kreger AM, Wang Y, et al. 2015. Neuroepithelial circuit formed by innervation of sensory enteroendocrine cells. *J. Clin. Investig.* 125:782–86
137. Bellono NW, Bayrer JR, Leitch DB, Castro J, Zhang C, et al. 2017. Enterochromaffin cells are gut chemosensors that couple to sensory neural pathways. *Cell* 170:185–98.e16
138. Kaelberer MM, Buchanan KL, Klein ME, Barth BB, Montoya MM, et al. 2018. A gut-brain neural circuit for nutrient sensory transduction. *Science* 361:eaat5236
139. McMahon SB, Koltzenburg M, Tracey I, Turk D. 2013. *Wall & Melzack's Textbook of Pain*. Philadelphia: Elsevier/Saunders. 6th ed.
140. Prato V, Taberner FJ, Hockley JR, Callejo G, Arcourt A, et al. 2017. Functional and molecular characterization of mechanoinensitive “silent” nociceptors. *Cell Rep.* 21:3102–15
141. Marshall KL, Saade D, Ghitani N, Coombs AM, Szczot M, et al. 2020. PIEZO2 in sensory neurons and urothelial cells coordinates urination. *Nature* 588:290–95
142. Kumada M, Terui N, Kuwaki T. 1990. Arterial baroreceptor reflex: its central and peripheral neural mechanisms. *Progress Neurobiol.* 35:331–61
143. Miglis MG, Muppidi S. 2019. Ion channels PIEZO2 identified as the long-sought baroreceptor mechanosensors for blood pressure control, and other updates on autonomic research. *Clin. Auton. Res.* 29:9–11
144. Won J, Vang H, Lee P, Kim Y, Kim H, et al. 2017. Piezo2 expression in mechanosensitive dental primary afferent neurons. *J. Dent. Res.* 96:931–37
145. Emrick J, von Buchholtz L, Ryba N. 2020. Transcriptomic classification of neurons innervating teeth. *J. Dent. Res.* 99:1478–85
146. Moayedi Y, Duenas-Bianchi LF, Lumpkin EA. 2018. Somatosensory innervation of the oral mucosa of adult and aging mice. *Sci. Rep.* 8:9975
147. Du G, Li L, Zhang X, Liu J, Hao J, et al. 2020. Roles of TRPV4 and piezo channels in stretch-evoked Ca²⁺ response in chondrocytes. *Exp. Biol. Med.* 245:180–89
148. Lee W, Leddy HA, Chen Y, Lee SH, Zelenski NA, et al. 2014. Synergy between Piezo1 and Piezo2 channels confers high-strain mechanosensitivity to articular cartilage. *PNAS* 111:E5114–22
149. Lee W, Guilak F, Liedtke W. 2017. Role of Piezo channels in joint health and injury. *Curr. Top. Membr.* 79:263–73
150. Assaraf E, Blecher R, Heinemann-Yerushalmi L, Krief S, Vinestock RC, et al. 2020. Piezo2 expressed in proprioceptive neurons is essential for skeletal integrity. *Nat. Commun.* 11:3168
151. Wu Z, Grillet N, Zhao B, Cunningham C, Harkins-Perry S, et al. 2017. Mechanosensory hair cells express two molecularly distinct mechanotransduction channels. *Nat. Neurosci.* 20:24–33
152. Beurg M, Fettiplace R. 2017. PIEZO2 as the anomalous mechanotransducer channel in auditory hair cells. *J. Physiol.* 595:7039–48

153. Chambers MC, Maclean B, Burke R, Amodei D, Ruderman DL, et al. 2012. A cross-platform toolkit for mass spectrometry and proteomics. *Nat. Biotechnol.* 30:918–20
154. Southam L, Gilly A, Süveges D, Farmaki A-E, Schwartzentruber J, et al. 2017. Whole genome sequencing and imputation in isolated populations identify genetic associations with medically-relevant complex traits. *Nat. Commun.* 8:15606
155. Eberhardt E, Havlicek S, Schmidt D, Link AS, Neacsu C, et al. 2015. Pattern of functional TTX-resistant sodium channels reveals a developmental stage of human iPSC- and ESC-derived nociceptors. *Stem Cell Rep.* 5:305–13
156. Jones I, Yelhekar TD, Wiberg R, Kingham PJ, Johansson S, et al. 2018. Development and validation of an in vitro model system to study peripheral sensory neuron development and injury. *Sci. Rep.* 8:15961
157. Alshawaf AJ, Viventi S, Qiu W, D'Abaco G, Nayagam B, et al. 2018. Phenotypic and functional characterization of peripheral sensory neurons derived from human embryonic stem cells. *Sci. Rep.* 8:603
158. McDermott LA, Weir GA, Themistocleous AC, Segerdahl AR, Blesneac I, et al. 2019. Defining the functional role of Na_v1.7 in human nociception. *Neuron* 101:905–19.e8
159. Schrenk-Siemens K, Pohle J, Rostock C, El Hay MA, Lam RM, et al. 2019. HESC-derived sensory neurons reveal an unexpected role for PIEZO2 in nociceptor mechanotransduction. bioRxiv 741660. <https://doi.org/10.1101/741660>
160. Kupari J, Usoskin D, Parisien M, Lou D, Hu Y, et al. 2020. Single cell transcriptomics of primate sensory neurons identifies cell types associated with human chronic pain. *Nat. Commun.* 12:1510
161. Syeda R, Xu J, Dubin AE, Coste B, Mathur J, et al. 2015. Chemical activation of the mechanotransduction channel Piezo1. *eLife* 4:e07369
162. Wang Y, Chi S, Guo H, Li G, Wang L, et al. 2018. A lever-like transduction pathway for long-distance chemical- and mechano-gating of the mechanosensitive Piezo1 channel. *Nat. Commun.* 9:1300
163. Feng J, Luo J, Yang P, Du J, Kim BS, Hu H. 2018. Piezo2 channel-Merkel cell signaling modulates the conversion of touch to itch. *Science* 360:530–33
164. Gnanasambandam R, Ghatak C, Yasmann A, Nishizawa K, Sachs F, et al. 2017. GsMTx4: mechanism of inhibiting mechanosensitive ion channels. *Biophys. J.* 112:31–45
165. Lewis AH, Cui AF, McDonald MF, Grandl J. 2017. Transduction of repetitive mechanical stimuli by Piezo1 and Piezo2 ion channels. *Cell Rep.* 19:2572–85
166. Wu J, Goyal R, Grandl J. 2016. Localized force application reveals mechanically sensitive domains of Piezo1. *Nat. Commun.* 7:12939
167. Liu C, Li T, Chen J. 2019. Role of high-throughput electrophysiology in drug discovery. *Curr. Protoc. Pharmacol.* 87:e69
168. Mohanraj B, Hou C, Meloni GR, Cosgrove BD, Dodge GR, Mauck RL. 2014. A high throughput mechanical screening device for cartilage tissue engineering. *J. Biomech.* 47:2130–36
169. Gregurec D, Senko AW, Chuvilin A, Reddy PD, Sankararaman A, et al. 2020. Magnetic vortex nanodiscs enable remote magnetomechanical neural stimulation. *ACS Nano* 14:8036–45
170. Montel L, Sotiropoulos A, Hénon S. 2019. The nature and intensity of mechanical stimulation drive different dynamics of MRTF-A nuclear redistribution after actin remodeling in myoblasts. *PLOS ONE* 14:e0214385
171. Matsui TS, Wu H, Deguchi S. 2018. Deformable 96-well cell culture plate compatible with high-throughput screening platforms. *PLOS ONE* 13:e0203448
172. Xu J, Mathur J, Vessières E, Hammack S, Nonomura K, et al. 2018. GPR68 senses flow and is essential for vascular physiology. *Cell* 173:762–75.e16
173. Orefice LL, Zimmerman AL, Chirila AM, Sleboda SJ, Head JP, Ginty DD. 2016. Peripheral mechanosensory neuron dysfunction underlies tactile and behavioral deficits in mouse models of ASDs. *Cell* 166:299–313
174. Neubarth NL, Emanuel AJ, Liu Y, Springel MW, Handler A, et al. 2020. Meissner corpuscles and their spatially intermingled afferents underlie gentle touch perception. *Science* 368:eabb2751

Contents

It's Better To Be Lucky Than Smart <i>H.R. Kaback</i>	1
Short- and Long-Term Adaptation to Altered Levels of Glucose: Fifty Years of Scientific Adventure <i>Kosaku Uyeda</i>	31
From Bioorganic Models to Cells <i>Stephen J. Benkovic</i>	57
Structural Mechanisms for Replicating DNA in Eukaryotes <i>Ilan Attali, Michael R. Botchan, and James M. Berger</i>	77
Mechanisms of Vertebrate DNA Interstrand Cross-Link Repair <i>Daniel R. Semlow and Johannes C. Walter</i>	107
Repair of DNA Double-Strand Breaks by the Nonhomologous End Joining Pathway <i>Benjamin M. Stinson and Joseph J. Loparo</i>	137
Repair of DNA Breaks by Break-Induced Replication <i>Z.W. Kockler, B. Osia, R. Lee, K. Musmaker, and A. Malkova</i>	165
The Long Road to Understanding RNAPII Transcription Initiation and Related Syndromes <i>Emmanuel Compe and Jean-Marc Egly</i>	193
Designing Biological Circuits: Synthetic Biology Within the Operon Model and Beyond <i>Max A. English, Raphaël V. Gayet, and James J. Collins</i>	221
Understanding the Function of Mammalian Sirtuins and Protein Lysine Acylation <i>Miao Wang and Hening Lin</i>	245
Molecular Epigenetics: Chemical Biology Tools Come of Age <i>John D. Bagert and Tom W. Muir</i>	287
Influenza Virus RNA-Dependent RNA Polymerase and the Host Transcriptional Apparatus <i>Tim Kruschuns, Maria Lukarska, Nadia Naffakh, and Stephen Cusack</i>	321

The Roots of Genetic Coding in Aminoacyl-tRNA Synthetase Duality <i>Charles W. Carter Jr. and Peter R. Wills</i>	349
Synonymous but Not Silent: The Codon Usage Code for Gene Expression and Protein Folding <i>Yi Liu, Qian Yang, and Fangzhou Zhao</i>	375
Cullin-RING Ubiquitin Ligase Regulatory Circuits: A Quarter Century Beyond the F-Box Hypothesis <i>J. Wade Harper and Brenda A. Schulman</i>	403
An Overview of Microcrystal Electron Diffraction (MicroED) <i>Xuelang Mu, Cody Gillman, Chi Nguyen, and Tamir Gonen</i>	431
Preparing Better Samples for Cryo-Electron Microscopy: Biochemical Challenges Do Not End with Isolation and Purification <i>Robert M. Glaeser</i>	451
Optobiochemistry: Genetically Encoded Control of Protein Activity by Light <i>Jihye Seong and Michael Z. Lin</i>	475
Introduction to the Theme on Membrane Channels <i>Gunnar von Heijne</i>	503
The Form and Function of PIEZO2 <i>Marcin Szczot, Alec R. Nickolls, Ruby M. Lam, and Alexander T. Chesler</i>	507
Structural Mechanism of Transport of Mitochondrial Carriers <i>J.J. Ruprecht and E.R.S. Kunji</i>	535
Membrane Exporters of Fluoride Ion <i>Benjamin C. McIlwain, Michal T. Ruprecht, and Randy B. Stockbridge</i>	559
Chaperoning SNARE Folding and Assembly <i>Yongli Zhang and Frederick M. Hughson</i>	581
Tunnels for Protein Export from the Endoplasmic Reticulum <i>I. Raote and V. Malhotra</i>	605
Quality Control of Procollagen in Cells <i>Shinya Ito and Kazuhiro Nagata</i>	631
Posttranslational Regulation of HMG CoA Reductase, the Rate-Limiting Enzyme in Synthesis of Cholesterol <i>Marc M. Schumacher and Russell A. DeBose-Boyd</i>	659
PI(4,5)P ₂ Clustering and Its Impact on Biological Functions <i>Yi Wen, Volker M. Vogt, and Gerald W. Feigenson</i>	681

Mechanisms for Regulating and Organizing Receptor Signaling by Endocytosis <i>Mark von Zastrow and Alexander Sorkin</i>	709
Structural Insights Accelerate the Discovery of Opioid Alternatives <i>Tao Che and Bryan L. Roth</i>	739
A Natural Product Chemist's Guide to Unlocking Silent Biosynthetic Gene Clusters <i>Brett C. Covington, Fei Xu, and Mohammad R. Seyedsayamdost</i>	763
Molecules from the Microbiome <i>Emilee E. Shine and Jason M. Crawford</i>	789
Glycyl Radical Enzymes and Sulfonate Metabolism in the Microbiome <i>Yifeng Wei and Yan Zhang</i>	817

Errata

An online log of corrections to *Annual Review of Biochemistry* articles may be found at <http://www.annualreviews.org/errata/biochem>

Conclusion- Questions I will address in this thesis

“In all ages there have been thoughtful people who have tried to bring order out of the chaos...the modern science employs the method of experiment, the accouterments of the laboratory and the procedure of objective observation” - Frank A Geldard

I titled this thesis “The Cells and Molecules Underlying Mechanosensation” because I wanted to highlight my investigations into understanding which cells, and what molecules are needed to transduce mechanical information necessary for our fitness and survival. I targeted the molecule Piezo2, which has known mechanosensitive properties, to investigate the functional roles of specific populations of neurons with altered mechanosensitivity. I will thoroughly investigate the importance of specific cells expressing the molecule, Piezo, in two vital bodily functions, reproduction and gut motility. These series of experiments will integrate molecules, cells, circuits, and behavior. I will also delve into our use of modern tools to better understand the organization of the somatosensory and re-taxonomize groups of sensory neurons by their transcriptomic profiles and functional roles.

The 2nd chapter explores the importance of mechanosensation for the vital function of mating success. We know that the loss of Piezo2 reduces the ability to detect gentle stimuli. We reasoned that behaviors, such as copulation, require a significant amount of tactile information. With the tools to model *Piezo2* loss of function, we had an opportunity to see if altering the perception of touch would also alter sexual reproduction. I will endeavor to find a class of sensory neuron that relies particularly heavily on *Piezo2* and gauge the overall role of Piezo2 in building the sensory precepts that are important for survival and reproduction.

The 3rd chapter explores the importance of interoceptive mechanosensation. The response profiles of primary sensory neurons innervating non-cutaneous targets have largely been uncharacterized thus far. By investigating neurons that innervate the gastrointestinal tract and Piezo2 in neurons innervating the gastrointestinal system of the mouse to better understand the importance of mechanosensation in bowel motility and gastrointestinal health.

The 4th chapter consists of two publications which describe the impact single cell sequencing has on the taxonomic classification and organization of sensory neurons. It explores the relationship between transduction molecules, such as Piezo2, and transcriptomic class identity.

Finally I will discuss the impact of these projects and how studying the cells and molecules underlying mechanosensation has advanced our understanding of how the somatosensory system works. I will also discuss some open questions which have surfaced from these investigations and highlight promising future directions.

Chapter 1 References

1. Le Pichon, C.E., and Chesler, A.T. (2014). The functional and anatomical dissection of somatosensory subpopulations using mouse genetics. *Frontiers in Neuroanatomy* 8. 10.3389/fnana.2014.00021.
2. Julius, D. (2013). TRP channels and pain. *Annual review of cell and developmental biology* 29, 355-384.
3. Zimmerman, A., Bai, L., and Ginty, D.D. (2014). The gentle touch receptors of mammalian skin. *Science* 346, 950-954.
4. Abraira, V.E., and Ginty, D.D. (2013). The sensory neurons of touch. *neuron* 79, 618-639.
5. Nguyen, M.Q., Wu, Y., Bonilla, L.S., von Buchholtz, L.J., and Ryba, N.J. (2017). Diversity amongst trigeminal neurons revealed by high throughput single cell sequencing. *PloS one* 12, e0185543.
6. Rachlin, H. (2005). What Müller's law of specific nerve energies says about the mind. *Behavior and Philosophy*, 41-54.
7. Bridges, J.W. (1912). Doctrine of Specific Nerve Energies. *The Journal of Philosophy, Psychology and Scientific Methods* 9, 57-65. 10.2307/2013786.
8. Finger, S. (1994). *Origins of neuroscience: A history of explorations into brain function* (Oxford University Press).
9. Boring, E.G. (1950). Great Men and Scientific Progress. *Proceedings of the American Philosophical Society* 94, 339-351.
10. Norrsell, U., Finger, S., and Lajonchere, C. (1999). Cutaneous sensory spots and the "law of specific nerve energies": history and development of ideas. *Brain research bulletin* 48, 457-465.
11. Young, T. (1802). II. The Bakerian Lecture. On the theory of light and colours. *Philosophical transactions of the Royal Society of London*, 12-48.
12. Young, T. (1802). XIV. An account of some cases of the production of colours, not hitherto described. *Philosophical Transactions of the Royal Society of London*, 387-397.
13. Norrsell, U. (2000). History of Neuroscience: Magnus Gustaf Blix (1849-1904) Neurophysiological, Physiological, and Engineering Virtuoso. *Journal of the History of the Neurosciences* 9, 238-249.

14. Eccles, J.C. (1975). Letters from CS Sherrington, FRS, to Angelo Ruffini between 1896 and 1903. *Notes and Records of the Royal Society of London* 30, 69-88.
15. Morcos, J., and Wang, A. (2015). History of the Neurosciences in the United States of America. *International Neuroscience Journal* 1, 47-48.
16. Sherrington, C. (1952). *The integrative action of the nervous system* (CUP Archive).
17. Adrian, E.D., and Zotterman, Y. (1926). The impulses produced by sensory nerve-endings: Part II. The response of a Single End-Organ. *The Journal of physiology* 61, 151.
18. Loewenstein, W.R., and Rathkamp, R. (1958). Localization of generator structures of electric activity in a Pacinian corpuscle. *Science* 127, 341-341.
19. Brown, A., and Iggo, A. (1967). A quantitative study of cutaneous receptors and afferent fibres in the cat and rabbit. *The Journal of physiology* 193, 707.
20. Perl, E. (1968). Myelinated afferent fibres innervating the primate skin and their response to noxious stimuli. *The Journal of physiology* 197, 593-615.
21. Burgess, P., Petit, D., and Warren, R.M. (1968). Receptor types in cat hairy skin supplied by myelinated fibers. *Journal of neurophysiology* 31, 833-848.
22. Handwerker, H. (1996). Sixty years of C-fiber recordings from animal and human skin nerves: historical notes. *Progress in Brain Research* 113, 39-51.
23. Kandel, E.R., Schwartz, J.H., Jessell, T.M., Siegelbaum, S., Hudspeth, A.J., and Mack, S. (2000). *Principles of neural science* (McGraw-hill New York).
24. Rice, F., and Albrecht, P. (2008). 6.01-Cutaneous mechanisms of tactile perception: morphological and chemical organization of the innervation to the skin (elsevier).
25. Mense, S. (1990). Relationship between functional and morphological properties in single primary afferent neurons. In *The Primary Afferent Neuron: A Survey of Recent Morpho-Functional Aspects*, (Springer), pp. 201-211.
26. Hoheisel, U., and Mense, S. (1986). Non-myelinated afferent fibres do not originate exclusively from the smallest dorsal root ganglion cells in the cat. *Neuroscience letters* 72, 153-157.
27. Gardner, E.P., and Martin, J.H. (2000). Coding of sensory information. *Principles of neural science* 4, 411-429.
28. Perl, E. (1980). Afferent basis of nociception and pain: evidence from the characteristics of sensory receptors and their projections to the spinal dorsal horn. *Research Publications-Association for Research in Nervous and Mental Disease* 58, 19-45.
29. Nagi, S.S., Marshall, A.G., Makdani, A., Jarocka, E., Liljencrantz, J., Ridderström, M., Shaikh, S., O'Neill, F., Saade, D., and Donkervoort, S. (2019). An ultrafast system for signaling mechanical pain in human skin. *Science advances* 5, eaaw1297.
30. Mishqat, I. (2017). *The Formation of Reticular Theory*. Published online 2017-06-19.
31. Deiters, V.S., and Guillery, R. (2013). Otto Friedrich Karl Deiters (1834–1863). *Journal of Comparative Neurology* 521, 1929-1953.
32. Iggo, A., and Andres, K. (1982). Morphology of cutaneous receptors. *Annual review of neuroscience* 5, 1-31.
33. Deiters, O. (1865). *Untersuchungen über Gehirn und Rückenmark des Menschen und der Säugethiere* (F. Veiweg).
34. Bentivoglio, M., and Pacini, P. (1995). Filippo Pacini: a determined observer. *Brain research bulletin* 38, 161-165.
35. Lee, F.C. (1936). A study of the Pacinian corpuscle. *Journal of Comparative Neurology* 64, 497-522.
36. Verrillo, R.T. (2014). *Sensory Research: Multimodal Perspectives* (Taylor & Francis).
37. Alvarez-Buylla, R., and De Arellano, J.R. (1952). Local responses in Pacinian corpuscles. *American Journal of Physiology-Legacy Content* 172, 237-244.
38. Piccinin, M.A., Miao, J.H., and Schwartz, J. (2018). Histology, meissner corpuscle.

39. Cauna, N. (1956). Nerve supply and nerve endings in Meissner's corpuscles. *American Journal of Anatomy* **99**, 315-350.
40. Cauna, N. (1956). Structure and origin of the capsule of Meissner's corpuscle. *The Anatomical Record* **124**, 77-93.
41. Chouchkov, C., and Chouchkov, C. (1978). Ultrastructure and morphological classification. *Cutaneous Receptors*, 9-32.
42. Handler, A., and Ginty, D.D. (2021). The mechanosensory neurons of touch and their mechanisms of activation. *Nature Reviews Neuroscience* **22**, 521-537.
43. Rutlin, M., Ho, C.-Y., Abaira, V.E., Cassidy, C., Bai, L., Woodbury, C.J., and Ginty, D.D. (2014). The cellular and molecular basis of direction selectivity of A δ -LTMRs. *Cell* **159**, 1640-1651.
44. Ghitani, N., Barik, A., Szczot, M., Thompson, J.H., Li, C., Le Pichon, C.E., Krashes, M.J., and Chesler, A.T. (2017). Specialized mechanosensory nociceptors mediating rapid responses to hair pull. *Neuron* **95**, 944-954. e944.
45. Geldard, F.A. (1972). *The Human Senses: By Frank A. Geldard*. 2d Ed (J. Wiley).
46. Zimmermann, K., Hein, A., Hager, U., Kaczmarek, J.S., Turnquist, B.P., Clapham, D.E., and Reeh, P.W. (2009). Phenotyping sensory nerve endings in vitro in the mouse. *Nature protocols* **4**, 174-196.
47. Aldridge, S., and Teichmann, S.A. (2020). Single cell transcriptomics comes of age. *Nature Communications* **11**, 4307.
48. Lein, E., Borm, L.E., and Linnarsson, S. (2017). The promise of spatial transcriptomics for neuroscience in the era of molecular cell typing. *Science* **358**, 64-69.
49. Lacar, B., Linker, S.B., Jaeger, B.N., Krishnaswami, S.R., Barron, J.J., Kelder, M.J., Parylak, S.L., Paquola, A.C., Venepally, P., and Novotny, M. (2016). Nuclear RNA-seq of single neurons reveals molecular signatures of activation. *Nature communications* **7**, 11022.
50. Chiu, I.M., Barrett, L.B., Williams, E.K., Strohlic, D.E., Lee, S., Weyer, A.D., Lou, S., Bryman, G.S., Roberson, D.P., and Ghasemlou, N. (2014). Transcriptional profiling at whole population and single cell levels reveals somatosensory neuron molecular diversity. *Elife* **3**, e04660.
51. Li, C.-L., Li, K.-C., Wu, D., Chen, Y., Luo, H., Zhao, J.-R., Wang, S.-S., Sun, M.-M., Lu, Y.-J., and Zhong, Y.-Q. (2016). Somatosensory neuron types identified by high-coverage single-cell RNA-sequencing and functional heterogeneity. *Cell research* **26**, 83-102.
52. Usoskin, D., Furlan, A., Islam, S., Abdo, H., Lönnerberg, P., Lou, D., Hjerling-Leffler, J., Haeggström, J., Kharchenko, O., and Kharchenko, P.V. (2015). Unbiased classification of sensory neuron types by large-scale single-cell RNA sequencing. *Nature neuroscience* **18**, 145-153.
53. Nguyen, M.Q., Le Pichon, C.E., and Ryba, N. (2019). Stereotyped transcriptomic transformation of somatosensory neurons in response to injury. *Elife* **8**, e49679.
54. Sharma, N., Flaherty, K., Lezgiyeva, K., Wagner, D.E., Klein, A.M., and Ginty, D.D. (2020). The emergence of transcriptional identity in somatosensory neurons. *Nature* **577**, 392-398.
55. von Buchholtz, L.J., Lam, R.M., Emrick, J.J., Chesler, A.T., and Ryba, N.J.P. (2020). Assigning transcriptomic class in the trigeminal ganglion using multiplex in situ hybridization and machine learning. *PAIN* **161**, 2212-2224. [10.1097/j.pain.0000000000001911](https://doi.org/10.1097/j.pain.0000000000001911).
56. Caterina, M.J., Schumacher, M.A., Tominaga, M., Rosen, T.A., Levine, J.D., and Julius, D. (1997). The capsaicin receptor: a heat-activated ion channel in the pain pathway. *Nature* **389**, 816-824.

57. Bautista, D.M., Siemens, J., Glazer, J.M., Tsuruda, P.R., Basbaum, A.I., Stucky, C.L., Jordt, S.-E., and Julius, D. (2007). The menthol receptor TRPM8 is the principal detector of environmental cold. *Nature* *448*, 204-208.
58. Bautista, D.M., Movahed, P., Hinman, A., Axelsson, H.E., Sterner, O., Högestätt, E.D., Julius, D., Jordt, S.-E., and Zygmunt, P.M. (2005). Pungent products from garlic activate the sensory ion channel TRPA1. *Proceedings of the National Academy of Sciences* *102*, 12248-12252.
59. Bautista, D.M., Jordt, S.-E., Nikai, T., Tsuruda, P.R., Read, A.J., Poblete, J., Yamoah, E.N., Basbaum, A.I., and Julius, D. (2006). TRPA1 mediates the inflammatory actions of environmental irritants and proalgesic agents. *Cell* *124*, 1269-1282.
60. Jordt, S.-E., Bautista, D.M., Chuang, H.-H., McKemy, D.D., Zygmunt, P.M., Högestätt, E.D., Meng, I.D., and Julius, D. (2004). Mustard oils and cannabinoids excite sensory nerve fibres through the TRP channel ANKTM1. *Nature* *427*, 260-265.
61. Rutishauser, U., Acheson, A., Hall, A.K., Mann, D.M., and Sunshine, J. (1988). The neural cell adhesion molecule (NCAM) as a regulator of cell-cell interactions. *Science* *240*, 53-57.
62. Hynes, R.O. (2002). Integrins: bidirectional, allosteric signaling machines. *cell* *110*, 673-687.
63. Levayer, R., and Lecuit, T. (2013). Oscillation and polarity of E-cadherin asymmetries control actomyosin flow patterns during morphogenesis. *Developmental cell* *26*, 162-175.
64. Scholz, N., Monk, K.R., Kittel, R.J., and Langenhan, T. (2016). Adhesion GPCRs as a putative class of metabotropic mechanosensors. *Adhesion G protein-coupled receptors: molecular, physiological and pharmacological principles in health and disease*, 221-247.
65. Corey, D., and Hudspeth, A. (1979). Ionic basis of the receptor potential in a vertebrate hair cell. *Nature* *281*, 675-677.
66. Walker, R.G., Willingham, A.T., and Zuker, C.S. (2000). A *Drosophila* mechanosensory transduction channel. *Science* *287*, 2229-2234.
67. O'Hagan, R., Chalfie, M., and Goodman, M.B. (2005). The MEC-4 DEG/ENaC channel of *Caenorhabditis elegans* touch receptor neurons transduces mechanical signals. *Nature neuroscience* *8*, 43-50.
68. Gustin, M.C., Zhou, X.-L., Martinac, B., and Kung, C. (1988). A mechanosensitive ion channel in the yeast plasma membrane. *Science* *242*, 762-765.
69. Sukharev, S.I., Blount, P., Martinac, B., Blattner, F.R., and Kung, C. (1994). A large-conductance mechanosensitive channel in *E. coli* encoded by *mscL* alone. *Nature* *368*, 265-268.
70. Martinac, B., Adler, J., and Kung, C. (1990). Mechanosensitive ion channels of *E. coli* activated by amphipaths. *Nature* *348*, 261-263.
71. Martinac, B., Buechner, M., Delcour, A.H., Adler, J., and Kung, C. (1987). Pressure-sensitive ion channel in *Escherichia coli*. *Proceedings of the National Academy of Sciences* *84*, 2297-2301.
72. Chalfie, M., and Au, M. (1989). Genetic control of differentiation of the *Caenorhabditis elegans* touch receptor neurons. *Science* *243*, 1027-1033.
73. Zhang, W., Cheng, L.E., Kittelmann, M., Li, J., Petkovic, M., Cheng, T., Jin, P., Guo, Z., Göpfert, M.C., and Jan, L.Y. (2015). Ankyrin repeats convey force to gate the NOMPC mechanotransduction channel. *Cell* *162*, 1391-1403.
74. Yan, Z., Zhang, W., He, Y., Gorczyca, D., Xiang, Y., Cheng, L.E., Meltzer, S., Jan, L.Y., and Jan, Y.N. (2013). *Drosophila* NOMPC is a mechanotransduction channel subunit for gentle-touch sensation. *Nature* *493*, 221-225.

75. Goodman, M.B., Ernstrom, G.G., Chelur, D.S., O'Hagan, R., Yao, C.A., and Chalfie, M. (2002). MEC-2 regulates *C. elegans* DEG/ENaC channels needed for mechanosensation. *Nature* *415*, 1039-1042.
76. Bagriantsev, S.N., Ang, K.-H., Gallardo-Godoy, A., Clark, K.A., Arkin, M.R., Renslo, A.R., and Minor Jr, D.L. (2013). A high-throughput functional screen identifies small molecule regulators of temperature-and mechano-sensitive K2P channels. *ACS chemical biology* *8*, 1841-1851.
77. Duggan, A., García-Añoveros, J., and Corey, D.P. (2000). Insect mechanoreception: What a long, strange TRP it's been. *Current Biology* *10*, R384-R387.
78. Gillespie, P.G., and Walker, R.G. (2001). Molecular basis of mechanosensory transduction. *Nature* *413*, 194-202.
79. Petit, C. (2006). From deafness genes to hearing mechanisms: harmony and counterpoint. *Trends in molecular medicine* *12*, 57-64.
80. Lumpkin, E.A., and Bautista, D.M. (2005). Feeling the pressure in mammalian somatosensation. *Current opinion in neurobiology* *15*, 382-388.
81. McBride Jr, D.W., and Hamill, O.P. (1993). Pressure-clamp technique for measurement of the relaxation kinetics of mechanosensitive channels. *Trends in neurosciences* *16*, 341-345.
82. McCarter, G.C., Reichling, D.B., and Levine, J.D. (1999). Mechanical transduction by rat dorsal root ganglion neurons in vitro. *Neuroscience letters* *273*, 179-182.
83. Delmas, P., Hao, J., and Rodat-Despoix, L. (2011). Molecular mechanisms of mechanotransduction in mammalian sensory neurons. *Nature Reviews Neuroscience* *12*, 139-153.
84. Drew, L.J., Wood, J.N., and Cesare, P. (2002). Distinct mechanosensitive properties of capsaicin-sensitive and-insensitive sensory neurons. *The Journal of neuroscience* *22*, RC228.
85. Coste, B., Mathur, J., Schmidt, M., Earley, T.J., Ranade, S., Petrus, M.J., Dubin, A.E., and Patapoutian, A. (2010). Piezo1 and Piezo2 are essential components of distinct mechanically activated cation channels. *Science* *330*, 55-60.
86. Chalfie, M. (2009). Neurosensory mechanotransduction. *Nature reviews Molecular cell biology* *10*, 44-52.
87. Delmas, P., and Coste, B. (2013). Mechano-gated ion channels in sensory systems. *Cell* *155*, 278-284.
88. Zaydman, M.A., Silva, J.R., and Cui, J. (2012). Ion channel associated diseases: overview of molecular mechanisms. *Chemical reviews* *112*, 6319-6333.

Chapter 2

Piezo2 and perineal mechanosensation are essential for sexual function

*This chapter is presented in the form it was published in the Journal Science with the following citation:

Lam, R. M., von Buchholtz, L. J., Falgairolle, M., Osborne, J., Frangos, E., Servin-Vences, M. R., ... & Chesler, A. T. (2023). PIEZO2 and perineal mechanosensation are essential for sexual function. *Science*, 381(6660), 906-910.

DOI:10.1126/science.adg0144

Contributions: R.M.L. conceptualized this project, developed the methodology, collected data, performed formal analysis and conducted the investigation. RML drafted, reviewed and edited all versions of the manuscript in collaboration with the supervising authors.



SENSATION

PIEZO2 and perineal mechanosensation are essential for sexual function

Ruby M. Lam^{1,2}, Lars J. von Buchholtz³, Melanie Falgairolle¹, Jennifer Osborne¹, Eleni Frangos¹, M. Rocio Servin-Vences⁴, Maximilian Nagel¹, Minh Q. Nguyen³, Monesha Jayabalan¹, Dimah Saade⁵, Ardem Patapoutian⁴, Carsten G. Bönnemann⁵, Nicholas J. P. Ryba³, Alexander T. Chesler^{1,5*}

Despite the potential importance of genital mechanosensation for sexual reproduction, little is known about how perineal touch influences mating. We explored how mechanosensation affords exquisite awareness of the genitals and controls reproduction in mice and humans. Using genetic strategies and in vivo functional imaging, we demonstrated that the mechanosensitive ion channel PIEZO2 (piezo-type mechanosensitive ion channel component 2) is necessary for behavioral sensitivity to perineal touch. PIEZO2 function is needed for triggering a touch-evoked erection reflex and successful mating in both male and female mice. Humans with complete loss of PIEZO2 function have genital hyposensitivity and experience no direct pleasure from gentle touch or vibration. Together, our results help explain how perineal mechanoreceptors detect the gentlest of stimuli and trigger physiologically important sexual responses, thus providing a platform for exploring the sensory basis of sexual pleasure and its relationship to affective touch.

Sexual reproduction is a fundamental driver for animal behavior, and adaptations required for courtship, including sexual ornamentation and ritual displays, are cornerstones of evolutionary theory (1–3). Visual, auditory, and olfactory cues promote mating in various mammalian species (4–8); however, the act of copulation itself can be considered a specialized form of touch endowed with its own cortical field (9). Although the discovery of the mechanically gated ion-channel PIEZO2 (piezo-type mechanosensitive ion channel component 2) (10) has spurred remarkable progress in our understanding of discriminative touch (11, 12), far less is known about mechanosensation in the genitals (13, 14), including how it triggers physiological responses and elicits pleasure. We hypothesized that sexual touch might exhibit unusual response specialization to control mating and provide affective and motivational feedback. We also expected that there would be sexual dimorphism both in sensation and in responses triggered by genital-innervating mechanosensors. To test these hypotheses, we developed a series of behavioral and functional imaging assays to probe the role of PIEZO2 in genital mechanosensation and sexual function. In addition, by exploring the impact of PIEZO2 loss of function caused by a rare inherited syndrome, we

determined how these findings relate to human sexual experience.

Unusual sensitivity and PIEZO2 dependence of perineal touch

A standard touch sensitivity test uses calibrated von Frey filaments to measure detection threshold. In mice, von Frey sensitivity of the glabrous hind-paw and hairy skin of the face have similar withdrawal thresholds (15–17) despite very different patterns of innervation (18). We adapted this assay to compare stimulation of the perineum (the region extending from the anus to the genitals in male and female mice) with that of the plantar surface of the paw. In the hind-paw assay, mice respond by withdrawing the paw with no indication of pain or distress. Our data (Fig. 1A) match literature reports, with filaments ≥ 0.4 g eliciting responses in the majority of trials, but filaments ≤ 0.16 g rarely provoking reaction (15, 17). By contrast, stimulation of the perineum evoked a highly stereotyped startle and investigative response (movie S1) both in male and female mice. Even the finest filament available (0.008 g) elicited this reaction from every animal (Fig. 1B), demonstrating exquisite sensitivity of the perineum to forces below those that reliably trigger responses from other sites, even in mice with profound allodynia (15, 17); female mice were marginally but consistently more sensitive than males (Fig. 1B).

The mechanically activated ion channel PIEZO2 is essential for discriminative touch in mice and humans (11, 12). We anticipated that this mechanoreceptor would also be responsible for the sensitivity of the perineum. *Piezo2*-null mice die as neonates (19); therefore, we generated conditional genetic deletions using a *Hoxb8-Cre* line (*Piezo2*^{Hoxb8}) to target cells below the mid-thoracic region (17). We used

this strategy to assess the role of PIEZO2 in perigenital sensation and observed profound loss of behavioral response to von Frey filaments (Fig. 1C), with the highest force tested (1.4 g) eliciting responses in only ~40% of trials (movie S1). Local inhibition of the perineum with lidocaine attenuated von Frey responses of controls (fig. S1), and *Piezo2*^{Hoxb8} responses to noxious mechanical pinprick were indistinguishable from those of controls (Fig. 1C and movie S1). Therefore, the *Piezo2*^{Hoxb8} deficit is likely to be sensory rather than related to a movement disorder (20). These experiments demonstrated that PIEZO2 is crucial for triggering behavioral responses to the gentlest of perigenital touch in mice; without this touch receptor, von Frey stimulation of the genital region rarely elicited responses even at intensities considered noxious.

We previously studied a rare cohort of people with biallelic loss-of-function variants of *PIEZO2* who have sensory deficits fully consistent with those described in animal models (11, 21). In our clinical interviews, five adult human subjects with *PIEZO2*-deficiency syndrome (three male and two female) reported severe hyposensitivity in genital sensation (table S1); however, comprehensive quantitative testing has not been possible. One individual adult male consented to quantitative sensory testing of his genitalia during clinical evaluation. His penile von Frey detection threshold (3.1 ± 1.5 g) was far higher than values reported in the literature: 0.3 to 0.6 g in a similar location (22). He had difficulty detecting pressure below 1 kg/cm² at the midshaft and was insensitive to strong vibration at 50 and 100 Hz, which is consistent with our findings in mice. By contrast, literature values for penile fine-touch pressure thresholds in a range of healthy men are far lower (23), and vibration is normally readily detected (23).

Anatomy of perineal neurons

Somatosensory neurons in the lower body have soma in lumbar (L1 to L6) and sacral (S1 to S4) dorsal root ganglia (DRG) (24). However, few details about the types or sensitivity of neurons that target the genitals are known. Multicolor cholera toxin subunit-b (CTB) tracing from both hind-paw and genitals robustly labeled neurons in S1 and S2 DRG (fig. S2A) and distinguished neurons that target perigenital subregions (Fig. 1, D and E). Injections to the perineum, prepuce, and glans (male mice) or vaginal opening (female mice) resulted in largely nonoverlapping labeling of neurons with a range of cell diameters (Fig. 1D and fig. S2B). In both sexes, dense projections targeted the (L6 to S2) spinal cord, with perineal neurons (Fig. 1, D and E, cyan) synapsing in the touch recipient zone (25) of the lateral dorsal horn (Fig. 1E and fig. S2C). Neurons innervating male prepuce (Fig. 1, D and E, yellow) projected to a

¹National Center for Complementary and Integrative Health (NCCIH), Bethesda, MD 20892, USA. ²Brown-National Institutes of Health Graduate Partnerships Program, Brown University, Providence, RI 02912, USA. ³National Institute of Dental and Craniofacial Research, Bethesda, MD 20892, USA. ⁴Howard Hughes Medical Institute, Department of Neuroscience, Dorris Neuroscience Center, The Scripps Research Institute, La Jolla, CA 92037, USA. ⁵National Institute of Neurological Disorders and Stroke, Bethesda, MD 20892, USA.

*Corresponding author. Email: alexander.chesler@nih.gov

medial portion of the touch zone (Fig. 1E), whereas glans axons (Fig. 1, D and E, magenta) terminated proximal to the central canal (Fig. 1E). In females, axons from the vaginal opening targeted the medial dorsal horn, whereas those from the prepuce, which includes the clitoris, closely resembled those from the glans in males.

To visualize the peripheral anatomy of touch neurons in the perineum, we generated mice in which *Piezo2*-expressing neurons were selectively labeled by crossing a *Piezo2-Cre* allele (26) into a neural-specific *Snap25-LSL-GFP* reporter line (27). Green fluorescent protein (GFP) staining of cleared skin demonstrated that the perineum was densely innervated with lanceolate and circumferential endings surrounding hair follicles (Fig. 1F), which is consistent with innervation by a broad range of low-threshold mechanosensory neurons (LTMRs) and the *PIEZO2*-dependent behavioral sensitivity of mice to perineal touch.

Perineal sensory neurons exhibit high sensitivity to punctate stimulation

We developed a sacral ganglia imaging preparation to compare neural responses to a range of gentle and intense mechanical stimuli (28) applied to the hind-paw and perineum (fig. S3 and movie S2). Neurons innervating paw glabrous skin divided into LTMRs and high-threshold mechanosensory neurons (HTMRs) on the basis of their response selectivity (Fig. 2A; fig. S3; and supplementary materials, materials and methods). HTMRs that innervate the paw outnumbered LTMRs by a factor of 2. In particular, LTMRs exhibited graded von Frey sensitivity (Fig. 2A and fig. S3D) and could be activated by forces as low as 0.008 g, whereas HTMRs were essentially silent at forces below 0.4 g, matching behavioral withdrawal threshold and implicating HTMRs in this response. By contrast, perineal sensation was dominated by LTMRs, with ~60% of mechanosensory neurons responding to gentle stimuli (Fig. 2B and figs. S3 and S4) and broad similarity between male and female mice (fig. S4). Almost all perineal mechanosensors could be activated by von Frey stimulation (Fig. 2B, figs. S3, S4), and their calcium (GCaMP) signals were markedly stronger than for paw-innervating neurons (fig. S3D). Few HTMRs responded to the fine filaments that reliably evoked behavioral responses (Fig. 1B and movie S1). Therefore, both male and female mice are attuned to perineal LTM input, and the stereotyped reaction to genital touch is not a sign of pain.

A broad role for *PIEZO2* in perineal sensation

To measure the contribution of *PIEZO2* to perigenital touch and to dissect the mechanism underlying the extreme sensitivity to von Frey stimulation, we next used the sacral imaging platform to selectively image cells that lack this stretch-gated ion channel (fig. S4D).

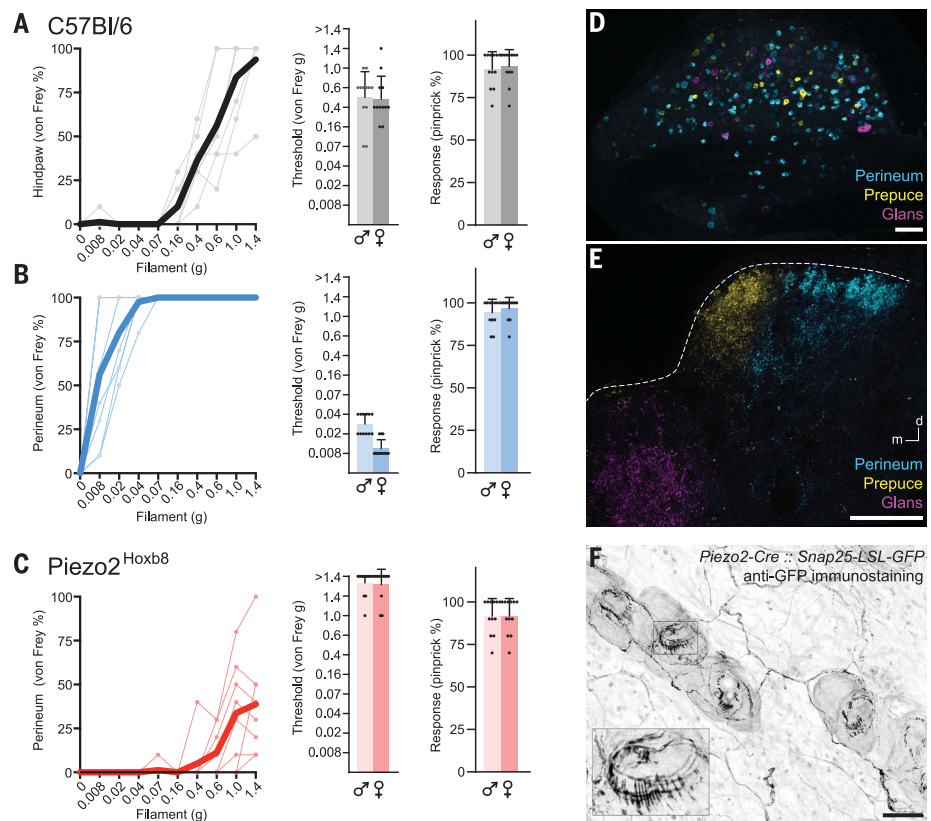


Fig. 1. Behavioral sensitivity of mice to perineal touch and underlying anatomy. (A to C) Reaction of mice to punctate touch (A) wild-type hind-paw, (B) wild-type perineum, and (C) *Piezo2^{Hoxb8}* perineum. (Left) Example responses for individual mice (points and thin lines; four males and four females) and mean (solid lines) to a series of calibrated von Frey filaments (grams, each tested 10 times per mouse). (Middle) Quantitation of von Frey threshold ($\geq 5/10$; $n = 12$ males and 12 females). Thresholds are different between all three groups [one-way analysis of variance (ANOVA) on ranks $P < 0.001$]. Wild-type females exhibited a lower perineal touch threshold than that of males (Mann-Whitney t test; $P < 0.0001$); there were no significant differences in other responses (supplementary materials, statistical reporting). (D and E) Triple-color retrograde CTB tracing from the perineum (cyan), prepuce (yellow), and glans (magenta) showing (D) cell bodies of lumbar-sacral sensory neurons in the DRG and (E) termini in the dorsal spinal cord. The dotted line indicates approximate extent of dorsal horn. In (E) and (F), $n = 4$ mice. Scale bars, 100 μm . (F) Anatomy of sensory ending of *Piezo2*-expressing sensory neurons in the perineum. (Inset) A magnified view of a single hair (boxed) highlighting prominent lanceolate and circumferential endings ($n = 2$ males and 1 female). Scale bar, 50 μm .

As expected, deletion of *Piezo2* (*Piezo2^{ckO}*) dramatically affected the mechanosensitivity of genital-innervating neurons. The great majority of responses to air puff, vibration, and brush were eliminated. Thus, mechanosensory neurons were only stimulated by pinch and were almost exclusively HTMRs (fig. S4E). The overall number of HTMRs was similar between wild-type and *Piezo2^{ckO}* mice (fig. S4F), which is consistent with earlier studies (17, 20, 21). *Piezo2^{ckO}* mice responses to von Frey stimulation were substantially reduced and recapitulated those of control perineal HTMRs (Fig. 2, C to E). These results likely explain the absence of behavioral reactions to von Frey stimulation in *Piezo2^{Hoxb8}* mice (Fig. 1C), support the hypothesis that perineal LTMRs drive this characteristic withdrawal in wild-type mice

(movie S1), and are consistent with human reports and sensory testing (table S1).

A subset of touch neurons is required for mechanically induced erection responses

Perineal investigation and touch precedes mating in many species, including mice (29). These behaviors are linked to motivational drive in both partners and trigger physiological reflexes. For example, gentle retraction of the prepuce induces penile cupping (erection) and flipping (ejaculation) in spinalized rodents (30). We reasoned that mechanosensory input drives the erection reflex and developed an assay to monitor this in restrained awake mice. A soft, transparent tube was used to gently retract the prepuce, allowing the physiological erection reflex (extension of the penis into the tube)

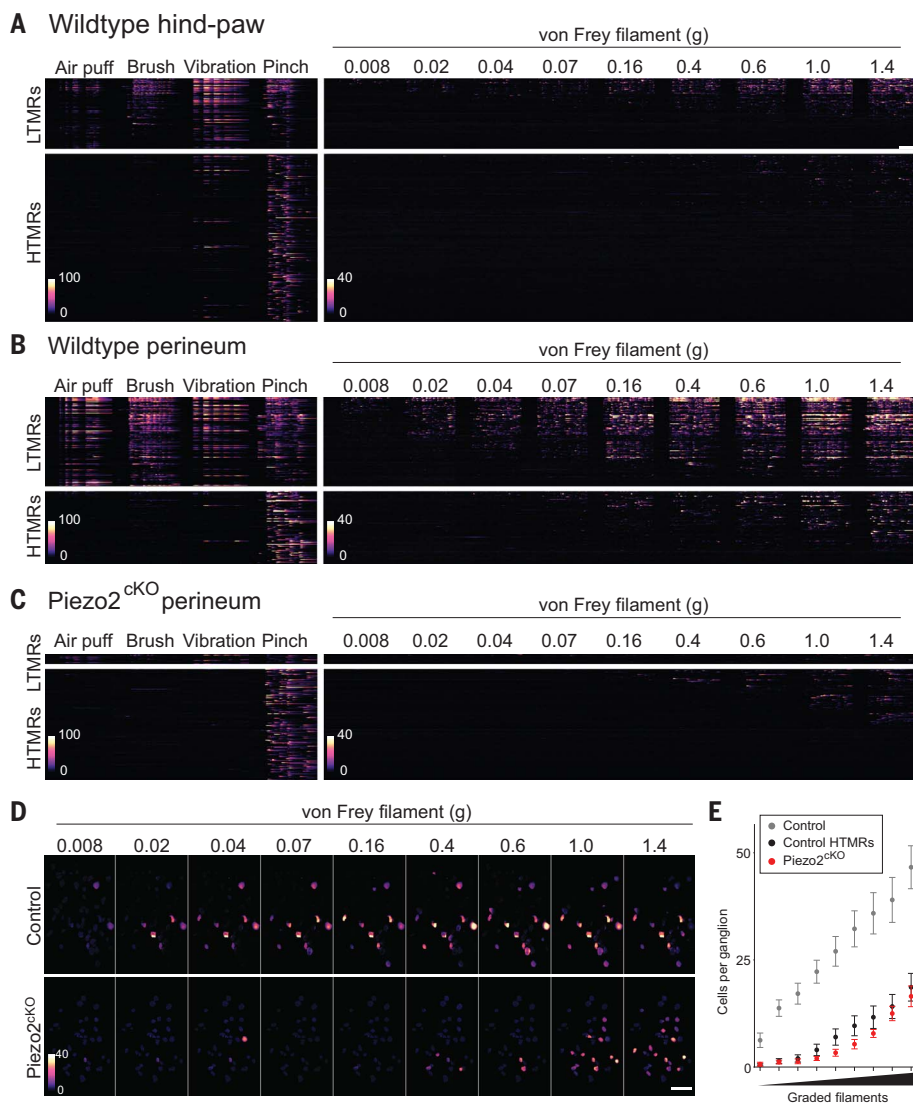


Fig. 2. Functional characterization of perineal mechanoreceptors and role of PIEZO2. (A to C) Heatmaps representing calcium (GCaMP6f) responses to (left) repetitive application of naturalistic stimuli and (right) graded von Frey stimulation. LTMRS and HTMRS are separated, and relative fluorescence changes ($\Delta F/F$) are colored as indicated. Scale bar, 10 s. (A) Wild-type hind-paw, $n = 4$ mice. (B) Wild-type perineum, $n = 4$ mice. (C) Piezo2^{cKO} perineum, $n = 6$ mice. Additional analysis is provided in figs. S3 and S4. (D) Spatial activity maps of control and Piezo2^{cKO} neurons to von Frey filaments. Scale indicates response intensity. Scale bar, 100 μm . (E) Quantitation of von Frey responsive neurons in control mice (gray), Piezo2^{cKO} mice (red), and response profile of control HTMRS (black) (mean \pm SEM, $n = 8$ control mice, $n = 6$ Piezo2^{cKO} mice). Piezo2^{cKO} mice had fewer von Frey responsive neurons at all filament strengths (Mann Whitney U test; $P < 0.0087$).

to be scored. Wild-type controls responded in almost every single trial (Fig. 3A); isoflurane anesthesia completely eliminated responses, and local numbing of the perineum with lidocaine greatly dampened the reflex (fig. S5). As we anticipated, Piezo2^{Hoxb8} mice only very rarely exhibited penile extension in response to prepulse retraction (Fig. 3A).

Piezo2^{Hoxb8} mice exhibit broad loss of touch but also have proprioceptive (and potentially other mechanosensory) deficits (17, 28). There-

fore, we examined mice with more selective Piezo2 deletions. Piezo2^{Pvalb} mice (in which Piezo2 is inactivated by using *parvalbumin*-driven *Cre*) lack proprioceptive input but still respond to gentle touch (20). These mice had perfectly normal responses to prepulse retraction (Fig. 3A) despite severe ataxia. We also generated Piezo2 deletions using an *Scn10a-Cre* line, which is commonly used to target a broad range of nociceptors, including HTMRS (31). Perineal HTMR responses are PIEZO2

independent (Fig. 2 and fig. S4); therefore, these mice (Piezo2^{Scn10a}) were predicted to have normal proprioception, touch, and consequently erection reflexes. Piezo2^{Scn10a} mice walked with normal gait, and recombination of *Scn10a-Cre* in sacral ganglia neurons was faithful (Fig. 3, B and C, and fig. S6A), with only a few large-diameter *Scn10a*-negative LTMRS labeled (fig. S6A). Nonetheless, Piezo2^{Scn10a} mice displayed severe deficits in their erection reflex, closely recapitulating the phenotype of Piezo2^{Hoxb8} animals (Fig. 3A) and the effects of lidocaine (fig. S5A). Single-cell sequencing data from lumbar DRG (32) and trigeminal neurons (33) validate *Scn10a* as a robust marker for nociceptors but reveal expression in c-fiber LTMRS (cLTMRS). We used in situ hybridization (ISH) to confirm coexpression of *Scn10a*, the cLTMRS marker *Tyrosine hydroxylase* (*Th*) (24), and *Piezo2* in sacral ganglia (Fig. 3C), with only very limited recombination in other potential LTMRS (fig. S6A). Because cLTMRS responses to gentle mechanical stimulation depend on *Piezo2* expression (34), these data strongly suggest a causal role for perineal cLTMRS input in triggering the erection reflex. Consistent with this hypothesis, tdTomato-positive lanceolate endings (typical of cLTMRS) surround perineal hair follicles in *Scn10a-Cre*, *Ai9* mice (Fig. 3D). Moreover, functional imaging of perineal touch responses in *Scn10a-Cre*, *Ai95* mice revealed that neurons responding to gentle mechanical stimuli (fig. S6, B and C) had uniform small diameters, as would be expected for cLTMRS (24, 34).

Severely impaired sexual function in mice lacking PIEZO2

Loss of a touch-induced erection response in Piezo2^{Hoxb8} males should impair mating. Indeed, 10 pairs of mating-age Piezo2^{Hoxb8} males and females housed together for 6 months never produced pups, whereas wild-type (C57Bl/6) controls delivered 61 litters in this time (range, five to seven litters per pair). To assess copulatory success more directly, we also examined the frequency of vaginal plug formation after introducing virgin females in estrus to single housed males; to eliminate bias from prior experience, all mice were naïve. For C57Bl/6 mice, 7 from 10 homozygous pairings had plugs after 4 hours (Fig. 3E). By contrast, plugs were never seen for Piezo2^{Hoxb8} male mice when paired either with Piezo2^{Hoxb8} or wild-type females (Fig. 3E). As predicted from their normal erection reflexes, Piezo2^{Pvalb} males successfully mated with C57Bl/6 females despite severe ataxia (Fig. 3E). However, Piezo2^{Scn10a} males failed to plug receptive C57Bl/6 females, substantiating the importance of PIEZO2-dependent mechanosensory input for male mating behavior (Fig. 3E). Although loss of erection reflexes may explain why Piezo2^{Hoxb8} mice fail to breed, mechanosensation probably has additional

roles in mating. For example, female mice have similar PIEZO2-dependent perineal mechanosensitivity to males (fig. S4) and are even more sensitive to perigenital touch (Fig. 1); *Piezo2*^{Hoxb8} females exhibited strong mating deficits when paired with wild-type males: 9 from 10 remained unplugged after 4 hours (Fig. 3E).

Ethogram analysis of female intruder assays (Fig. 3F) assess motivation by quantifying stereotyped male behaviors, including partner-grooming, anogenital chemosensory investigation, and mounting attempts (35, 36). We analyzed behavior for 1 hour after introduction of receptive females (supplementary materials, materials and methods). Control animals exhibited considerable variation in mating behavior (Fig. 3F) but in every case ($n = 10$ pairs of mice) engaged in chemosensory investigation and mounting attempts shortly after introduction of the female. Similarly, pairs of *Piezo2*^{Hoxb8} males and females ($n = 10$ pairs) (Fig. 3F) as well as male or female *Piezo2*^{Hoxb8} mice paired with C57Bl/6 partners ($n = 10$ pairs in each case) (fig. S5B) exhibited strong sexually motivated behavior, not very different from controls. However, *Piezo2*^{Hoxb8} males never achieved intromission, which was regularly observed in wild-type controls. Similarly, *Piezo2*^{Scn10a} males paired with receptive C57Bl/6 females showed normal sexual motivation ($n = 10$ males and 10 females) (fig. S5B) but without copulatory success (Fig. 3E). Moreover, *Piezo2*^{Hoxb8} females paired with C57Bl/6 males also engaged in premating behavior, including male mounting attempts (fig. S5B), but *Piezo2*^{Hoxb8} females adopted a sit-rejection posture, preventing intromission (37). These data show that mechanosensation plays a substantial role in productive mating and exposes dimorphic need for PIEZO2 and gentle touch in sexual function.

Impact of PIEZO2 in human sexual experience

The genital sensation of a man with complete loss of PIEZO2 function and comprehensive touch- and proprioception-related studies of individuals with PIEZO2-deficiency syndrome (11, 21) demonstrate strongly conserved roles for PIEZO2 in mammalian mechanosensation. For humans, sexual experience is not simply related to reproduction but is central to large parts of many people's social lives and behavior. Information from human clinical evaluations ($n = 5$; three men and two women) (table S1) provided several consistent themes about the role of gentle touch in sex. First, these individuals with biallelic loss of function (table S1A) had diagnostic clinical presentation, with loss of proprioception, absent vibration sensing, highly elevated touch threshold, and scoliosis but no cognitive difficulties, and all underwent puberty without clinically relevant problems. Second, all five people with PIEZO2 deficiency reported being sexually active and able to be

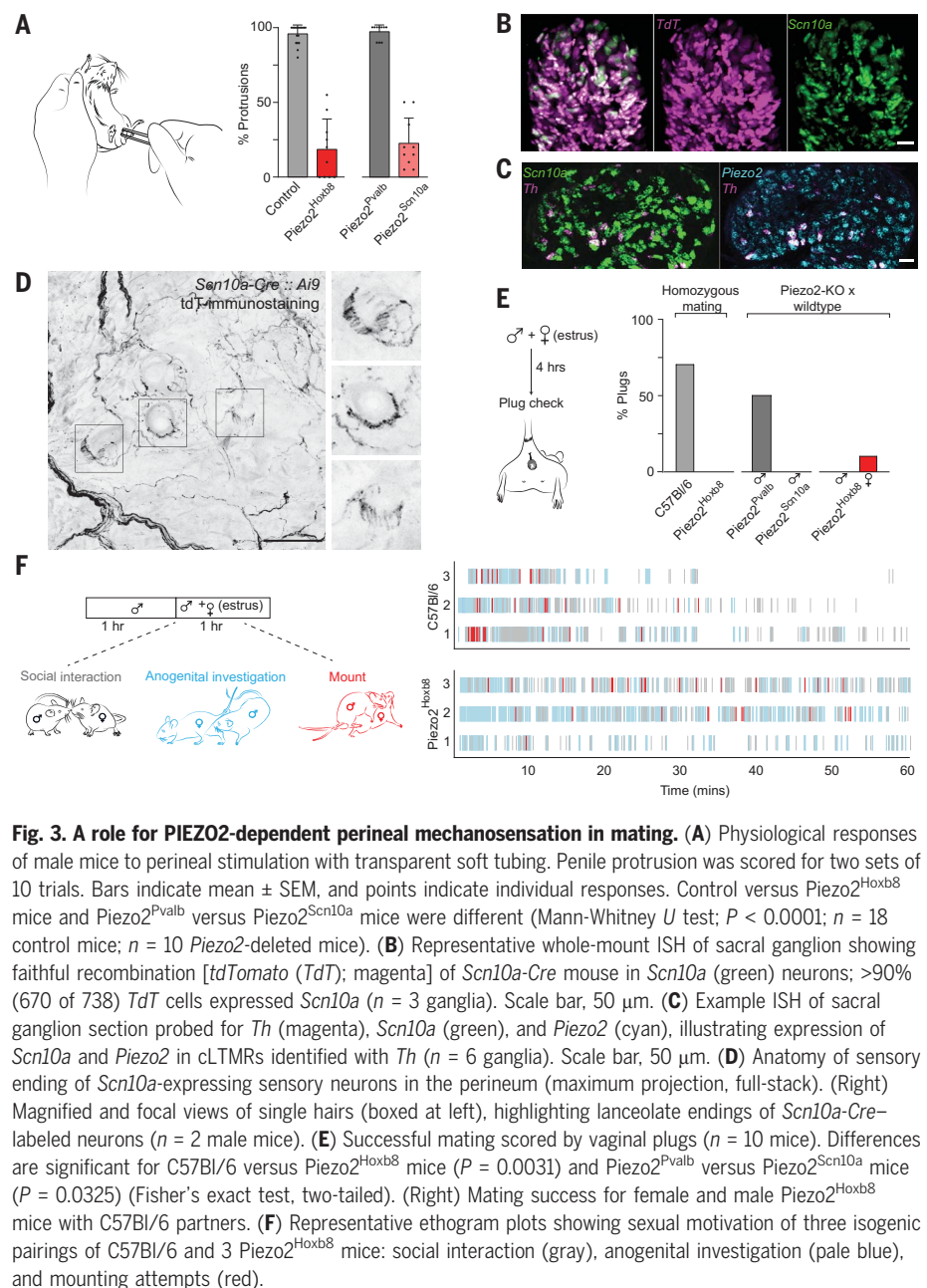


Fig. 3. A role for PIEZO2-dependent perineal mechanosensation in mating. (A) Physiological responses of male mice to perineal stimulation with transparent soft tubing. Penile protrusion was scored for two sets of 10 trials. Bars indicate mean \pm SEM, and points indicate individual responses. Control versus *Piezo2*^{Hoxb8} mice and *Piezo2*^{Pvalb} versus *Piezo2*^{Scn10a} mice were different (Mann-Whitney U test; $P < 0.0001$; $n = 18$ control mice; $n = 10$ *Piezo2*-deleted mice). (B) Representative whole-mount ISH of sacral ganglion showing faithful recombination [*tdTomato* (*TdT*); magenta] of *Scn10a-Cre* mouse in *Scn10a* (green) neurons; $>90\%$ (670 of 738) *TdT* cells expressed *Scn10a* ($n = 3$ ganglia). Scale bar, 50 μ m. (C) Example ISH of sacral ganglion section probed for *Th* (magenta), *Scn10a* (green), and *Piezo2* (cyan), illustrating expression of *Scn10a* and *Piezo2* in cLTMRs identified with *Th* ($n = 6$ ganglia). (D) Anatomy of sensory ending of *Scn10a*-expressing sensory neurons in the perineum (maximum projection, full-stack). (Right) Magnified and focal views of single hairs (boxed in left), highlighting lanceolate endings of *Scn10a-Cre*-labeled neurons ($n = 2$ male mice). (E) Successful mating scored by vaginal plugs ($n = 10$ mice). Differences are significant for C57Bl/6 versus *Piezo2*^{Hoxb8} mice ($P = 0.0031$) and *Piezo2*^{Pvalb} versus *Piezo2*^{Scn10a} mice ($P = 0.0325$) (Fisher's exact test, two-tailed). (Right) Mating success for female and male *Piezo2*^{Hoxb8} mice with C57Bl/6 partners. (F) Representative ethogram plots showing sexual motivation of three isogenic pairings of C57Bl/6 and 3 *Piezo2*^{Hoxb8} mice: social interaction (gray), anogenital investigation (pale blue), and mounting attempts (red).

aroused by physical genital stimulation, erotic thoughts, or videos, reflecting motivation seen in *Piezo2*^{Hoxb8} mice (Fig. 3F). Third, individuals with PIEZO2 deficiency reported delayed, attenuated, or absent physiological responses to gentle genital stimulation. This included clinical diagnosis of hypo-orgasmia for the male and anorgasmia for the female participants, which again is consistent with the animal model. However, the five people had strategies to compensate for deficits in genital sensation (table S1B).

Discussion

Erogenous touch conveys different meanings according to circumstance; however, many key

details remain unknown. We explored how deficits in PIEZO2-dependent mechanosensation interfere with perigenital sensation, physiological response, copulation, and reproduction. Our results demonstrate that PIEZO2-dependent touch is required for all of these in mice.

Anatomical studies have identified specialized corpuscles composed of myelinated afferents likely involved in genital sensation (38, 39). Our data strongly implicate an additional type of touch neuron, the perineal cLTMRs, as crucial drivers of sexual function. Previous studies in mice and humans suggest specialized roles for cLTMRs in conveying affective and pleasurable touch (40, 41). Thus, it is of note that five

individuals without *PIEZO2* function described sexual activity as satisfying and rewarding despite marked mechanosensory deficits and clinical evaluations of hypo-orgasmia (men) and anorgasmia (women). We have previously shown that for humans, other types of sensory input can compensate for deficits caused by loss of *PIEZO2* function (11). For example, these individuals use vision to overcome proprioceptive deficits and mechanonociception or thermosensation to mitigate deficits in touch (11). This is also true for human sexual touch (table S1). Nonetheless, the crucial role of *PIEZO2* for perineal touch in mice and humans may have therapeutic potential: Topical *PIEZO2* inhibitors could provide targeted relief of genital hypersensitivity and pain, whereas agonists of *PIEZO2* are candidates for alleviating genital hyposensitivity.

There are a number of limitations to this work. For example, *PIEZO2* deficiency is extremely rare, and we were unable to carry out detailed quantitative sensory testing in a larger group of human subjects. Additionally, functional imaging experiments were carried out in anesthetized mice, precluding evaluation of responses during mating. Moreover, although we showed the necessity of gentle touch input for mating, we have not yet demonstrated the sufficiency of this sensory pathway for sexual function in awake behaving animals. We also anticipate that there are likely to be additional specialized roles for mechanosensory neurons in mating that were not revealed in this study.

Even the very gentlest of perineal touches elicits a highly stereotyped startle reaction from mice that is easy to anthropomorphize (movie S1). This *PIEZO2*-dependent response is quite different from touch to other parts of the body, which typically evokes more modest reactions and does so only at much greater forces. *PIEZO2*-dependent perineal touch is also a crucial driver of successful mating both for male and female mice. Future studies should help define addi-

tional subtypes of sensory neurons needed for sexually dimorphic reactions and how perineal sensation is organized in the spinal cord and brain to prioritize salience. Ultimately, however, the profound impact of *PIEZO2* deficiency that we describe provides a sensory basis at the molecular and cellular level for an aspect of life that throughout history has engaged in human imagination (42) and thought (1).

REFERENCES AND NOTES

1. C. Darwin, *The Descent of Man and Selection in Relation to Sex* (Murray, 1871), vols. 1 and 2.
2. J. J. Dinsmore, *Auk* **87**, 305–320 (1970).
3. S. J. Gould, *Evolution* **28**, 191–220 (1974).
4. M. A. Changizi, Q. Zhang, S. Shimajo, *Biol. Lett.* **2**, 217–221 (2006).
5. B. D. Charlton, M. S. Martin-Wintle, M. A. Owen, H. Zhang, R. R. Swaisgood, *R. Soc. Open Sci.* **5**, 181323 (2018).
6. V. S. Mandiyani, J. K. Coats, N. M. Shah, *Nat. Neurosci.* **8**, 1660–1662 (2005).
7. L. Stowers, T. E. Holy, M. Meister, C. Dulac, G. Koentges, *Science* **295**, 1493–1500 (2002).
8. C. C. Voigt et al., *J. Mammal.* **89**, 1401–1410 (2008).
9. C. A. Kell, K. von Kriegstein, A. Rösler, A. Kleinschmidt, H. Laufs, *J. Neurosci.* **25**, 5984–5987 (2005).
10. B. Coste et al., *Science* **330**, 55–60 (2010).
11. A. T. Chesler et al., *N. Engl. J. Med.* **375**, 1355–1364 (2016).
12. S. S. Ranade et al., *Nature* **516**, 121–125 (2014).
13. Y. Garcia-Mesa et al., *J. Anat.* **238**, 446–454 (2021).
14. Y. Garcia-Mesa et al., *J. Anat.* **239**, 892–902 (2021).
15. I. Abdus-Saboor et al., *Cell Rep.* **28**, 1623–1634.e4 (2019).
16. T. Hua et al., *Nat. Neurosci.* **23**, 854–868 (2020).
17. S. E. Murthy et al., *Sci. Transl. Med.* **10**, eaat9897 (2018).
18. V. E. Abraira, D. D. Ginty, *Neuron* **79**, 618–639 (2013).
19. K. Nonomura et al., *Nature* **541**, 176–181 (2017).
20. S.-H. Woo et al., *Nat. Neurosci.* **18**, 1756–1762 (2015).
21. M. Szczot et al., *Sci. Transl. Med.* **10**, eaat9892 (2018).
22. M. L. Sorrells et al., *BJU Int.* **99**, 864–869 (2007).
23. C. B. Bleustein, H. Eckholdt, J. C. Arezzo, A. Melman, *J. Urol.* **169**, 2266–2269 (2003).
24. L. Li et al., *Cell* **147**, 1615–1627 (2011).
25. V. E. Abraira et al., *Cell* **168**, 295–310.e19 (2017).
26. S. H. Woo et al., *Nature* **509**, 622–626 (2014).
27. L. Madisen et al., *Neuron* **85**, 942–958 (2015).
28. K. L. Marshall et al., *Nature* **588**, 290–295 (2020).
29. F. A. Beach, *Horm. Behav.* **7**, 105–138 (1976).
30. B. D. Sachs, *Physiol. Behav.* **24**, 489–492 (1980).
31. N. Agarwal, S. Offermanns, R. Kuner, *Genesis* **38**, 122–129 (2004).
32. N. Sharma et al., *Nature* **577**, 392–398 (2020).
33. M. Q. Nguyen, C. E. Le Pichon, N. Ryba, *eLife* **8**, e49679 (2019).

34. L. J. von Buchholtz et al., *Neuron* **109**, 285–298.e5 (2021).
35. C. J. Burnett et al., *eLife* **8**, e44527 (2019).
36. S. X. Zhang et al., *Nature* **597**, 245–249 (2021).
37. X. Zhou et al., *Science* **379**, 820–825 (2023).
38. R. D. Johnson, Z. Halata, *J. Comp. Neurol.* **312**, 299–310 (1991).
39. D. Ohmori, *Anat. Embryol.* **70**, 347–410 (1924).
40. D. Huzard et al., *Sci. Adv.* **8**, eabo7566 (2022).
41. H. Olsson et al., *Nat. Neurosci.* **5**, 900–904 (2002).
42. M. Vatsyayana, *The Kama Sutra of Vatsyayana*, R. F. Burton, B. Indrajit, S. P. Bhide, Transl. (1883).

ACKNOWLEDGMENTS

We thank T. Delong, M. Singh, and M. Bradson for distributing questionnaires to human subjects and collating clinical notes; members of the clinical staff at NCCIH and Bönnemann groups for support in arranging human studies; and M. Szczot, N. Ghitani, D. Macdonald, and R. Hardy for input and expertise with animal experiments. Hormone analysis was carried out by the University of Virginia Center for Research in Reproduction Ligand Assay and Analysis Core. **Funding:** This work was supported by the National Institutes of Health, NCCIH Z01-ZIAAT000028 (to A.T.C.); National Institutes of Health, NIDCR Z01-ZIADE000561 (to N.J.P.R.); National Institutes of Health, NINDS Z01-ZIANS003129 (to C.G.B.); and the Howard Hughes Medical Institute (to A.P.) **Author contributions:** Conceptualization: R.M.L., N.J.P.R., and A.T.C. Methodology: R.M.L., M.F., L.J.v.B., E.F., C.G.B., N.J.P.R., and A.T.C. Investigation: R.M.L., M.F., J.O., E.F., M.R.S.-V., M.N., M.Q.N., M.J., and D.S. Funding acquisition: A.P., C.G.B., N.J.P.R., and A.T.C. Supervision: A.P., C.G.B., N.J.P.R., and A.T.C. Writing – original draft: R.M.L., L.J.v.B., N.J.P.R., and A.T.C. Writing – review and editing: R.M.L., M.F., L.J.v.B., E.F., A.P., C.G.B., N.J.P.R., and A.T.C. **Competing interests:** The authors declare that they have no competing interests. **Data and materials availability:** All data generated and/or analyzed during the current study are provided in the supplementary materials and/or have been deposited in Dryad. **License information:** Copyright © 2023 the authors, some rights reserved; exclusive licensee American Association for the Advancement of Science. No claim to original US government works. <https://www.science.org/about/science-licenses-journal-article-reuse>. This article is subject to HHMI's Open Access to Publications policy. HHMI lab heads have previously granted a nonexclusive CC BY 4.0 license to the public and a sublicensable license to HHMI in their research articles. Pursuant to those licenses, the author-accepted manuscript (AAM) of this article can be made freely available under a CC BY 4.0 license immediately upon publication.

SUPPLEMENTARY MATERIALS

[science.org/doi/10.1126/science.adg0144](https://doi.org/10.1126/science.adg0144)
Materials and Methods
Figs. S1 to S7
Table S1
References (43–46)
Movies S1 and S2

Submitted 27 November 2022; accepted 13 July 2023
10.1126/science.adg0144



PIEZO2 and perineal mechanosensation are essential for sexual function

Ruby M. Lam, Lars J. von Buchholtz, Melanie Falgairolle, Jennifer Osborne, Eleni Frangos, M. Rocio Servin-Vences, Maximilian Nagel, Minh Q. Nguyen, Monesha Jayabalan, Dimah Saade, Ardem Patapoutian, Carsten G. Bnnemann, Nicholas J. P. Ryba, and Alexander T. Chesler

Science, **381** (6660), .

DOI: 10.1126/science.adg0144

Editor's summary

It is well known that the genitals are unusually sensitive, and that genital touch is crucial for mating and associated pleasure, but the underlying basis is not completely understood. By studying mice and humans with a rare inherited mechanosensory syndrome, Lam *et al.* identified a mechanism involving the mechanoreceptor PIEZO2 that is responsible for determining genital sensitivity (see the Perspective by George and Abaira). Their results highlight the importance of touch for driving physiological responses needed for sexual function. The identification of PIEZO2 and a specific type of touch neuron as key mediators might help in the development of therapeutic approaches for both hypo- and hypersensitivity that interfere with the enjoyment of sex. —Mattia Maroso

View the article online

<https://www.science.org/doi/10.1126/science.adg0144>

Permissions

<https://www.science.org/help/reprints-and-permissions>

Use of this article is subject to the [Terms of service](#)

Science (ISSN) is published by the American Association for the Advancement of Science. 1200 New York Avenue NW, Washington, DC 20005. The title *Science* is a registered trademark of AAAS.

Copyright © 2023 The Authors, some rights reserved; exclusive licensee American Association for the Advancement of Science. No claim to original U.S. Government Works



Supplementary Materials for

PIEZO2 and perineal mechanosensation are essential for sexual function

Ruby M. Lam *et al.*

Corresponding author: Alexander T. Chesler, alexander.chesler@nih.gov

Science **381**, 897 (2023)
DOI: 10.1126/science.adg0144

The PDF file includes:

Materials and Methods
Figs. S1 to S7
Table S1
References

Other Supplementary Material for this manuscript includes the following:

Movies S1 and S2

Methods

Experimental Model and Subject Details

Clinical evaluation

5 patients with two PIEZO2 loss-of-function alleles were surveyed and evaluated at the National Institutes of Health (NIH) under a research protocol approved by the Institutional Review Boards of National Institute of Neurological Disorders and Stroke (NINDS, protocols 12-N-0095 / 12-N-0077) between April 2015 and May 2023.

Animals

All experiments using animals strictly followed National Institutes of Health (NIH) guidelines and were approved by the National Institute of Neurological Disorders and Stroke (NINDS) or the Scripps Research Institute in compliance with regulatory standards established by the Association for Assessment and Accreditation of Laboratory Animal Care International (AAALAC) Animal Care and Use Committees. Adult male and female mice were used as indicated in the text; for behavioral studies and mating, animals were between 6 and 16 weeks at the start of the experiment; functional imaging was performed on animals weighing between 20 and 35g (10-16 weeks); histology used mice from 5-16 weeks. For all studies, age-matched knockout and wild type littermates were tested at the same age in each cohort. Ai95 (27) mice (B6;129S-*Gt(ROSA)26Sor^{tm95.1(CAG-GCaMP6f)Hze}/J*, Jackson Laboratory) were crossed into a *Piezo2^{fllox/fllox}* background (21). *Piezo2^{ckO}* was induced by intrajugular and intraperitoneal injection of AAV9-CAG-Cre into neonates as described previously (21). This approach was extensively quantitated (21), results in GCaMP expression in 30-80% of sensory neurons with no apparent selectivity (34) and eliminates PIEZO2 function from more than 90% of GCaMP-expressing cells (21, 34). Cre-driver lines were used to knockout *Piezo2* in select subsets of neurons using *Hoxb8-Cre* (17), *Scn10a-Cre* (31) and *Pvalb-Cre* (27). *Scn10a-Cre* was crossed into an Ai9 (B6.Cg-*Gt(ROSA)26Sor^{tm9(CAG-tdTomato)Hze}/J*, Jackson Laboratory) background (43) for anatomical characterization and to *Piezo2^{fllox/fllox}* (12) or Ai95 to examine function. We also crossed *Piezo2-Cre* (*Piezo2^{tm1.1(cre)Apat}*) mice (26) with a *Snap25-GFP* (*Snap25^{tm1.1Hze}*) Cre-reporter line (27) to examine perineal skin projections of cLTMRs.

In vivo epifluorescence calcium imaging of sacral ganglia

Mice were anesthetized with isoflurane and transferred to a custom platform which exposed the genital area for stimulus application. Briefly, the head was loosely secured to the nose cone and hand warmers were used to maintain body temperature. The dorsal aspect of the sacrum was surgically exposed after partial removal of the gluteus medius and stabilized with a spinal clamp (Narishige STS-A). Using a dental drill, the dorsal root ganglia in the pelvis was exposed by removing a portion of the auricular surface along with the posterior articular process of the 6th Vertebra and the first anterior articular process of the sacrum (S1) or posterior articular process (S2); hemostatic dental sponges (Pfizer Gel Foam) were applied as needed to control bleeding. Following surgery, the animal was transferred to the stage of a custom tilting light microscope (Thorlabs Cerna) equipped with a 4X, 0.28 NA air objective (Olympus). GCaMP6f fluorescence images were acquired with a CMOS camera (PCO Panda 4.2) using a standard green fluorescent protein (GFP) filter cube in 40 second epochs at 5 Hz. Mechanical stimuli applied to the animal skin included a series of pressurized air puffs from a Picospritzer (25psi,

for 0.2, 1, 3 and 5 seconds), vibration at (50, 75, 100, 125 and 150 Hz for 3 seconds each), manual gentle brushing with an acrylic brush, skin pinch with forceps (Students) and von Frey filaments stimulation (0.008g, 0.02g, 0.04g, 0.07g, 0.16g, 0.4g, 0.06g, 1.0g, and 1.4g filaments). Regions of interest (ROI) outlining responding cells were drawn in FIJI/ImageJ and relative change of GCaMP6f fluorescence was calculated as percent $\Delta F/F$. Contaminant signal e.g., from out-of-focus tissue and neighboring cells was removed by subtracting the fluorescence of a donut-shaped area surrounding each ROI using a custom MATLAB script (44). Overlapping ROIs and rare spontaneously active cells were excluded from the analysis. Imaging episodes were concatenated for display as traces or activity heatmaps. Data shown in figures come from equal numbers of male and female mice.

Background fluorescence noise was calculated for each ROI as the standard deviation of the bottom 25% of all data points as described previously (44). A transient rise in fluorescence was considered significant if its peak exceeded 15 times this value. Cells were defined as HTMRs if they responded primarily only to pinch and/or high force von Frey filaments and as LTMRs if they were activated by any or all gentle stimuli. To do this computationally (34), cells were classified as air-puff cells if they had significant responses to air-puff that were at least 2 times as strong as their brush response. Vibration cells had significant vibration responses and a ratio of vibration responses to all other responses greater than 3. Brush cells had a significant brush response, a ratio of brush to air-puff response greater than 2 and a ratio of pinch to brush responses greater than 3. Mixed responders had significant air-puff and brush responses with a ratio between 0.5 and 2 and ratios of pinch to low-threshold smaller than 3. Air-puff cells, vibration cells, brush cells and mixed responders all detect low force stimuli and are therefore classified as LTMRs. HTMRs were defined as cells that had a significant response to pinch and had a ratio of high threshold to low threshold peak responses of at least 3. Cells that only responded significantly to von Frey stimulation were also classified as HTMRs.

von Frey thresholds were determined as the smallest force filament eliciting a significant response that was maintained in at least 50% of episodes with increasing filament force. The area under the curve for a given stimulus and cell was calculated by adding up all $\Delta F/F$ data points above baseline from the onset of stimulation to the end of the episode.

Spatial maps of activity were generated by calculating the standard deviation for each pixel over a stimulation episode in FIJI/ImageJ as described previously (34). Cell type specific maps (LTMRs vs. HTMRs) were generated by multiplying standard deviation images for the preferred stimulus of each cell with a binary mask outlining the cell. All LTMRs and HTMRs within the field of view were then aggregated by maximum intensity projection. The resulting map distinguishes between LTMRs and HTMRs and provides an estimate of the response magnitude as well as the shape and location of a cell.

von Frey stimulation

Mice were individually habituated on a mesh floor covered by a transparent glass vessel for 1 hour. Nylon monofilaments (Stoelting) were directly applied to the glabrous skin of the hind-paw or to the perineum until the filament bent slightly. Withdrawal, flinch and jump responses within the following 1 second was recorded. This single force touch was repeated 10 times for each filament with ascending forces of (0.008g, 0.02g, 0.04g, 0.07g, 0.16g, 0.4g, 0.06g, 1.0g, and 1.4g) until the animals responded 100% of the time for two filaments in a row. Animals receiving lidocaine treatment were injected intradermally in 5 locations around the genital area (total volume: 125 μ l 1% lidocaine).

Female intruder assay and vaginal plug assessment of mating success

All trials probing social and sexual interactions were conducted in home cages without bedding covered by clear plexiglass to allow videography and accurate scoring of behavior. All experiments were conducted during the dark cycle and all animals were sexually naive. Mice were between 8 and 16 weeks of age. In a separate cohorts of 10 mice, blood tests (early light cycle, Ligand Assay and Analysis Core, University of Virginia) confirmed that $Piezo2^{Hoxb8}$ and control males exhibited testosterone and FSH levels that fall within the normal adult range (fig. S7A, B), males had similar gonadal size (mass of dissected testis) relative to total body weight (fig. S7C). We also confirmed that $Piezo2^{Hoxb8}$ and control females exhibited comparable estrus cycle length by examining vaginal lavage on a daily basis at the start of the dark cycle (fig. S7D). Male mice used for female intruder behavior assays were singly housed and adapted to the test chamber for 1 hour. Females were group housed and were evaluated by vaginal lavage and cytology to confirm estrus immediately before their introduction to the test cage. The male was removed after 3 hours; male behavior was scored for the first hour of interaction using BORIS software (45). Vaginal copulatory plugs were assessed one hour after the male was removed.

Penile Protrusion Test

Animals, restrained by scruffing, were held in a supine position allowing clear tubing (Tygon S3™ E-3603 F ACFUN007) to be applied around the base of the penis immediately over the external prepuce. Each animal was custom fitted with tubing of optimal inner diameter for gentle prepuce retraction over 5 test trials. Once the correctly sized tubing was determined, 10 tests were performed in succession. The protrusion of the internal prepuce as the penis extended into the tube away from the body wall was scored. The test assay was repeated the following day for an additional 10 trials and results pooled.

Histology

Retrograde tracing of sensory innervation used CTB-488, CTB-555, and CTB-647 (ThermoFisher) in 0.2% in PBS. C57Bl/6 Mice were anaesthetized with 2% isoflurane, hair was removed from area of interest and CTB was injected subcutaneously and unilaterally. Paw, glabrous skin (2-4 injections, ~2 μ l); perineum (5-10 injections ~4 μ l); prepuce / external vagina (2-4 injections ~2 μ l); glans (1-2 injections ~2 μ l) and opening of vagina (internal vagina, 1-2 injections ~2 μ l). After 10-14 days, mice were perfused with 4% paraformaldehyde (PFA) in phosphate buffered saline (PBS), the L6-S2 spinal segments and DRGs were dissected and postfixed (4% PFA) overnight at 4°C. The spinal segments and DRGs were transferred to PBS and embedded in a 5% agar/PBS solution. Transverse sections (60 μ m for spinal cord and 100 μ m for DRGs) were cut on a vibratome. Sections were then mounted on slides and cover slipped with Vectashield Vibrance (Vector laboratories).

To study sensory innervation of the perineum, mice were anesthetized with 2% isoflurane, hair was removed, and the skin cleaned before perfusion with 4% PFA. Skin was dissected, scraped of excess fat and postfixed (4% PFA, overnight). Tissue was washed PBS with 0.3% Triton X-100 (PBST) every hour for 5-8 hours, incubated with primary (1:1000 chicken anti-GFP or rabbit anti-RFP, Abcam) in PBST containing 10% donkey serum and 20% DMSO (DS PBST, room temperature, 3–5 days). Primary antibody was removed with PBST washes (5–8, 1h) and transferred to secondary antibodies (1:200, donkey anti-chicken-FITC or anti-rabbit-Rhodamine-Red-X, Jackson ImmunoResearch) in DS PBST, room temperature, 2

days. Tissue was then washed with PBS every hour for 5 hours and dehydrated in 50%, 75, 100% methanol for 1 hour each, and then left in 100% methanol overnight. Finally, the skin was cleared in BABB (benzyl alcohol; benzyl benzoate, 1:2, Sigma) at room temperature and mounted on slides. Images were acquired using an Olympus BX63L confocal microscope with 10X (air) or 30X (oil) objectives.

For whole-mount ISH, fresh DRGs were dissected from animals and processed as previously described (34). Whole unmounted DRGs were dissected and placed into 0.2 ml tubes with 4% paraformaldehyde in phosphate buffered saline (PBS) for 90 mins on ice. Ganglia were washed 3 times in PBS and ISH was performed using Hybridization Chain Reaction (version 3, Molecular Instrument) as previously described (34). For RNAscope ISH (Biotechne), fresh frozen sections were collected and processed according to the manufacturer's instructions.

Study design and statistics

No study size calculations or randomization were used in experimental design. Investigators were not blinded to study groups where PIEZO2 mutants displayed obvious phenotypic traits e.g., Piezo2^{Hoxb8}, Piezo2^{Pvalb}, Piezo2^{eKO} or for human subjects. Investigators were blinded for studies of Piezo2^{Scn10a} mice that do not display a readily observable deficit. When applicable (i.e., for von Frey, pinprick, penile protrusion test, and female intruder assay) scoring was done by two separate investigators and results were pooled. Statistical analysis was performed in Graphpad Prism or Python/Scipy and included two-tailed t-test, parametric one-way ANOVA and Tukey's multiple comparison test for normally distributed data as well as non-parametric Mann-Whitney U test, one-way ANOVA on ranks (Kruskal-Wallis H) followed by Dunn's multiple comparison test for data where normality cannot be assumed. Proportions of binary data were analyzed with a two-tailed Fisher's exact test.

Statistical reporting

Fig. 1A-C. Nonparametric T-tests (Mann-Whitney) were used to compare male and female groups (n=12 in each group); wildtype perineal responses were different $P < 0.0001$ whereas hind-paw responses $p = 0.4600$, and Piezo2^{Hoxb8} perineal touch $p > 0.9999$ were not significantly different. No significant differences between males and females were found for pinprick responses; T-test(parametric); male vs female hind-paws $p = 0.6893$ $t = 0.4052$, $df = 22$; wildtype perineum. $p = 0.4078$ $t = 0.8439$, $df = 22$; Piezo2^{Hoxb8} perineum $p > 0.9999$ $t = 0.000$, $df = 22$ (n=12 in each group).

Male and female data points were pooled to compare von Frey response thresholds and pinprick responses between the 3 groups (Hind-paw, wildtype perineum and Piezo2^{Hoxb8} perineum, n=24 in each group). For von Frey responses statistically significant difference were found between all three groups: one-way ANOVA on ranks (Kruskal-Wallis test) $H(df=2, n=72) = 62.03$ $p < 0.0001$ followed by Dunn's multiple comparison test: hind-paw vs wildtype perineum, $p < 0.0001$; wildtype perineum vs Piezo2^{Hoxb8} perineum $p < 0.0001$; hind-paw vs Piezo2^{Hoxb8} perineum $p = 0.0006$. For pinprick, no statistically significant difference were found between all three groups: parametric one-way ANOVA $F(df=2, 72) = 1.027$ $p = 0.3635$, followed by Tukey's multiple comparison test: hind-paw vs wildtype genitals $p = 0.8010$; wildtype genitals vs Piezo2^{Hoxb8} genitals $p = 0.3311$; hind-paw vs Piezo2^{Hoxb8} genitals $p = 0.7076$.

Fig. 2E. Numbers of graded von Frey responsive neurons in control and Piezo2^{CKO} (control n=8, Piezo2^{CKO} n=6) were analyzed by Mann Whitney U test: 0.008g U=5.5 p=0.0087; 0.02g U=0, p=0.0012; 0.04g U=0, p=0.0012; 0.07g U=0, p=0.0012; 0.16g U=0, p=0.0012; 0.4g U=0, p=0.0012; 0.6g U=0, p=0.0012; 1.0g U=2.0 p=0.0027; 1.4g U=1.0 p<0.0018.

Fig. 3A. Quantification of Penile protrusion test. control vs Piezo2^{Hoxb8} Mann-Whitney U (n=18 control, 10 Piezo2^{Hoxb8}) p<0.0001; Piezo2^{Scn10a} vs Piezo2^{Pvalb} Mann-Whitney U (n=10 Piezo2^{Scn10a}, 10 Piezo2^{Pvalb}) p<0.0001.

Fig. 3E. Proportions of females displaying vaginal plugs were analyzed with a two tailed Fisher's exact test. C57Bl/6 vs Piezo2^{Hoxb8} p=0.0031; Piezo2^{Pvalb} vs Piezo2^{Scn10a} p=0.0325.

fig. S3D. Mean area under the curve (AUC) of fluorescence signals was analyzed by a two tailed t-test. LTMRs (paw n=108, genitals n=307): 0.008g t=2.56 p=0.011; 0.02g t=3.43 p=0.00067; 0.04g t=3.29 p=0.0011; 0.07g t=3.66 p=0.000043; 0.16g t=4.67 p<0.00001; 0.4g t=4.13 p<0.00001; 0.6g t=4.34 p=0.000017; 1.0g t=4.02 p=0.000068; 1.4g t=4.66 p<0.00001. HTMRs (paw n=257, genitals n=233): 0.008g t=1.49 p=0.14 n.s.; 0.02g t=2.36 p=0.018; 0.04g t=2.52 p=0.012; 0.07g t=3.33 p=0.00093; 0.16g t=4.67 p<0.00001; 0.4g t=4.89 p<0.00001; 0.6g t=4.19 p=0.000033; 1.0g t=5.65 p<0.00001; 1.4g t=7.46 p<0.00001.

fig. S4F. Numbers of LTMRs and HTMRs per mouse (control n=8, Piezo2^{CKO} n=6) were analyzed by Mann Whitney U test, LTMRs were different U=0 p=0.0012, HTMRs were not significantly different U=23.5 p=0.5.

fig. S7. Piezo2^{Hoxb8} mice have normal sex hormone levels, genital development and estrus 15 cycling. (A, B) Sex-hormone level was determined for 10 age matched control and Piezo2^{Hoxb8} males; a range of ages were used to mirror the ages of mice used for behavioral and functional imaging experiments. FSH and testosterone fall within the normal range for all animals: FSH levels were not significantly different between Control (n=10) and Piezo2^{Hoxb8} males (n=10); unequal variances T-test (Welches) t(df=16.14) = 0.3472, p = 0.7329 ns; testosterone levels were not significantly different between Control (n=10) and Piezo2^{Hoxb8} males (n=10); unequal variances T-test (Welches) t(df=12.43) = 1.193, p = 0.2552 ns. (C) There was no difference in testis-mass relative to mouse body weight between Control (n=4) and Piezo2^{Hoxb8} (n=4); unequal variances T-test (Welches) t(df=3.752) = 1.304 P value=0.2666 ns. (D) Estrus was monitored for groups of 10 control and Piezo2^{Hoxb8} females over a period of 20 days, demonstrating number of estrus cycles was not significantly different between Control (n=10) and Piezo2^{Hoxb8} females (n=10); unpaired T-test t(df=18) = 1.524 p=0.1449 ns.

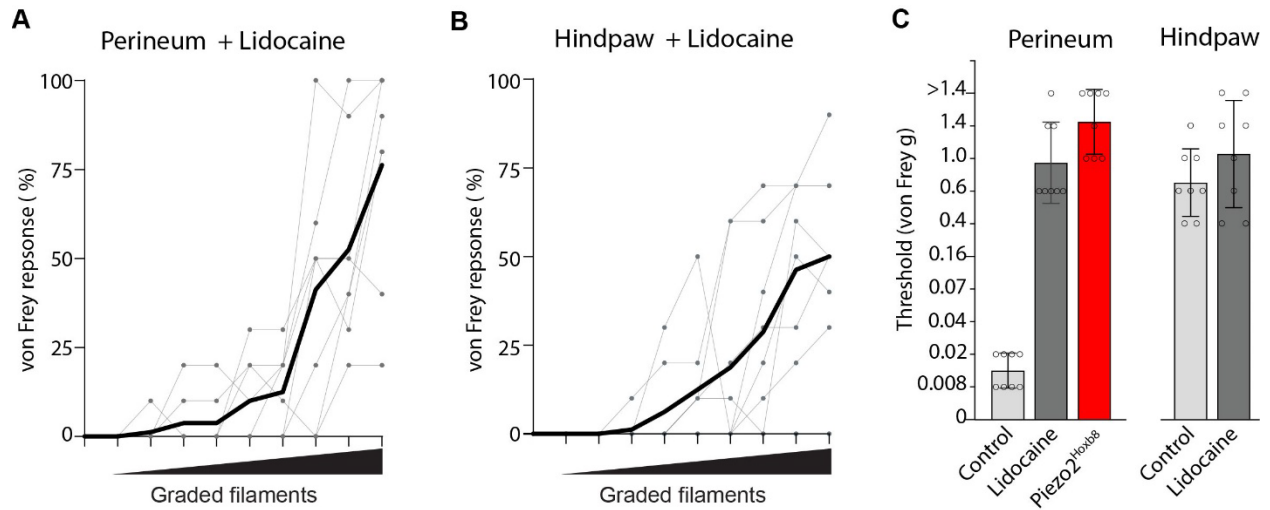


fig. S1. Local anesthetic inhibition of peripheral touch. Reaction of mice to punctate touch of (A) the perineum and (B) the hindpaw after application of the local anesthetic lidocaine to the test region ($n = 8$ animals, 4 male, 4 female). Left panels show the responses for individual mice (points and thin lines) and mean (solid lines) to the standard series (Fig. 1) of graded von Frey filaments (each tested 10 times per mouse). (C) Quantification of von Frey behavior (threshold defined as $\geq 5/10$) and includes data for control and Piezo2^{Hoxb8} mice replotted from Fig. 1 for comparison. Lidocaine treatment increased the threshold for punctate touch detection in the perineum ($p = 0.0145$) making sensitivity indistinguishable from that of Piezo2^{Hoxb8} mice ($p > 0.9999$ n.s.). The hind-paw was less sensitive than the perineum to this type of touch (Fig. 1) and threshold was not significantly changed by lidocaine treatment ($p > 0.9999$ n.s.). Kruskal-Wallis test H ($df=2$, $n=40$) $=24.19$ $p < 0.0001$ followed by Dunn's multiple comparison test. Male and female data points were pooled for statistical analysis.

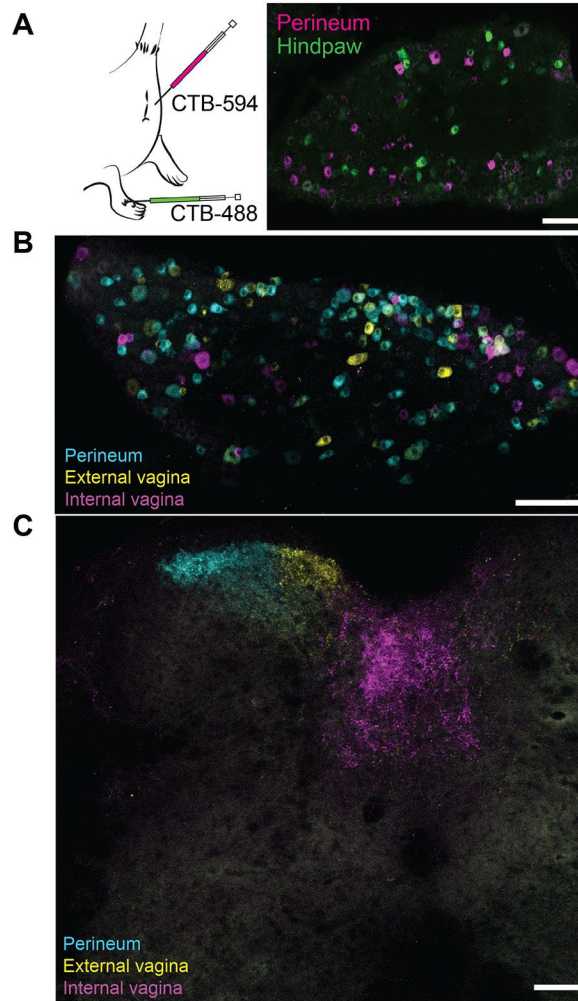


fig. S2. Characterization of sacral DRG neurons innervating the genitals. A) Dual color retrograde CTB labeling from the hind paw (green) and genitals (magenta) of a male mouse illustrating rich innervation of both targets by separate populations of sensory neurons with soma in a sacral ganglion; similar patterns of labeling were observed in both S1 and S2 ganglia (n = 2 male, 2 female). (B, C) Triple color retrograde CTB tracing from the perineum (cyan), external vagina / prepuce (yellow) and internal vagina (magenta) showing (B) cell bodies of lumbar-sacral sensory neurons in the DRG and (C) termini in the dorsal spinal cord (n=2 mice); scale bars = 100 μ m.

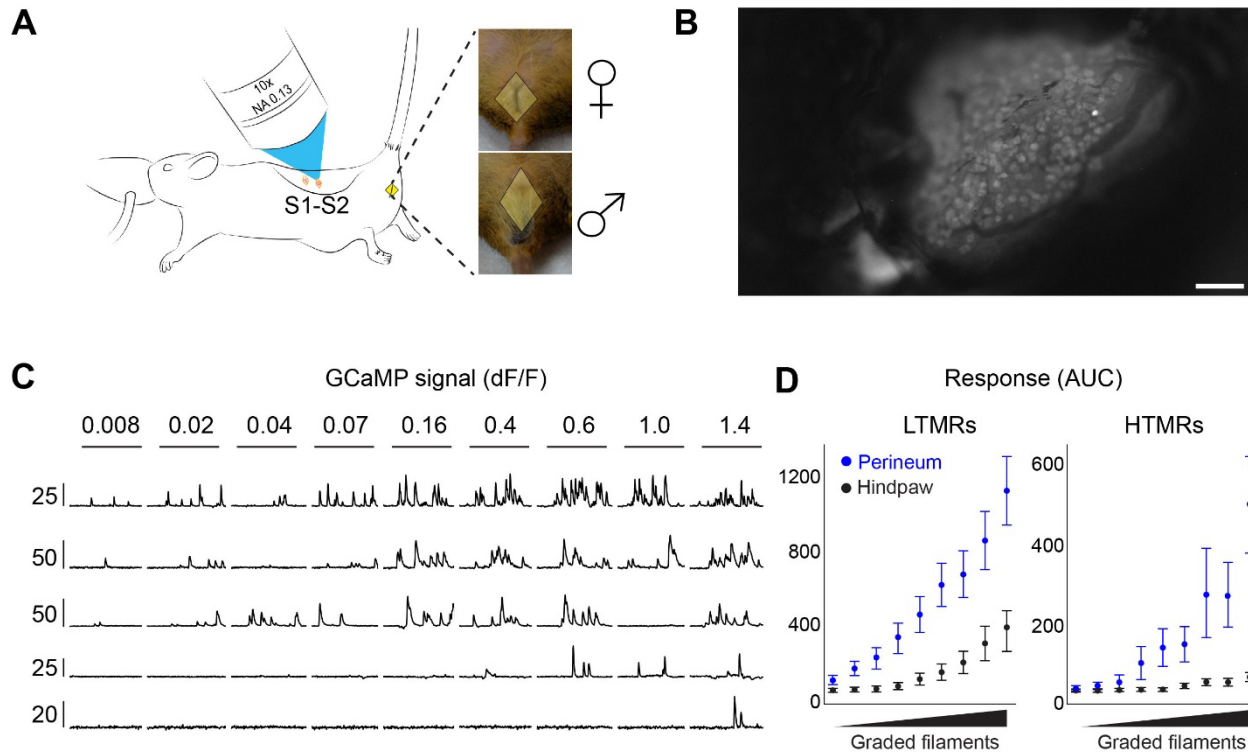


fig. S3. Functional imaging to measure mechanosensory differences between perineal and paw innervating neurons. **(A)** An *in vivo* sacral ganglion Ca-imaging preparation was modified to characterize perineal mechanoreceptors. **(B)** Baseline image of a sacral ganglion prepared for functional imaging; scale bar = 200 μm , see Movie S2 for details of stimulation and response. **(C)** Five representative example GCaMP6f transients from perineal neurons that exhibited differential genital von Frey sensitivity normalized to their maximal response (scale bars, left, $\Delta F/F$, %). **(D)** Quantitation of von Frey stimulation of the perineum and paws for LTMRs (left) and HTMRs (right): the mean area under the curve (AUC) per cell is displayed for each von Frey filament (mean \pm 95% confidence interval). Perineal stimulation resulted in significantly larger cell responses for all filaments in LTMRs (two-tailed t-test, $p < 0.012$) and for filaments $\geq 0.02\text{g}$ in HTMRs ($p < 0.018$).

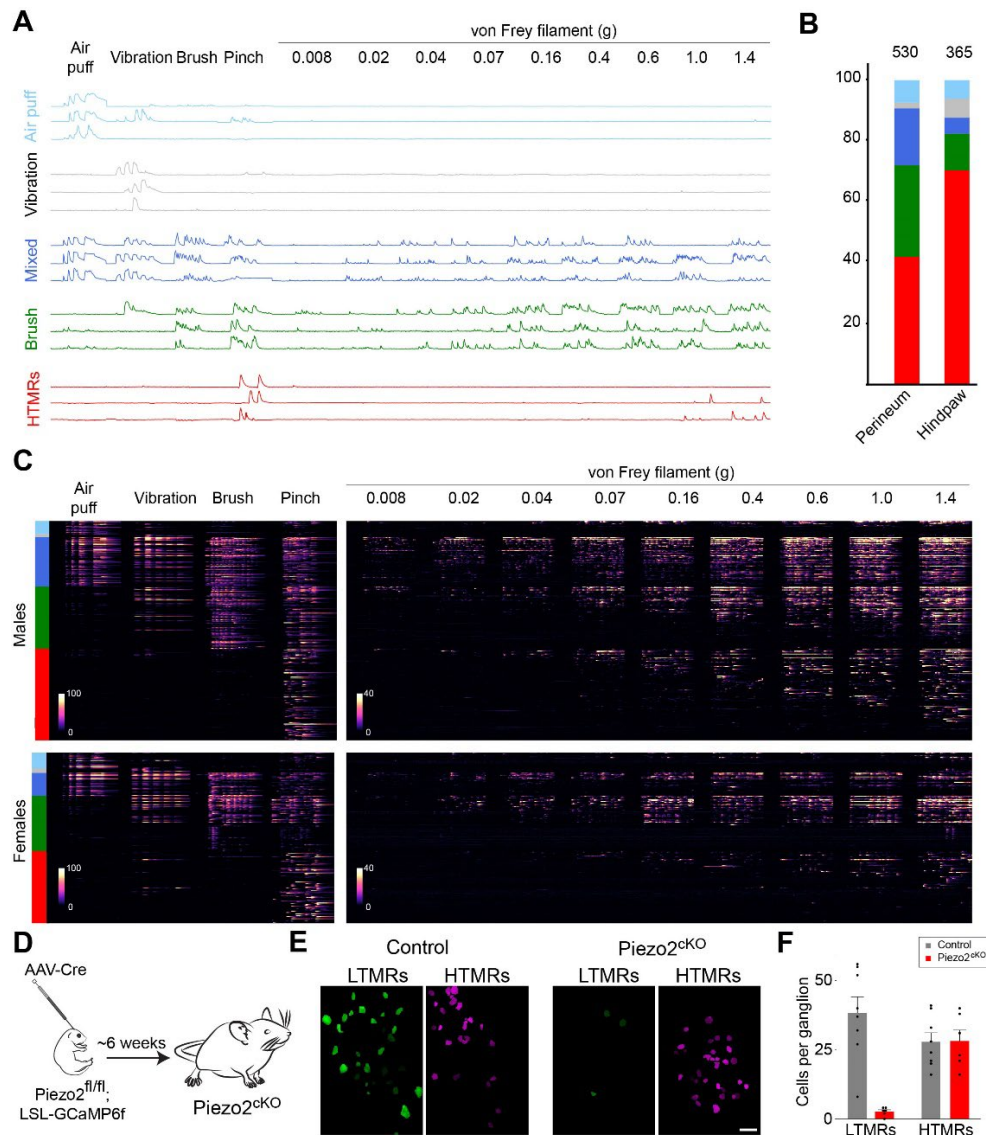


fig. S4. Functional diversity of perineal mechanosensitive neurons and the role of PIEZO2. **A)** Representative GCaMP6f transients from categorized neurons showing 4 classes of LTMRs that respond to one or more types of gentle stimulus and HTMRs that only detect noxious mechanical stimulation (pinch, see Methods). **(B)** Relative abundance of categorized neurons for perineum or hind-paw and total numbers of mechanosensory neurons (perineum, n=8 mice, 4 male, 4 female; hind-paw n=4 mice, 2 male, 2 female). **(C)** Heatmaps representing GCaMP6f responses from perineal mechanosensory neurons to repetitive application of naturalistic stimuli (left panels) and graded von Frey (right panels). Responses from male and female mice (n=4 each) are separated and displayed by functional category (indicated by colored bars); scale: $\Delta F/F$ responses. **(D)** Schematic of strategy for generating and functionally characterizing perineal *Piezo2* knockout neurons (*Piezo2*^{cKO}). **(E-F)** LTMRs and HTMRs were defined by their mechanosensory responses (see Methods). **(E)** Example activity maps showing responding LTMRs and HTMRs for control and *Piezo2*^{cKO}; standard deviation $\Delta F/F$ responses, scale bar = 50 μ m. **(F)** Quantitation of LTMRs and HTMRs per ganglion (control n=8, *Piezo2*^{cKO} n=6, same number of males and females; mean \pm s.e.m.); LTMRs were significantly reduced by *Piezo2*^{cKO} (Mann Whitney U test, p=0.0012), HTMRs: no significant differences (Mann Whitney U test, p=0.5 n.s.).

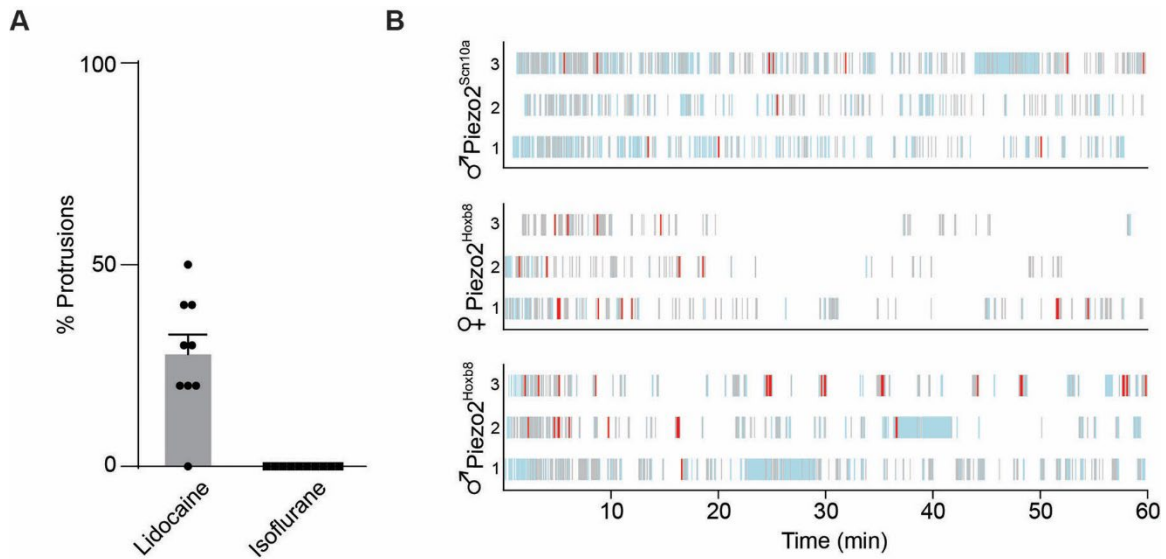


fig. S5. Perineal sensation profoundly affects physiological reflex responses but not sexual motivated behaviors. **A)** Physiological responses of male mice to perineal stimulation with transparent soft tubing. Penile protrusion into the tube was scored for two sets of ten trials (bars are mean \pm s.e.m., individual responses shown as points). Local (lidocaine) and general (2% isoflurane) anesthesia significantly decreased penile protrusion events relative to controls (Mann-Whitney U-test $p < 0.0001$, $n = 18$, Control, see Fig. 4; and $n = 9$, Lidocaine; $n = 10$, Isoflurane). **(B)** Sexual motivation was assessed using a female intruder assay for additional combinations of mice that exhibited deficits in mating success (plug formation); behaviors scored include social interaction (gray), anogenital investigation (pale blue), and mounting attempts; shown are representative ethogram plots for 3 $Piezo2^{Scn10a}$ males x C57Bl/6 females, 3 $Piezo2^{Hoxb8}$ females x C57Bl/6 males and 3 $Piezo2^{Hoxb8}$ males x C57Bl/6 females for the first hour after introduction of the female in estrus.

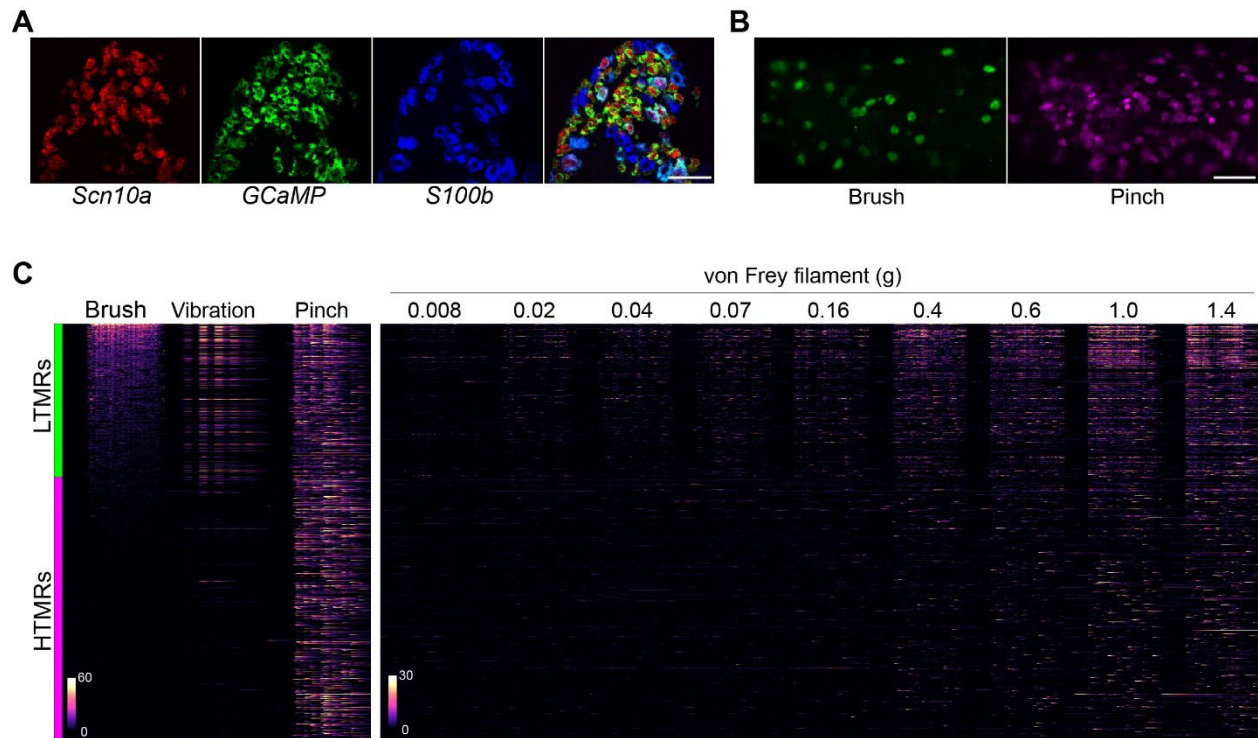


fig. S6. Characterization of genital-innervating neurons in *Scn10a-Cre::Ai95* mice. **(A)** Example ISH image of sacral ganglion section probed for expression of *Scn10a* (red), *GCaMP* (green-GFP probe) and *S100b* (blue) illustrating the fidelity of recombination (*GCaMP*-expression) in *Scn10a*-positive neurons. Note that there are very few *S100b*-positive, *Scn10a*-negative A-LTMRs that express *GCaMP*; similar results were observed in 5 ganglia. **(B)** Example maximum projection Ca-imaging responses of sacral DRG neurons in *Scn10a-Cre::Ai95* mice to perineal brush (green) or pinch (magenta). Note the uniform size of brush responding LTMRs and their correspondence with the size of pinch responsive HTMRs, indicating that the vast majority are cLTMRs; scale bar = 50 μ m, similar results were observed in 5 mice. **(C)** Heatmaps representing *GCaMP6f* responses to repetitive application of naturalistic stimuli (left panels) and graded von Frey stimulation (right panels); $\Delta F/F$ responses are represented by color coding 0-60%, left panels, 0-30%, right panels. The relative abundance of LTMRs (37%) and HTMRs (63%) is indicated to the left of the heatmaps.

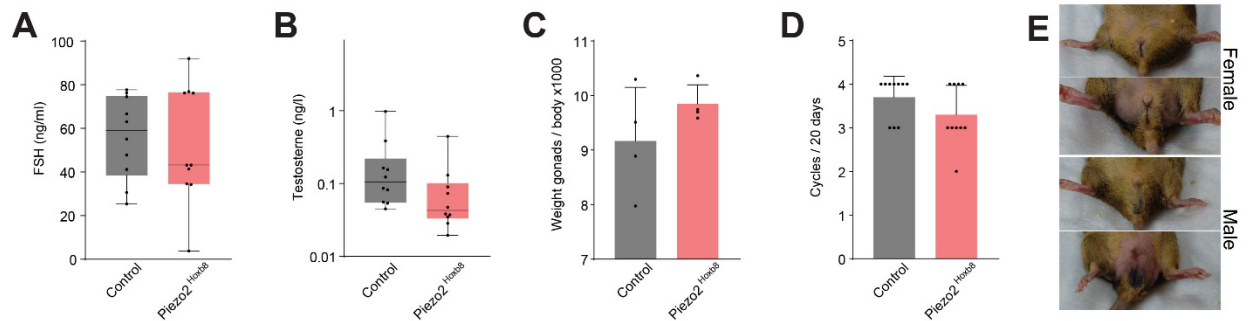


fig. S7. Piezo2^{Hoxb8} mice have normal sex hormone levels, genital development and estrus cycling. **A, B)** Sex-hormone level was determined for 10 age matched control and Piezo2^{Hoxb8} males; a range of ages were used to mirror the ages of mice used for behavioral and functional imaging experiments. Both **(A)** FSH and **(B)** testosterone fall within the normal range for all animals, similarly, **(C)** there was no difference in testis-mass relative to mouse body weight (n=4, per group). **(D)** Estrus was monitored for groups of 10 control and Piezo2^{Hoxb8} females over a period of 20 days, demonstrating similar cycling times for each group. **(E)** Notably, loss of mechanosensation correlated with genital overgrooming observed in Piezo2^{Hoxb8} mice (9/20 females, top panels; 8/20 males, lower panels) but not littermate controls (0/40). Interestingly, an overgrooming phenotype has been observed in male but not female rats with reduced genital sensory input (46).

table S1

A. Relevant genotypic and phenotypic details of human subjects

Subject	Male-1	Male-2	Male-3	Female-1	Female-2
Age	20	47	53	35	40
Allele 1	c.7730 C>A Ser2577 Stop	c.2004delG Gly668 Stop	c.6496G>T Glu2166 Stop	c.3241C>T Arg1051 Stop	c.3241C>T Arg1051 Stop
Allele 2	IVS47+1 G>A (Splice junction)	c.2004delG Gly668 Stop	c.6496G>T Glu2166 Stop	c.3241C>T Arg1051 Stop	c.3241C>T Arg1051 Stop
Major symptoms	Profound absence of proprioception, vibratory sense and discriminatory touch perception specifically on glabrous skin and deficiency of allodynia without loss of deep pressure, temperature or other pain sensation (11, 21).				
Other notes	No reported delayed puberty			No reported delayed puberty or amenorrhea	

B. Responses to genital sensitivity and sexual response related questions

	PIEZO2-LOFs N = 5		Controls N = 10	
	Yes	No	Yes	No
Are you sexually active?	5	0	10	0
Does physical stimulation alone produce arousal?	5	0	9	1
Are erotic thoughts or videos sufficient to produce arousal without touch?	5 ^a	0	10	0
Can you perceive external genital sensation?	3 ^b	2	10	0
Have you experienced an orgasm?	3	2	9	1
Is physical stimulation and/or sex satisfying?	4	1	10	0
Males	N = 3		N = 5	
Can you distinguish between a squeeze of the gland vs. shaft?	3	0	5	0
Females	N = 2		N = 5	
Is lubrication normal?	0	2	5	0

^a One male reported that erotic thoughts/videos are "sufficient to produce erection, but not a full erection".

^b Anecdotes: "If my genitals are being touched by a woman in a subtle way and I can't see it with my eyes, I hardly have any physical of [sic] sexual sensation"; "If the touch is very subtle, I don't feel it."; "Yes, but I need additional stimulation around my genitals, more friction, extra pressure."

Movie S1. Example behavioral responses of wildtype (C57Bl/6, left) and Piezo2^{HoxB8} (right) male mice to 0.04g von Frey filament and pinprick (as indicated) applied to the perineum. Videos were synchronized and slowed down four-times so that application of stimulus and responses of the strains can be compared.

Movie S2. Example of sacral ganglion functional imaging showing application of naturalistic and von Frey stimuli to the perineum and synchronized real time GCaMP6f fluorescence changes in a control male animal.

References and Notes

1. C. Darwin, *The Descent of Man and Selection in Relation to Sex* (Murray, 1871), vols. 1 and 2.
2. J. J. Dinsmore, Courtship Behavior of the greater bird of paradise. *Auk* **87**, 305–321 (1970).
3. S. J. Gould, The origin and function of ‘bizarre’ structures: Antler size and skull size in the ‘Irish elk,’ *Megaloceros giganteus*. *Evolution* **28**, 191–220 (1974).
4. M. A. Changizi, Q. Zhang, S. Shimojo, Bare skin, blood and the evolution of primate colour vision. *Biol. Lett.* **2**, 217–221 (2006).
5. B. D. Charlton, M. S. Martin-Wintle, M. A. Owen, H. Zhang, R. R. Swaisgood, Vocal behaviour predicts mating success in giant pandas. *R. Soc. Open Sci.* **5**, 181323 (2018).
6. V. S. Mandiyan, J. K. Coats, N. M. Shah, Deficits in sexual and aggressive behaviors in *Cnga2* mutant mice. *Nat. Neurosci.* **8**, 1660–1662 (2005).
7. L. Stowers, T. E. Holy, M. Meister, C. Dulac, G. Koentges, Loss of sex discrimination and male-male aggression in mice deficient for TRP2. *Science* **295**, 1493–1500 (2002).
8. C. C. Voigt, O. Behr, B. Caspers, O. von Helversen, M. Knörnschild, F. Mayer, M. Nagy, Songs, scents, and senses: Sexual selection in the greater sac-winged bat, *Saccopteryx bilineata*. *J. Mammal.* **89**, 1401–1410 (2008).
9. C. A. Kell, K. von Kriegstein, A. Rösler, A. Kleinschmidt, H. Laufs, The sensory cortical representation of the human penis: Revisiting somatotopy in the male homunculus. *J. Neurosci.* **25**, 5984–5987 (2005).
10. B. Coste, J. Mathur, M. Schmidt, T. J. Earley, S. Ranade, M. J. Petrus, A. E. Dubin, A. Patapoutian, Piezo1 and Piezo2 are essential components of distinct mechanically activated cation channels. *Science* **330**, 55–60 (2010).
11. A. T. Chesler, M. Szczot, D. Bharucha-Goebel, M. Čeko, S. Donkervoort, C. Laubacher, L. H. Hayes, K. Alter, C. Zampieri, C. Stanley, A. M. Innes, J. K. Mah, C. M. Grosmann, N. Bradley, D. Nguyen, A. R. Foley, C. E. Le Pichon, C. G. Bönnemann, The role of PIEZO2 in human mechanosensation. *N. Engl. J. Med.* **375**, 1355–1364 (2016).
12. S. S. Ranade, S.-H. Woo, A. E. Dubin, R. A. Moshourab, C. Wetzel, M. Petrus, J. Mathur, V. Bégay, B. Coste, J. Mainquist, A. J. Wilson, A. G. Francisco, K. Reddy, Z. Qiu, J. N. Wood, G. R. Lewin, A. Patapoutian, Piezo2 is the major transducer of mechanical forces for touch sensation in mice. *Nature* **516**, 121–125 (2014).
13. Y. García-Mesa, L. Cárcaba, C. Coronado, R. Cobo, J. Martín-Cruces, J. García-Piqueras, J. Feito, O. García-Suárez, J. A. Vega, Glans clitoris innervation: PIEZO2 and sexual mechanosensitivity. *J. Anat.* **238**, 446–454 (2021).
14. Y. García-Mesa, J. García-Piqueras, R. Cobo, J. Martín-Cruces, I. Suazo, O. García-Suárez, J. Feito, J. A. Vega, Sensory innervation of the human male prepuce: Meissner’s corpuscles predominate. *J. Anat.* **239**, 892–902 (2021).
15. I. Abdus-Saboor, N. T. Fried, M. Lay, J. Burdge, K. Swanson, R. Fischer, J. Jones, P. Dong, W. Cai, X. Guo, Y.-X. Tao, J. Bethea, M. Ma, X. Dong, L. Ding, W. Luo, Development

- of a mouse pain scale using sub-second behavioral mapping and statistical modeling. *Cell Rep.* **28**, 1623–1634.e4 (2019).
16. T. Hua, B. Chen, D. Lu, K. Sakurai, S. Zhao, B.-X. Han, J. Kim, L. Yin, Y. Chen, J. Lu, F. Wang, General anesthetics activate a potent central pain-suppression circuit in the amygdala. *Nat. Neurosci.* **23**, 854–868 (2020).
 17. S. E. Murthy, M. C. Loud, I. Daou, K. L. Marshall, F. Schwaller, J. Kühnemund, A. G. Francisco, W. T. Keenan, A. E. Dubin, G. R. Lewin, A. Patapoutian, The mechanosensitive ion channel Piezo2 mediates sensitivity to mechanical pain in mice. *Sci. Transl. Med.* **10**, eaat9897 (2018).
 18. V. E. Abraira, D. D. Ginty, The sensory neurons of touch. *Neuron* **79**, 618–639 (2013).
 19. K. Nonomura, S.-H. Woo, R. B. Chang, A. Gillich, Z. Qiu, A. G. Francisco, S. S. Ranade, S. D. Liberles, A. Patapoutian, Piezo2 senses airway stretch and mediates lung inflation-induced apnoea. *Nature* **541**, 176–181 (2017).
 20. S.-H. Woo, V. Lukacs, J. C. de Nooij, D. Zaytseva, C. R. Criddle, A. Francisco, T. M. Jessell, K. A. Wilkinson, A. Patapoutian, Piezo2 is the principal mechanotransduction channel for proprioception. *Nat. Neurosci.* **18**, 1756–1762 (2015).
 21. M. Szczot, J. Liljencrantz, N. Ghitani, A. Barik, R. Lam, J. H. Thompson, D. Bharucha-Goebel, D. Saade, A. Necaie, S. Donkervoort, A. R. Foley, T. Gordon, L. Case, M. C. Bushnell, C. G. Bönnemann, A. T. Chesler, PIEZO2 mediates injury-induced tactile pain in mice and humans. *Sci. Transl. Med.* **10**, eaat9892 (2018).
 22. M. L. Sorrells, J. L. Snyder, M. D. Reiss, C. Eden, M. F. Milos, N. Wilcox, R. S. Van Howe, Fine-touch pressure thresholds in the adult penis. *BJU Int.* **99**, 864–869 (2007).
 23. C. B. Bleustein, H. Eckholdt, J. C. Arezzo, A. Melman, Quantitative somatosensory testing of the penis: Optimizing the clinical neurological examination. *J. Urol.* **169**, 2266–2269 (2003).
 24. L. Li, M. Rutlin, V. E. Abraira, C. Cassidy, L. Kus, S. Gong, M. P. Jankowski, W. Luo, N. Heintz, H. R. Koerber, C. J. Woodbury, D. D. Ginty, The functional organization of cutaneous low-threshold mechanosensory neurons. *Cell* **147**, 1615–1627 (2011).
 25. V. E. Abraira, E. D. Kuehn, A. M. Chirila, M. W. Springel, A. A. Toliver, A. L. Zimmerman, L. L. Orefice, K. A. Boyle, L. Bai, B. J. Song, K. A. Bashista, T. G. O’Neill, J. Zhuo, C. Tsan, J. Hoynoski, M. Rutlin, L. Kus, V. Niederkofler, M. Watanabe, S. M. Dymecki, S. B. Nelson, N. Heintz, D. I. Hughes, D. D. Ginty, The cellular and synaptic architecture of the mechanosensory dorsal horn. *Cell* **168**, 295–310.e19 (2017).
 26. S. H. Woo, S. Ranade, A. D. Weyer, A. E. Dubin, Y. Baba, Z. Qiu, M. Petrus, T. Miyamoto, K. Reddy, E. A. Lumpkin, C. L. Stucky, A. Patapoutian, Piezo2 is required for Merkel-cell mechanotransduction. *Nature* **509**, 622–626 (2014).
 27. L. Madisen, A. R. Garner, D. Shimaoka, A. S. Chuong, N. C. Klapoetke, L. Li, A. van der Bourg, Y. Niino, L. Egolf, C. Monetti, H. Gu, M. Mills, A. Cheng, B. Tasic, T. N. Nguyen, S. M. Sunkin, A. Benucci, A. Nagy, A. Miyawaki, F. Helmchen, R. M. Empson, T. Knöpfel, E. S. Boyden, R. C. Reid, M. Carandini, H. Zeng, Transgenic mice for

- intersectional targeting of neural sensors and effectors with high specificity and performance. *Neuron* **85**, 942–958 (2015).
28. K. L. Marshall, D. Saade, N. Ghitani, A. M. Coombs, M. Szczot, J. Keller, T. Ogata, I. Daou, L. T. Stowers, C. G. Bönnemann, A. T. Chesler, A. Patapoutian, PIEZO2 in sensory neurons and urothelial cells coordinates urination. *Nature* **588**, 290–295 (2020).
 29. F. A. Beach, Sexual attractivity, proceptivity, and receptivity in female mammals. *Horm. Behav.* **7**, 105–138 (1976).
 30. B. D. Sachs, Sexual reflexes of spinal male house mice. *Physiol. Behav.* **24**, 489–492 (1980).
 31. N. Agarwal, S. Offermanns, R. Kuner, Conditional gene deletion in primary nociceptive neurons of trigeminal ganglia and dorsal root ganglia. *Genesis* **38**, 122–129 (2004).
 32. N. Sharma, K. Flaherty, K. Lezgiyeva, D. E. Wagner, A. M. Klein, D. D. Ginty, The emergence of transcriptional identity in somatosensory neurons. *Nature* **577**, 392–398 (2020).
 33. M. Q. Nguyen, C. E. Le Pichon, N. Ryba, Stereotyped transcriptomic transformation of somatosensory neurons in response to injury. *eLife* **8**, e49679 (2019).
 34. L. J. von Buchholtz, N. Ghitani, R. M. Lam, J. A. Licholai, A. T. Chesler, N. J. P. Ryba, Decoding cellular mechanisms for mechanosensory discrimination. *Neuron* **109**, 285–298.e5 (2021).
 35. C. J. Burnett, S. C. Funderburk, J. Navarrete, A. Sabol, J. Liang-Guallpa, T. M. Desrochers, M. J. Krashes, Need-based prioritization of behavior. *eLife* **8**, e44527 (2019).
 36. S. X. Zhang, A. Lutas, S. Yang, A. Diaz, H. Fluhr, G. Nagel, S. Gao, M. L. Andermann, Hypothalamic dopamine neurons motivate mating through persistent cAMP signalling. *Nature* **597**, 245–249 (2021).
 37. X. Zhou, A. Li, X. Mi, Y. Li, Z. Ding, M. An, Y. Chen, W. Li, X. Tao, X. Chen, Y. Li, Hyperexcited limbic neurons represent sexual satiety and reduce mating motivation. *Science* **379**, 820–825 (2023).
 38. R. D. Johnson, Z. Halata, Topography and ultrastructure of sensory nerve endings in the glans penis of the rat. *J. Comp. Neurol.* **312**, 299–310 (1991).
 39. D. Ohmori, Über die entwicklung der innervation der genitalapparate als peripheren aufnahmeapparat der genitalen reflexe. *Anat. Embryol.* **70**, 347–410 (1924).
 40. D. Huzard, M. Martin, F. Maingret, J. Chemin, F. Jeanneteau, P.-F. Mery, P. Fossat, E. Bourinet, A. François, The impact of C-tactile low-threshold mechanoreceptors on affective touch and social interactions in mice. *Sci. Adv.* **8**, eabo7566 (2022).
 41. H. Olausson, Y. Lamarre, H. Backlund, C. Morin, B. G. Wallin, G. Starck, S. Ekholm, I. Strigo, K. Worsley, Å. B. Vallbo, M. C. Bushnell, Unmyelinated tactile afferents signal touch and project to insular cortex. *Nat. Neurosci.* **5**, 900–904 (2002).
 42. M. Vatsyayana, *The Kama Sutra of Vatsyayana*, R. F. Burton, B. Indrajit, S. P. Bhide, Transl. (1883).
 43. L. Madisen, T. A. Zwingman, S. M. Sunkin, S. W. Oh, H. A. Zariwala, H. Gu, L. L. Ng, R. D. Palmiter, M. J. Hawrylycz, A. R. Jones, E. S. Lein, H. Zeng, A robust and high-

- throughput Cre reporting and characterization system for the whole mouse brain. *Nat. Neurosci.* **13**, 133–140 (2010).
44. N. Ghitani, A. Barik, M. Szczot, J. H. Thompson, C. Li, C. E. Le Pichon, M. J. Krashes, A. T. Chesler, Specialized mechanosensory nociceptors mediating rapid responses to hair pull. *Neuron* **95**, 944–954.e4 (2017).
 45. O. Friard, M. Gamba, BORIS: A free, versatile open-source event-logging software for video/audio coding and live observations. *Methods Ecol. Evol.* **7**, 1325–1330 (2016).
 46. C. L. Moore, Sex differences in self-grooming of rats: Effects of gonadal hormones and context. *Physiol. Behav.* **36**, 451–455 (1986).

Chapter 3

PIEZO2 in somatosensory neurons controls gastrointestinal transit

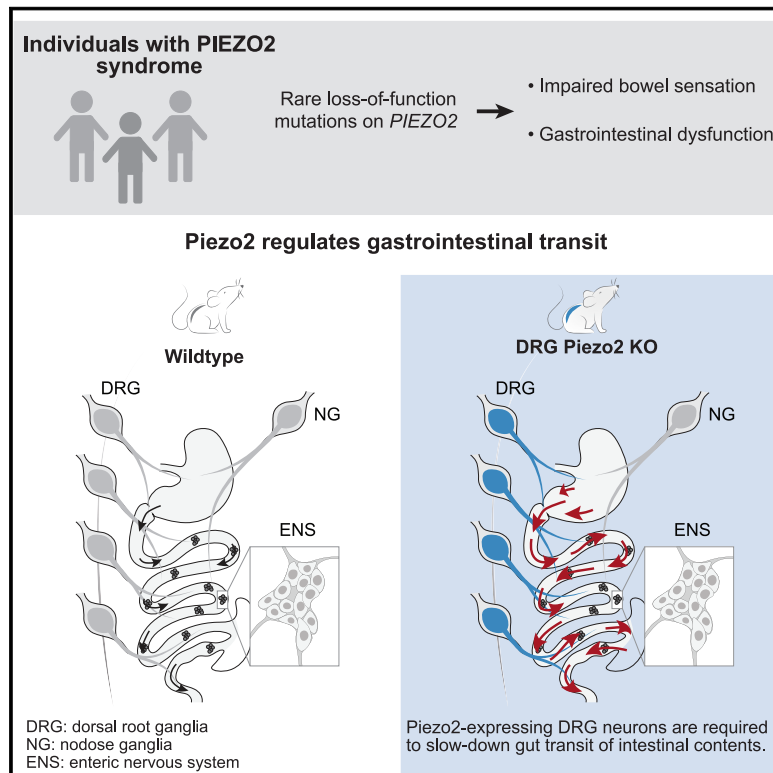
*This chapter is presented in the form it was published in the journal Cell with the following citation

Servin-Vences, M.R., **Lam, R.M.**, ... Chesler, A.T., & Patapoutian, A. (2023) "PIEZO2 in somatosensory neurons controls gastrointestinal transit" Cell. 2023 August 3 186(16)P3386-3399.E15 doi:<https://doi.org/10.1016/j.cell.2023.07.006>

Contributions: R.M.L. Conceptualized, developed methodology, collected data, performed formal analysis and conducted the investigation. Specifically, RML developed and performed all in vivo calcium imaging experiments. The results of RML investigations are reported in Figure1, Figure6, Figure S1, Figure S6. RML analyzed and generated aforementioned figures and wrote methods pertaining to in vivo calcium imaging. RML reviewed and edited all versions of the manuscript

PIEZO2 in somatosensory neurons controls gastrointestinal transit

Graphical abstract



Authors

M. Rocio Servin-Vences, Ruby M. Lam, Alize Koolen, ..., Carsten G. Bönnemann, Alexander T. Chesler, Ardem Patapoutian

Correspondence

alexander.chesler@nih.gov (A.T.C.),
ardem@scripps.edu (A.P.)

In brief

Piezo2 in dorsal root ganglia neurons is required to sense gut content and slow down food transit rates in the stomach, small intestine, and colon.

Highlights

- Individuals with PIEZO2 syndrome present impaired bowel sensation and GI dysfunction
- Piezo2 in DRG neurons plays an important role in regulating gut motility
- Lack of Piezo2 from sensory neurons accelerates gastric emptying and intestinal transit
- DRG neurons detect colon distension via Piezo2



Article

PIEZO2 in somatosensory neurons controls gastrointestinal transit

M. Rocio Servin-Vences,^{1,2} Ruby M. Lam,^{3,4,5} Alize Koolen,^{1,2} Yu Wang,^{1,2} Dimah N. Saade,³ Meaghan Loud,^{1,2} Halil Kacmaz,^{6,7} Suzanne Frausto,^{1,2} Yunxiao Zhang,^{1,2} Arthur Beyder,^{6,7} Kara L. Marshall,⁸ Carsten G. Bönnemann,³ Alexander T. Chesler,^{3,5,*} and Ardem Patapoutian^{1,2,9,*}

¹Department of Neuroscience, Dorris Neuroscience Center, Scripps Research, San Diego, CA, USA

²Howard Hughes Medical Institute, Chevy Chase, MD, USA

³National Institute of Neurological Disorders and Stroke, National Institutes of Health, Bethesda, MD, USA

⁴NIH-Brown University Graduate Program in Neuroscience, Providence, RI, USA

⁵National Center for Complementary and Integrative Health, National Institutes of Health, Bethesda, MD, USA

⁶Division of Gastroenterology and Hepatology, Enteric Neuroscience Program (ENSP), Mayo Clinic, Rochester, MN, USA

⁷Department of Physiology and Biomedical Engineering, Mayo Clinic, Rochester, MN, USA

⁸Department of Neuroscience, Baylor College of Medicine, Jan and Dan Duncan Neurological Research Institute, Houston, TX, USA

⁹Lead contact

*Correspondence: alexander.chesler@nih.gov (A.T.C.), ardem@scripps.edu (A.P.)

<https://doi.org/10.1016/j.cell.2023.07.006>

SUMMARY

The gastrointestinal tract is in a state of constant motion. These movements are tightly regulated by the presence of food and help digestion by mechanically breaking down and propelling gut content. Mechanical sensing in the gut is thought to be essential for regulating motility; however, the identity of the neuronal populations, the molecules involved, and the functional consequences of this sensation are unknown. Here, we show that humans lacking PIEZO2 exhibit impaired bowel sensation and motility. Piezo2 in mouse dorsal root, but not nodose ganglia is required to sense gut content, and this activity slows down food transit rates in the stomach, small intestine, and colon. Indeed, Piezo2 is directly required to detect colon distension *in vivo*. Our study unveils the mechanosensory mechanisms that regulate the transit of luminal contents throughout the gut, which is a critical process to ensure proper digestion, nutrient absorption, and waste removal.

INTRODUCTION

Neural mechanisms regulate key functions of the gastrointestinal (GI) tract, including motility, which is necessary to break down the ingested food, to absorb its components and to eliminate waste.¹ After swallowing, food moves in an orderly way through specialized compartments, each with distinct functions. Thus, the propulsion of gut contents is tightly regulated. Throughout the GI tract, mechanical mixing is a key process which enhances efficiency of chyme breakdown and keeps ingested contents moving.² Well-defined efferent motor programs mediate gut motility through stereotyped movements (e.g., peristalsis, segmentation and “migrating motor complexes”^{1–3}) that are initiated and controlled by complex neural inputs that respond to chemical and mechanical stimuli.^{4–6} However, little is known about the molecular mechanisms that coordinate and initiate motility along the GI tract, including the molecular identity of mechanosensors within the gut, as well as the key sensory neurons that modulate motility along the GI tract.

There are three major afferent neural pathways in the gut. The enteric nervous system (ENS) is intrinsic to the gut and functions to initiate local motility reflexes.^{5,7} Vagal neurons from the

nodose ganglion and somatosensory neurons from dorsal root ganglia (DRGs) are extrinsic to the GI tract, yet both richly innervate the gut.^{8–10} It is generally accepted that nodose neurons play key roles in mediating homeostatic gut-brain signaling,^{11–14} whereas DRG neurons are critically important for sensing gut inflammation and evoking pain.^{15,16} A conserved feature of all three gut afferent systems is that they contain neurons that detect and respond to chemical and mechanical stimuli.^{8,17–20} However, many of these studies are performed *in situ*, at the whole-ganglion level, and do not distinguish the specific role and outcomes of mechanosensation versus chemosensation. Furthermore, far less is known about the molecular mechanisms that control the transit of ingested contents along the GI tract *in vivo*.

PIEZO2 is a mechanically gated ion channel that is the receptor for gentle touch and proprioception in mice and humans.^{21–23} More recently, work by our group and others have shown that PIEZO2 also has critical functions in interoception, including sensing lung inflation²⁴ and bladder filling.²⁵ Notably, this molecule is expressed in all three gut-innervating neural systems—the enteric,^{18,19} vagal,^{8,24,26,27} and somatosensory systems^{23,28,29}—yet, its function in any of these systems is unknown. Here, we



Identifier	2	4*	3*	6*	11 ⁺	12 ⁺	8 ⁺
Age	9	12	14	17	31	36	42
Gender	F	F	M	M	F	F	F
Sensory Deficits							
How often do you feel pain in your rectum or anus while trying to have bowel movements?			Sometimes				
How often after a bowel movement did you feel unfinished? (that you had not passed all your stool?)	Often		Rarely	Sometimes	Sometimes	Rarely	Sometimes
How often did you feel like you need to empty your bowels right away or else you would have an accident?				2-6 times		2-6 times	2-6 times
How much did feeling you need to empty your bowels right-away interfere with your day-to-day activities?				A little bit		Somewhat	
How much did feeling you needed to empty your bowels right away bother you?						Quite a bit	Somewhat
Gastrointestinal-related Symptoms							
How often did you pass very hard or lumpy stools?	2-6 days	One day	2-6 days	One day	2-6 days	One day	
How often did you usually strain while trying to have bowel movements?	Always	Sometimes	Sometimes	Sometimes	Sometimes		
How much did you usually strain while trying to have bowel movements?	Quite a bit	A little bit	Very much	A little bit	A little bit		
How many days did you have loose or watery stools?			2-6 days	One day		2-6 days	One day
How much did having loose or watery stools bother you?			Quite a bit	Somewhat		Quite a bit	Somewhat
How much did having loose or watery stools interfere with your day-to-day activities?			A little bit	A little bit		Somewhat	A little bit

Frequency NA No path High

Figure 1. Gastrointestinal dysfunction in individuals deficient in *PIEZO2*

Summary of responses obtained from *PIEZO2*-deficient individuals to GI-PROMIS questionnaires. Data indicate the subject identifier, age at which the questionnaires were answered and gender. Data are organized by ascending age (top set of rows) and symptoms are categorized in sensory deficits and GI problems, which span constipation and diarrhea. Each question assessed symptoms from the 7 days prior to the survey. Unless otherwise noted, the color code illustrates the following: gray represents the average response from 1,177 healthy control participants, which indicates no pathology and is typically close to never experience or lacking the particular symptom in the past 7 days; blue: rarely; yellow: sometimes; orange: often, red: always. Therefore, every color except for gray indicates a deviation from the average. Blank indicates unanswered questions. Individual identifier corresponds to those published in our previous urinary function study.²⁵ The symbol “*” denotes those subjects who experienced neonatal and childhood constipation, “+” indicates lack of medical history concerning their GI behaviors in childhood. NA, not answered; No path, no pathology.

collected clinical data from a group of *PIEZO2*-deficient individuals and used genetic mouse models to interrogate the role of Piezo2 in gut transit.

RESULTS

Gastrointestinal dysfunction in individuals deficient in *PIEZO2*

To better understand the role of *PIEZO2* in human GI function, we assessed the GI health and medical history of human subjects carrying *PIEZO2* loss-of-function variants (n = 7; ages 9–42). Previous sequencing analysis on these subjects discovered a variety of nonsense mutations (Figure S1),^{22,25,30} the majority of which caused a stop codon before the channel pore, rendering a non-active channel. We additionally used PROMIS (patient-reported outcomes measurement information system) questionnaires, a clinical tool developed by the National Institute of Health to capture and evaluate general GI symptoms.^{31,32} These GI questionnaires are widely used as patient-reported health information and capture answers only from the previous 7 days to the survey. The responses obtained from the *PIEZO2*-deficient in-

dividuals were contrasted with the 1,177 control answers from general-population volunteers^{31,32} (Figure 1). We observed different GI dysfunctions in children, adolescent, and adult subjects, namely: at early age *PIEZO2*-deficient subjects frequently reported lumpy stools, teenagers had lumpy and watery stools, and older adults tended to have watery stools (Figure 1; 7 subjects answered the survey out of 12 individuals that were medically assessed). Additionally, *PIEZO2*-deficient children reported needing constant strain during bowel movements, whereas older individuals had a sudden urgency to evacuate their bowels. Eight individuals (three who completed the surveys and five who just provided medical history) reported childhood constipation that improved or disappeared with age, and the oldest adult (42 years old) reported having recurrent diarrhea that was improved with dietary changes. Remarkably, six *PIEZO2*-deficient subjects reported difficulties in sensing bowel movements, instead, they determined successful stool passage by relying on sound, smell, and/or vision. Three individuals follow a specific daily bowel regimen to cope with their lack of bowel movement sensation, while three other individuals reported soiling accidents. Additionally, five patients reported taking medication to aid with GI

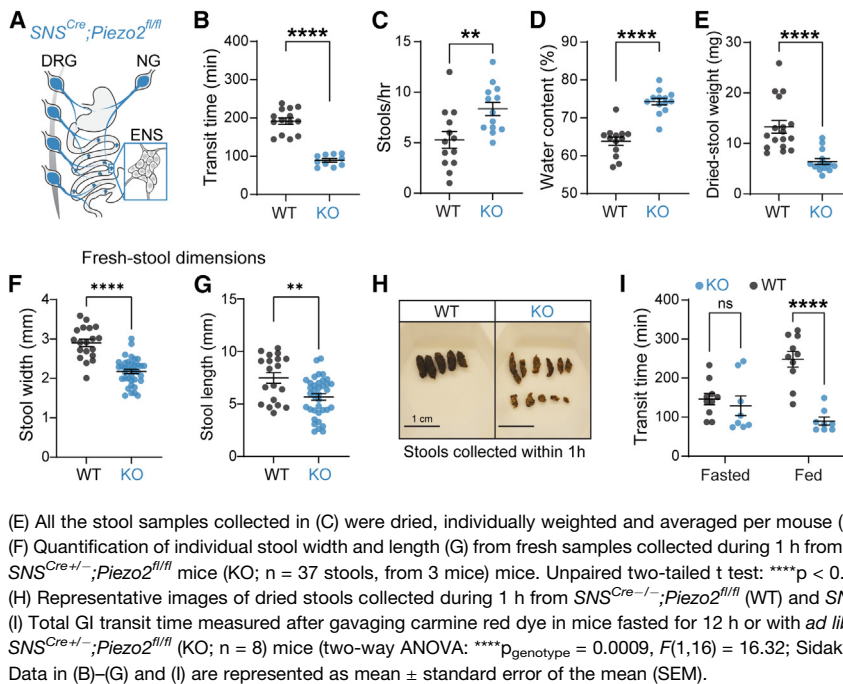


Figure 2. Piezo2 in sensory neurons is required for gastrointestinal function in mice

(A) Illustration of the *SNS^{Cre};Piezo2*-targeting coverage of extrinsic neurons that innervate the GI tract. Blue designates *Piezo2* deletion in nodose ganglia (NG) and DRG neurons, but not ENS.
(B) Total GI transit time measured after gavaging carmine red dye into *SNS^{Cre-/-};Piezo2^{fl/fl}* (wild type [WT]; n = 14) and *SNS^{Cre+/-};Piezo2^{fl/fl}* (KO; n = 10) mice (unpaired two-tailed t test: ****p < 0.0001, t(22) = 9.301).
(C) Number of stools expelled per mouse during 1 h of collection from *SNS^{Cre-/-};Piezo2^{fl/fl}* (WT; n = 13 mice) and *SNS^{Cre+/-};Piezo2^{fl/fl}* (KO; n = 13 mice) (unpaired two-tailed t test: **p = 0.0076, t(24) = 2.916).
(D) Water content present in the stool samples from (C) as a percent of the total composition (unpaired two-tailed t test: ****p < 0.0001, t(24) = 7.418).

distress. Although access to *PIEZO2*-deficient individuals is rare, the captured information allowed us to formulate hypotheses regarding the role of *PIEZO2* in GI function, such as *PIEZO2* is necessary for normal gut function. Thus, these findings suggest that *PIEZO2*-deficient individuals have impaired sensation in bowel function that affects their quality of life and suggest that the mechanosensitive channel *PIEZO2* plays a crucial role in human GI physiology and pathophysiology.

Piezo2 in sensory neurons is required for gastrointestinal function in mice

Intrinsic and extrinsic neuronal innervation of the gut are essential for normal GI motility. Vagotomies commonly result in delayed gastric emptying,^{3,33} lack of ENS results in Hirschsprung's disease that causes the inability to pass stool through the colon,³⁴ and spinal cord injuries often lead to fecal incontinence and constipation.³⁵ In order to establish the role of neuronal *Piezo2* in GI physiology, we used transgenic mouse models to ablate *Piezo2* from peripheral sensory neurons. We used the *Scn10a^{Cre}* driver line (*SNS^{Cre}*), which expresses Cre recombinase under the regulatory elements of the *Scn10a* gene (which encodes the voltage gated sodium channel Na_v1.8) to target peripheral sensory neurons.³⁶ First, we established the extent of recombination in the three sources of gut innervation: enteric, DRG, and vagal. Previous reports have shown that the *SNS^{Cre}* driver recombines in about 80% of neurons from the vagal and DRG,^{36–38} but not in other cell types such as intestinal enterochromaffin cells.³⁸ However, there is little information about its efficiency in enteric neurons along the GI tract. To validate the *SNS^{Cre}* dependent recombination in the ENS, we crossed *SNS^{Cre+/-}* mice to *Ai9^{fl/fl}* mice³⁹ and detected partial signal along the GI tract (Figure S2A). To verify that there is minimal co-expression between *Piezo2* and *Scn10a* transcripts in enteric

neurons, we mined a single-cell transcriptomic dataset⁴⁰ and observed almost no overlap between *Piezo2* and *Scn10a* expression (Figure S2B). Given these observations, *SNS^{Cre}* spares *Piezo2* expression in the ENS; therefore, we do not anticipate that the resulting phenotypes will depend on *Piezo2* expression in the ENS.

Next, we studied the effects of *Piezo2* deletion in GI function, by evaluating the GI transit time, evacuation frequency, and stool water content using the *SNS^{Cre}* driver in a *Piezo2^{fl/fl}* mouse (Figure 2A). To measure whole GI transit, we gavaged mice with carmine red, a non-absorbable red dye with no nutritional value. We then recorded the time for the first appearance of colored feces. We observed a robust transit time acceleration in the conditional knockout (*SNS^{Cre+/-};Piezo2^{fl/fl}*, referred to here as *Piezo2^{SNS}*) mice, compared with the wild-type (WT) (*SNS^{Cre-/-};Piezo2^{fl/fl}*, *Piezo2^{WT}*) littermate controls (Figure 2B). Notably, *Piezo2* deletion did not affect small intestine and colon length (Figure S2C). Moreover, the *Piezo2^{SNS}* mice expelled a greater number of stools during 1 h of sample collection and presented a significant increase in stool water content in comparison with the *Piezo2^{WT}* littermates (Figures 2C and 2D). In agreement with the higher amount of water content, the dried-stool weight from the *Piezo2^{SNS}* mice was significantly smaller in comparison with the *Piezo2^{WT}* controls (Figures 2E and 2H), suggesting that the accelerated transit did not allow time for adequate water absorption. Additionally, we observed smaller dimensions in freshly collected stools from *Piezo2^{SNS}* mice in comparison with the *Piezo2^{WT}* controls (Figures 2F and 2G). We measured food and water consumption using comprehensive lab monitoring system (CLAMS) for 7 days to investigate whether *Piezo2^{SNS}* mice adapted their consumption in response to their faster GI transit; we found no difference in food and water intake (Figure S2D). Altogether, these results indicate that the *Piezo2^{SNS}* mice have

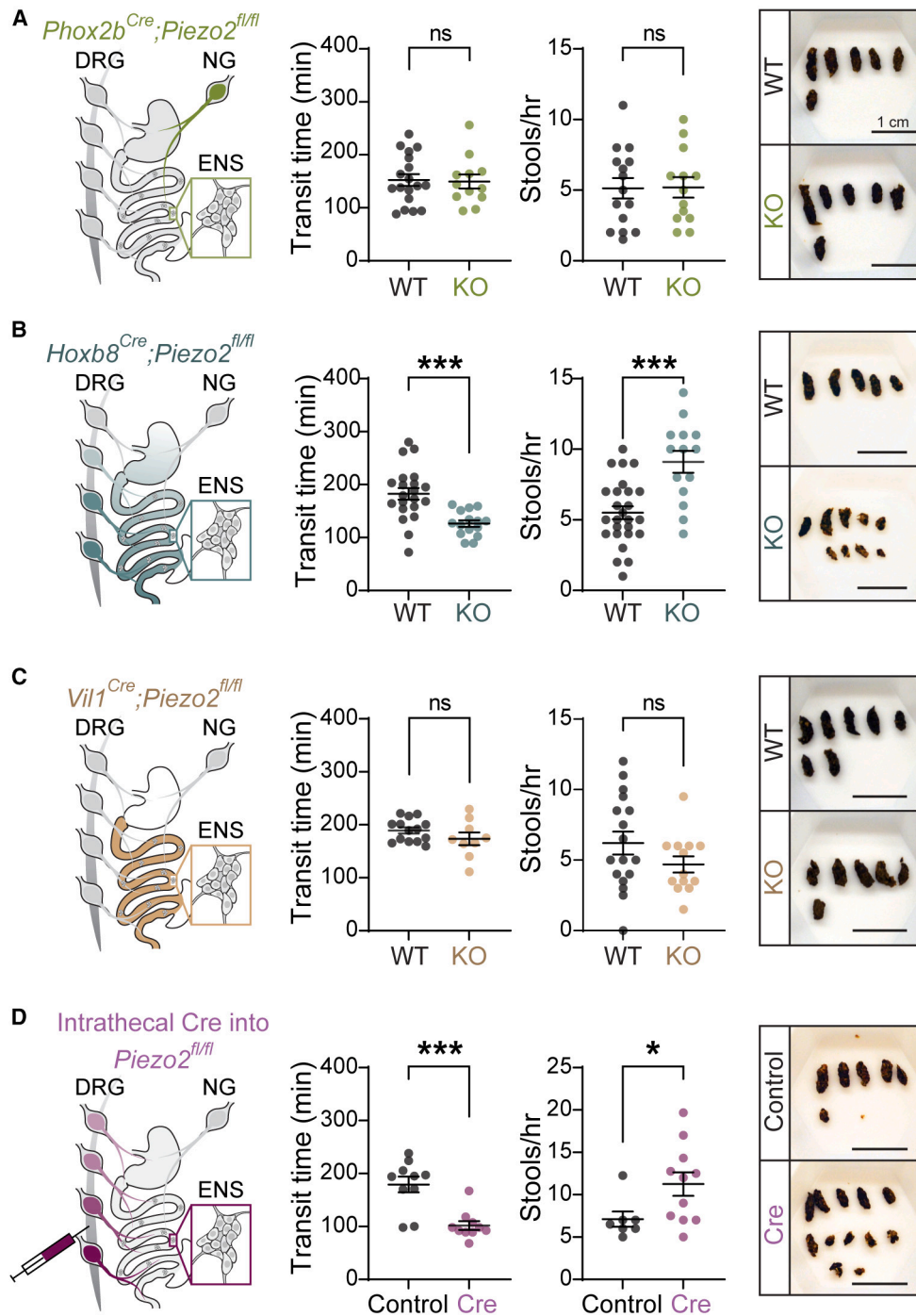


Figure 3. Piezo2 in DRG neurons is required for gastrointestinal transit in mice

(A) Illustration of the *Phox2b^{Cre};Piezo2* targeting coverage in neurons innervating the GI tract, green designates *Piezo2* deletion in nodose, but not in DRG and enteric neurons (left). Total GI transit time after gavaging carmine red into *Phox2b^{Cre-/-};Piezo2^{fl/fl}* (WT; n = 18) and *Phox2b^{Cre+/+};Piezo2^{fl/fl}* (KO; n = 12) mice (unpaired two-tailed t test: p = 0.8735, t(28) = 0.1607; ns, not statistically significant) (middle left). Number of stools expelled during 1 h of collection from *Phox2b^{Cre-/-};Piezo2^{fl/fl}* (WT; n = 15) and *Phox2b^{Cre+/+};Piezo2^{fl/fl}* (KO; n = 13) mice (unpaired two-tailed t test: p = 0.9548, t(26) = 0.05727; ns, not statistically significant) (middle right). Representative images of dried stools collected during 1 h from *Phox2b^{Cre-/-};Piezo2^{fl/fl}* (WT) and *Phox2b^{Cre+/+};Piezo2^{fl/fl}* (KO) mice (right). Scale bar represents 1 cm.

(B) Illustration of the *Hoxb8^{Cre};Piezo2* targeting coverage in the GI epithelium and neurons innervating the GI tract, teal color designates *Piezo2* deletion in DRG neurons and enterochromaffin cells of intestinal epithelia, but not in enteric and nodose neurons (left). Total GI transit time after gavaging carmine red into *Hoxb8^{Cre-/-};Piezo2^{fl/fl}* (WT; n = 21) and *Hoxb8^{Cre+/+};Piezo2^{fl/fl}* (KO; n = 15) mice (unpaired two-tailed t test: ***p = 0.0003, t(34) = 4.004) (middle left). Number of

(legend continued on next page)

accelerated GI transit resulting in shorter transit time and a diarrhea-like phenotype (Table S1).

To investigate whether the presence of intestinal contents is important to modulate the quickening of the GI transit, we compared gut transit between mice fasted for 12 h and mice fed *ad libitum*, which already had food contents along the GI tract. Interestingly, we did not observe any transit difference in fasted *Piezo2^{SNS}* and *Piezo2^{WT}* mice (Figure 2I). Importantly, these results suggest that the mechanical signals exerted by the intestinal contents are directly or indirectly sensed by Piezo2 to modulate GI transit *in vivo*. Moreover, these results suggest that Piezo2-dependent slowdown in gut transit occurs only in filled GI tracts, presumably assisting food digestion and absorption. Thus, subsequent experiments were performed under *ad libitum* conditions.

Piezo2 in somatosensory neurons is required for gastrointestinal transit in mice

Piezo2 is expressed in cells that influence GI motility, including extrinsic neurons of spinal and vagal origin that innervate the gut,^{8,28} and in enterochromaffin cells of the small intestine and colon.^{41,42} We undertook a targeted approach utilizing genetic and viral methods to identify the specific contributions of Piezo2-dependent mechanotransduction in gut transit. We used *Phox2b^{Cre}* and *Vil1^{Cre}* drivers to target nodose neurons and gut epithelial cells respectively, as well as the *Hoxb8^{Cre}* line to target both caudal DRGs and gut epithelial cells, and finally we intrathecally injected an AAV-PHP.s virus to drive Cre recombinase expression in DRGs neurons.

Previous studies have demonstrated the importance of nodose innervation in GI function.^{9,10,14,43} To investigate if vagal sensory neurons could be controlling the faster GI transit seen in the *Piezo2^{SNS}* mice, we employed a *Phox2b^{Cre}* driver line.⁴⁴ As *Phox2b* transcript is widely detected in enteric neurons,^{18,19} we crossed the *Ai9^{fl/fl}* reporter mice to the *Phox2b^{Cre}* driver to validate the recombination in the ENS. We observed sparse labeling through the gut (Figure S3A), suggesting that in our hands and for our purpose, this *Phox2b^{Cre}* driver mainly targets the nodose ganglia. To evaluate the mechanosensory role of vagal innervation in GI transit time, evacuation frequency, and stool water content, we deleted Piezo2 from nodose neurons by crossing a *Phox2b^{Cre}* driver to *Piezo2^{fl/fl}* mice. Surprisingly,

we found that *Phox2b^{Cre+/-};Piezo2^{fl/fl}* (*Piezo2^{Phox2b}*) mice did not show any difference in transit time and defecation frequency in comparison with their WT littermate controls (*Phox2b^{Cre-/-};Piezo2^{fl/fl}*, *Piezo2^{WT}*) (Figure 3A; Table S1). Consistent with this finding, the water content, dried-stool weight, and fresh-fecal dimensions from *Piezo2^{Phox2b}* mice were similar to the *Piezo2^{WT}* littermates (Figures S3C and S3D). This indicates that loss of Piezo2 in vagal sensory neurons is insufficient to cause the accelerated GI transit observed in the *Piezo2^{SNS}* model.

Next, to investigate the concurrent contribution of DRG neurons and gut epithelial cells in GI transit, we used the *Hoxb8^{Cre}* driver, which spares nodose ganglia and expresses the Cre recombinase in a gradient pattern targeting cells below the mid-thoracic region.⁴⁵ We validated this driver by crossing it with an *H2b-mCherry* reporter line, which drives nuclear-localized mCherry in Cre-expressing cells,⁴⁶ to evaluate the recombination efficiency within the ENS, we used whole-mount preparations of mucosal-free intestinal tissues. We confirmed the gradient expression pattern in gut muscle, however nuclei from enteric neurons lacked mCherry expression along the GI tract (Figure S3A), thus *Hoxb8^{Cre}* is unable to target enteric neurons. When we assessed the GI function in *Hoxb8^{Cre+/-};Piezo2^{fl/fl}* (*Piezo2^{Hoxb8}*) mice, we observed accelerated GI transit, increased defecation frequency, increased water content, and decreased stool size (dried and fresh) in comparison with the WT (*Hoxb8^{Cre-/-};Piezo2^{fl/fl}*, *Piezo2^{WT}*) littermates (Figures 3B, S3E, and S3F; Table S1), phenocopying the *Piezo2^{SNS}* model. Moreover, by using a videorecorder⁴⁷ to identify the colored fecal pellets, an accelerated transit was again observed in *Piezo2^{Hoxb8}* mice (Figure S3G), further confirming the consistency of the phenotype. This approach was utilized to minimize any potential stress on the mice during the experiments.⁴⁷ Overall, these results suggest that Piezo2-expressing intestinal epithelial cells or spinal afferents, rather than enteric or nodose neurons, are responsible for the accelerated GI transit phenotype.

Enterochromaffin cells are a subtype of enteroendocrine cells that have been associated with gut motility.^{48,49} Additionally, Piezo2 is expressed in enterochromaffin cells from the small intestine^{41,50} and colon,^{42,48,51} and its deletion was shown to prolong GI transit time in fasted mice.^{48,49} To test whether

stools expelled during 1 h of collection from *Hoxb8^{Cre-/-};Piezo2^{fl/fl}* (WT; n = 26) and *Hoxb8^{Cre+/-};Piezo2^{fl/fl}* (KO; n = 14) mice (unpaired two-tailed t test: ***p = 0.0001, t(38) = 4.316) (middle right). Representative images of dried stools collected during 1 h from *Hoxb8^{Cre-/-};Piezo2^{fl/fl}* (WT) and *Hoxb8^{Cre+/-};Piezo2^{fl/fl}* (KO) mice (right). Scale bar represents 1 cm.

(C) Illustration of the *Vil1^{Cre};Piezo2* targeting coverage in the GI epithelium, tan color designates *Piezo2* deletion in enterochromaffin cells of intestinal epithelia, but not in nodose, DRG and enteric neurons (left). Total GI transit time after carmine red gavage into *Vil1^{Cre-/-};Piezo2^{fl/fl}* (WT; n = 14) and *Vil1^{Cre+/-};Piezo2^{fl/fl}* (KO; n = 9) mice (unpaired two-tailed t test: p = 0.1980, t(21) = 1.329; ns, not statistically significant) (middle left). Number of stools expelled during 1 h of collection from *Vil1^{Cre-/-};Piezo2^{fl/fl}* (WT; n = 17) and *Vil1^{Cre+/-};Piezo2^{fl/fl}* (KO; n = 13) mice (unpaired two-tailed t test: p = 0.1622, t(28) = 1.436; ns, not statistically significant) (middle right). Representative images of dried stools collected during 1 h from *Vil1^{Cre-/-};Piezo2^{fl/fl}* (WT) and *Vil1^{Cre+/-};Piezo2^{fl/fl}* (KO) mice (right). Scale bar represents 1 cm.

(D) Illustration of the experimental model to target *Piezo2*-expressing DRG neurons, plum color designates *Piezo2* deletion in DRG neurons, but not in enterochromaffin cells, nodose and enteric neurons (left). Total GI transit time after gavaging carmine red into *Piezo2^{fl/fl}::PHP.s-tdTomato* (Control; n = 10) and *Piezo2^{fl/fl}::PHP.s-iCre* (Cre; n = 10) mice (Mann-Whitney test: ***p = 0.0005 two-tailed, U = 7) (middle left). Number of stools expelled during 1 h of collection from *Piezo2^{fl/fl}::PHP.s-tdTomato* (Control; n = 7) and *Piezo2^{fl/fl}::PHP.s-iCre* (Cre; n = 11) mice (Mann-Whitney test: *p = 0.0208 two-tailed, U = 13.5) (middle right). Representative images of dried stools collected during 1 h from *Piezo2^{fl/fl}::PHP.s-tdTomato* (Control) and *Piezo2^{fl/fl}::PHP.s-iCre* (Cre) mice (right). Scale bar represents 1 cm.

Data in (A)–(D) are represented as mean ± SEM.

enterochromaffin cell mechanosensitivity contributes to gut transit in presence of luminal contents, we used an intestinal epithelial *Villin^{Cre}* (*Vil1^{Cre}*⁵²) driver to remove Piezo2 from enterochromaffin cells. We observed a similar GI transit time in *Vil1^{Cre+/-};Piezo2^{fl/fl}* (*Piezo2^{Vil1}*) compared with the WT littermate controls (*Vil1^{Cre-/-};Piezo2^{fl/fl}*, *Piezo2^{WT}*) (Figure 3C). Consistently, defecation frequency, water content, stool size, and weight from *Piezo2^{Vil1}* mice were all similar to the *Piezo2^{WT}* controls (Figures 3C, S3H, and S3I; Table S1). Interestingly, these findings suggest that Piezo2 deficiency in enterochromaffin cells is not by itself required for regulating luminal-content transit *in vivo*. Previous studies suggested that Piezo2 deficiency in enterochromaffin cells causes a slight GI transit delay.^{48,49} The difference between these studies might be due to variations in nutrients and microbiota across laboratories. Importantly, as shown above, the accelerated gut transit when Piezo2 is ablated from DRGs and enterochromaffin cells via the *Hoxb8^{Cre}* driver and is robust between institutions (Scripps and Mayo Clinic), suggesting a dominant role of DRGs in gut motility.

To determine whether Piezo2-expressing DRG neurons are responsible for the accelerated transit phenotype, we intrathecally injected peripheral neuron-selective PHP.s viral particles⁵³ carrying a Cre recombinase construct or a fluorescent protein as a control into adult *Piezo2^{fl/fl};Ai9^{fl/+}* mice in between lumbar levels 5 and 6 (Figures 3D and S3B). This viral strategy was necessary because no existing driver lines targeted just DRG neurons while sparing nodose and enteric ganglia. Mice with ablated Piezo2 from DRG neurons (*Piezo2^{DRG}*) presented a profound decrease in the GI transit time in comparison with the WT littermate controls (*Piezo2^{control}*) (Figure 3D; Table S1). Consistently, the defecation frequency was increased (Figure 3D, right-most panels). Remarkably, loss of Piezo2 in DRG neurons is sufficient to drive accelerated GI transit. Notably, as this viral strategy allowed us to induce the phenotype in adult mice (Figures 3D, S3J, and S3K), we can exclude the possibility that the accelerated GI transit is consequence of a developmental deficit. These findings indicate that Piezo2 in DRGs is crucial for the maintenance of gut transit homeostasis.

Neuronal Piezo2 mediates gastric emptying, intestinal transit, and colonic transit in mice

Our GI transit experiments and previous studies provide information on the time required for intestinal contents to travel from the stomach to the evacuation point,^{47,54–56} but they lacked details about the transit throughout the intermediate regions of the gut. To investigate whether Piezo2-expressing somatosensory neurons modulate motility along the entire GI tract or in discrete regions, we functionally evaluated gastric emptying, intestinal transit, and colonic transit. We returned to the *SNS^{Cre};Piezo2* mouse for these experiments to consistently and uniformly access the majority of the Piezo2-expressing DRG neurons. To probe the function of Piezo2 in gastric emptying, we gavaged *Piezo2^{SNS}* and WT littermates with a non-absorbable, near-infrared fluorescent dye (GastroSense-750) (Figure 4A). Mice were euthanized at different time points after gavage and the GI tract was harvested and imaged using the IVIS-Lumina S5 system to determine where dye had accumulated. To measure gastric emptying, the fluorescence inten-

sity from the stomach was compared with the rest of the small and large intestines and expressed as percentage of the total signal. We consistently observed faster gastric emptying in *Piezo2^{SNS}* mice at 30 and 45 min after the gavage in comparison with the *Piezo2^{WT}* controls (Figure 4B). This indicates that Piezo2 in sensory neurons regulates the rate of stomach emptying.

We previously found that Piezo2 deletion from nodose neurons had no effect on overall GI transit (Figure 3A). Nonetheless, given the importance of vagal innervation in stomach function, we tested the contribution of Piezo2-expressing nodose neurons in gastric emptying. We gavaged *Piezo2^{Pbox2b}* and WT littermates with GastroSense-750 and imaged gut tissues 45 min after gavage (Figure S4A). Consistent with our previous results, we observed no difference in gastric emptying between *Piezo2^{Pbox2b}* and *Piezo2^{WT}* controls (Figures S4B and S4C). Consistently, these results revealed that removing Piezo2 from nodose neurons is insufficient to accelerate stomach emptying.

Next, we tested whether the small intestine contributes to the accelerated transit observed in *Piezo2^{SNS}* mice. We implanted catheters into the duodenum to directly infuse dyes and to quantify the intestinal transit when the stomach is bypassed (Figure 4C). We first infused carmine red through the intestinal catheter and recorded the time until the first colored fecal pellet appeared. We observed a significant decrease in intestinal transit time in *Piezo2^{SNS}* compared with WT littermate mice (Figure 4D). These findings reveal that removing Piezo2 from sensory neurons accelerates small intestine transit, suggesting that Piezo2 neurons may be able to modulate small intestine transit independently of stomach emptying activity.

Finally, we directly examined colonic transit by implanting catheters into the cecum to infuse dyes into the proximal colon and circumvent the influence of stomach and small intestine (Figure 4E). When we infused carmine red through the cecal catheter and quantified the time until the first colored fecal pellet appeared, we observed a significant decrease in colonic transit time in *Piezo2^{SNS}* mice compared with WT littermates (Figure 4F). These data show that Piezo2 deficiency in sensory neurons affects the transit of gastric and intestinal contents, indicating that Piezo2-sensory neurons modulate propulsive motility in the stomach, small intestine, and colon in the presence of luminal contents.

The sympathetic innervation exerts a predominantly inhibitory effect on GI muscle.^{57–59} Thus, to obtain further mechanistic insight into how Piezo2 acts on GI transit, we performed a celiac ganglionectomy (CGX) (Figure 4G) to partially denervate the upper GI tract and release the sympathetic inhibition on muscle contraction. We hypothesized that by partially removing sympathetic input, the GI transit in WT mice would speed up. When we performed GI transit experiments before and after CGX, we observed a significant reduction on the WT gut transit time after CGX and no change in *Piezo2^{SNS}* (Figure 4H). The CGX procedure was not sufficient to mimic the *Piezo2^{SNS}* acceleration, possibly due to an incomplete denervation. These findings suggest that the sensory effects on gut transit are going through sympathetic motor action and that removal of Piezo2-extrinsic sensory innervation produce a ceiling effect in GI transit acceleration.

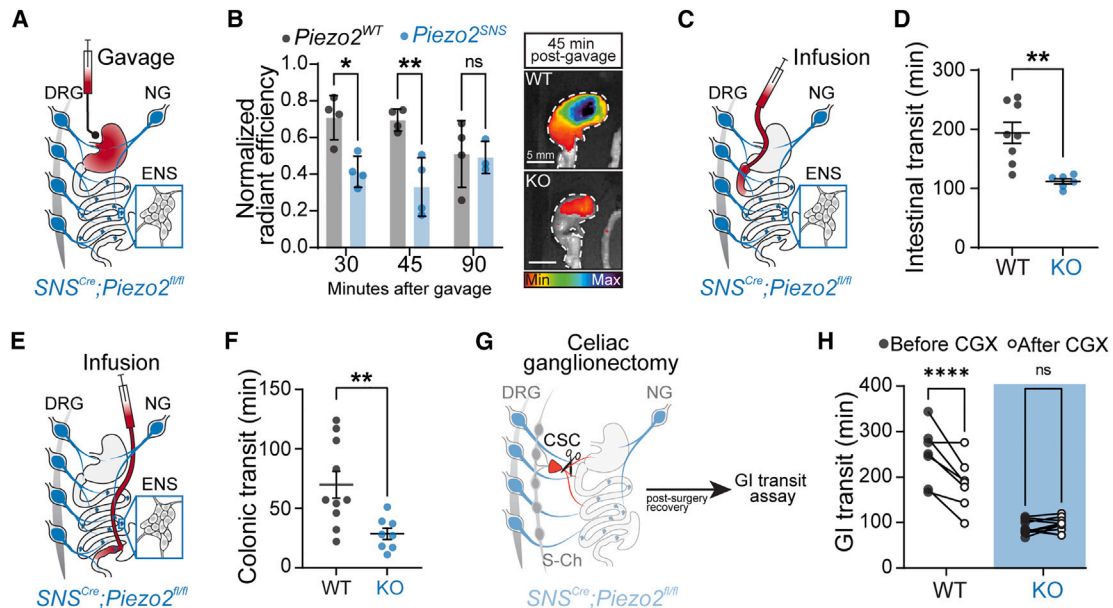


Figure 4. Neuronal Piezo2 mediates gastric emptying, intestinal and colonic transit in mice

(A) Illustration of the strategy to test gastric emptying in *Piezo2^{SNS}* mice.

(B) Quantification of the percentage of gastric emptying observed after gavaging the far-red dye GastroSense-750 at different time points in *SNS^{Cre-/-};Piezo2^{fl/fl}* (*Piezo2^{WT}*; n = 3–4 mice per time point) and *SNS^{Cre+/-};Piezo2^{fl/fl}* (*Piezo2^{SNS}*; n = 4 per time point) mice (two-way ANOVA: *** $p_{\text{genotype}} = 0.0005$, $F(1,17) = 18.40$; Sidak's p_{adjusted} : $p_{30 \text{ min}} = 0.0122$; ** $p_{45 \text{ min}} = 0.0022$; $p_{90 \text{ min}} = 0.9970$) (left). Representative images of dye release from stomachs 45 min after gavaging *SNS^{Cre-/-};Piezo2^{fl/fl}* (WT) and *SNS^{Cre+/-};Piezo2^{fl/fl}* (KO) mice (right). The stomach is outlined by a white dashed line, scale bar represents 5 mm and pseudocolor scale indicates the dye intensity. Data represented as mean \pm standard deviation (SD).

(C) Schematic of the duodenal infusion in *Piezo2^{SNS}* mice through an implanted catheter.

(D) Quantification of intestinal transit time measured after infusing carmine red into the duodenum of *SNS^{Cre-/-};Piezo2^{fl/fl}* (WT; n = 8) and *SNS^{Cre+/-};Piezo2^{fl/fl}* (KO; n = 6) (Mann-Whitney test: ** $p = 0.0013$ two-tailed, U = 1). Data represented as mean \pm SEM.

(E) Schematic of the colonic infusion in *Piezo2^{SNS}* mice through an implanted catheter.

(F) Quantification of colonic transit time measured after infusing carmine red into the cecum of *SNS^{Cre-/-};Piezo2^{fl/fl}* (WT; n = 10) and *SNS^{Cre+/-};Piezo2^{fl/fl}* (KO; n = 8) (unpaired two-tailed t test: ** $p = 0.0071$, $t(16) = 3.083$). Data represented as mean \pm SEM.

(G) Schematic of the celiac ganglia denervation (CGX) in *Piezo2^{SNS}* mice. S-Ch, sympathetic chain; CSC, celiac superior complex.

(H) Quantification of GI transit time measured before and after CGX in *SNS^{Cre-/-};Piezo2^{fl/fl}* (WT; n = 7) and *SNS^{Cre+/-};Piezo2^{fl/fl}* (KO; n = 10) (two-way ANOVA: **** $p_{\text{genotype}} < 0.0001$, $F(1,15) = 46.80$; Sidak's p_{adjusted} : **** $p_{\text{WT}} < 0.0001$; $p_{\text{KO}} = 0.8409$; ns, not statistically significant).

Piezo2-expressing somatosensory neurons innervate the GI tract

Next, we examined whether Piezo2-expressing DRG neurons directly project into the GI tract, their morphological endings, and the innervated layer (namely, muscle or mucosa). For this, AAV9 particles encoding a Cre-dependent GFP reporter (AAV9-*flex-GFP*⁶⁰) were injected intrathecally into *Piezo2^{Cre}* mice⁶¹ (*Piezo2-ires-Cre::AAV9-flex-GFP*, *Piezo2^{GFP}*) (Figure 5A). This approach enabled us to specifically visualize Piezo2-DRG endings within the GI tract while sparing vagal and enteric innervation. We mapped and quantified the nerve terminals through image analysis of whole-mount preparations (Figures 5B and 5C). Interestingly, whole-mount visualization of *Piezo2^{GFP}* stomach primarily revealed intraganglionic varicose endings (IGVEs) (Figure 5D). We found no intramuscular arrays or mucosal endings along the GI tract from *Piezo2^{GFP}* mice. Although no function has yet been assigned, the IGVE innervation pattern matched previous descriptions of spinal afferents detected in stomach and colon.^{62,63} We observed Piezo2 terminals innervating the small intestine and detected IGVEs and single axons traversing large distances. Further down the GI tract, the colon presented

the highest innervation density and the most abundant IGVE network (Figures 5B and 5C). These findings are consistent with previous studies indicating that spinal innervation is denser toward the large intestine^{28,37}; however, it is important to note that we intrathecally injected between lumbar levels 5 and 6, resulting in a gradient pattern of infection with the highest efficiency close to the injection area⁶⁴ (Figure S5A). Therefore, the observed innervation pattern could be additionally explained by our technical approach. Our data revealed that Piezo2 sensory endings from DRG origin innervate the stomach, small intestine, and colon with a predominant morphology of IGVEs.

Piezo2-expressing DRG neurons detect colon distention

In humans, stool expulsion has been associated with high amplitude propagating contractions that span the entire colon,^{65–67} yet stool evacuation can similarly occur in the absence of this activity by voluntary contracting the abdominal wall and recruiting pelvic floor muscles.⁶⁵ Furthermore, due to the arrival of fecal content, the rectum expands prior to defecation. Nonetheless, *PIEZO2*-deficient individuals perceive the act of evacuation differently because they lack bowel sensation. However, it is

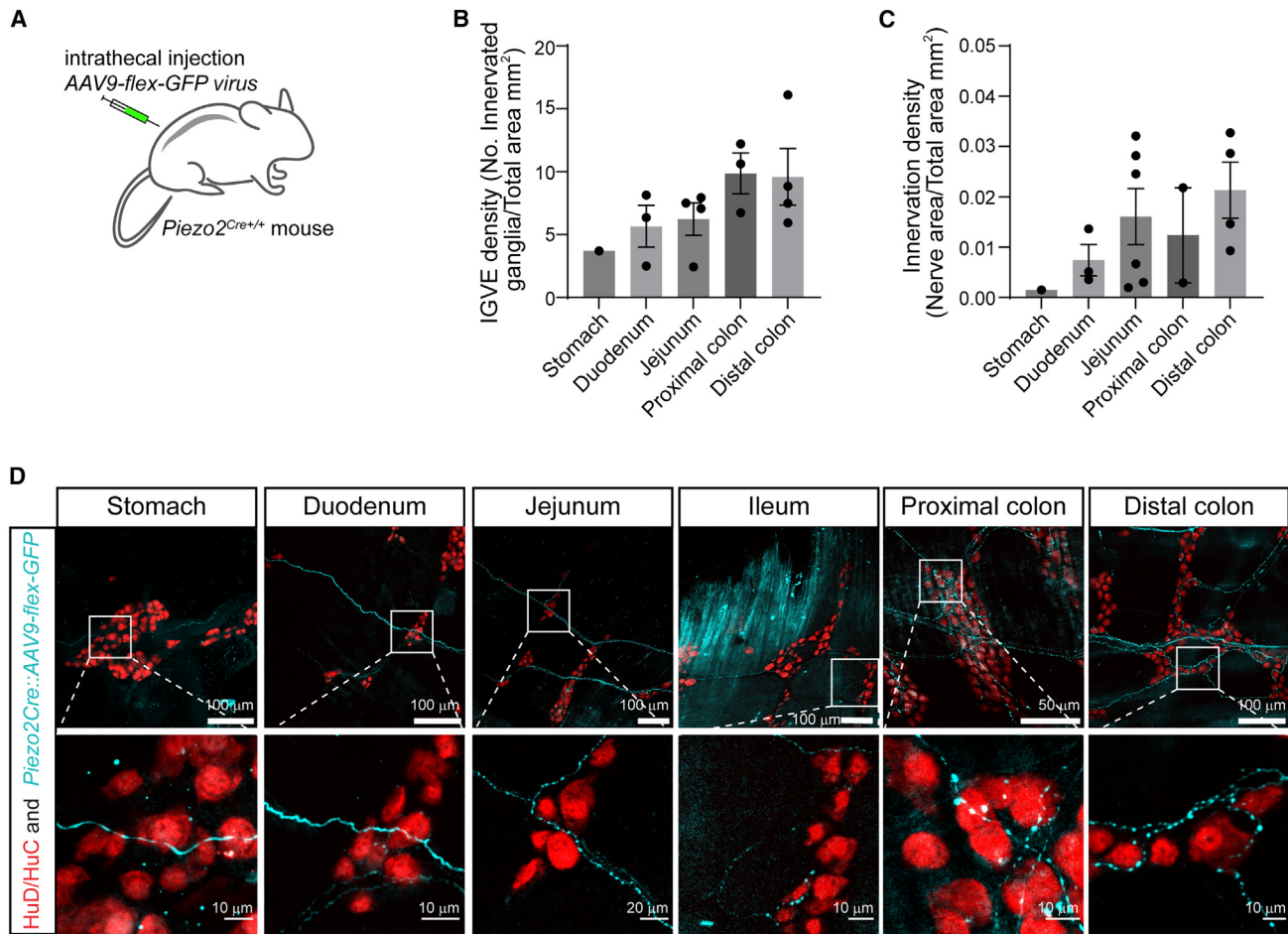
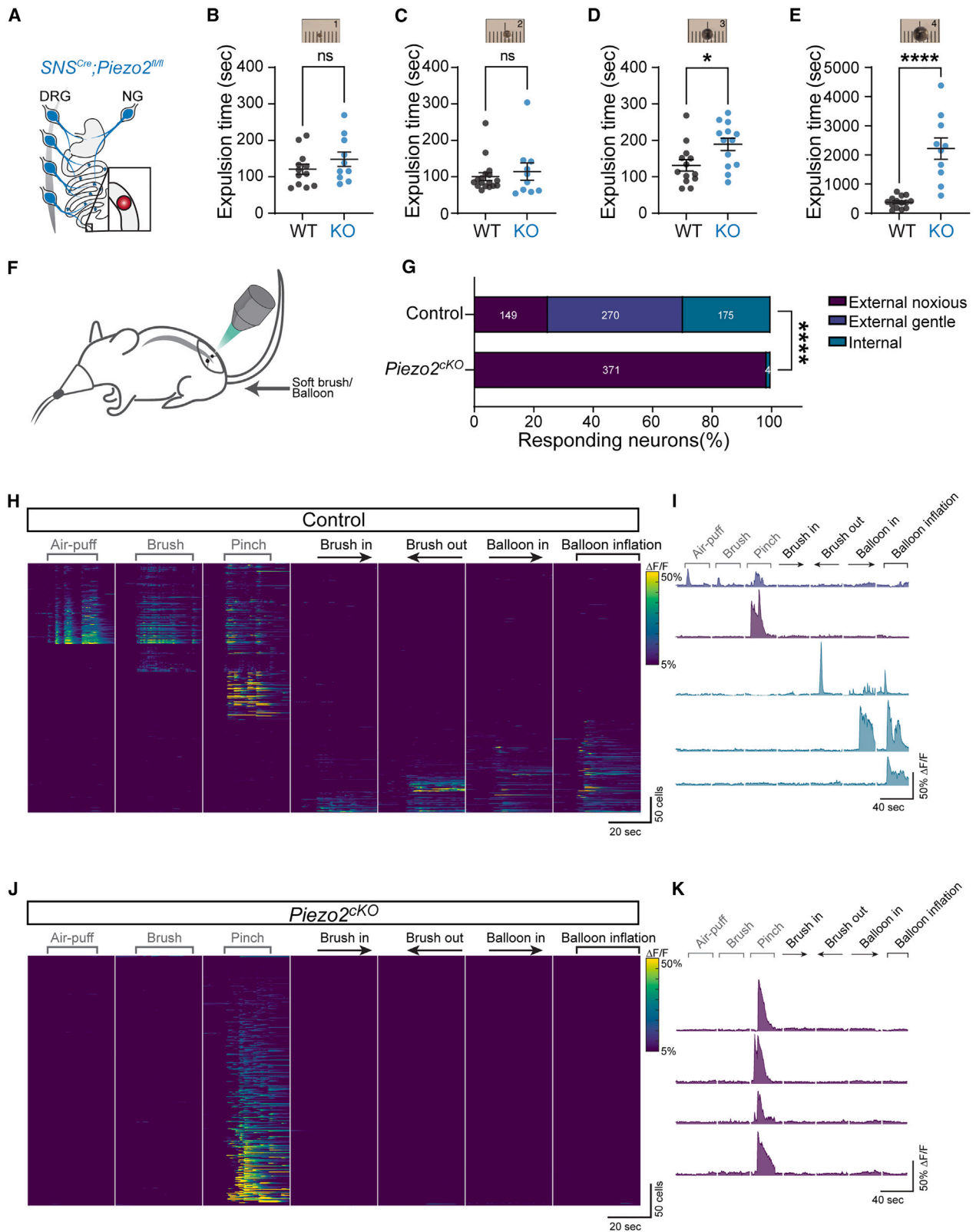


Figure 5. Piezo2 dorsal-root-ganglion neurons innervate the gastrointestinal tract

(A) Illustration of the strategy to assess DRG neuronal innervation by intrathecally injecting AAV9-flex-GFP particles into *Piezo2^{Cre+/+}* mice.
 (B) Quantification of the IGVE density, defined as the number of enteric ganglia innervated by IGVE in the total area across the whole GI tract. Data represented as mean \pm SEM.
 (C) Quantification of total innervation density, defined as innervated nerve area by the total area across the GI tract. Data represented as mean \pm SEM.
 (D) Representative images of stomach, small intestine, and colon. The enteric neuron nuclei were labeled with HuD/HuC antibody and represented in red. Piezo2-positive nerve endings are shown in cyan. Scale bar values are shown in each picture.

unclear whether difficulties in detecting rectal distention affect the overall defecation process. To examine the mouse response to rectum distention, we introduced glass beads into *Piezo2^{SNS}* and *Piezo2^{WT}* mice and quantify the expulsion time (Figure 6A). It is worth noting that the colonic contents of *Piezo2^{SNS}* and *Piezo2^{WT}* mice differ in size and water content (Figures 2D–2H). The mean width of fresh *Piezo2^{SNS}* stools is 2.17 mm (± 0.34 , standard deviation), which is significantly smaller than the stools from the *Piezo2^{WT}* littermates: 2.90 mm (± 0.41 , standard deviation) (Figure 2F). Given these differences, we tested a range of bead sizes. We did not observe any significant difference between the expulsion time in *Piezo2^{SNS}* and *Piezo2^{WT}* littermate mice when 1- and 2-mm beads were used (Figures 6B and 6C). However, when we used larger 3-mm beads, *Piezo2^{SNS}* mice presented a small but significant increase in bead expulsion time in comparison with the *Piezo2^{WT}* littermates (Figure 6D). Additionally, we tested 3-mm beads on

Piezo2^{Phox2b} and *Piezo2^{Hoxb8}* mice. We did not observe a significant difference in bead-expulsion time in *Piezo2^{Phox2b}* mice, yet there was a significant delay in the *Piezo2^{Hoxb8}* mice (Figures S6A and S6B; Table S1). To confirm the effect of Piezo2 deficiency on rectum motility, we reasoned that an even larger bead (4 mm) would cause a more pronounced motility delay in *Piezo2^{SNS}* mice and additionally mimic impacted stools presented in humans who experience constipation. Remarkably, when we tested 4-mm beads, we saw a stark delay in the bead expulsion time in the *Piezo2^{SNS}* mice in comparison with the *Piezo2^{WT}* controls (Figure 6E). This transit effect was observed in *Piezo2^{DRG}*, but not when Piezo2 was deleted from enterochromaffin cells (Figures S6C and S6D; Table S1). Interestingly, when we tested the expulsion of 4-mm beads in mice that underwent CGX, we did not observe any significant difference in motility before and after the CGX procedure (Figure S6E). These findings suggest that the lack of Piezo2 impairs the



(legend on next page)

detection of distension, consequently delaying the initiation of mechanically induced peristalsis of large contents in rectum. Interestingly, this mechanism appears to engage a different circuit than the baseline gut transit, which recruits sympathetic output (Figure 4H). Furthermore, as *Piezo2^{SNS}* and *Piezo2^{WT}* mice have different stool dimensions, it is possible that Piezo2 neurons have an additional role in regulating stool shape and size.

So far, our findings indicate that Piezo2-positive DRG fibers are present throughout the GI tract, and that motility is affected in Piezo2-deficient mice in all investigated gut regions. Next, we asked whether Piezo2 is directly required to sense mechanical stimulation within the gut. For this purpose, we adopted a colon preparation where we introduced a soft brush and inflated a balloon into the colon of anesthetized mice, while simultaneously recording DRG neuron activity using the calcium-sensitive indicator GCaMP6f (Figure 6F). Given the extensive research studying skin responses in DRG neurons,^{68–70} we opted to do external stimulation of the perineal skin as a control. We expected to activate different types of sensory neurons through mechanical stimulation of the skin and colon. Since DRG neurons primarily innervate the skin,^{37,68} we anticipated a large number and diversity of neurons that respond to external skin stimuli compared with colon-innervating neurons. From skin-innervating neurons, we expected to record activity from high-threshold mechanoreceptors (HTMRs) that respond to noxious stimuli (such as pinching), as well as responses from low-threshold mechanoreceptors (LTMRs) activated by air puffs, skin brushing, and noxious stimuli. For these experiments, we used *Hoxb8^{Cre+/-};Piezo2^{fl/fl};GCaMP6f^{+/+}* (*Piezo2^{CKO}*) mice and as control *Hoxb8^{Cre+/-};GCaMP6f^{+/+}* (*Piezo2^{WT}*). This approach enabled us to monitor the calcium signal from sacral DRG neurons in *Piezo2^{CKO}* and WT littermates. As internal stimulation, we utilized a soft brush movement and inflated a balloon inside the colon. We hypothesized that DRG neurons expressing Piezo2 detect colon stretch to allow calcium influx. *Piezo2^{WT}* mice exhibited rapid and robust

responses in sacral level 1 (S1) neurons after the skin stimulation with air puffs, a gentle stroke, and a noxious pinch in the perineal area (Figures 6G, 6H, S6F, and SG). We additionally observed calcium responses when introducing and removing a soft brush into the colon, and after inflating a colonic balloon in *Piezo2^{WT}* mice (Figures 6G–6I and S6F–S6H). Furthermore, many neurons exhibiting calcium activity can be segregated by the location of the applied stimulus (external or internal), this demonstrates that neurons innervating the colon are different neurons from those innervating the skin, even if they share the same ganglia (Figure 6H, S6I, and S6J). Consistent with previous findings,⁷⁰ responses to gentle stimuli (air puff and brush stroke) were markedly attenuated in somatosensory neurons from *Piezo2^{CKO}* mice (Figures 6G and 6J), corroborating the role of Piezo2 in the sense of touch. Strikingly, all responses to colonic stimuli (brush insertion and extraction, and balloon inflation) were abolished in DRG neurons from *Piezo2^{CKO}* mice, and only the response to painful pinch remained (Figures 6G, 6J, 6K, S6F, and S6G). This indicates that Piezo2 from DRG neurons is a key sensor of colon stretch.

DISCUSSION

The importance of gut motility and its control has been recognized since the 18th century.⁷ The GI tract is extensively innervated by the ENS,^{18,19,71} vagal afferents,^{8,9} and somatosensory neurons of the thoracic, lumbar, and sacral DRG.^{28,72} Here, we find that ingested contents provide mechanical feedback through activation of Piezo2 to dramatically slow the gut transit. Remarkably, using an array of conditional knockout mice, we uncovered that this food-dependent brake relies exclusively and unexpectedly on DRG mechanosensory input through sympathetic output (Figure S6K).

Whereas gut transit plays a major role in efficient digestion and nutrient absorption, defecation is another critical function of the lower GI tract that is known to be independently controlled.⁷³

Figure 6. Piezo2-expressing DRG neurons detect colon distention

(A) Illustration of the Cre line used for the glass bead expulsion test.

(B–E) Measurement of expulsion time in *SNS^{Cre+/-};Piezo2^{fl/fl}* (WT) and *SNS^{Cre+/-};Piezo2^{fl/fl}* (KO) mice following the insertion of a glass bead into their colons. Representative pictures of used beads are shown above each plot.

(B) 1-mm bead (unpaired two-tailed t test: $p = 0.2592$, $t(20) = 1.161$; ns, not statistically significant).

(C) 2-mm bead (Mann-Whitney test: $p = 0.9900$ two-tailed, $U = 84.5$; ns, not statistically significant).

(D) 3-mm bead (unpaired two-tailed t test: $*p = 0.0196$, $t(24) = 2.500$).

(E) 4-mm bead (unpaired two-tailed t test: $****p < 0.0001$, $t(22) = 5.910$).

(F) Illustration of *in vivo* calcium imaging recording in anesthetized mice focused on Sacral DRGs.

(G) Comparison of calcium responses of DRG neurons obtained after stimulating Control (*Hoxb8^{Cre+/-};GCaMP6f^{+/+}*, $n = 594$ cells; from 6 mice) and *Piezo2^{CKO}* (*Hoxb8^{Cre+/-};Piezo2^{fl/fl};GCaMP6f^{+/+}*, $n = 376$ cells; from 6 mice) mice (chi-squared test: $****p < 0.0001$, $\chi^2(2) = 501.5$). The responses are classified in three categories: internal: corresponds to the colonic stimulation with the soft brush and balloon; external noxious: response to only anal skin pinch; external gentle: cells that responded to air puff and/or brush on the surface of the anal skin, if they additionally responded to pinch, they were included in this category. The insets represent the numbers of recorded cells per category.

(H) Heatmap showing calcium responses (as $\Delta F/F$) recorded from Control (*Hoxb8^{Cre+/-};GCaMP6f^{+/+}*) DRG neurons. Neurons were functionally classified based on their response to stimuli and sorted by $\Delta F/F$. External (air puff, brush, and pinch) and internal (brush insertion and extraction, balloon insertion, and inflation) stimulations are shown on top of heatmap.

(I) Calcium representative traces from individual neurons are shown and color coded for the categories showed on (G), blue LTMRs, purple HTMRs, and teal for gut responding neurons.

(J) Heatmap showing calcium responses recorded from *Piezo2^{CKO}* (*Hoxb8^{Cre+/-};Piezo2^{fl/fl};GCaMP6f^{+/+}*) DRG neurons. External and internal stimulations are shown.

(K) Calcium representative traces from individual neurons are shown and color coded as in the categories showed on (G).

Data in (B)–(E) are represented as mean \pm SEM.

Notably, Piezo2-knockout mice exhibited a delayed evacuation in bead-expulsion assays (3 and 4 mm) and exhibited diarrhea-like behavior, possibly due to a failure to reabsorb water caused by the reduced transit time. Interestingly, human subjects with PIEZO2 deficiency also exhibit frequent GI dysregulation that ranges from constipation to diarrhea, consistent with the diverse roles of Piezo2 in controlling gut motility and defecation in mice.

Our data have therapeutic implications for a range of GI disorders. We anticipate that inhibition and activation of PIEZO2 could enhance or slow gut transit, respectively. Furthermore, using *in vivo* functional imaging, we found that Piezo2 is essential for all types of mechanosensation by DRG neurons innervating the colon in male and female mice. It is notable that stimulation using balloon inflation produces forces well into the noxious range.^{74–76} Intriguingly, conditional deletion of Piezo2 in neurons expressing *Scn10a* produced similar phenotypes to broadly knocking out this mechanoreceptor for all DRG neurons, suggesting a potential role of Piezo2 in gut mechano-nociception. These results are consistent with the findings from the accompanying paper (Wolfson et al.⁸⁵), where Piezo2 ablation using *CDx2^{Cre};Piezo2^{fl/fl}* decreased behavioral responses to colon distension. Although we could not detect the specific neuronal population that responds to both skin and colon stimulation,⁸⁵ we reasoned this may be due to differences in experimental approaches: (1) areas of stimulation to elicit noxious responses (back hairy skin vs perineal area) and (2) DRG recording levels (L6/S1 vs. S1/S2).

Taken together, our data provide a molecular and cellular explanation for how gut contents trigger mechanosensory-DRG neurons to control transit through the GI system. Whether Piezo2 in sensory endings detects the luminal contents passing through the gut or the constant gut contractions triggered by luminal contents is currently unknown. Future studies should reveal the role of this mechanosensitive ion channel in the vagal and enteric neurons, as well as how the different neuronal and non-neuronal systems interact to coordinate gut motility when environmental factors (diet, stressors, and exercise) change. Lastly, it has been shown that the sensitivity of gut-innervating mechanosensory neurons can be significantly sensitized by inflammation common to a range of GI disorders.^{77–79} Most notably inflammatory bowel disease (IBD), which can be extremely painful, causes diarrhea or constipation, and yet we lack effective treatment. Determining how PIEZO2 function is altered during GI disease will be particularly important.

Limitations of the study

Our study provides clear evidence of how neurons in the sacral DRGs innervate the colon and respond to stretch via Piezo2. It will be crucial to expand this approach and record more neurons from DRGs in the thoracic and lumbar DRGs levels which target upper regions of the GI tract. To achieve this, it will be necessary to develop methods that selectively probe the proximal subregions of the GI tract and unveil the precise functions of Piezo2 in these compartments, as we have accomplished here for the colon. Furthermore, transcriptomic data have shown that *Piezo2* is expressed in multiple DRG types.^{28,80,81} It will be fascinating to discern whether specific subtypes of GI-innervating DRG neu-

rons have select roles in regulating motility modalities such as mixing, segmentation, and peristalsis.

STAR★METHODS

Detailed methods are provided in the online version of this paper and include the following:

- KEY RESOURCES TABLE
- RESOURCE AVAILABILITY
 - Lead contact
 - Material availability
 - Data and code availability
- EXPERIMENTAL MODEL AND STUDY PARTICIPANT DETAILS
 - Mice
 - Human subjects
- METHOD DETAILS
 - Recombinant viruses
 - Surgeries
 - Intrathecal injections
 - Intra-intestinal catheter implantation
 - Celiac ganglionectomy
 - Treatments
 - Histology
 - Behavioral and physiological assays
 - Imaging
- QUANTIFICATION AND STATISTICAL ANALYSIS

SUPPLEMENTAL INFORMATION

Supplemental information can be found online at <https://doi.org/10.1016/j.cell.2023.07.006>.

ACKNOWLEDGMENTS

We thank M. Szczot and Felipe Meira de Faria from Linköping University for their support to develop the *in vivo* colonic preparation. We thank R. Hill, R. Pak, and A. Dubin for their feedback on the manuscript. We also thank K. Spencer, the Nikon Center of Excellence Imaging Center, and the Scripps Research Department of Animal Resources for support services. This work was supported by the Howard Hughes Medical Institute, NIH grant R35 NS105067 (A.P.), and the intramural program of the NIH, the National Center for Complementary and Integrative Health, and National Institute of Neurological Disorders and Stroke (A.T.C.).

AUTHOR CONTRIBUTIONS

M.R.S.-V., A.P., and A.T.C. conceived and designed the study. M.R.S.-V., R.M.L., A.K., Y.W., M.L., S.F., and H.K. performed experiments and analyzed data. R.M.L. performed and analyzed *in vivo* DRG recordings. H.K. performed and analyzed videorecorded GI transit experiments. Y.Z. performed analysis of scRNA-seq from Zeisel et al.⁴⁰ M.R.S.-V., A.P., and A.T.C. wrote the manuscript. All authors provided input and reviewed the manuscript.

DECLARATION OF INTERESTS

The authors declare no competing interests.

INCLUSION AND DIVERSITY

We support inclusive, diverse, and equitable conduct of research.

Received: November 27, 2022
Revised: April 24, 2023
Accepted: July 6, 2023
Published: August 3, 2023

REFERENCES

- Sanders, K.M., Koh, S.D., Ro, S., and Ward, S.M. (2012). Regulation of gastrointestinal motility—insights from smooth muscle biology. *Nat. Rev. Gastroenterol. Hepatol.* 9, 633–645. <https://doi.org/10.1038/nrgastro.2012.168>.
- Huizinga, J.D., Chen, J.H., Zhu, Y.F., Pawelka, A., McGinn, R.J., Bardakjian, B.L., Parsons, S.P., Kunze, W.A., Wu, R.Y., Bercik, P., et al. (2014). The origin of segmentation motor activity in the intestine. *Nat. Commun.* 5, 3326. <https://doi.org/10.1038/ncomms4326>.
- Deloose, E., Janssen, P., Depoortere, I., and Tack, J. (2012). The migrating motor complex: control mechanisms and its role in health and disease. *Nat. Rev. Gastroenterol. Hepatol.* 9, 271–285. <https://doi.org/10.1038/nrgastro.2012.57>.
- Brookes, S.J.H., Spencer, N.J., Costa, M., and Zagorodnyuk, V.P. (2013). Extrinsic primary afferent signalling in the gut. *Nat. Rev. Gastroenterol. Hepatol.* 10, 286–296. <https://doi.org/10.1038/nrgastro.2013.29>.
- Furness, J.B. (2012). The enteric nervous system and neurogastroenterology. *Nat. Rev. Gastroenterol. Hepatol.* 9, 286–294. <https://doi.org/10.1038/nrgastro.2012.32>.
- Mercado-Perez, A., and Beyder, A. (2022). Gut feelings: mechanosensing in the gastrointestinal tract. *Nat. Rev. Gastroenterol. Hepatol.* 19, 283–296. <https://doi.org/10.1038/s41575-021-00561-y>.
- Spencer, N.J., and Hu, H. (2020). Enteric nervous system: sensory transduction, neural circuits and gastrointestinal motility. *Nat. Rev. Gastroenterol. Hepatol.* 17, 338–351. <https://doi.org/10.1038/s41575-020-0271-2>.
- Zhao, Q., Yu, C.D., Wang, R., Xu, Q.J., Dai Pra, R., Zhang, L., and Chang, R.B. (2022). A multidimensional coding architecture of the vagal interoceptive system. *Nature* 603, 878–884. <https://doi.org/10.1038/s41586-022-04515-5>.
- Bai, L., Mesgarzadeh, S., Ramesh, K.S., Huey, E.L., Liu, Y., Gray, L.A., Aitken, T.J., Chen, Y., Beutler, L.R., Ahn, J.S., et al. (2019). Genetic identification of vagal sensory neurons that control feeding. *Cell* 179, 1129–1143.e23. <https://doi.org/10.1016/j.cell.2019.10.031>.
- Williams, E.K., Chang, R.B., Strohlic, D.E., Umans, B.D., Lowell, B.B., and Liberles, S.D. (2016). Sensory neurons that detect stretch and nutrients in the digestive system. *Cell* 166, 209–221. <https://doi.org/10.1016/j.cell.2016.05.011>.
- Prescott, S.L., and Liberles, S.D. (2022). Internal senses of the vagus nerve. *Neuron* 110, 579–599. <https://doi.org/10.1016/j.neuron.2021.12.020>.
- Saper, C.B., Chou, T.C., and Elmquist, J.K. (2002). The need to feed: homeostatic and hedonic control of eating. *Neuron* 36, 199–211. [https://doi.org/10.1016/S0896-6273\(02\)00969-8](https://doi.org/10.1016/S0896-6273(02)00969-8).
- Kim, M., Heo, G., and Kim, S.Y. (2022). Neural signalling of gut mechanosensation in ingestive and digestive processes. *Nat. Rev. Neurosci.* 23, 135–156. <https://doi.org/10.1038/s41583-021-00544-7>.
- Han, W., Tellez, L.A., Perkins, M.H., Perez, I.O., Qu, T., Ferreira, J., Ferreira, T.L., Quinn, D., Liu, Z.-W., Gao, X.-B., et al. (2018). A neural circuit for gut-induced reward. *Cell* 175, 665–678.e23. <https://doi.org/10.1016/j.cell.2018.08.049>.
- Grundy, L., Erickson, A., and Brierley, S.M. (2019). Visceral pain. *Annu. Rev. Physiol.* 81, 261–284. <https://doi.org/10.1146/annurev-physiol-020518-114525>.
- Kyloh, M., Nicholas, S., Zagorodnyuk, V.P., Brookes, S.J., and Spencer, N.J. (2011). Identification of the visceral pain pathway activated by noxious colorectal distension in mice. *Front. Neurosci.* 5, 16.
- Zheng, Y., Liu, P., Bai, L., Trimmer, J.S., Bean, B.P., and Ginty, D.D. (2019). Deep sequencing of somatosensory neurons reveals molecular determinants of intrinsic physiological properties. *Neuron* 103, 598–616.e7. <https://doi.org/10.1016/j.neuron.2019.05.039>.
- Drokhlyansky, E., Smillie, C.S., Van Wittenberghe, N.V., Ericsson, M., Griffin, G.K., Eraslan, G., Dionne, D., Cuoco, M.S., Goder-Reiser, M.N., Sharova, T., et al. (2020). The human and mouse enteric nervous system at single-cell resolution. *Cell* 182, 1606–1622.e23. <https://doi.org/10.1016/j.cell.2020.08.003>.
- Morarach, K., Mikhailova, A., Knoflach, V., Memic, F., Kumar, R., Li, W., Erfors, P., and Marklund, U. (2021). Diversification of molecularly defined myenteric neuron classes revealed by single-cell RNA sequencing. *Nat. Neurosci.* 24, 34–46. <https://doi.org/10.1038/s41593-020-00736-x>.
- Parpaite, T., Brosse, L., Séjourné, N., Laur, A., Mechoukhi, Y., Delmas, P., and Coste, B. (2021). Patch-seq of mouse DRG neurons reveals candidate genes for specific mechanosensory functions. *Cell Rep.* 37, 109914. <https://doi.org/10.1016/j.celrep.2021.109914>.
- Woo, S.H., Lukacs, V., de Nooij, J.C., Zaytseva, D., Criddle, C.R., Francisco, A., Jessell, T.M., Wilkinson, K.A., and Patapoutian, A. (2015). Piezo2 is the principal mechanotransduction channel for proprioception. *Nat. Neurosci.* 18, 1756–1762. <https://doi.org/10.1038/nn.4162>.
- Chesler, A.T., Szczot, M., Bharucha-Goebel, D., Čeko, M., Donkervoort, S., Laubacher, C., Hayes, L.H., Alter, K., Zampieri, C., Stanley, C., et al. (2016). The role of PIEZO2 in human mechanosensation. *N. Engl. J. Med.* 375, 1355–1364. <https://doi.org/10.1056/NEJMoa1602812>.
- Ranade, S.S., Woo, S.H., Dubin, A.E., Moshourab, R.A., Wetzel, C., Petrus, M., Mathur, J., Bégay, V., Coste, B., Mainquist, J., et al. (2014). Piezo2 is the major transducer of mechanical forces for touch sensation in mice. *Nature* 516, 121–125. <https://doi.org/10.1038/nature13980>.
- Nonomura, K., Woo, S.H., Chang, R.B., Gillich, A., Qiu, Z., Francisco, A.G., Ranade, S.S., Liberles, S.D., and Patapoutian, A. (2017). Piezo2 senses airway stretch and mediates lung inflation-induced apnoea. *Nature* 541, 176–181. <https://doi.org/10.1038/nature20793>.
- Marshall, K.L., Saade, D., Ghitani, N., Coombs, A.M., Szczot, M., Keller, J., Ogata, T., Daou, I., Stowers, L.T., Bönnemann, C.G., et al. (2020). PIEZO2 in sensory neurons and urothelial cells coordinates urination. *Nature* 588, 290–295. <https://doi.org/10.1038/s41586-020-2830-7>.
- Kupari, J., Häring, M., Agirre, E., Castelo-Branco, G., and Erfors, P. (2019). An atlas of vagal sensory neurons and their molecular specialization. *Cell Rep.* 27, 2508–2523.e4. <https://doi.org/10.1016/j.celrep.2019.04.096>.
- Zeng, W.Z., Marshall, K.L., Min, S., Daou, I., Chapleau, M.W., Abboud, F.M., Liberles, S.D., and Patapoutian, A. (2018). PIEZO2s mediate neuronal sensing of blood pressure and the baroreceptor reflex. *Science* 362, 464–467. <https://doi.org/10.1126/science.aau6324>.
- Hockley, J.R.F., Taylor, T.S., Callejo, G., Wilbrey, A.L., Gutteridge, A., Bach, K., Winchester, W.J., Bulmer, D.C., McMurray, G., and Smith, E.S.J. (2019). Single-cell RNAseq reveals seven classes of colonic sensory neuron. *Gut* 68, 633–644. <https://doi.org/10.1136/gutjnl-2017-315631>.
- Murthy, S.E., Loud, M.C., Daou, I., Marshall, K.L., Schwaller, F., Kühnemund, J., Francisco, A.G., Keenan, W.T., Dubin, A.E., Lewin, G.R., et al. (2018). The mechanosensitive ion channel Piezo2 mediates sensitivity to mechanical pain in mice. *Sci. Transl. Med.* 10. <https://doi.org/10.1126/scitranslmed.aat9897>.
- Szczot, M., Nickolls, A.R., Lam, R.M., and Chesler, A.T. (2021). The form and function of PIEZO2. *Annu. Rev. Biochem.* 90, 507–534. <https://doi.org/10.1146/annurev-biochem-081720-023244>.
- Khanna, P., Agarwal, N., Khanna, D., Hays, R.D., Chang, L., Bolus, R., Melmed, G., Whitman, C.B., Kaplan, R.M., Ogawa, R., et al. (2014). Development of an online library of patient-reported outcome measures in gastroenterology: the GI-PRO database. *Am. J. Gastroenterol.* 109, 234–248. <https://doi.org/10.1038/ajg.2013.401>.

32. Spiegel, B.M.R., Hays, R.D., Bolus, R., Melmed, G.Y., Chang, L., Whitman, C., Khanna, P.P., Paz, S.H., Hays, T., Reise, S., et al. (2014). Development of the NIH Patient-Reported Outcomes Measurement Information System (PROMIS) gastrointestinal symptom scales. *Am. J. Gastroenterol.* *109*, 1804–1814. <https://doi.org/10.1038/ajg.2014.237>.
33. Ross, B., Watson, B.W., and Kay, A.W. (1963). Studies on the effect of vagotomy on small intestinal motility using the radiotelemetering capsule. *Gut* *4*, 77–81. <https://doi.org/10.1136/gut.4.1.77>.
34. Heuckeroth, R.O. (2018). Hirschsprung disease — integrating basic science and clinical medicine to improve outcomes. *Nat. Rev. Gastroenterol. Hepatol.* *15*, 152–167. <https://doi.org/10.1038/nrgastro.2017.149>.
35. Camilleri, M. (2021). Gastrointestinal motility disorders in neurologic disease. *J. Clin. Invest.* *131*. <https://doi.org/10.1172/JCI143771>.
36. Agarwal, N., Offermanns, S., and Kuner, R. (2004). Conditional gene deletion in primary nociceptive neurons of trigeminal ganglia and dorsal root ganglia. *Genesis* *38*, 122–129. <https://doi.org/10.1002/gene.20010>.
37. Muller, P.A., Schneeberger, M., Matheis, F., Wang, P., Kerner, Z., Ilanges, A., Pellegrino, K., del Mármol, J., Castro, T.B.R., Furuichi, M., et al. (2020). Microbiota modulate sympathetic neurons via a gut–brain circuit. *Nature* *583*, 441–446. <https://doi.org/10.1038/s41586-020-2474-7>.
38. Gautron, L., Sakata, I., Udit, S., Zigman, J.M., Wood, J.N., and Elmquist, J.K. (2011). Genetic tracing of Nav1.8-expressing vagal afferents in the mouse. *J. Comp. Neurol.* *519*, 3085–3101. <https://doi.org/10.1002/cne.22667>.
39. Madisen, L., Zwingman, T.A., Sunkin, S.M., Oh, S.W., Zariwala, H.A., Gu, H., Ng, L.L., Palmiter, R.D., Hawrylycz, M.J., Jones, A.R., et al. (2010). A robust and high-throughput Cre reporting and characterization system for the whole mouse brain. *Nat. Neurosci.* *13*, 133–140. <https://doi.org/10.1038/nn.2467>.
40. Zeisel, A., Hochgerner, H., Lönnerberg, P., Johnsson, A., Memic, F., van der Zwan, J., Häring, M., Braun, E., Borm, L.E., La Manno, G., et al. (2018). Molecular architecture of the mouse nervous system. *Cell* *174*, 999–1014.e22. <https://doi.org/10.1016/j.cell.2018.06.021>.
41. Alcaïno, C., Knutson, K.R., Treichel, A.J., Yildiz, G., Strega, P.R., Linden, D.R., Li, J.H., Leiter, A.B., Szurszewski, J.H., Farrugia, G., et al. (2018). A population of gut epithelial enterochromaffin cells is mechanosensitive and requires Piezo2 to convert force into serotonin release. *Proc. Natl. Acad. Sci. USA* *115*, E7632–E7641. <https://doi.org/10.1073/pnas.1804938115>.
42. Wang, F., Knutson, K., Alcaïno, C., Linden, D.R., Gibbons, S.J., Kashyap, P., Grover, M., Oeckler, R., Gottlieb, P.A., Li, H.J., et al. (2017). Mechanosensitive ion channel Piezo2 is important for enterochromaffin cell response to mechanical forces. *J. Physiol.* *595*, 79–91. <https://doi.org/10.1113/JP272718>.
43. Ichiki, T., Wang, T., Kennedy, A., Pool, A.H., Ebisu, H., Anderson, D.J., and Oka, Y. (2022). Sensory representation and detection mechanisms of gut osmolality change. *Nature* *602*, 468–474. <https://doi.org/10.1038/s41586-021-04359-5>.
44. Scott, M.M., Williams, K.W., Rossi, J., Lee, C.E., and Elmquist, J.K. (2011). Leptin receptor expression in hindbrain GLP-1 neurons regulates food intake and energy balance in mice. *J. Clin. Invest.* *121*, 2413–2421. <https://doi.org/10.1172/JCI43703>.
45. Witschi, R., Johansson, T., Morscher, G., Scheurer, L., Deschamps, J., and Zeilhofer, H.U. (2010). Hoxb8-Cre mice: a tool for brain-sparing conditional gene deletion. *Genesis* *48*, 596–602. <https://doi.org/10.1002/dvg.20656>.
46. Peron, S.P., Freeman, J., Iyer, V., Guo, C., and Svoboda, K. (2015). A cellular resolution map of barrel cortex activity during tactile behavior. *Neuron* *86*, 783–799. <https://doi.org/10.1016/j.neuron.2015.03.027>.
47. Kacmaz, H., Alto, A., Knutson, K., Linden, D.R., Gibbons, S.J., Farrugia, G., and Beyder, A. (2021). A simple automated approach to measure mouse whole gut transit. *Neurogastroenterol. Motil.* *33*, e13994. <https://doi.org/10.1111/nmo.13994>.
48. Treichel, A.J., Finholm, I., Knutson, K.R., Alcaïno, C., Whiteman, S.T., Brown, M.R., Matveyenko, A., Wegner, A., Kacmaz, H., Mercado-Perez, A., et al. (2022). Specialized mechanosensory epithelial cells in mouse gut intrinsic tactile sensitivity. *Gastroenterology* *162*, 535–547.e13. <https://doi.org/10.1053/j.gastro.2021.10.026>.
49. Jones, L.A., Jin, B., Martin, A.M., Wei, L., de Fontgalland, D., Hollington, P., Wattchow, D.A., Rabbitt, P., Sposato, L., Spencer, N.J., et al. (2022). Diminished Piezo2-dependent tactile sensitivity occurs in aging human gut and slows gastrointestinal transit in mice. *Gastroenterology* *162*, 1755–1757.e2. <https://doi.org/10.1053/j.gastro.2022.01.043>.
50. Bai, T., Li, Y., Xia, J., Jiang, Y., Zhang, L., Wang, H., Qian, W., Song, J., and Hou, X. (2017). Piezo2: a candidate biomarker for visceral hypersensitivity in irritable bowel syndrome? *J. Neurogastroenterol. Motil.* *23*, 453–463. <https://doi.org/10.5056/jnm16114>.
51. Billing, L.J., Larraufie, P., Lewis, J., Leiter, A., Li, J., Lam, B., Yeo, G.S., Goldspink, D.A., Kay, R.G., Gribble, F.M., et al. (2019). Single cell transcriptomic profiling of large intestinal enteroendocrine cells in mice – identification of selective stimuli for insulin-like peptide-5 and glucagon-like peptide-1 co-expressing cells. *Mol. Metab.* *29*, 158–169. <https://doi.org/10.1016/j.molmet.2019.09.001>.
52. Madison, B.B., Dunbar, L., Qiao, X.T., Braunstein, K., Braunstein, E., and Gumucio, D.L. (2002). Cis elements of the villin gene control expression in restricted domains of the vertical (crypt) and horizontal (duodenum, cecum) axes of the intestine. *J. Biol. Chem.* *277*, 33275–33283. <https://doi.org/10.1074/jbc.M204935200>.
53. Chan, K.Y., Jang, M.J., Yoo, B.B., Greenbaum, A., Ravi, N., Wu, W.L., Sánchez-Guardado, L., Lois, C., Mazmanian, S.K., Deverman, B.E., et al. (2017). Engineered AAVs for efficient noninvasive gene delivery to the central and peripheral nervous systems. *Nat. Neurosci.* *20*, 1172–1179. <https://doi.org/10.1038/nn.4593>.
54. Muller, P.A., Koscsó, B., Rajani, G.M., Stevanovic, K., Berres, M.-L., Hashimoto, D., Mortha, A., Leboeuf, M., Li, X.-M., Mucida, D., et al. (2014). Crosstalk between muscularis macrophages and enteric neurons regulates gastrointestinal motility. *Cell* *158*, 300–313. <https://doi.org/10.1016/j.cell.2014.04.050>.
55. Dey, N., Wagner, V.E., Blanton, L.V., Cheng, J., Fontana, L., Haque, R., Ahmed, T., and Gordon, J.I. (2015). Regulators of gut motility revealed by a gnotobiotic model of diet-microbiome interactions related to travel. *Cell* *163*, 95–107. <https://doi.org/10.1016/j.cell.2015.08.059>.
56. Schepper, S.D., Verheijden, S., Aguilera-Lizarraga, J., Viola, M.F., Boesmans, W., Stakenborg, N., Voytyuk, I., Schmidt, I., Boeckx, B., de Castèleré, I.D., et al. (2018). Self-maintaining gut macrophages are essential for intestinal homeostasis. *Cell* *175*, 400–415.e13. <https://doi.org/10.1016/j.cell.2018.07.048>.
57. Browning, K.N., and Travagli, R.A. (2014). Central nervous system control of gastrointestinal motility and secretion and modulation of gastrointestinal functions. *Compr. Physiol.* *4*, 1339–1368. <https://doi.org/10.1002/cphy.c130055>.
58. Jacobson, A., Yang, D., Vella, M., and Chiu, I.M. (2021). The intestinal neuro-immune axis: crosstalk between neurons, immune cells, and microbes. *Mucosal Immunol.* *14*, 555–565. <https://doi.org/10.1038/s41385-020-00368-1>.
59. Mayer, E.A. (2011). Gut feelings: the emerging biology of gut–brain communication. *Nat. Rev. Neurosci.* *12*, 453–466. <https://doi.org/10.1038/nrn3071>.
60. Oh, S.W., Harris, J.A., Ng, L., Winslow, B., Cain, N., Mihalas, S., Wang, Q., Lau, C., Kuan, L., Henry, A.M., et al. (2014). A mesoscale connectome of the mouse brain. *Nature* *508*, 207–214. <https://doi.org/10.1038/nature13186>.
61. Woo, S.H., Ranade, S., Weyer, A.D., Dubin, A.E., Baba, Y., Qiu, Z., Petrus, M., Miyamoto, T., Reddy, K., Lumpkin, E.A., et al. (2014). Piezo2 is required for Merkel-cell mechanotransduction. *Nature* *509*, 622–626. <https://doi.org/10.1038/nature13251>.

62. Spencer, N.J., Kyloh, M., and Duffield, M. (2014). Identification of different types of spinal afferent nerve endings that encode noxious and innocuous stimuli in the large intestine using a novel anterograde tracing technique. *PLoS One* 9, e112466. <https://doi.org/10.1371/journal.pone.0112466>.
63. Spencer, N.J., Kyloh, M., Beckett, E.A., Brookes, S., and Hibberd, T. (2016). Different types of spinal afferent nerve endings in stomach and esophagus identified by anterograde tracing from dorsal root ganglia. *J. Comp. Neurol.* 524, 3064–3083. <https://doi.org/10.1002/cne.24006>.
64. Moreno, A.M., Alemán, F., Catroli, G.F., Hunt, M., Hu, M., Dailamy, A., Pla, A., Woller, S.A., Palmer, N., Parekh, U., et al. (2021). Long-lasting analgesia via targeted in situ repression of Nav1.7 in mice. *Sci. Transl. Med.* 13, eaay9056. <https://doi.org/10.1126/scitransmed.aay9056>.
65. Bampton, P.A., Dinning, P.G., Kennedy, M.L., Lubowski, D.Z., deCarle, D., and Cook, I.J. (2000). Spatial and temporal organization of pressure patterns throughout the unprepared colon during spontaneous defecation. *Am. J. Gastroenterol.* 95, 1027–1035. <https://doi.org/10.1111/j.1572-0241.2000.01839.x>.
66. Kamm, M.A., van der Sijp, J.R., and Lennard-Jones, J.E. (1992). Colorectal and anal motility during defaecation. *Lancet* 339, 820. [https://doi.org/10.1016/0140-6736\(92\)91957-a](https://doi.org/10.1016/0140-6736(92)91957-a).
67. Bassotti, G., and Gaburri, M. (1988). Manometric investigation of high-amplitude propagated contractile activity of the human colon. *Am. J. Physiol.* 255, G660–G664. <https://doi.org/10.1152/ajpgi.1988.255.5.G660>.
68. Abraira, V.E., and Ginty, D.D. (2013). The sensory neurons of touch. *Neuron* 79. <https://doi.org/10.1016/j.neuron.2013.07.051>. <https://www.ncbi.nlm.nih.gov/pmc/articles/PMC3811145/>.
69. Szczot, M., Lijencrantz, J., Ghitani, N., Barik, A., Lam, R., Thompson, J.H., Bharucha-Goebel, D., Saade, D., Necaie, A., Donkervoort, S., et al. (2018). PIEZO2 mediates injury-induced tactile pain in mice and humans. *Sci. Transl. Med.* 10, eaat9892. <https://doi.org/10.1126/scitransmed.aat9892>.
70. von Buchholtz, L.J., Ghitani, N., Lam, R.M., Licholai, J.A., Chesler, A.T., and Ryba, N.J.P. (2021). Decoding cellular mechanisms for mechanosensory discrimination. *Neuron* 109, 285–298.e5. <https://doi.org/10.1016/j.neuron.2020.10.028>.
71. Li, Z., Hao, M.M., Van den Haute, C., Baekelandt, V., Boesmans, W., and Vanden Berghe, P. (2019). Regional complexity in enteric neuron wiring reflects diversity of motility patterns in the mouse large intestine. *eLife* 8, e42914. <https://doi.org/10.7554/eLife.42914>.
72. Niu, X., Liu, L., Wang, T., Chuan, X., Yu, Q., Du, M., Gu, Y., and Wang, L. (2020). Mapping of extrinsic innervation of the gastrointestinal tract in the mouse embryo. *J. Neurosci.* 40, 6691–6708. <https://doi.org/10.1523/JNEUROSCI.0309-20.2020>.
73. Heitmann, P.T., Vollebregt, P.F., Knowles, C.H., Lunniss, P.J., Dinning, P.G., and Scott, S.M. (2021). Understanding the physiology of human defaecation and disorders of continence and evacuation. *Nat. Rev. Gastroenterol. Hepatol.* 18, 751–769. <https://doi.org/10.1038/s41575-021-00487-5>.
74. Mueller-Tribbensee, S.M., Karna, M., Khalil, M., Neurath, M.F., Reeh, P.W., and Engel, M.A. (2015). Differential contribution of TRPA1, TRPV4 and TRPM8 to colonic nociception in mice. *PLoS One* 10, e0128242. <https://doi.org/10.1371/journal.pone.0128242>.
75. Laird, J.M.A., Olivar, T., Roza, C., De Felipe, C., Hunt, S.P., and Cervero, F. (2000). Deficits in visceral pain and hyperalgesia of mice with a disruption of the tachykinin NK1 receptor gene. *Neuroscience* 98, 345–352. [https://doi.org/10.1016/S0306-4522\(00\)00148-2](https://doi.org/10.1016/S0306-4522(00)00148-2).
76. Zagorodnyuk, V.P., Kyloh, M., Nicholas, S., Peiris, H., Brookes, S.J., Chen, B.N., and Spencer, N.J. (2011). Loss of visceral pain following colorectal distension in an endothelin-3 deficient mouse model of Hirschsprung's disease. *J. Physiol.* 589, 1691–1706. <https://doi.org/10.1113/jphysiol.2010.202820>.
77. Hockley, J.R.F., Boundouki, G., Cibert-Goton, V., McGuire, C., Yip, P.K., Chan, C., Tranter, M., Wood, J.N., Nassar, M.A., Blackshaw, L.A., et al. (2014). Multiple roles for Nav1.9 in the activation of visceral afferents by noxious inflammatory, mechanical, and human disease-derived stimuli. *Pain* 155, 1962–1975. <https://doi.org/10.1016/j.pain.2014.06.015>.
78. Martinez, V., and Melgar, S. (2008). Lack of colonic inflammation-induced acute visceral hypersensitivity to colorectal distension in Nav1.9 knockout mice. *Eur. J. Pain* 12, 934–944. <https://doi.org/10.1016/j.ejpain.2007.12.011>.
79. Willemze, R.A., Luyer, M.D., Buurman, W.A., and de Jonge, W.J. (2015). Neural reflex pathways in intestinal inflammation: hypotheses to viable therapy. *Nat. Rev. Gastroenterol. Hepatol.* 12, 353–362. <https://www.nature.com/articles/nrgastro.2015.56>.
80. Usoskin, D., Furlan, A., Islam, S., Abdo, H., Lönnnerberg, P., Lou, D., Hjerling-Leffler, J., Haeggström, J., Kharchenko, O., Kharchenko, P.V., et al. (2015). Unbiased classification of sensory neuron types by large-scale single-cell RNA sequencing. *Nat. Neurosci.* 18, 145–153. <https://doi.org/10.1038/nn.3881>.
81. Li, C.-L., Li, K.-C., Wu, D., Chen, Y., Luo, H., Zhao, J.-R., Wang, S.-S., Sun, M.-M., Lu, Y.-J., Zhong, Y.-Q., et al. (2016). Somatosensory neuron types identified by high-coverage single-cell RNA-sequencing and functional heterogeneity. *Cell Res.* 26, 83–102. <https://doi.org/10.1038/cr.2015.149>.
82. Spencer, N.J., Hibberd, T.J., Travis, L., Wiklendt, L., Costa, M., Hu, H., Brookes, S.J., Wattchow, D.A., Dinning, P.G., Keating, D.J., et al. (2018). Identification of a rhythmic firing pattern in the enteric nervous system that generates rhythmic electrical activity in smooth muscle. *J. Neurosci.* 38, 5507–5522. <https://doi.org/10.1523/JNEUROSCI.3489-17.2018>.
83. Druckmann, S., Feng, L., Lee, B., Yook, C., Zhao, T., Magee, J.C., and Kim, J. (2014). Structured synaptic connectivity between hippocampal regions. *Neuron* 81, 629–640. <https://doi.org/10.1016/j.neuron.2013.11.026>.
84. Ghitani, N., Barik, A., Szczot, M., Thompson, J.H., Li, C., Le Pichon, C.E., Krashe, M.J., and Chesler, A.T. (2017). Specialized mechanosensory nociceptors mediating rapid responses to hair-pull. *Neuron* 95, 944–954.e4. <https://doi.org/10.1016/j.neuron.2017.07.024>.
85. Wolfson, R.L., Abdelaziz, A., Rankin, G., Kushner, S., Qi, L., Mazor, O., Choi, N., Sharma, N., and Ginty, D.D. (2023). DRG afferents that mediate physiologic and pathologic mechanosensation from the distal colon. *Cell* 186. <https://doi.org/10.1016/j.cell.2023.07.007>.

STAR★METHODS

KEY RESOURCES TABLE

REAGENT or RESOURCE	SOURCE	IDENTIFIER
Antibodies		
Rabbit monoclonal anti-HuC/HuD (1:500 whole-mount)	Abcam	Cat# ab184267; RRID: AB_2864321
Chicken polyclonal anti-GFP (1:100 whole-mount)	AVES	Cat# GFP-1020; RRID: AB_2307313
Goat anti-rabbit, Alexa Fluor 555 (1:1000 whole-mount)	Invitrogen	A-21428; RRID: AB_2313773
Goat anti-chicken, Alexa Fluor 647 (1:1000 whole-mount)	Invitrogen	A-21449; RRID: AB_2313773
Bacterial and virus strains		
CAG-iCre	Druckmann et al. ⁸³	Addgene Cat# 51904
CAG-tdTomato	Edward Boyden	Addgene Cat# 59462
AAV9-pCAG-FLEX-egfp-wpre	Oh et al. ⁶⁰	Addgene viral prep # 51502-AAV9
Chemicals, peptides, and recombinant proteins		
Carmine red	Sigma-Aldrich	Cat# C1022; CAS: 1390-65-4
GastroSense-750	PerkinElmer	Cat# NEV11121
Methylcellulose 400 cP	Sigma-Aldrich	Cat# M0262; CAS: 9004-67-5
Triton X-100	Sigma-Aldrich	Cat# T8787; CAS: 9036-19-5
Normal goat serum	Life Technologies	PCN5000
DMSO	Sigma-Aldrich	D8418
Paraformaldehyde 16% solution	Electron Microscopy Sciences	15710
EasyIndex	Lifecanvas technologies	EI-500-1.52
ProLongGlass	Invotrogen	P36981
ProLongGlass with NucBlue	Invitrogen	P36981
F-68	Fisher Scientific	Cat # 24-040-032
Fast Green	Sigma-Aldrich	F7252; CAS: 2353-45-9
Experimental models: Organisms/strains		
Mouse: SNS ^{Cre} ; Nav1.8Cre; Tg(Scn10a-cre)1Rkun	Kind gift from Rohini Kuner (Heidelberg University) ³⁶	MGI: 3042874
Mouse: <i>Piezo2</i> ^{fl/fl} ; B6(SJL)- <i>Piezo2</i> ^{tm2.2Apat/J}	Woo et al. ⁶¹	JAX: 027720
Mouse: <i>Phox2b</i> ^{Cre} ; B6(Cg)-Tg(Phox2b-cre)3Jke/J	Scott et al. ⁴⁴	JAX: 016223
Mouse: <i>Vil1</i> ^{Cre} ; B6.Cg-Tg(Vil1-cre)1000Gum/J	Madison et al. ⁵²	JAX: 021504
Mouse: <i>Hoxb8</i> ^{Cre} ; Tg(Hoxb8-cre)1403Uze	Witschi et al. ⁴⁵	MGI: 4881836
Mouse: <i>Piezo2</i> ^{Cre} ; <i>Piezo2</i> -EGFP-IRES-Cre; B6(SJL)- <i>Piezo2</i> ^{tm1.1(cre)Apat/J}	Woo et al. ⁶¹	JAX: 027719
Mouse: <i>Ai9</i> ^{fl/fl} ; Gt(ROSA)26Sor ^{tm9(CAG-tdTomato)Hze}	Madisen et al. ³⁹	JAX: 007909
Mouse: Rosa26 LSL H2b-mCherry; B6;a29S-Gt(ROSA)26Sor ^{tm1.1Ksvcl/J}	Peron et al. ⁴⁶	JAX: 023139
Software and algorithms		
ImageJ/FIJI	NIH	http://imagej.nih.gov/ij
GraphPad-PRISM	GraphPad	www.graphpad.com
Living Image	PerkinElmer	www.perkinelmer.com
MATLAB	MathWorks	https://www.mathworks.com
Other		
Gastric catheter for rat (for small intestine)	Instech	Cat# C30PU-RGA1439
Gastric catheter for rat (for colon)	Instech	Cat# C30PU-MGA1909
Vicryl suture 5-0	Fisher Scientific	50-118-0846
Ethilon nylon suture 7-0	Ethicon	1647G

(Continued on next page)

Continued

REAGENT or RESOURCE	SOURCE	IDENTIFIER
One-channel vascular buttons	Instech	Cat# VABM1B/22
Protective aluminum cap	Instech	Cat# VABM1C
Handling tool for magnetic-mouse-vascular-access button	Instech	Cat# VABMG
Disposable surgical drape	Jorgesen Laboratories, Inc	Cat# J0258
Spinal clamp	Narishige STS-A	STS-A
Disposable animal feeding needles	Fisher Scientific	01-208-89
Digital caliper	Jiavarry	kachi*steel452
Hamilton syringes	Hamilton	80408
Needles for Hamilton syringes (26s gauge, small Hub RN needle, 10 mm length, 4 point style, 30 C angle.	Hamilton	7804-04
Gavage canula	Fisher Scientific	NC1191503
Stickers for stomach and colon imaging (iSpacer 0.5 mm deep)	SunJin Lab	IS011
Stickers for small intestine imaging (iSpacer 0.25 mm deep)	SunJin Lab	IS203
Silicon isolators to image DRGs and nodose ganglia	Electron Microscopy Sciences	1224SK
Sylgard	Dow Chemical Company	04019862
1 mm glass beads	Sigma-Aldrich	Z250473
2 mm glass beads	Millipore-Sigma	K52444614 021
3 mm glass beads	Fisher Scientific	11-312A
4 mm glass beads	Fisher Scientific	11-312B

RESOURCE AVAILABILITY

Lead contact

Further information and requests for reagents and recourses should be directed to A. Patapoutian (ardem@scripps.edu).

Material availability

This study did not generate new unique reagents.

Data and code availability

- All data reported in this paper will be shared by the [lead contact](#) upon request.
- This paper does not report original code.
- Any additional information required to reanalyze the data reported in this paper is available from the [lead contact](#) upon request.

EXPERIMENTAL MODEL AND STUDY PARTICIPANT DETAILS

Mice

Mice were group housed in standard housing under 12–12 hr light–dark cycle and *ad libitum* access to water and standard chow unless noted otherwise. Room temperature was kept at around 22 °C and humidity between 30–80% (not controlled). Mice were kept on pelleted paper bedding and provided with nesting material and a polyvinyl chloride pipe for enrichment. Mice were routinely monitored for undesirable infection agents. *SNS^{Cre}* (a generous gift from Rohini Kuner), *Phox2b^{Cre}* (JAX: 016223), *Hoxb8^{Cre}* (MGI: 4884836), *Vil1^{Cre}* (JAX: 021504), *Ai9^{fl/fl}* (JAX: 007906), *LSL-H2b-mCherry* (JAX: 023139) and *Piezo2^{fl/fl}* (JAX: 027720) strains were maintained on C57BL/6J background, while *Piezo2^{Cre}* (JAX: 027719) on CD1. Age-matched littermates between 2 and 5 months were used for all *in vivo* experiments and histology analysis. All studies employed a mixture of male and female mice. All *in vivo* experiments were replicated with at least 3 mouse litters. Littermates were randomly assigned to experimental groups. All mice were drug naïve. The experimenter was blind to genotype when possible. *Piezo2^{Hoxb8}* and *Piezo2^{DRG}* have obvious proprioception deficits, so the experimenter was not blind to genotype for these groups. All the experimental protocols were approved by The Scripps Research Institute Institutional Animal Care and Use Committee and were in accordance with the guidelines from the NIH.

The following breeding scheme was used for the different Cre drivers: *Cre^{+/-};Piezo2^{fl/+} X Piezo2^{fl/fl}*.

Human subjects

Loss-of-function mutations in *PIEZO2* are rare. Twelve individuals with *PIEZO2* loss-of-function mutations were surveyed evaluated at the National Institutes of Health (NIH) under research protocol approved by the Institutional Review Boards of National Institute of Neurological Disorders and Stroke (NINDS, protocol 12-N-0095) between April 2015 and May 2020. Subjects were recruited from all over the world and their age ranged between 9 to 42 years at the time of the evaluation. Parents assisted with information gathering from their children. The subject identifier published in the current study corresponds to the same identifier previously used to investigate urinary function.²⁵ Written informed consent and/or assent (for minor individuals) was obtained from each participant in the study. Detailed history, clinical evaluation and testing have been previously described.^{22,25} PROMIS questionnaires, a clinical tool developed by the National Institute of Health,^{31,32} were used to capture general GI symptoms from the seven days prior to the survey. Only seven subjects completed these PROMIS questionnaires, and their mutations are described in [Table S1](#).

METHOD DETAILS

Recombinant viruses

CAG-iCre⁸³ and CAG-tdTomato plasmids were obtained from Addgene (51904 and 59462 respectively). PHP.s particles were produced in-house, titrated by qPCR and aliquoted into 5 μ l and flash-frozen for long-term storage. AAV9 viral preps were acquired from Addgene (51502-AAV9).

Surgeries

Mice were anaesthetized with isoflurane (4% for induction and 1.5%–2% for maintenance) and kept on a heating pad during the procedure. Ophthalmic ointment was applied to the eyes. Skin at the surgical area was shaved, hair removed and sterilized using ethanol and iodine. After surgery, mice were transferred to a warm cage to recover, subcutaneous injection of flunixin was given for 2 days and topical antibiotic ointment was used for post-operative care.

Intrathecal injections

Mice were injected at 6–7 weeks of age. After pre-surgical care, a 1.5 cm incision was made starting at the level of femur-hip connection extending towards through the midline of the back towards the head. 7 μ l of viral particles in PBS with 0.001% F-68 (24-040-032) and 0.01% FastGreen (F7252) were injected into the L5-L6 intervertebral space using a 25 μ l Hamilton syringe. The skin was closed, and post-surgical care was provided.

For whole-mount analysis, *Piezo2*^{Cre} mice were injected with AAV9-*flex-GFP* (1 \times 10¹³ VG per ml, 7 μ l), tissues were collected at least four weeks after infection. For GI transit assessment, *Piezo2*^{fl/fl}; *Ai9*^{fl/+} mice were injected with PHP.s-*iCre* or PHP.s-CAG-*tdTomato* (1 \times 10¹³ VG per ml, 7 μ l) allowed to recover for a minimum of 4 weeks before behavior tests. Consistent with previous studies on the role of *Piezo2* in proprioception,²¹ we observed that 8 out of 11 *Piezo2*^{D^{RG}} mice lacked proprioception in their hindlimbs. All 11 mice were included in the analysis.

Intra-intestinal catheter implantation

For this procedure, mice were at least 8 weeks of age. Mice were anesthetized with isoflurane, pre-surgical care, and aseptic preparation was taken. An abdominal midline incision through the skin and muscle was performed, extending from the xyphoid process about 1.5 cm caudally. A second 1-cm incision was made between the scapulae for catheter externalization. The skin was separated from the subcutaneous tissue to form a subcutaneous tunnel between the neck and abdomen incisions to facilitate catheter placement. A small puncture hole was made on the left side of the abdominal wall to insert the catheter (C30PU-RGA1439). The stomach was externalized, and a purse-string stitch was made at the edge of the fundus and corpus on the side of the greater curvature of the stomach using 7-0 non-absorbable Ethilon suture (1647G). Then, a puncture was made at the center of the purse-string stitch to insert and advance the catheter 2.5 cm distal to the pyloric sphincter (intraduodenal catheter). While for the intracecal catheter, a puncture was made on the larger curvature of the cecum to insert and advance the catheter 1 cm, at the edge of the colon and cecal junction. The cecal catheter was secured to the tissue with sterile surgical drape (J0258). The catheter was secured by the purse-string suture at the catheter collar. The abdominal cavity was irrigated with sterile saline and the abdominal wall was closed. The other end of the catheter was attached to a vascular button (VABM1B/22), sutured to the muscle layer at the interscapular site and the incision was closed. The vascular button was closed with a protective aluminum cap (VABM1C) to prevent catheter obstruction. Mice were provided with subcutaneous flunixin and moistened chow for 2 days after surgery. Mice were allowed to recover for 7–10 days prior to behavioral experiments.

Celiac ganglionectomy

For this procedure, mice were at least 8 weeks of age. Mice were anesthetized with isoflurane, pre-surgical care, and aseptic preparation was taken. A midline abdominal incision was made, starting from xyphoid process, extending about 2–3 cm caudally. The small intestine and colon were externalized and kept on a moist, sterilized gauze. The celiac and superior mesenteric arteries were identified to locate the Celiac Superior Complex, care was taken to localize the three fused ganglia and fully remove them by carefully separating them from the arteries and excising them from the body. The abdominal cavity was irrigated with sterile saline

before returning the small and large intestines to their original position. The abdominal wall and skin were then closed. Post-surgery mice received subcutaneous flunixin for two days and allowed to recover for 10 days prior to behavioral experiments.

Treatments

Oral gavage

Mice were gavaged with volumes ranging from 100–500 μ l of carmine red or GastrSense-750. All gavages were performed between 8:00–9:00 am local time. After carmine-red gavage, mice were monitored every 15 min for presence of the first red fecal pellet.

Intraduodenal and intracecal infusions

Mice were tested 7–10 days after catheter implantation. Infusions were performed between 8:00–8:30 am local time. All mice were fed *ad libitum* before experiments and solutions were infused via intraduodenal or intracecal catheters using a handling tool for the vascular button (VABMG). 100 μ l and 50 μ l of carmine red was infused through the intraduodenal and intracecal catheter respectively.

Histology

Whole-mount preparation of GI tissues, nodose ganglia and DRGs

Mice were terminally anaesthetized with isoflurane, euthanized by cervical dislocation, and intracardially perfused with ice-cold PBS and ice-cold 4% PFA (1224SK). Nodose and DRGs were extracted and post-fixed in 4% PFA for 1 hr before being washed with PBS. Nodose and DRGs were mounted onto silicone isolators (70345–39) and mounted using EasyIndex (ei-500–1.52).

Gastrointestinal tissues were extracted and washed with PBS to remove all intestinal contents. Gut tissues were opened and pinned onto sylgard-coated dishes. Gut samples were post-fixed in 4% PFA at 4 °C overnight before being washed in PBS. The mucosa was carefully dissected from the muscularis. Tissues were blocked with gentle agitation for 2 hrs at room temperature in (5% normal goat serum, 20% DMSO, 75% PBST (PBS with 0.3% TritonX-100)). Primary antibodies were added to the blocking buffer at appropriate concentrations and incubated for two days at 4 °C. Tissues were washed 3 times in PBST and then incubated in blocking buffer with secondary antibodies overnight at 4 °C. Samples were again washed 3 times in PBST and mounted with ProLongGlass with NucBlue.

Behavioral and physiological assays

Whole gastrointestinal transit

Mice fed *ad libitum* were gavaged with 300 μ l of carmine red solution (6% w/v carmine red in 0.5% 400 cP methylcellulose) and placed individually into clean cages with access to chow pellets and water. All gavages were performed between 8:00–9:00 am local time. Feces were monitored every 15 minutes until the first colored fecal pellet appeared. The time from gavage to the initial appearance of the dye in the feces was recorded as the whole GI transit time. Mice used to test whole GI transit were also used for colon motility experiments, and stool collection analysis. The experiments were conducted with a minimum of seven days in between each test.

For experiments comparing GI transit between fasted and fed conditions, mice were fasted 12 hrs prior to the gavage with free access to water. Mice were gavaged with 500 μ l of carmine red solution and placed individually into clean cages with access to water but no access to food. Seven days later, same mice were fed *ad libitum*, gavaged with 500 μ l of carmine red and placed individually into clean cages with access to chow pellets and water. The time from gavage to the first colored fecal pellet was recorded as the GI transit time.

For the experiment from Figure S3G, an automatic stool detection was employed as described previously.⁴⁷ Mice were located in custom chambers where fecal pellets were recorded, and offline analysis was used for image processing.

Gastric emptying evaluation

A day prior to the experiment, all hair was removed from the abdominal area. Mice fed *ad libitum* were gavaged with 100 μ l of GastroSense-750 dissolved in PBS (NEV11121) as per manufacturer instructions. Mice were gavaged between 8:00–8:30 am local time and relocated into their cage with access to water and food *ad libitum*. Mice were anesthetized with isoflurane at 30, 45 or 90 min after gavage. The full GI tract was harvested and immediately imaged using the IVIS-Lumina S5 system. For analysis, Living Image Software (64-bit) version 4.7.4 (Perkin Elmer) was used to draw ROIs delineating the stomach and the rest of the GI tract. The radiant efficiency from the stomach was compared to the rest of the small and large intestines and expressed as percentage of the total gut signal.

Small and large intestinal transit

Mice fed *ad libitum* were infused with 100 μ l or 50 μ l of carmine red into intraduodenal or intracecal catheter respectively. Infusions were performed between 8:00–8:30 am local time. Mice were placed individually into clean cages with access to chow pellets and water. After infusions, mice were monitored every 15 min for the presence of the first red fecal pellet.

Stool collection and analysis

Mice were located in acrylic chambers with mesh bottom (Ugo Basile), allowing feces to fall through immediately after excretion. Collection times were kept consistent to prevent circadian cycle influences. Fresh stools were collected only for one hour, placed in 1.5 ml Eppendorf tubes and capped to prevent water loss. After the one-hour collection period, colon motility was tested. Collected

stool samples were weighted, and oven-dried at 120 °C overnight. Following drying, samples were weighted again, and the water content was determined. To obtain the “Dried-stool weight”, single feces were weighted, and their weights were averaged to obtain the mean weight of individual stools per mouse.

To assess dimensions of fresh feces, stools were collected immediately after evacuation for one hour, and their width and length were measured using a digital caliper.

Colon motility assay

Mice were kept in acrylic chambers with mesh bottom (Ugo Basile) one hour before starting the bead expulsion test. This time was used to ensure that the distal colon lacked fecal pellets that could interfere with the entrance of the glass bead. Mice fed *ad libitum* were anesthetized with isoflurane, then a glass bead was inserted 2 cm into the colon with a gavage cannula. The time for the bead release was recorded, every experiment was performed twice with 3-7 days in between trials and results were averaged. Experiments times were kept consistent to prevent circadian cycle influences. This experiment was performed twice per mouse to obtain an average expulsion time. Only mice that recovered from anesthesia within 60 sec were included in the quantification. For the 4-mm bead experiment, mice weighted at least 24 gr.

Food and water consumption

Food and water intake was evaluated using Comprehensive Lab Animal Monitoring System (CLAMS, Columbus Instruments). This system continuously tracks food and water intake. Mice were kept under 12–12 hr light–dark cycle and *ad libitum* access to water and standard chow. Mice were individually housed and allowed to adapt to the environmental chamber for 3 days before data collection. The data were gathered over 7 days and averaged.

Imaging

In vivo epifluorescence calcium imaging of sacral ganglia

Mice were placed on a mesh floor for 1hr to defecate freely. Scruffing and lower abdomen massage was applied before being anesthetized with isoflurane to facilitate bowel emptying and transferred to a custom platform. Lower limbs and tail were restrained on this platform to free the anal area and hand warmers were used to maintain body temperature. To image the sacral ganglia, the dorsal aspect of the sacrum was surgically exposed after partial removal of the gluteus medius and stabilized with a spinal clamp (Narishige STS-A). Using a dental drill, the dorsal root ganglia in the pelvis was exposed by removing a portion of the auricular surface along with the posterior articular process of the 6th vertebra and the posterior articular process (S2); hemostatic dental sponges (Pfizer Gel Foam) were applied as needed to control bleeding. Following surgery, the animal was transferred to the stage of a custom tilting light microscope (Thorlabs Cerna) equipped with a 4X, 0.28 NA air objective (Olympus). GCaMP6f fluorescence images were acquired with a CMOS camera (PCO Panda 4.2) using a standard green fluorescent protein (GFP) filter cube in 40 sec epochs at a sampling rate of 5hz. After 40 sec, each epoch was stopped to prepare for the following stimulus. This pause is denoted by white lines on heatmaps and blank spaces in the representative traces.

Mechanical stimulation during in vivo calcium imaging of sacral ganglia

The external mechanical stimuli applied to the animal skin (around the anus) included a series of pressurized air puffs from a Picospritzer (25 psi, for 0.2, 1, 3 and 5 sec), manual gentle brushing with a dental acrylic brush and a perineal skin pinch with forceps (Students, F.S.T.). Internal mechanical stimuli were applied by placing a lubricated gavage tip 4 cm into the rectum and snaking the tip of a dental-soft brush flosser attached to a wire through it. The brush was then pushed out of the gavage tip 2 cm for a total colon depth of 6 cm. Lubricated custom balloons, also built on the backbone of the gavage tip (01-208-89), were placed 6 cm into the colon of the mouse and inflated until an internal pressure of 100 mmHg, 150 mmHg and 200 mmHg.

In vivo calcium imaging analysis

Analysis of calcium imaging was performed as previously described.⁶⁴ Regions of interest (ROI) outlining responding cells were drawn in FIJI/ImageJ and relative change of GCaMP6f fluorescence was calculated as percent $\Delta F/F$. Responder cells were chosen if they presented a calcium increase after a given stimulus, the activation threshold was set as $\Delta F/F > 5\%$. Rare cells with spontaneous activity during baseline were excluded from the analysis, as well as cells that remained active for the rest of the experiment after a stimulus (range: 10-50 neurons per mouse). All imaging videos were corrected for movement with Linear SIFT in ImageJ. Contaminant signal e.g., from out-of-focus tissue and neighboring cells was removed by subtracting the fluorescence of a donut-shaped area surrounding each ROI using a custom MATLAB script. Overlapping ROIs and rare spontaneously active cells were excluded from the analysis. Imaging episodes lasted 40 sec (200 frames) and consisted of the baseline recording (8 seconds), and the application and response to the stimulus. Imaging episodes were recorded in rapid series and stopped during the time that took to prepare the following stimulus. Then, the seven episodes from these experiments were concatenated so the activity of each neuron could be tracked across all episodes, where each row represents the activity of the same neuron over time and illustrated as traces or activity heatmaps as $\Delta F/F$. Cells were manually sorted on heatmaps based on their stimulus response: Each cell's response was assigned as responding to external only (puff, brush, pinch), internal only (internal bush, balloon inflate), or both. Cells that responded to internal and external stimulation were excluded from the analysis, as these neurons were likely recruited by anus stimulation as a consequence of movement at this physical boundary when stimulation was applied. The cells that responded to just external stimuli were grouped by brush and pinch responding or pinch only responding neurons and further displayed in descending $\Delta F/F$ order. To generate spatial maps of activity (Figures S6I and S6J) that represent active pixels during external and internal epochs, we calculated the standard deviation for each pixel over a stimulation episode in ImageJ/FIJI as described previously.⁶⁹

To quantify the percentage of responder cells, all cells were binarized as responders or not for the histograms. Then, all cells that responded to a given stimuli were pooled and considered as 100% of responder neurons. The neurons that responded after brush (insertion and removal) and balloon (insertion and inflation) into the colon stimulation were classified as “Internal” responders. “External noxious” corresponds to the neuronal responses detected after pinching the anal skin with forceps. “External gentle” includes the responses obtained after the air puff and/or the gentle brush on the anal skin, if these cells additionally responded to pinch, they were included in this category. The $\Delta F/F$ for external stimulation (“outside noxious” and “outside gentle”) ranged from 5%-60%, whereas the responses after colonic stimulation usually were between 5%-30%.

Moreover, two independent analyses were performed: 1) a blinded analysis in which a researcher, unaware of mice genotype, received processed intensity data and evaluated the percentage of responder cells, 2) an unblinded analysis was conducted by the researcher who performed the experiments to determine the responder neurons. Next, the results from both approaches were compared, and the proportion of responding cells remained unchanged in every category.

Confocal microscopy

Mounted nodose and DRGs samples were imaged on either a Nikon C2 or Nikon AX scope confocal microscope using a 20x/0.75 NA objective or a 16x/0.80W respectively. Images were acquired using NIS-Elements.

Quantification of nerve density in stomach, small intestine and colon

Regions of $80\ \mu\text{m} \times 80\ \mu\text{m} \times 20\ \mu\text{m}$ (x,y,z) were randomly selected and maximally projected over z using customized ImageJ scripts in the whole stacks of stomach, small intestine and colon from *Piezo2^{Cre/+}* mice that were intrathecally injected with AAV9-*flex-GFP*. Areas containing nerve fibers were automatically segmented using auto thresholding in ImageJ. IGVE were quantified manually as LabeledGanglia/TotalArea. Nerve density was calculated as NerveArea/TotalArea. Only views containing nerve signals were retained for quantification. We quantified 6 biological replicates.

QUANTIFICATION AND STATISTICAL ANALYSIS

Unless otherwise specified, data was expressed as means \pm standard error of the mean (SEM) in figures and text. Normality tests were used, and parametric or non-parametric tests were performed as appropriate. Unpaired two-tailed t tests or Mann-Whitney test were performed. Two-way ANOVA was used to make comparisons across more than two groups. Statistical analysis was performed using GraphPad Prism 9.4 for Windows, GraphPad Software, San Diego, California, USA. Test, statistics, significance levels, and sample sizes for each experiment are listed on the figure legends. No statistical test was used to pre-determine sample size, instead sample size was determined by animal availability and previous studies in the field.

Supplemental figures

Loss-of-function mutations of subjects with PIEZO2 syndrome.

Subject identifier (same as in ²)	Sex	Mutation	Mutation type	Reference
2	F	c. 5053C>T, (p.R1685*) c. 5053C>T, (p.R1685*)	Premature stop mutation before the pore.	22, 25, 30
3	M	1. c.7440+1 G>A, IVS47+1 G>A 20 c.7730C>A, p.S2577*	1. Splice variant resulting in premature stop before the pore. 2. Premature stop mutation before the pore.	25, 30
4	F	1. c.1278C>G, (p.Y426*) 2. c.6005_6006insC, p.H2002fs	1. Premature stop mutation before the pore. 2. Insertion resulting in a frameshift and a premature stop before the pore.	25, 30
6	M	c.1384C>T, (p.R462*) c.1384C>T, (p.R462*)	Premature stop mutation before the pore.	25, 30
8	M	c.2004delG, (p.G668*) c.2004delG, (p.G668*)	Premature stop mutation before the pore.	25, 30
11	F	c.3241C>T; (p.Arg1051*)	Premature stop mutation before the pore.	25, 30
12	F	c.3241C>T; (p.Arg1051*)	Premature stop mutation before the pore.	25, 30

The GI PROMIS questionnaires were completed by four females and three males. Loss-of-function mutations are specified per subject, as well as the reference in which the mutation was characterized.

Figure S1. Loss-of-function mutations of subjects with PIEZO2 syndrome, related to Figure 1

The GI PROMIS questionnaires were completed by four females and three males. Loss-of-function mutations are specified per subject, as well as the reference in which the mutation was characterized.

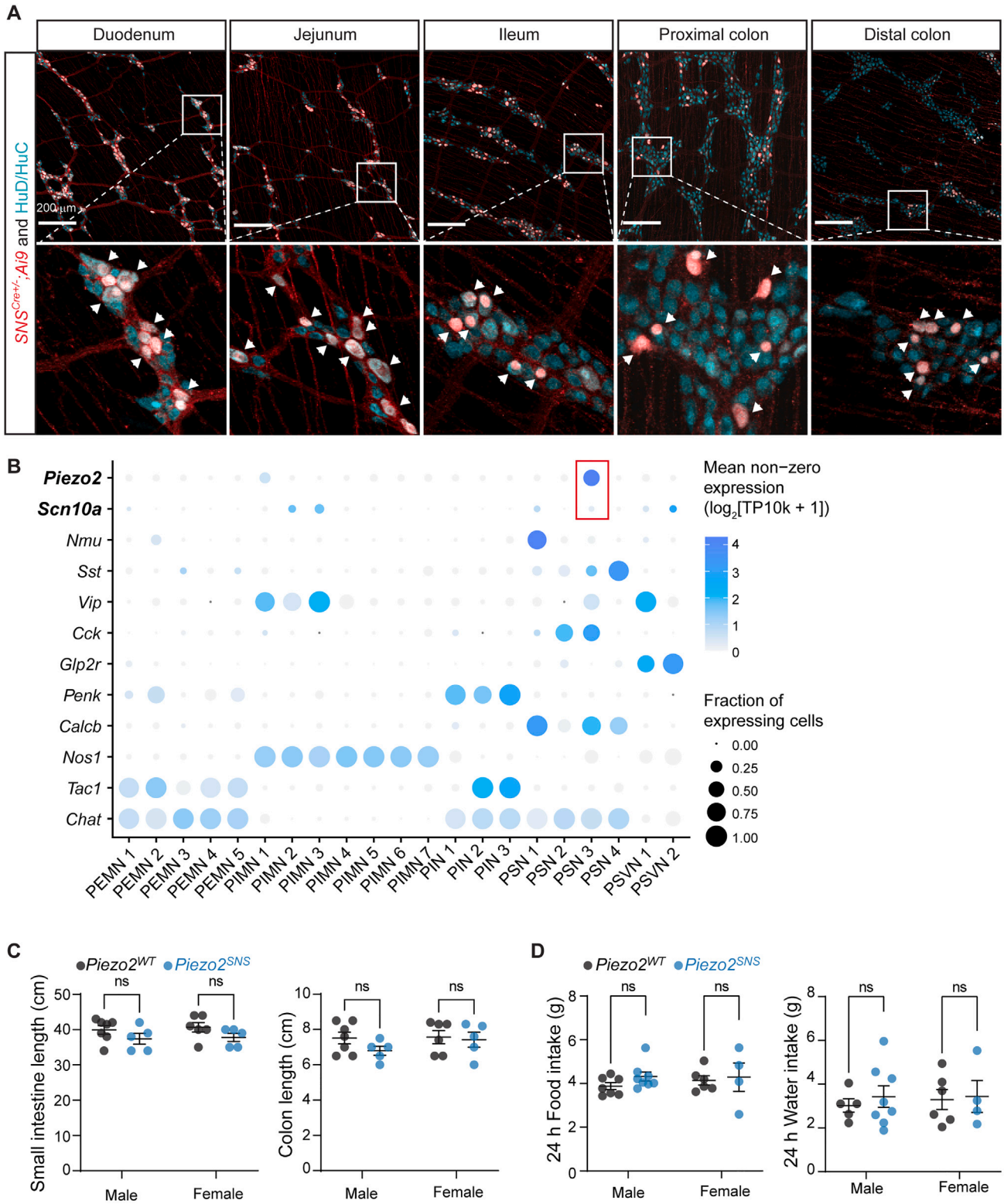


Figure S2. Characterization and validation of *SNS^{Cre+/-};Ai9^{fl/+}* mice in enteric neurons along the GI tract, related to Figure 2

(A) Representative images from whole-mount preparations of small and large intestine of *SNS^{Cre+/-};Ai9^{fl/+}*. Enteric neuron nuclei are labeled with HuD/HuC and represented in cyan. SNS positive fibers are represented in red. Scale bar indicates 200 μ m. Arrowheads point to enteric neurons labeled in the *SNS^{Cre+/-};Ai9^{fl/+}* mouse.

(legend continued on next page)

(B) Fraction of expressing cells (dot size) and mean expression levels of genes (rows) in enteric neurons. Red inset shows the comparison between *Piezo2* and *Scn10a* transcript from enteric neurons. Data mined from Drokhyansky et al.¹⁸

(C) Comparison of small intestine (left) and colon (right) length from *Piezo2*^{WT} (n = 12) and *Piezo2*^{SNS} (n = 10) mice. Two-way ANOVA for small intestine: $p_{\text{genotype}} = 0.0568$. Two-way ANOVA for colon: $p_{\text{genotype}} = 0.2400$; ns, not statistically significant.

(D) Comparison of food (left) and water (right) intake during 24 h (7-day average from CLAMs data) from *Piezo2*^{WT} (n = 13) and *Piezo2*^{SNS} (n = 12) mice. Two-way ANOVA for food intake: $p_{\text{genotype}} = 0.3147$. Two-way ANOVA for water intake: $p_{\text{genotype}} = 0.6060$; ns, not statistically significant. Data in (C) and (D) are represented as mean \pm SEM.

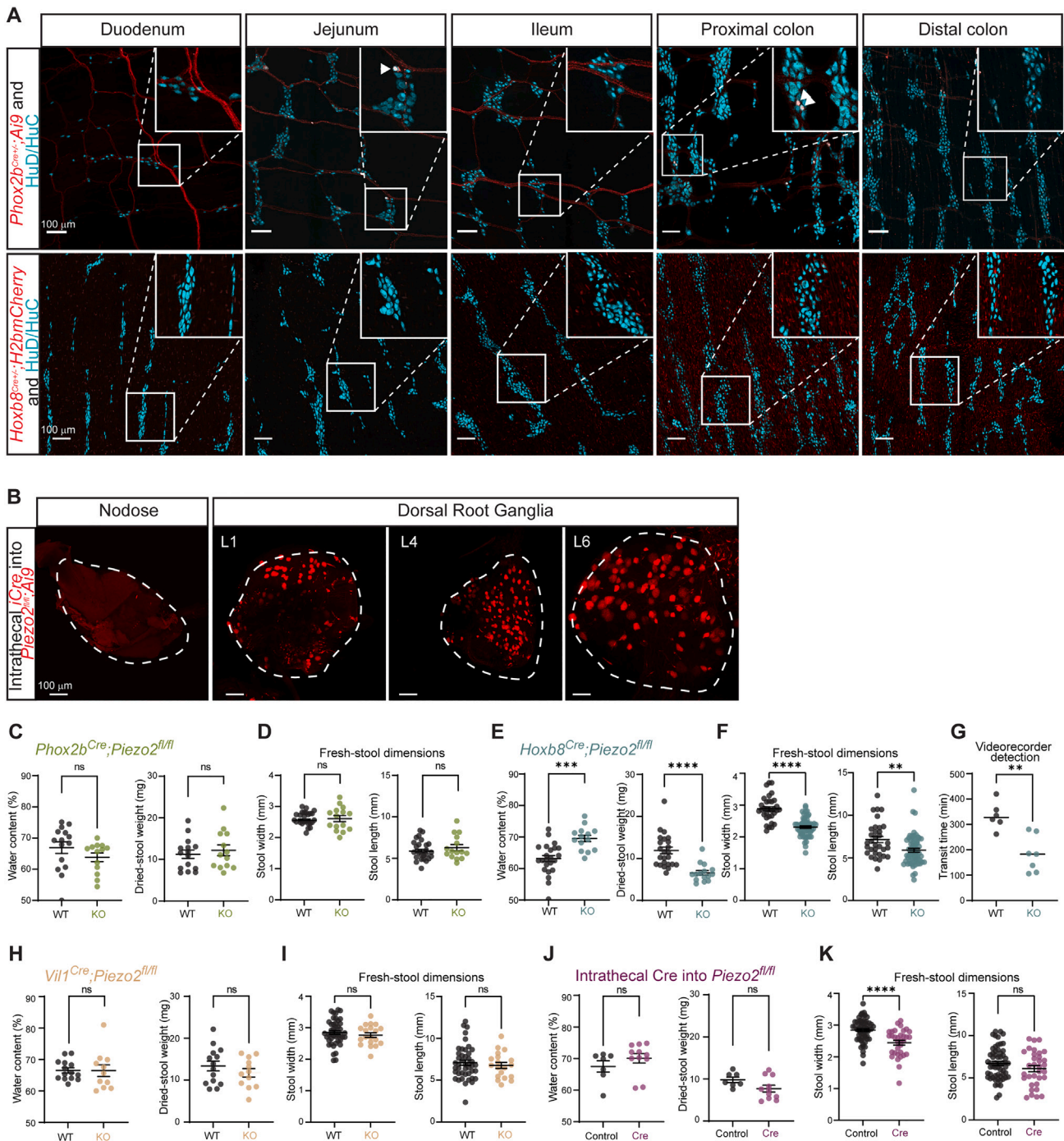


Figure S3. Validation of *Phox2b*^{Cre/+};*Ai9*^{fl/+} and *Hoxb8*^{Cre/+};*H2bmCherry*^{+/-} mice, related to Figure 3

(A) Representative images of whole-mount preparation of small and large intestine from *Phox2b*^{Cre/+};*Ai9*^{fl/+} mice (top) and *Hoxb8*^{Cre/+};*H2bmCherry*^{+/-} (bottom). Enteric neuron nuclei are labeled with HuD/HuC and represented in cyan. *Phox2b* positive fibers and *Hoxb8* positive nuclei are represented in red. Scale bars indicate 100 μ m.

(B) Representative images of nodose ganglia and DRGs 4 weeks after intrathecal injection into *Piezo2*^{fl/fl};*Ai9*^{fl/+} mice with PHP.s-*iCre* viral particles. Scale bars indicate 100 μ m.

(C) Quantification of fecal water content (left) and individual dried-stool weight (right) from *Phox2b*^{Cre/+};*Piezo2*^{fl/fl} (WT; n = 15) and *Phox2b*^{Cre/+};*Piezo2*^{fl/fl} (KO; n = 13) mice. Unpaired two-tailed t test for water content: p = 0.2011. Unpaired two-tailed t test for stool weight: p = 0.5591; ns, not statistically significant.

(legend continued on next page)

(D) Width (left) and length (right) quantification of fresh stools collected during 1 h from *Phox2b*^{Cre-/-};*Piezo2*^{fl/fl} (WT; n = 39 stools, from 12 mice) and *Phox2b*^{Cre+/-};*Piezo2*^{fl/fl} mice (KO; n = 15 stools, from 6 mice). Unpaired two-tailed t test for stool width: p = 0.5610. Unpaired two-tailed t test for stool length: p = 0.3103; ns, not statistically significant.

(E) Quantification of stool water content (left) from *Hoxb8*^{Cre-/-};*Piezo2*^{fl/fl} (WT; n = 25) and *Hoxb8*^{Cre+/-};*Piezo2*^{fl/fl} (KO; n = 14) mice (unpaired two-tailed t test: ***p = 0.0001, t(37) = 4.253). Quantification of dried-stool weight (right) from *Hoxb8*^{Cre-/-};*Piezo2*^{fl/fl} (WT; n = 25) and *Hoxb8*^{Cre+/-};*Piezo2*^{fl/fl} (KO; n = 15) mice (unpaired two-tailed t test: ****p < 0.0001, t(38) = 4.857).

(F) Width (left) and length (right) quantification of fresh stools collected during 1 h from *Hoxb8*^{Cre-/-};*Piezo2*^{fl/fl} (WT; n = 33 stools, from 8 mice) and *Hoxb8*^{Cre+/-};*Piezo2*^{fl/fl} mice (KO; n = 61 stools, from 7 mice). Unpaired two-tailed t test: ****p < 0.0001, t(92) = 8.034) and **p = 0.0026, t(92) = 3.102).

(G) Quantification of GI transit time after carmine red gavage from *Hoxb8*^{Cre-/-};*Piezo2*^{fl/fl} (WT; n = 6) and *Hoxb8*^{Cre+/-};*Piezo2*^{fl/fl} (KO; n = 7) mice (Mann-Whitney test: **p = 0.0047, two-tailed, U = 2) detected via videorecorder method.⁴⁷

(H) Quantification of fecal water content (left) and dried-stool weight (right) from *Vil1*^{Cre-/-};*Piezo2*^{fl/fl} (WT; n = 14) and *Vil1*^{Cre+/-};*Piezo2*^{fl/fl} (KO; n = 11) mice. Unpaired two-tailed t test for water content: p = 0.9642. Unpaired two-tailed t test for stool weight: p = 0.3145; ns, not statistically significant.

(I) Width (left) and length (right) quantification of fresh stools collected during 1 h from *Vil1*^{Cre-/-};*Piezo2*^{fl/fl} (WT; n = 44 stools, from 7 mice) and *Vil1*^{Cre+/-};*Piezo2*^{fl/fl} mice (KO; n = 19 stools, from 3 mice). Unpaired two-tailed t test for stool width: p = 0.4162. Unpaired two-tailed t test for stool length: p = 0.5438; ns, not statistically significant.

(J) Quantification of stool water content (left) and dried-stool weight (right) from Control (n = 7) and *iCre* (n = 11) mice. Unpaired two-tailed t test for water content: p = 0.2912. Unpaired two-tailed t test for stool weight: p = 0.0835; ns, not statistically significant.

(K) Width (left) and length (right) quantification of fresh stools collected during 1 h from *Piezo2*^{fl/fl} injected with PHP.s-*tdTomato* (Control; n = 59 stools, from 8 mice) and *Piezo2*^{fl/fl} injected with PHP.s-*iCre* (Cre; n = 33 stools, from 6 mice). Unpaired two-tailed t test for stool width: ****p < 0.0001, t(90) = 4.762). Unpaired two-tailed t test for stool length: p = 0.1532; ns, not statistically significant.

Data in (C)–(F) and (H)–(K) are represented as mean ± SEM.

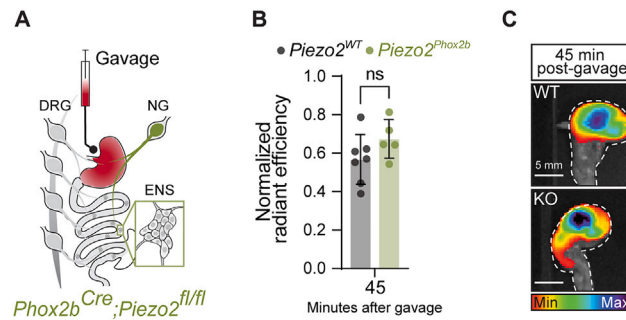


Figure S4. Gastric emptying is not affected by *Piezo2* deletion in nodose neurons, related to Figure 4

(A) Illustration of the strategy to test gastric emptying in mice.

(B) Quantification of percentage of gastric emptying observed 45 min after gavaging GastroSense-750 in *Phox2b*^{Cre-/-};*Piezo2*^{fl/fl} (*Piezo2*^{WT}; n = 7) and *Phox2b*^{Cre+/-};*Piezo2*^{fl/fl} (*Piezo2*^{Phox2b}; n = 5) mice (Mann-Whitney test: p = 0.1061 two-tailed, U = 7; ns, not statistically significant). Data represented as mean ± SD.

(C) Representative images of dye emptying 45 min after stomach gavage in *Phox2b*^{Cre-/-};*Piezo2*^{fl/fl} (WT) and *Phox2b*^{Cre+/-};*Piezo2*^{fl/fl} (KO) mice. Scale bars represents 5 mm, and pseudocolor scale indicates the dye intensity (bottom).

Labeling after AAV9-Flex-GFP intrathecal injection into *Piezo2^{Cre+/+}* mice

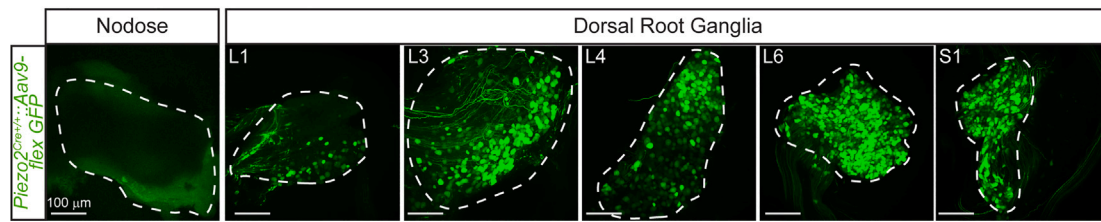


Figure S5. DRG validation after intrathecal injection of AAV9-Flex-GFP particles into *Piezo2^{Cre+/+}* mice, related to Figure 5
Whole-mount representative images of nodose and DRGs 4 weeks after intrathecal injection of AAV9-Flex-GFP particles into *Piezo2^{Cre+/+};Ai9^{fl/+}* mice. All scale bars represent 100 μm .

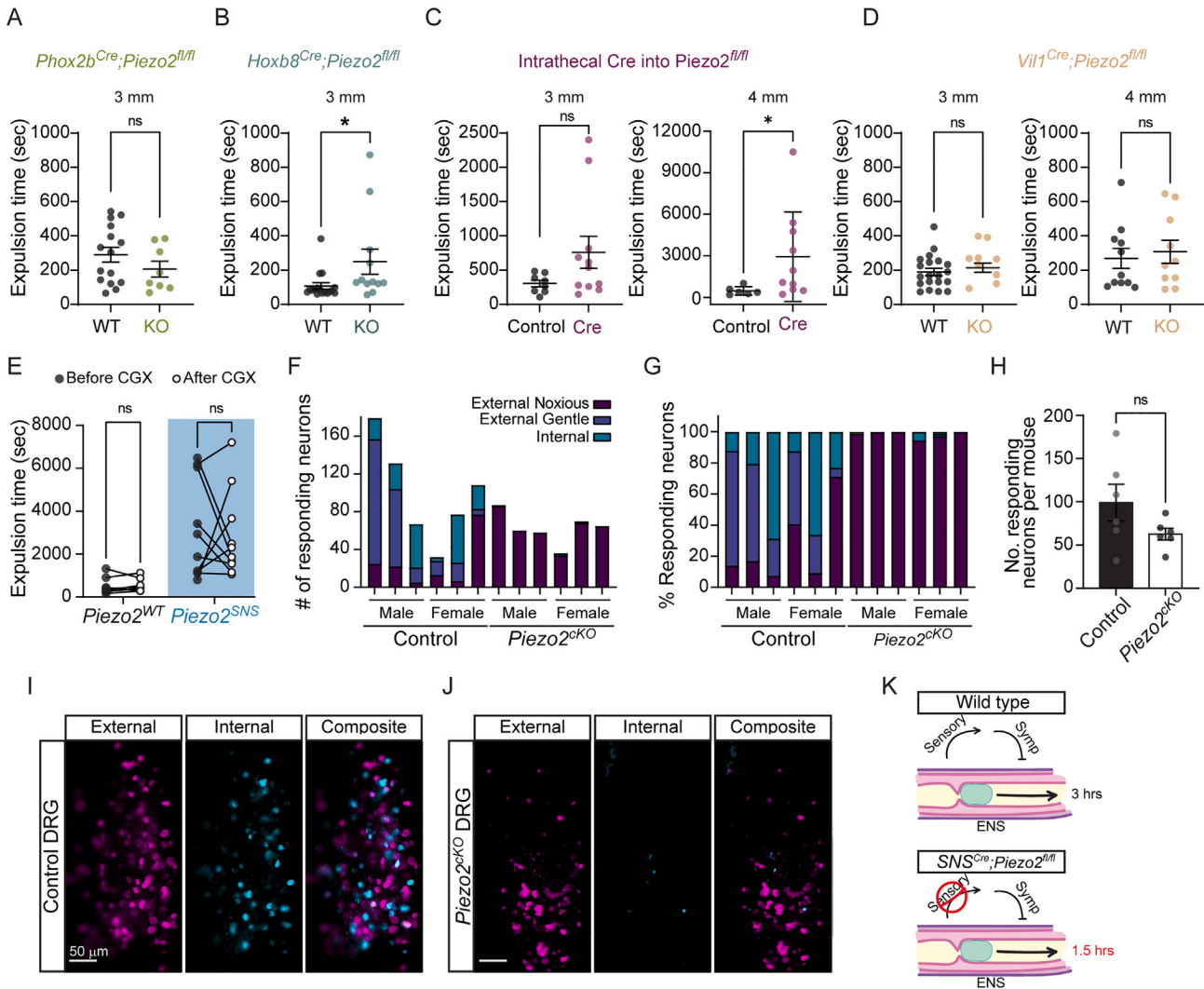


Figure S6. Colon motility responses from *Phox2b*^{Cre+/-};*Piezo2*^{fl/fl}, *Hoxb8*^{Cre+/-};*Piezo2*^{fl/fl}, *Vil1*^{Cre+/-};*Piezo2*^{fl/fl}, and *Piezo2*^{fl/fl};*Ai9*^{fl/+} mice intrathecally injected with PHP.s-iCre particles, related to Figure 6

(A) Expulsion time after bead insertion into colon of *Phox2b*^{Cre+/-};*Piezo2*^{fl/fl} (WT; n = 15) and *Phox2b*^{Cre+/-};*Piezo2*^{fl/fl} (KO; n = 8) mice, 3-mm glass beads (unpaired two-tailed t test: p = 0.2401, t(21) = 1.209; ns, not statistically significant).

(B) Expulsion time after using 3 mm beads in *Hoxb8*^{Cre+/-};*Piezo2*^{fl/fl} (WT; n = 17) and *Hoxb8*^{Cre+/-};*Piezo2*^{fl/fl} (KO; n = 12) (Mann-Whitney test: *p = 0.0208 two-tailed, U = 50).

(C) Colon motility test in *Piezo2*^{fl/fl}::PHP.s-tdTomato (Control; n = 8) and *Piezo2*^{fl/fl}::PHP.s-iCre (Cre; n = 11) mice using 3 mm beads (Mann-Whitney test: p = 0.1288 two-tailed, U = 25; ns, not statistically significant) (left). Expulsion time after 4-mm bead introduction into the rectum of Control (n = 10) and Cre (n = 6) mice (Mann-Whitney test: *p = 0.0312 two-tailed, U = 10) (right).

(D) Colon motility test in *Vil1*^{Cre+/-};*Piezo2*^{fl/fl} (WT; n = 20) and *Vil1*^{Cre+/-};*Piezo2*^{fl/fl} (KO; n = 14) using 3 mm bead (unpaired two-tailed t test: p = 0.4737, t(32) = 0.7250; ns, not statistically significant) (left). Expulsion time after using 4-mm beads in *Vil1*^{Cre+/-};*Piezo2*^{fl/fl} (WT; n = 11) and *Vil1*^{Cre+/-};*Piezo2*^{fl/fl} (KO; n = 10) (unpaired two-tailed t test: p = 0.6622, t(19) = 0.4438; ns, not statistically significant) (right).

(E) Colon motility test using 4-mm beads in *SNS*^{Cre+/-};*Piezo2*^{fl/fl} (*Piezo2*^{WT}, n = 7) and *SNS*^{Cre+/-};*Piezo2*^{fl/fl} (*Piezo2*^{SNS}, n = 10) mice before and after CGX (two-way ANOVA: p_{before/after CGX} = 0.8057, F(1,15) = 0.06268; **p_{genotype} = 0.0019, F(1,15) = 14.16; Sidak's p_{adjusted-pWT} = 0.9992; p_{KO} = 0.8916; ns, not statistically significant).

(F) Classification of number of responding neurons per female and male mice across genotypes (Control: *Hoxb8*^{Cre+/-};*GCaMP6f*^{+/+} and *Piezo2*^{CKO}: *Hoxb8*^{Cre+/-};*Piezo2*^{fl/fl}; *GCaMP6f*^{+/+} mice).

(G) Proportion of responding neurons per female and male mice across genotypes from (F).

(H) Comparison of total of responding neurons per genotype (unpaired two-tailed t test: p = 0.1340, t(10) = 1.631; ns, not statistically significant). Data represented as mean ± SEM.

(legend continued on next page)

(I) Spatial activity map of one representative DRG from a control mouse. Images display standard deviations, which indicate the pixels with the most change in fluorescence during internal and external stimuli. All the images collected during external stimuli (air puff, brush, and pinch on skin) and internal stimuli (brush insertion and retraction from colon, balloon insertion and balloon inflation) from one Control mouse ($Hoxb8^{Cre+/-};GCaMP6f^{+/+}$) were pooled to build the spatial activity map. Scale bar represents 50 μm .

(J) Representative images of standard deviations from all images corresponding to external stimuli and all internal stimuli from one $Piezo2^{cKO}$ ($Hoxb8^{Cre+/-};Piezo2^{fl/fl};GCaMP6f^{+/+}$) mouse. Scale bar represents 50 μm .

(K) Hypothetical model for controlling baseline GI transit. As the intestine fills with contents, enteric neurons initiate peristalsis to move contents along the gut.⁸² Extrinsic sensory neurons detect mechanical cues from the gut in a Piezo2-dependent manner, to slow down GI transit via sympathetic motor actions. Conversely, mice lacking Piezo2 from DRG neurons fail to communicate with the sympathetic branch, resulting in accelerated gut motility.

Chapter 4

Functional characterization of molecules and cells that shape somatosensory responses

* This chapter includes two publications presented in the form it was published in the journal Pain and Neuron respectively with the following citations

Part 1

von Buchholtz, Lars J., **Ruby M. Lam**, Joshua J. Emrick, Alexander T. Chesler, and Nicholas JP Ryba. "Assigning transcriptomic class in the trigeminal ganglion using multiplex *in situ* hybridization and machine learning." *Pain* 161, no. 9 (2020): 2212.

Part 2

von Buchholtz, Lars J., Nima Ghitani, **Ruby M. Lam**, Julia A. Licholai, Alexander T. Chesler, and Nicholas JP Ryba. "Decoding cellular mechanisms for mechanosensory discrimination." *Neuron* 109, no. 2 (2021): 285-298.

Introduction

I opened this thesis with a chapter devoted to the classical organization schemes used throughout history to classify sensory neurons. As described in that chapter, organizational schemes revealed a significant amount of heterogeneity, overlap and confusion. In retrospect, it may be hubris that led some scientists to believe that there is a unifying logic to the organization at all. However, the experimentally verified existence of genetically targeted cell subpopulations that correspond to specific functional roles like *Nppb* cells for itch³ and *trpm8* for cold^{4,5}, suggests the existence of a labeled line organization where genetically defined subpopulations have distinct roles. These somatosensory examples, as well as the organizational principles in other senses such as vision⁶, taste⁷⁻¹⁰ and olfaction¹¹, continue to motivate many neuroscientists to understand and categorize them. In this chapter, I will delve into some of the efforts I have helped contribute towards taxonomizing transcriptomically defined clusters of primary somatosensory neurons. To do this we developed a simple, robust approach for mapping trigeminal neural classes to cells in trigeminal tissue sections. This method allowed us to expose their anatomical features including their distribution and projection targets as well as test predictions from these transcriptomic studies. We additionally functionally characterized neurons innervating the cheek and matched those neurons to their transcriptomically defined class. Finally, I investigated how important mechanical transduction is for the stability of these transcriptionally defined classes by manipulating the expression of *Piezo2*.

Chapter 4

Part 1

* This section is presented in the form it was published in the journal *Pain* with the following citation and contributions

“von Buchholtz, Lars J., **Ruby M. Lam**, Joshua J. Emrick, Alexander T. Chesler, and Nicholas JP Ryba. "Assigning transcriptomic class in the trigeminal ganglion using multiplex *in situ* hybridization and machine learning." *Pain* 161, no. 9 (2020): 2212.”

Contributions: R.M.L. developed methodology, collected data, and performed formal analysis and conducted investigations. Specifically, the results of RML investigations are reported in the text of sections 2.2 and 3.5, Figure 5, Supplement Figure 6 and Table S1. RML also wrote the methods pertaining to aforementioned sections and reviewed the final versions of the manuscript.

Assigning transcriptomic class in the trigeminal ganglion using multiplex in situ hybridization and machine learning

Lars J. von Buchholtz^a, Ruby M. Lam^{b,c}, Joshua J. Emrick^a, Alexander T. Chesler^b, Nicholas J.P. Ryba^{a,*}

Abstract

Single cell sequencing has provided unprecedented information about the transcriptomic diversity of somatosensory systems. Here, we describe a simple and versatile in situ hybridization (ISH)-based approach for mapping this information back to the tissue. We illustrate the power of this approach by demonstrating that ISH localization with just 8 probes is sufficient to distinguish all major classes of neurons in sections of the trigeminal ganglion. To further simplify the approach and make transcriptomic class assignment and cell segmentation automatic, we developed a machine learning approach for analyzing images from multiprobe ISH experiments. We demonstrate the power of in situ class assignment by examining the expression patterns of voltage-gated sodium channels that play roles in distinct somatosensory processes and pain. Specifically, this analysis resolves intrinsic problems with single cell sequencing related to the sparseness of data leading to ambiguity about gene expression patterns. We also used the multiplex in situ approach to study the projection fields of the different neuronal classes. Our results demonstrate that the surface of the eye and meninges are targeted by broad arrays of neural classes despite their very different sensory properties but exhibit idiotypic patterns of innervation at a quantitative level. Very surprisingly, itch-related neurons extensively innervated the meninges, indicating that these transcriptomic cell classes are not simply labeled lines for triggering itch. Together, these results substantiate the importance of a sensory neuron's peripheral and central connections as well as its transcriptomic class in determining its role in sensation.

Keywords: Trigeminal, Transcriptomic class, Machine learning, Multiplex in situ hybridization, Gene expression, Peripheral targets

1. Introduction

The mammalian somatosensory system responds to mechanical, thermal, and chemical stimuli to provide valuable sensory information about both the environment and the internal physiological state.^{19,47,53} The sensory neurons of the trigeminal and dorsal root ganglia (DRG) are the primary somatosensory receptors, innervating the periphery and transmitting signals to the central nervous system. Recently single cell (sc) and single nuclear (sn) sequencing have defined an array of somatosensory neuronal classes and confirmed extensive similarity between these ganglia.^{7,13,24,31,32,42,48} Some of these classes correspond to cells that have been previously targeted genetically as they are defined by individual functional markers.^{3,11,27} Such experiments support the idea that genetically defined neural classes have distinct and specific roles.^{17,37} However, other transcriptomic classes are only distinguished by complex patterns of gene

expression.^{7,13,24,31,32,42,48} Moreover, these diagnostic genes tend to have less clear function in sensory detection raising questions as to the significance of transcriptomic class and their selectivity in somatosensation. A problem with sc-sequencing is that cell isolation destroys information about the in vivo system. Consequently, it has been difficult to explore how neural class is related to anatomical features of the cells including their projection patterns.

Single cell sequencing of other neuronal populations has also vastly expanded the view of their diversity by exposing a complex array of new transcriptomic classes.^{46,51} Just as in the somatosensory system, mapping the anatomical organization of these molecularly defined neural classes is a fundamental challenge. To address these inherent challenges, several groups have developed related in situ hybridization (ISH)-based methods^{6,30,41,49} that are effective at determining the cellular expression of many genes. These methods appear very powerful but require investment in probes and equipment as well as high-resolution imaging, precise alignment, and processing of massive data sets, limiting their widespread use. On the other hand, similar methods can be applied to a much smaller number of transcripts simplifying both methodology and analysis. For example, Spatial Genomic Analysis was developed to map cells in developing neural crest²⁵ by localizing just 35 genes. Similarly, an sc-quantitative polymerase chain reaction method has been used to classify somatosensory neurons using 28 genes.¹ Therefore, we reasoned that an even smaller number of highly expressed transcripts selectively marking partially overlapping sets of scRNA-defined cell classes might mean that multicolor ISH, low-resolution imaging, and just a few repeat cycles could be used to economically project transcriptomic classification of cells

Sponsorships or competing interests that may be relevant to content are disclosed at the end of this article.

^a National Institute of Dental and Craniofacial Research, Bethesda, MD, United States, ^b National Center for Integrative and Complementary Health, Bethesda, MD, United States, ^c Brown-National Institutes of Health Graduate Partnerships Program, Brown University, Providence, RI, United States

*Corresponding author. Address: National Institute of Dental and Craniofacial Research, Building 35, Room 3F220 Bethesda, MD 20892, United States. Tel.: 301-402-2401. E-mail address: nick.ryba@nih.gov (N.J.P. Ryba).

Supplemental digital content is available for this article. Direct URL citations appear in the printed text and are provided in the HTML and PDF versions of this article on the journal's Web site (www.painjournalonline.com).

PAIN 161 (2020) 2212–2224

© 2020 International Association for the Study of Pain

<http://dx.doi.org/10.1097/j.pain.0000000000001911>

to anatomical sections as a means to test and extend predictions from scRNA sequencing.

Here, we developed and refined this ISH-based approach to probe how neural diversity in the somatosensory system might orchestrate sensory discrimination and elicit select behavioral responses. To simplify analysis of the data and to make this type of strategy applicable to similar problems in other systems,^{46,51} we developed a powerful U-Net machine learning algorithm that automatically segments cells and assigns their classes. We then used this platform to characterize critical features of trigeminal sensory neurons including determining ion-channel expression profiles and examining peripheral targeting.

2. Material and methods

2.1. Probe selection and validation

Single cell RNA sequence data³² analyzed using the Seurat package developed in the Satija lab⁴⁰ were used to identify probes of multiplexed ISH. Potential probes were selected from genes that were prominent in the principle components used for clustering and were tested for their power at distinguishing trigeminal neural classes by analyzing their expression profiles in the sc-data. Criteria for probe selection included sharp boundaries in expression between classes, high level of expression in positive cells, and expression in a large proportion of cells that made up a positive class. The 15 probes chosen provided redundancy for identification of most neural classes (Fig. 1A) but only a small number of markers with potential to segregate some groups, for example, C1 from C2 or C9 from C10 could be identified.

2.2. Mice and retrograde tracing

Animal experiments were performed in strict accordance with the US National Institutes of Health guidelines for the care and use of laboratory animals and were approved by the NIDCR or NINDS ACUCs. C57BL/6N and FVB/N mice were purchased from Harlan. Mas-related G-protein-coupled receptor member A3 (*Mrgpra3*)-*Cre* mice¹⁷ were crossed to Ai14 tdTomato reporter mice (Jackson Labs). Both male and female mice were used for experiments.

Wheat germ agglutinin (WGA) coupled to Alexa594 (Invitrogen, Carlsbad, CA) was injected into various target fields to retrogradely label trigeminal neurons from their terminal processes. All labeling procedures used WGA-Alexa594 at 1 mg/mL; mice were anesthetized with isoflurane. To label the eye, the cornea was first abraded with a beveled 30-g syringe needle; 0.5- to 1- μ L WGA-Alexa594 was applied. To label the meninges, a midline incision into the skin allowed exposure of the skull, six 1-mm holes were drilled into the dorsal skull without perforating the meninges. Wells were built around each craniotomy with dental cement; 2 \times 0.5- μ L WGA-Alexa594 was applied to each well. Craniotomies were sealed with coverslips and dental cement, and the skin incision was closed and sutured. In all cases, animals were euthanized 16 to 20 hours after WGA-Alexa594 application and trigeminal ganglia dissected.

WGA-Alexa594 fluorescence was imaged in ISH-imaging buffer using 594-nm laser stimulation and a 9-nm wavelength scan, which helped separate signal from broader autofluorescence of the tissue. Slides were washed 3 times in 2 \times saline sodium citrate (SSC) and processed further for ISH.

2.3. In situ hybridization

Hybridization chain reaction (HCR) version 3.0⁸ was used for all ISH. Buffers and probes against the mouse genes *Cd34*, *Sstr2*, *Trpv1*, *Etv1*, *Tmem233*, *S100b*, *Synpr*, *Tmem45b*, *Calca*, *Trpa1*, *Mrgprd*, *Trpm8*,

Nppb, *Fxyd2*, *Nefn*, *Piezo2*, *Tubb3*, sodium channel protein type 1 subunit alpha (*Scn1a*), sodium channel protein type 8 subunit alpha (*Scn8a*), sodium channel protein type 10 subunit alpha (*Scn10a*), and sodium channel protein type 11 subunit alpha (*Scn11a*) and against *Cre* recombinase and *tdTomato* (*tdT*) were purchased from Molecular Instruments (Los Angeles, CA) as a mix of 10 or more oligonucleotide pairs per probe.

Trigeminal ganglia dissected from 2- to 6-month-old C57BL/6N or FVB/N mice were embedded in optimal cutting temperature medium and frozen at -80°C . Approximately 20- μ m sections were cut along a horizontal axis through the ganglion and mounted on microscope slides. Sections were dried (1 hour on a 37 $^{\circ}\text{C}$ hotplate), were fixed in on ice for 15 minutes 4% paraformaldehyde (Electron Microscopy Sciences, Hatfield, PA) in phosphate-buffered saline (PBS), and then were washed 6 times in PBS. Slides were dehydrated in an ethanol series (50%, 70%, 100%, and 100% for 5 minutes each) and stored for up to 1 week. This preparation resulted in excellent retention of sections through multiple rounds of hybridization and detection of probes but was not specifically optimized for preservation of signal.

Slides were dried completely, washed 3 times in PBS, and prehybridized for 30 minutes at 37 $^{\circ}\text{C}$ in HCR hybridization solution (Molecular Instruments). Hybridization and amplification were performed as described previously⁸ with minor modifications. Hybridization typically used 5 probes with adapters B1 to B5 at a concentration of 4 nM per probe in Coverwell incubation chambers (Grace Biolabs, Bend, OR) and was carried out for 48 to 72 hours at 37 $^{\circ}\text{C}$. Washing and preparation of amplifier hairpins for adapters B1 to B5 conjugated to Alexa488, Alexa514, Alexa561, Alexa594, and Alexa647 was as described by the manufacturer. Amplification was performed in a Coverwell chamber for 12 to 16 hours at room temperature in the dark. Slides were washed 2 times for 15 minutes in 5 \times SSC containing 0.1% Tween 20 and coverslipped in Imaging Buffer (3-U/mL pyranose oxidase, 0.8% D-glucose, 2 \times SSC, 10-mM Tris HCl pH 7.4).

After imaging, sections were rinsed in 2 \times SSC, and DNA probes and amplifiers were removed by incubation in 250-U/mL RNase-free DNase (Roche Diagnostics, Indianapolis, IN) for 90 minutes at room temperature. Sections were washed 6 times (5 minutes in 2 \times SSC) and prehybridized for the next round of hybridization with the next 5 probes. This procedure was repeated for up to 4 rounds of hybridization.

2.4. Confocal imaging and signal unmixing

Imaging was performed using a Zeiss LSM 880 confocal microscope with spectral detector using a 10 \times /0.45NA air objective with the pinhole opened to 132.9 μ m to allow capture of the whole section and provide enough signal intensity at this comparatively low magnification. Alexa647 was stimulated with a 633 laser and emission was collected from 644 to 752 nm. Alexa546 and Alexa594 were stimulated with 561 and 594 lasers, respectively, and wavelength scans with 9-nm windows were collected to allow unmixing signals from different fluorophores. To resolve Alexa488 from Alexa514, sequential wavelength scans with 3-nm windows were performed while stimulating with a 488-nm laser. Spectral unmixing was performed using Zeiss ZEN software.

Image series from consecutive hybridizations were combined by manually aligning transmitted light images from each imaging session using the TurboReg plugin in ImageJ/Fiji.

2.5. Unsupervised clustering of manually outlined cells

Data processing including the supervised vs unsupervised steps is schematically described in Figure S1 (available at <http://links.lww.com/PAIN/B13>). As a starting point, cell regions of interest

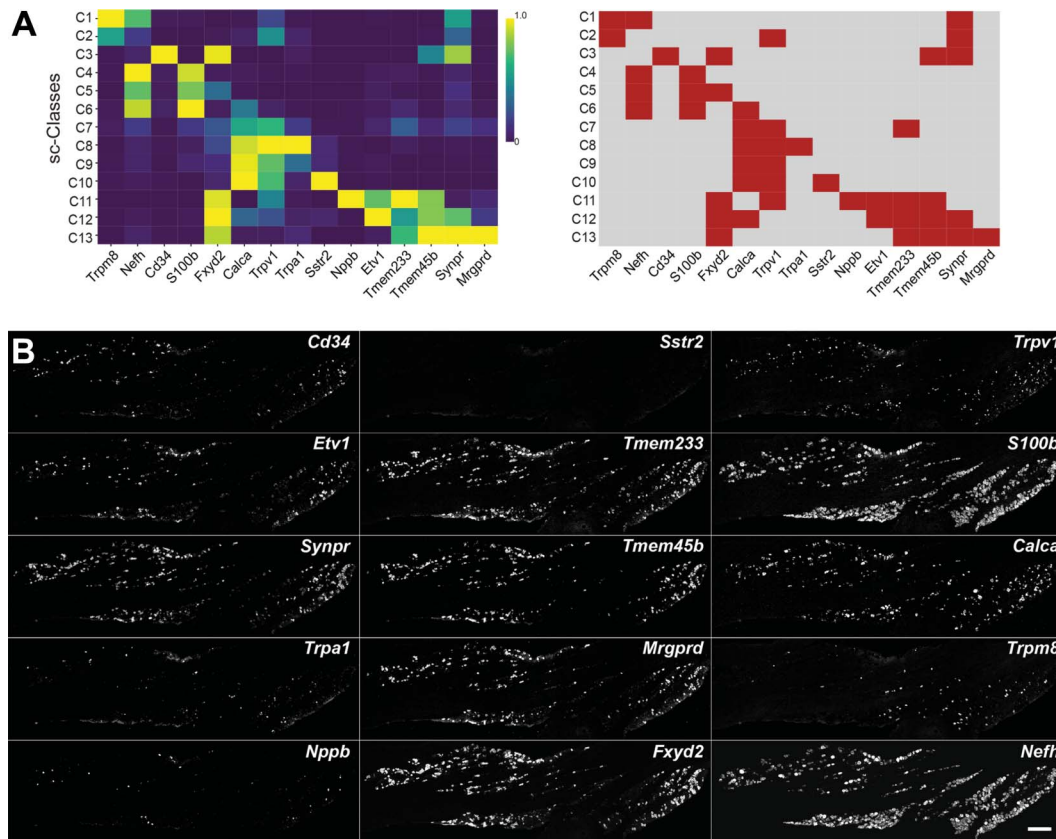


Figure 1. Approach for projecting transcriptomic class onto anatomical tissue sections. (A) Left, average expression levels of diagnostic markers in scRNA sequence analysis³²; genes are transient receptor potential cation channel subfamily M (melastatin) member 8 (*Trpm8*), neurofilament heavy (*Nefh*), transmembrane phosphoglycoprotein *Cd34*, S100 calcium-binding protein B (*S100b*), FXD domain containing ion transport regulator 2 (*Fxyd2*), calcitonin-related polypeptide alpha (*Calca*), transient receptor potential cation channel subfamily V member 1 (*Trpv1*), transient receptor potential cation channel, subfamily A, member 1 (*Trpa1*), somatostatin receptor 2 (*Sstr2*), natriuretic polypeptide B (*Nppb*), ETS translocation variant 1 (*Etv1*), transmembrane protein 233 (*Tmem233*), transmembrane protein 45B (*Tmem45b*), synaptorin (*Synpr*), and Mas-related G-protein-coupled receptor member D (*Mrgprd*). Right, a simplified binary analysis of their expression (red, positive; gray, negative) highlights their potential to combinatorially define trigeminal neural classes. (B) Images from 3 rounds of multiplexed ISH for a single section of a trigeminal ganglion from an FVB/N mouse are shown; the 5 probes used in each round of hybridization are displayed vertically. Note that for 14 probes clear positive and negative cells were identified; scale bar: 250 μ m. ISH, in situ hybridization.

(ROIs) in 4 complete ganglion sections were manually outlined in ImageJ (based on the individual ISH images), and mean fluorescence for each cell and probe was extracted using custom ImageJ macros. Further processing was performed using Python scripts: For subsequent clustering, local background in a ring around the cell was subtracted and the resulting values were standardized to mean 0 and variance 1 for each probe within a whole tissue section typically containing 1500 to 2000 cells.

The dimensionality of the data was then reduced from the 13 relevant probes (*Cd34*, *Trpv1*, *Etv1*, *Tmem233*, *S100b*, *Synpr*, *Tmem45b*, *Calca*, *Trpa1*, *Mrgprd*, *Trpm8*, *Nppb*, and *Fxyd2*) to a 2-dimensional representation by t-distributed stochastic neighbor embedding (tSNE). Cells clusters were identified using a density-based algorithm (https://github.com/alexandreday/fast_density_clustering) and mapped to the clusters derived from sc-sequencing based on their average expression of marker genes (see Fig. S1 for details, available at <http://links.lww.com/PAIN/B13>).

2.6. Automatic detection of cell classes using supervised Deep Learning

To automatically detect cell classes in tissue section images, we performed semantic segmentation by designing a custom Fully Convolutional Neural Network that follows the popular U-Net

architecture.³⁸ Several network designs and hyperparameters such as numbers of layers, learning rate, dropout rate, final activation function, and loss function were evaluated before settling on the final model.

The multichannel ISH input image data were first tiled into 256 \times 256 images, standardized to mean 0 and variance 1 for each probe channel and divided into training (96 images) and validation data (48 images). The desired output masks were generated as multihot encoded images (11 channels for 10 classes and background) from the hand-annotated ROIs and the cell class assignment from unsupervised clustering. To improve training performance, the available input data and their corresponding cell class masks were augmented by rotation and flipping. The final model closely mirrors the original U-Net architecture and contains 5 downward convolutional blocks with 2 layers each and 4 corresponding symmetric blocks for upconvolution. Image resolution was reduced to half in each consecutive block, and the number of channels was doubled starting from 16 in the first block. The output was a 256 \times 256 \times 11 matrix calculated by a softmax activation layer. The categorical cross-entropy loss function was optimized with an Adam optimizer at a learning rate of 0.0005 to convergence on the validation loss (\sim 120 epochs).

To achieve good class separation with the minimal number of hybridizations, we trained a model that takes 8 channels (*Tmem233*, *S100b*, *Calca*, *Trpa1*, *Mrgprd*, *Trpm8*, *Nppb*, and

Fxyd2) as an input. This model was validated and used to predict cells and their classes in WGA tracing experiments. To determine cell class identity of manually outlined WGA-labeled cells, the mean probability for each cell class was calculated for the ROI and the most probable cell class was assigned to the cell. Cells with a maximum class probability of less than 0.1 were kept unassigned. Rare retrogradely labeled cell classes (<5% from any target site) were manually inspected and corrected on a cell-by-cell basis.

To automatically segment cells, probability predictions for each class were first blurred with a Gaussian filter (3×3 kernel) and discretized by choosing the most probable class for each pixel. After morphological opening of the foreground classes with a 6×6 circular kernel, cells were segmented by a distance transform watershed algorithm.

Expression level of sodium channels was determined automatically by measuring signal intensity in segmented and classified cells. For comparison purposes, violin plots of channel expression in sc- and sn-data^{31,32} were generated. This representation is particularly useful for analyzing sparse transcriptomic data because it eliminates extremes (primarily from the zero values) thereby providing a valuable representation of gene expression across classes. The ISH data are not of this form, with no true zero value; we therefore calculated the relative standardized expression levels (mean = 0 and variance = 1) and used a histogram representation to approximate the violin plot of the transcriptomic data.

All computations were performed either in Python using Keras/Tensorflow, sklearn, Numpy, Pandas, skimage, opencv, and scipy libraries or in custom ImageJ macros. All code is available in Github (<https://github.com/lars-von-buchholtz/InSituClassification>).

3. Results

3.1. Development of an *in situ* hybridization approach for classifying trigeminal neurons

scRNA sequencing of trigeminal neurons defined about a dozen neuronal classes that closely matched classes identified by transcriptomic analysis of DRG neurons.³² More recent sn-analysis³¹ distinguished most of the same cell populations but further subdivided classes of putative large diameter neurons, which were much more prominently represented in this study. However, some of the diversity amongst nociceptors was not observed in the nuclei-based sequencing. Thus, only 10 of the 13 classes directly corresponded between studies. Here, we developed a simple, robust approach for mapping trigeminal neural classes to cells in tissue sections to expose their anatomical features including their distribution and projection targets as well as test predictions from these transcriptomic studies.

As a starting point, we performed quantitative ISH using an array of 15 genes that we predicted should, in combination, identify all the sc-sequence defined classes. The chosen marker genes featured prominently in the dimensional reduction (principal components) used in the scRNA-sequence cluster analysis. In the sc-data, each of these genes is present in a distinct subset of trigeminal neural classes. Importantly, the chosen transcripts were generally very good markers of the clusters where they were present, that is, because they were highly expressed genes, we were confident of their presence in the vast majority of cells, whereas they were essentially absent from other types of neuron (Fig. 1A). Thus, the combinatorial expression pattern of these transcripts would be expected to allow trigeminal neural classes

to be reliably distinguished, providing a framework for classifying cells *in situ* and a straightforward approach for testing predictions from the transcriptomic analyses.

Using the well-characterized HCR protocol,⁸ we performed 3 rounds of 5 probe ISH and used spectral unmixing to resolve specific signals from the 15 diagnostic probes (Fig. 1B). The HCR approach has the sensitivity and resolution to detect single transcripts when sections are imaged at high resolution.^{8,41} Importantly, however, for studying genes that are highly expressed in subsets of neurons, we could use lower magnification imaging, saving time, and reducing the complexity of data processing as well as maximizing the number of cells analyzed. Such integrated HCR signals have been shown to accurately quantify the relative expression level of a transcript between cells⁸ and thus served to quantitate the diagnostic genes at a cellular level. It should be noted, however, that higher resolution imaging is also possible and may be useful for genes with lower expression level.

Fourteen of the 15 probes clearly differentiated positive from negative cells, but the probe to *Sstr2* was not diagnostic at this magnification (Fig. 1B), thus clusters C9 and C10 cannot be resolved. These clusters also failed to segregate in sn-analysis,³¹ and few other distinguishing markers could be identified from the sc-data. Therefore, it is likely that C9 and C10 are broadly similar types of cells. In the future, higher resolution imaging and use of additional marker genes as well as increasing the gene coverage of the *Sstr2*-probe set may help resolve these 2 classes of neurons, which can be distinguished in transcriptomic analysis of DRG neurons.^{24,42,48}

In situ hybridization images from the 14 diagnostic probes could be aligned by simple translation and rotation (Fig. S2A, <http://links.lww.com/PAIN/B13>). After alignment, the ISH data (Fig. 1B) are equivalent to 91 different double-label experiments (Movie S1, available at <http://links.lww.com/PAIN/B14>) or 364 combinations of 3 markers applied to a single section. At the most basic analytical level, almost all the pairwise expression patterns that were predicted (Fig. 1A) were detected by ISH (Movie S1, available at <http://links.lww.com/PAIN/B14>). However, the expected division of *Trpm8*-expressing cells into groups expressing or not expressing *Nefh* (Fig. 1A) was graded rather than binary (positive vs negative, see Fig. S3A, <http://links.lww.com/PAIN/B13>). Although we might be able to divide 2 classes of *Trpm8*-neurons by thresholding *Nefh*-expression, this seemed arbitrary and subject to error. Thus, the *Nefh*-based ISH approach does not reliably distinguish classes C1 and C2. Interestingly, although this split was predicted by the cell-based analysis,³² it was not seen in nuclei-based sequencing.³¹ A second distinguishing marker that was predicted to divide the C1 and C2 clusters in the sc-analysis³² encodes the neuropeptide galanin (*Gal*). We therefore tested whether *Gal* expression subdivides the *Trpm8*-positive neurons into 2 groups using ISH (Fig. S3B, <http://links.lww.com/PAIN/B13>). Our results indicated that *Gal* is not coexpressed with *Trpm8* (Fig. S3B, <http://links.lww.com/PAIN/B13>), again matching sn-data. Therefore, the ISH data indicate that variation amongst *Trpm8* cells is more continuous than we had originally predicted³² supporting more recent results,³¹ which indicate that these neurons although not homogeneous, in fact comprise a single transcriptomic class with graded expression differences between the cells.

3.2. Classifying trigeminal neurons in manually segmented sections defines transcriptomic class

Trigeminal sections from 4 mice were analyzed by multiplexed ISH, and neurons were manually segmented to measure the

cellular expression of marker genes. For 3 of these animals, the nondiagnostic probes for *Nefh* and *Sstr2* were replaced with probes for other genes including neuronal β -tubulin (*Tubb3*, a pan-neuronal marker), providing a means to identify all somatosensory neurons in the sections. After alignment of images, all neurons in the sections were manually segmented using the signal in the 15 different ISH channels as a guide. The cellular expression levels of the 13 diagnostic markers in these manually segmented cells were determined based on signal intensity (see methods for details). The resulting 13-dimensional expression data were subjected to tSNE followed by density-based cluster identification to classify neurons (Fig. 2A). The relative expression of each marker gene at a cellular level in the classified neurons is shown (Fig. 2B) highlighting a close match with predictions (Fig. 1B) for 10 trigeminal neuronal classes. Importantly, these classes of neurons match those that were detected in both the cell and nuclear-based analyses.³¹ Nonetheless, cells with an expression profile corresponding to an 11th class C7 that was only identified in the sc-study,³² expressing *Trpv1* and *Tmem233* but not *Tmem45a* (Fig. 1B), were also found using ISH (Fig. S3C, <http://links.lww.com/PAIN/B13>). However, these neurons were rare and did not separate from C9/10 cells in the cluster analysis (Fig. 2).

Quantitative analysis of ISH based clustering revealed a high degree of consistency in representation of neural classes between sections from different mice (Fig. S4, <http://links.lww.com/PAIN/B13>). Therefore, we are confident that distribution of neural classes (Fig. 2C) is representative of the ganglion as a whole. Notably, the combined ISH patterns of the 13 diagnostic probes and the expression of the pan-neuronal marker *Tubb3* were almost identical (Fig. S5A, <http://links.lww.com/PAIN/B13>), confirming that the vast majority of trigeminal neurons were included in our classification. Thus, the multigene hybridization approach demonstrates the existence of at least 11 of the 13 types of trigeminal neuron predicted by scRNA sequencing³² and reveals their true representation in the ganglion.

Although primarily designed to identify the transcriptomic class of neurons in anatomical sections, the redundancy inherent in the probing strategy (Fig. 1A) meant that it could also be used to search for rare unexpected patterns of coexpression. By contrast, to sc-transcriptomic data where dropout and contamination generates ambiguity, the ISH approach allows an explicit check by visual examination. For instance, a small proportion of C6 neurons expressed the heat- and capsaicin-activated ion-channel *Trpv1* (Fig. S5C, <http://links.lww.com/PAIN/B13>). This expression profile likely identifies this group of neurons as the A δ -thermal nociceptors that have been reported to trigger rapid, *Trpv1*-dependent, withdrawal from noxious heat.²⁸ Importantly, these *Trpv1*, *Calca*, *S100b*-positive cells that were not directly identified in sc-analyses^{7,13,24,31,32,42,48} are predicted to play a distinct functional role from other C6 neurons.

3.3. A machine learning–based approach for segmenting neurons and assigning cell class

Although the manual segmentation approach (Fig. 2) allows for classification of cells in tissue sections, it is slow and defining the cell boundaries is often somewhat subjective. Therefore, we reasoned that automation would greatly increase throughput, decrease bias, and thus provide a versatile platform for answering questions about gene expression and neuronal connectivity in the trigeminal ganglion.

Ideally, we wanted to develop a procedure that could take unprocessed aligned ISH images, define cell boundaries, and assign transcriptomic class without relying on additional input

about cell shape. Unfortunately, traditional methods used in automated segmentation³⁵ were not suitable for the ISH images where signal had variable intensity across positive cells and was often overlapping between neighboring cells as well as regionally localized with perinuclear vs cytoplasmic staining for different probes (Fig. 1B). However, since each ISH image contains both information about cell structure as well as gene expression, we predicted that the combined images might define both cell boundaries and neuronal transcriptomic class. Therefore, instead of segmenting individual cells, we set out to develop a custom semisupervised Deep Learning algorithm using a fully convolutional Neural Net based on the U-Net architecture.³⁸ This approach uses the aligned individual ISH images as input and calculates the probability of each pixel being one of the 10 major classes (or non-neuronal, ie, not one of these classes; see Fig. S1 for a schematic description of all data-processing, available at <http://links.lww.com/PAIN/B13>). The Neural Net was trained on the manually outlined (supervised) cells that were assigned a class based on the unsupervised clustering described above (see Methods for details). Although we began by using the full data set, we realized that just a subset of the 13 genes (*Trpm8*, *S100b*, *Fxyd2*, *Calca*, *Trpa1*, *Nppb*, *Tmem233*, and *Mrgprd*, see Fig. 1A, Fig. S1, available at <http://links.lww.com/PAIN/B13>) should be sufficient to define the 10 neural classes that were distinguished in the manually segmented cells (Fig. 2) and here report results based on this 8-gene panel.

Just as we had hoped, the Neural Net transformed the ISH data of this 8-gene probe-set into images where cells and their classes were immediately recognizable (Fig. 3A). Indeed, cells were now easily segmented (Fig. 3B) using a standard watershed approach. Some of the ISH data, including the images shown (Fig. 3), had been manually segmented (revealing the “ground truth”) but had not been used to train the U-Net algorithm. The reliable segmentation and classification of neurons in these test sections of the trigeminal ganglion (Fig. 3B and Table 1) validate the automated Deep Learning approach; at a pixel level, the prediction displayed an accuracy of approx. 95%. One minor concern is that the neural net approach led to some distortion of cell size and shape that was most pronounced in areas where neurons were densely packed and ISH signals partially overlapped. This makes it difficult to assess how cell diameter varies across the various classes but does not alter conclusions about cellular identity (Table 1). Importantly, as demonstrated by comparing the combined predictions with *Tubb3* expression (Fig. S5B, <http://links.lww.com/PAIN/B13>), we found that almost all neurons were classified by the U-Net algorithm. Equally importantly, non-neuronal regions were also accurately reported. Notably, minor modifications to the code would make this U-Net based strategy generally applicable for analyzing other types of complex image-based data sets. Thus, we envision that analogous multiplexed ISH or antibody-based approaches coupled with automatic classification of cells could be easily adapted to other sc data sets and serve as a simple platform for mapping cell class to anatomical sections.

3.4. Expression of voltage-gated sodium channels in trigeminal neurons classes

sc-transcriptomic analyses make use of many variable genes in clustering data and thus can tolerate the sparse nature of the underlying data sets, the consequent dropout of specific transcripts as well as occasional capture of false positives. However, the expression of any individual gene will be distorted

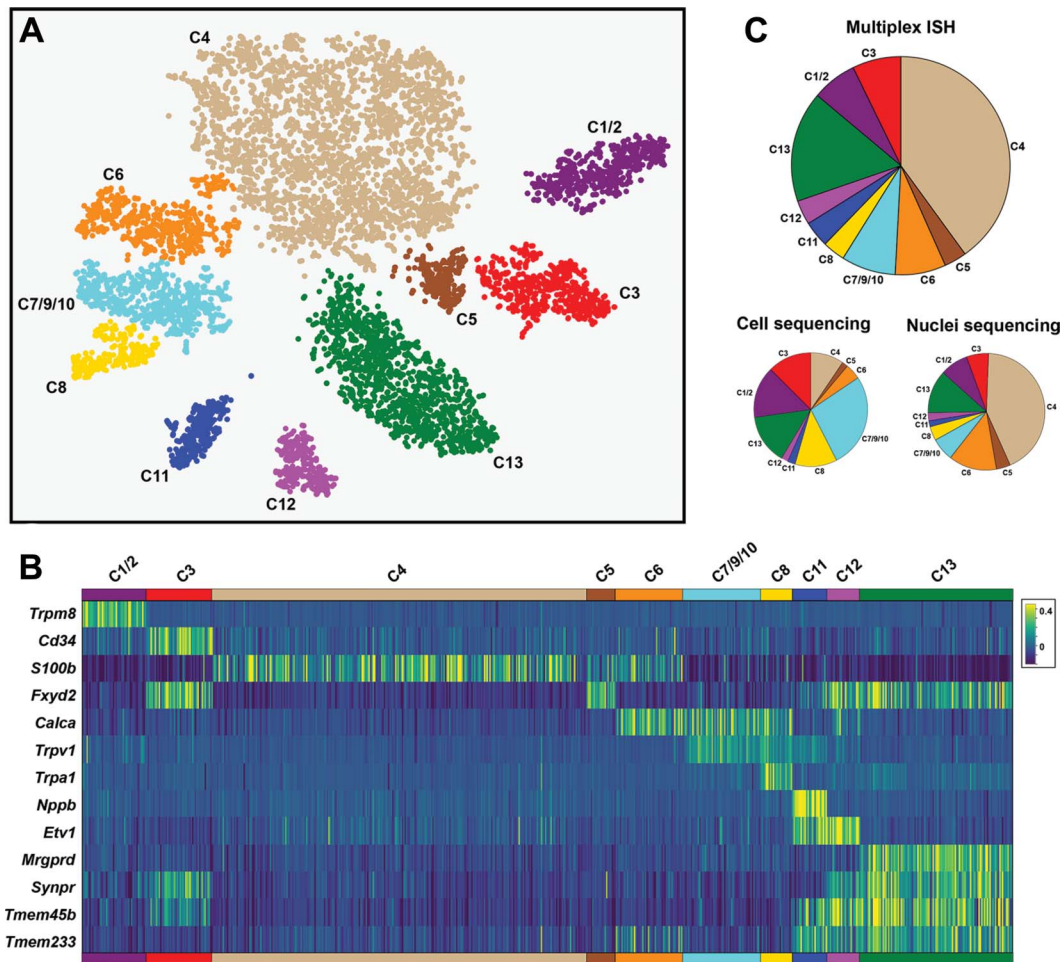


Figure 2. Multiplexed ISH-based classification of trigeminal neurons. Sections through trigeminal ganglia from 4 mice were subjected to multiplex ISH. Neurons from a single section for each mouse were manually segmented to measure ISH signal intensity at a cellular level. (A) tSNE representation and cluster analysis of ISH data for 13 probes showing that this approach segregated neurons into 10 groups. The correspondence of these groups with scRNA sequence defined transcriptomic classes (C1-C13) is indicated. (B) In situ hybridization signal intensity at a cellular level in the 7735 neurons; cells were ordered according to their cluster assignment with each vertical bar representing a different cell. (C) Pie charts comparing the proportions of trigeminal neurons assigned by class for multiplex ISH data, sc- and snRNA sequencing; note that cell sequencing underrepresents large diameter neuronal classes C4-C6 relative to other cells. ISH, in situ hybridization.

by these artefacts. By contrast, ISH more accurately reflects the cellular level of mRNAs, and thus, the multiplexed approach should provide a platform for measuring cellular expression of genes across cell classes. Here, we illustrate the power of this

approach by testing the expression profile of several voltage-gated sodium channels that are known to be differentially expressed in somatosensory neurons⁵² and play distinct roles in sensory detection.^{10,34,54}

Table 1
Accuracy of U-Net-based class predictions.

	U-net prediction 8 probes										
	C1/2	C3	C4	C5	C6	C7/9/10	C8	C11	C12	C13	ND
Manual segmentation/clustering											
C1/2	153	0	2	0	1	1	0	1	0	3	1
C3	2	94	6	26	1	2	0	1	2	20	7
C4	2	8	960	11	34	2	1	7	1	5	25
C5	0	13	3	48	0	0	0	0	1	4	1
C6	0	0	20	1	166	5	0	0	1	0	0
C7/9/10	2	1	8	2	32	79	6	1	7	11	2
C8	0	1	1	0	6	9	49	0	0	1	0
C11	1	0	8	0	0	0	0	82	2	2	0
C12	0	8	6	0	0	2	0	0	50	14	0
C13	0	1	8	2	0	1	0	0	2	387	3

Prediction accuracy and errors for all classes of trigeminal neuron in the validation set. Columns are predicted classes (ND, not determined); rows are the manually segmented, clustering based classification. Bold values highlight the proportion of predicted neurons that fall into a cell. Overall, prediction accuracy was 94.8% at a pixel level and 84.9% at the cellular level. It should be noted that when a subset of predicted neurons that did not match the manually segmented cells were examined, many turned out to have the gene expression profile of the predicted class rather than that of the manual segmentation approach. This is not surprising since manual segmentation relies on subjective assessment of cell boundaries and inaccuracies in this process are likely to affect classification for a subset of cells.

The patterns of expression of *Scn10a* (Na_v1.8, a tetrodotoxin [Ttx] insensitive channel) and *Scn1a* (a Ttx sensitive channel Na_v1.1) were very similar across the major neural classes in the sc- and sn-analyses (Fig. 4A). Expression of *Scn10a* in U-Net classified trigeminal neurons very closely matched the overall predictions from the sc-data (Fig. 4B). Notably using the ISH approach, each class of sensory neurons appeared quite homogeneous in its expression pattern closely following a unimodal distribution, but there were major differences in the mean expression level of the classes (Fig. 4B). By contrast, the sequence data were more ambiguous. This was particularly apparent for C3 or C7 to 10 cells where discontinuous violin plots (Fig. 4A) could be interpreted as only a subset of cells expressing this gene, or alternately as dropout of a moderately expressed transcript because of the sparse nature of the sequence information. The ISH indicates that the majority of neurons in these classes express *Scn10a* but that the average level of expression is low (Fig. 4B). Importantly, this sodium channel, which plays a crucial role in detecting painful input, is absent from the C1/2 cooling sensing neurons as well as the large diameter C4 and C5 putative mechanosensors but is present albeit at very different levels in all other classes.

The classes of neurons expressing *Scn1a* in the 3 data sets (sc- and sn-transcriptomic and ISH based) were also highly concordant (Fig. 4), emphasizing the effectiveness of the minimal U-Net approach at projecting the transcriptomic trigeminal neuronal class onto anatomical sections. Again, just as for *Scn10a*, the expression of *Scn1a* appeared homogeneous in most (8 of the 10) neuronal classes (Fig. 4B). This contrasted starkly with transcriptomic data where even the classes with the highest overall expression showed major dropout presumably because of the low to moderate expression of this gene resulted in false negatives in the transcriptomic data. Thus, these ISH gene expression data (Fig. 4B) not only validate sc-predictions but also extend them. C1/2, C4, and C5 neurons all express this sodium channel at a relatively high level with less expression detected in C3 neurons. C7/9/10, C11, C12, and C13 neurons were negative for this channel, while expression in C6 and C8 cells appeared heterogeneous with some neurons in these classes being negative and others strongly positive.

Interestingly, other voltage-gated sodium channels (*Scn11a* and *Scn8a*) were less consistent between the 2 transcriptomic data sets (Fig. 4A), probably reflecting their expression level, the depth of sequencing in the respective studies, instability of larger diameter neurons for the cell-based analysis, and perhaps differences in how these mRNAs are distributed in trigeminal neurons or regulated during cell isolation. By contrast, ISH analysis of *Scn11a* was diagnostic with each class exhibiting quite a homogeneous pattern of expression (Fig. 4B). The classes of neurons expressing this gene closely matched the expression profile of *Scn10a* except that *Scn11a* (a second Ttx-resistant channel, ie, selectively expressed in sensory neurons and involved in pain sensation) was not detected in the majority of C6 neurons that are predicted to represent A δ -nociceptors.^{2,14,42} Our ISH analysis revealed that *Scn8a* is primarily expressed in large diameter neurons with highest levels in C4, C5, and C6 cells (Fig. 4B), is also detectable in C1/2, C3 and C12 neurons, and is essentially absent from other trigeminal neuronal classes. Taken together, these data further validate the minimal ISH approach for classifying trigeminal neurons in anatomical sections and reveal its power for quantitative expression analysis by exposing the stereotyped, strongly class-related, differential expression of Ttx-sensitive and -insensitive sodium channels in the trigeminal neuronal classes.

3.5. Classifying trigeminal neurons innervating specialized sensory targets

The trigeminal nerves innervate diverse tissues and structures in the head and neck. Multiplex ISH-based neural classification provides an opportunity to probe the transcriptomic identity of neurons innervating quite different types of specialized sensory environments. Here, we illustrate this using a retrograde tracer (fluorescently labeled WGA) to mark neurons projecting to the surface of the eye or the meninges (Fig. 5A). After one round of imaging to identify the labeled neurons, the cells projecting to these targets were classified using the 8-probe U-Net approach (Fig. 5B). Our data, using a comprehensive and unbiased approach extend previous studies that have used candidate transgenes to label subsets of neurons innervating tissues.^{5,18,36}

An immediate surprise was that tracer applied to the surface of the eye labeled most classes of sensory neurons (Fig. 5C). However, the representation of these classes was dramatically different from the ganglion as a whole (Fig. 5C). The proportion of C8 cells (*Trpv1/Trpa1* expressing nociceptors) innervating the eye was increased more than 10-fold. Based on their expression profile, including prominent expression of *Trpa1*, we expect C8 neurons to respond to irritants including the lachrymatory agent from onions, a volatile electrophile that activates *Trpa1*.²⁶ C8 neurons also express *Calca*, consistent with previous studies demonstrating that CGRP-neurons innervate the cornea.⁵ Other peptidergic c-fibers C7/9/10 (*Trpv1*-positive, *Trpa1*-negative nociceptors) were not significantly different from their distribution in the whole ganglion, whereas C6 (CGRP-expressing A δ -nociceptors) was slightly underrepresented. A second class of cells that were particularly prominent and overrepresented in neurons targeting the eye were the C1/2 (cool responsive) cells (Fig. 5C), supporting previous studies showing the cornea to be strongly innervated by *Trpm8*-expressing cells.^{18,36} By contrast, other types of sensory neurons rarely innervated the eye including C3 (putative c-fiber low threshold mechanoreceptors, LTMRs) and the itch related class (C11). Since we did not exclusively target the cornea with our injections, some of the labeled neurons may innervate regions around the eye including the conjunctiva, which, unlike the cornea is known to be rich in *Mrgpra3* (C12) fibers.¹⁸ Major mechanosensory classes C4 (A-type LTMRs) and C13 (*Mrgprd*-expressing mechanonociceptors) were labeled at about 50% the expected frequency based on their distribution in the ganglion. Given the overall prominence of C4 and C13 neurons in the ganglion, this modest reduction still means that many putative mechanosensors target the eye. Since fast conducting mechanosensory neurons often make specialized connections in hairy and glabrous skin and exhibit select functions in gentle touch, it will be interesting to determine the terminal structure of these neurons and to assess what contribution they provide in corneal sensation.

Our results revealed that the meninges are also targeted by a broad mix of neurons but with a very different representation of classes (Fig. 5C). Specifically, C1/2 neurons, which prominently innervate the eye, rarely targeted the meninges and C8 neurons were completely absent. Remarkably the 2 classes of itch neurons (C11 and C12) prominently targeted this internal sensory environment (Fig. 5C). Initially, we were concerned that problems with the model and class assignment might be responsible for suggesting itch neurons project to a sensory environment that cannot be scratched. However, manual examination of positive neurons revealed that they were not misassigned by the model, with prominent expression of *Nppb*, a very selective marker for C11^{32,48} in WGA-labeled cells of this class (Fig. 6A). Since the classification of C12 cells in the eight-probe model relies on

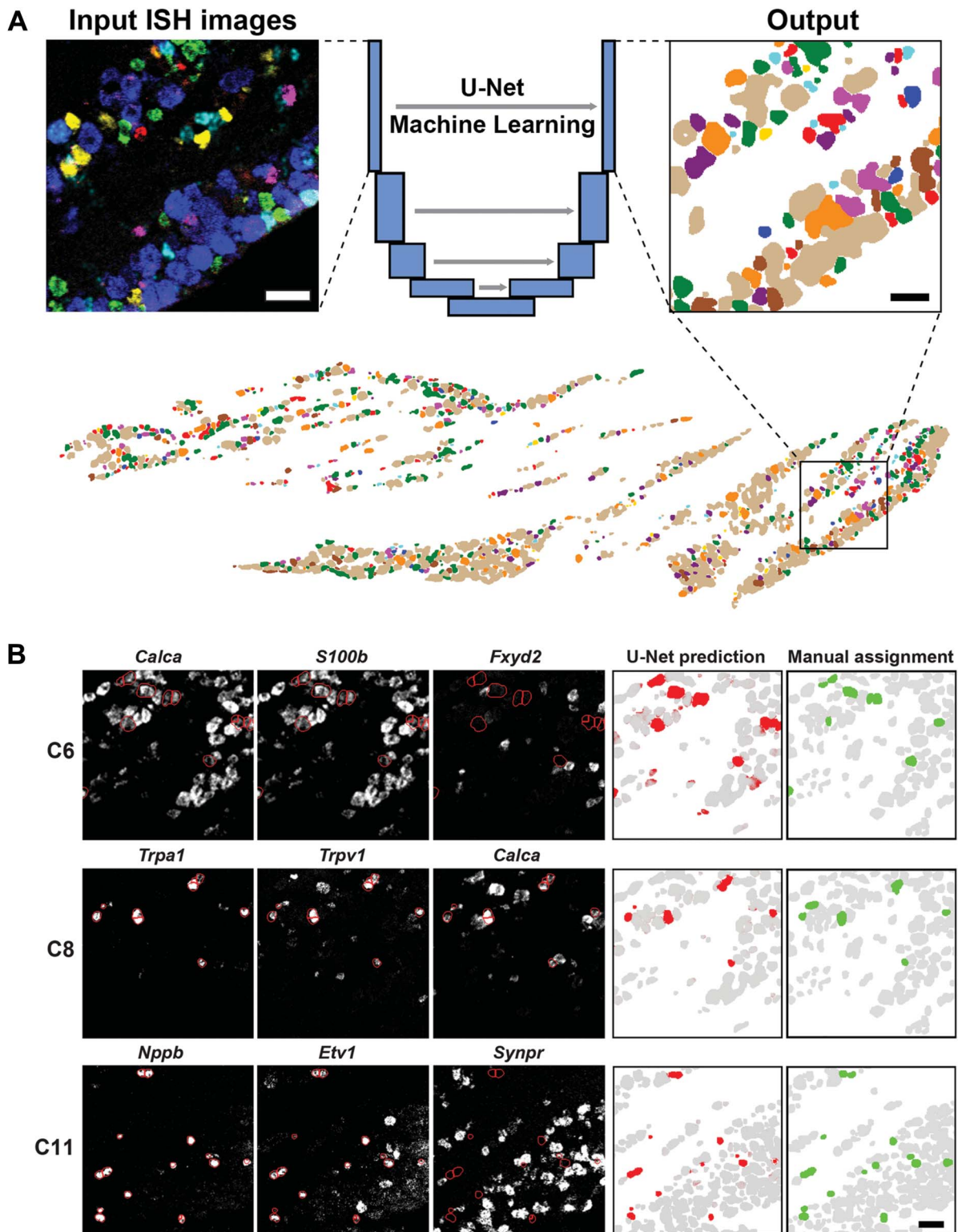


Figure 3. Classification of neurons from ISH images using machine learning. A U-Net Deep Learning algorithm was developed and trained to classify neurons directly from multiplexed ISH images. (A) Example of ISH image input to the U-Net (left panel, 6 non-overlapping probes shown) and the corresponding output (right panel, colored as in Fig. 3). The full ganglion prediction (lower panel) corresponds with the ISH images shown in Fig. 2. (B) Example predictions for 3 classes of trigeminal neurons. Key input ISH images (left 3 panels) overlaid with outlines of predicted cells (red) highlighting the expected patterns of gene expression: C6 cells express *S100b* and *Calca* but not *Fxyd2*; C8 cells express *Trpa1*, *Trpv1*, and *Calca*; C11 cells express *Nppb* and *Etv1* but not *Synpr*. The right 2 panels compare the U-Net prediction probability (red) and the manually segmented and tSNE assigned class (green). Gray represents prediction of other neural classes; scale bars 50 μ m. ISH, in situ hybridization.

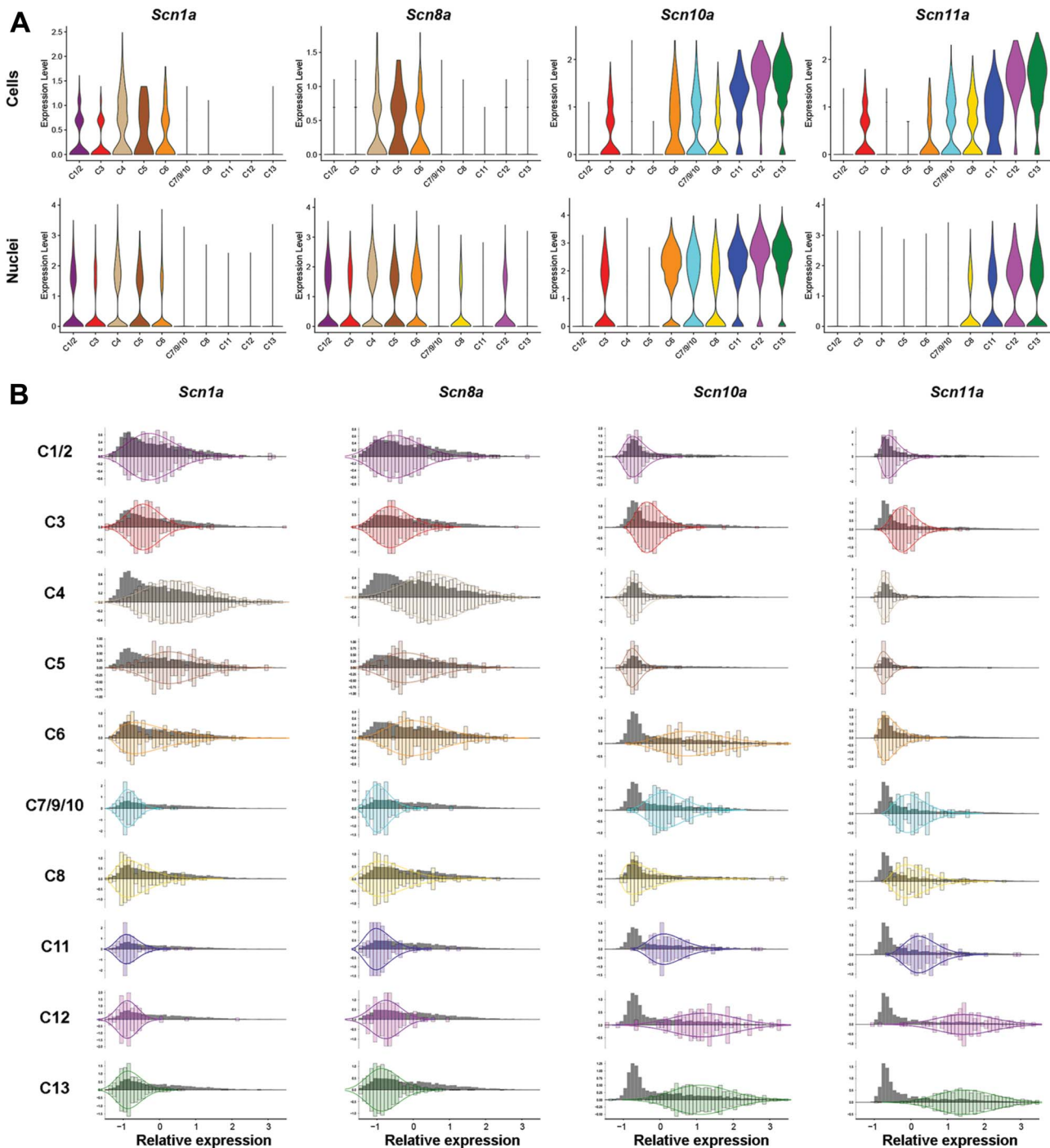


Figure 4. Analysis of voltage-gated sodium channel expression in classified neurons. (A) Violin plots of the expression of 4 voltage-gated ion channels across trigeminal neuronal classes in the (upper panels) cell-based³² and (lower panels) nucleus-based³¹ analyses. The y-axes indicate expression levels that were normalized as described previously,^{31,32} and the x-axes approximate the relative abundance of these expression levels. (B) Histograms of expression data for these ion channels across trigeminal neuronal classes identified using multigene ISH and the U-Net classification of neurons. Gray histograms depict the relative standardized expression levels (mean = 0, variance = 1) of the channel in all trigeminal neurons along the x-axis and relative abundance of expression levels along the y-axis; colored bars, its relative expression in cells of a particular class; colored curves are gamma distributions fitted to the expression data in a class; to help highlight the expression pattern of a channel in a defined class of cells, the class histograms and fitted curves have been reflected around the x-axis which was scaled to result in a total area under the curve of 1. ISH, in situ hybridization.

overlapping expression and absence of certain markers, we performed additional retrograde labeling experiments to specifically confirm that C12 (*Mrgpra3*-positive) neurons also project to the meninges. To do this, we used a well-characterized *Mrgpra3-Cre* transgenic mouse line¹⁷ to drive reporter gene expression and demonstrated that *Cre* and the reporter gene were

coexpressed in neurons retrogradely labeled from the meninges (**Fig. 6b**). Thus, both classes of sensory neurons that selectively trigger itch responses when stimulated through the skin also target the meninges.

The biggest differences in the innervation of the eye vs the meninges were the overrepresentation of C1/2 and C8 cells

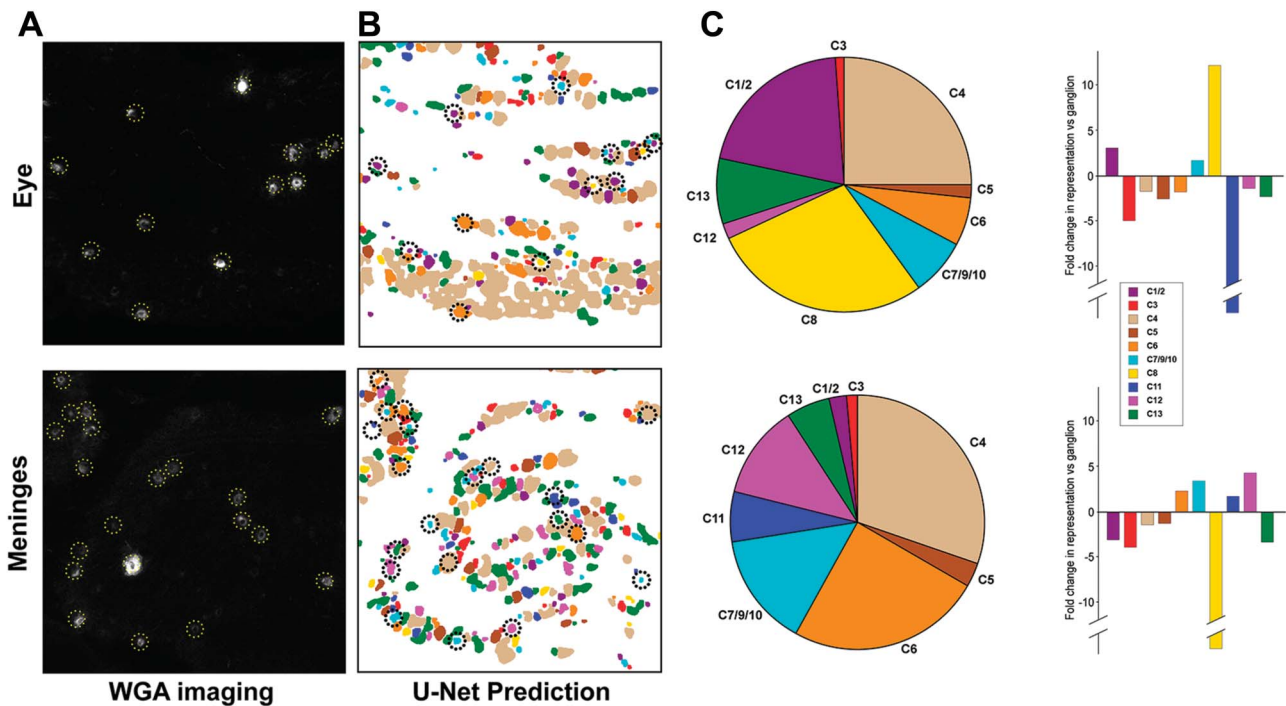


Figure 5. The eye and meninges are both innervated by a broad array of sensory neuron types. Fluorescently labeled WGA was used to retrogradely label neurons innervating peripheral sites. (A) Typical images of WGA tracing from the eye (primarily cornea) and meninges; yellow-dotted lines highlight WGA-positive cells. (B) Cell classes assigned using the 8-probe U-Net approach with WGA-positive cells circled (black-dotted lines; colors indicate cell class as defined in Fig. 3). (C) Left: pie charts representing innervation profiles of these 2 peripheral targets and right: bar graphs depicting the fold difference in the proportion of neurons labeled by tracer injection in a target site relative to the prevalence of those neurons in the ganglion assessed by the 8-probe U-Net method (see Table S1 for statistical analysis, available at <http://links.lww.com/PAIN/B13>). Data are from a single section through the trigeminal ganglion of 4 mice for each peripheral target; scale bar = 100 μ m. ISH, in situ hybridization; WGA, wheat germ agglutinin.

targeting the eye vs C11 and C12 cells projecting to the meninges. Intriguingly, the cell bodies of these 4 neuronal classes were differentially distributed within the trigeminal ganglion with this spatial segregation of classes conserved between animals (Fig. S6A, <http://links.lww.com/PAIN/B13>). Similar segregation of these classes extended to areas that do not target the eye and meninges (Fig. S6B, <http://links.lww.com/PAIN/B13>), perhaps hinting that other target tissues share the same differential innervation patterns. However, although it is attractive to speculate that these differences in spatial representation reflect differences in peripheral targeting, the eye and meninges were represented by broad and partially overlapping fields. Thus, it is also possible that developmental processes (rather than projection per se) result in this topographic segregation of neuronal classes in the ganglion.

C3 and C4 neurons (c- and A-type LTMRs) were underrepresented in meningeal projections as were C13 neurons (*Mrgprd*-expressing, nonpeptidergic nociceptors) but still account for about a third of all neurons targeting this tissue. It will be interesting to determine the types of stimuli these putative mechanosensors respond to, examine their sensory termini in the meninges, and assess if they play a specific role in types of migraine. Notably, the *Calca*-positive C6 and C7/9/10 (A- and c-type) peptidergic nociceptors were more than 2-fold enriched amongst the meningeal-labeled cells. Interestingly, we also discovered that all the meningeal C12 neurons (Fig. 6) expressed *Calca*, although this gene is normally present in just a fraction of the C12 cells in the whole ganglion (Fig. S7, <http://links.lww.com/PAIN/B13>). Thus, almost half of the trigeminal neurons innervating the meninges are positive for *Calca* and consequently express the neuropeptide CGRP, which is well known to play an important role in certain types of migraine headache.^{15,43}

4. Discussion

Here, we set out to develop a simple but robust platform for assigning transcriptomic class to trigeminal ganglion neurons in anatomical sections. Just 8 probes were required to identify all the major classes of neurons that are consistently defined by cell- and nuclear-based scRNA sequence analyses.^{31,32} Moreover, the hybridization images from these 8 probes were all that was needed for automated and rapid segmentation of cells and class assignment using a novel U-Net based approach that we developed. We demonstrate the power of this simple platform by determining the expression of functionally relevant sodium channels in the different classes of neuron and analyzing the neural classes innervating the eye and meninges. This approach provides a much more consistent view of gene expression, at a cellular level, than sc-transcriptomic analysis (Fig. 4) and is particularly valuable for moderately expressed genes where dropout in sc-sequencing is a major drawback. It also provides a rapid and unbiased means for linking anatomy to gene expression (Fig. 5).

A surprise from our study of tissue innervation was that transcriptomic class did not appear to be the sole predictor of a neuron's sensory role. For example, in the skin, C11 and C12 neurons selectively respond to pruritogens and trigger itch.^{4,23} We found that these cells also innervate the meninges where they must drive different perceptual and behavioral responses. One possibility is that these types of neurons have common sentinel-type roles, for example, as detectors of immune cell activity⁴⁴ or irritants in the different tissues. In this scenario, their differential central connectivity would then govern the consequences of their activation. Interestingly, it was recently shown that the lung is also innervated by C12 neurons,¹⁶ thus the meninges may not be

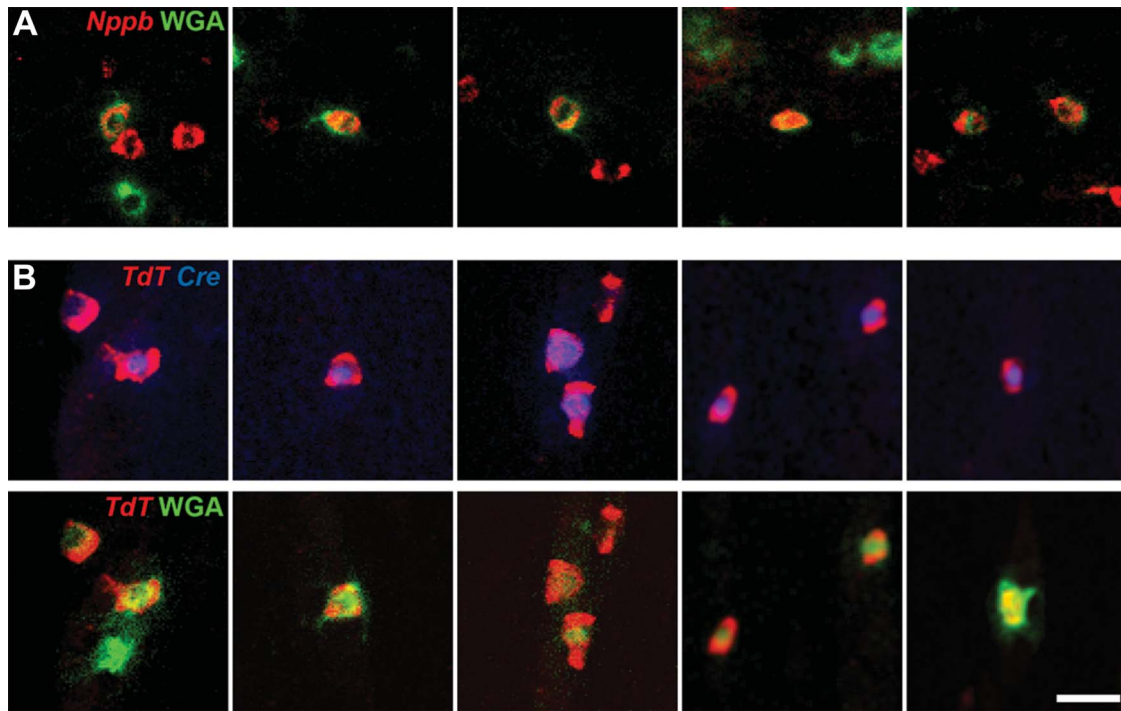


Figure 6. Itch-related neural classes target the meninges. (A) Selected images of fluorescent WGA tracing from the meninges (green) superimposed on ISH signal for *Nppb* (red) confirm that C11 neurons innervate the meninges. (B) Selected images from WGA-tracing in *Mrgpra3-Cre* transgenic mice crossed into an Ai14 *TdTomato* Cre-dependent reporter background showing coexpression of *Cre* (blue, upper panels) and *TdTomato* (red) in neurons labeled by fluorescent WGA tracing from the meninges (green, lower panels). Data are from single sections through the trigeminal ganglion of 4 mice for (A) and 3 mice for (B); scale bar, 40 μ m. WGA, wheat germ agglutinin.

unique in “repurposing” itch-related cells. Analogously, the innervation of the surface of the eye by C1/2 cool sensing neurons³⁷ is most likely not related to the cornea being an important structure for sensing environmental temperature. Instead, the cooling effect of evaporation is probably the main sensory cue, acting as a selective driver for lacrimal-gland stimulation.³⁶ Analogously, corneal C8 neurons (*Trpv1/Trpa1* positive) probably play a specialized protective role by driving tear production in response to irritants, something familiar to most people as a rather painless but nonetheless dramatic side effect of chopping onions. Thus, a sensory neuron’s gene-expression profile provides just one dimension of its identity rather than a direct indication of its sensory role. Our results strongly suggest that the significantly divergent patterns of connectivity amongst transcriptomically related neurons influence both their sensitivity and output. These conclusions about the functional flexibility of well-defined transcriptomic cell types are likely to be more widely applicable and not specific to peripheral sensory neurons.

Innervation of the meninges is particularly relevant in the context of headache and migraine. Thus, it was interesting that half the neurons targeting the meninges were from *Calca* (CGRP)-positive classes in keeping with the role of this neuropeptide in certain types of migraine.^{15,43} Perhaps surprisingly, other cell types expressing trigeminal genes with reported roles in driving headache, for example, *Trpm8*¹² (in C1/2 neurons) and *Trpa1*²¹ (in C8 cells) minimally targeted the meninges (Fig. 5). For C1/2 neurons, this is in line with previous reports of only very sparse innervation of the dura but does suggest that this gene that has been genetically linked to migraine in humans¹² may exert its effects at other target sites. Similarly, recent results suggest *Trpa1* agonists act at nonmeningeal sites to induce migraine.^{22,45} For example, selective ablation of *Trpv1*-expressing trigeminal neurons projecting to the nasal cavity blocked *Trpa1*-agonist-induced changes in meningeal

blood flow²² that are believed important in migraine induction. Moreover, *Trpa1* was recently reported to be expressed in cerebral artery endothelial cells and to drive changes in blood flow to the brain in response to *Trpa1* activation completely independent of the trigeminal system.⁴⁵ Since our data demonstrate that C8 neurons do not innervate the meninges, these mechanisms^{22,45} likely dominate the migraine-inducing effects of compounds such as mustard oil that potentially activate *Trpa1*.

The concept of neural class has been completely altered by recent large-scale scRNA sequencing efforts that have exposed new levels of transcriptomic diversity.^{46,51} Although there is evidence that at least some of these groupings delineate differences between cells, it is unclear how homogeneous each of these classes is.³³ Just as importantly, many of these new transcriptomic classes share extensive similarity with each other and subdivide known types of neurons without obvious functional implication. Mapping class to cells in tissues will likely help address these issues and will provide important insight into neural diversity. Several groups have reported powerful approaches to identify many different genetic targets in anatomical sections that could greatly extend the power of scRNA sequencing.^{6,30,41,49} However, these methods are generally complex, generate extremely large amounts of data, and consequently represent a major undertaking that may limit their use. The basic approach that we describe here for classification of trigeminal neurons represents a compromise between these technically challenging methods and more standard ISH that is often anecdotal and limited to just identifying predicted coexpression patterns. Even if full characterization of the myriad new transcriptomic classes in tissues as complex as the cortex would require localization of more genes than the trigeminal ganglion, the approach we have taken is easily scalable. Moreover, careful selection of probes should make it possible to specifically focus on the most relevant

cell types and to simplify the experimental platform. We envision that combining this type of ISH approach with viral tracing⁵⁰ will be particularly useful for exposing rules guiding long-range connectivity. Similarly, determining the transcriptomic class of functionally labeled neurons^{9,29,39} could be highly informative.

Here, we demonstrate how defining transcriptomic class of trigeminal neurons *in situ* reveals important aspects of their role in sensation. This approach should be easy to extend to DRG neurons simply by adding one additional gene (eg, parvalbumin, *Pvalb*) to classify proprioceptors. In the future, this type of neuronal classification will be especially useful for examining changes in gene expression induced by pathological conditions that trigger chronic pain.²⁰ Fully annotated code is available in Github (<https://github.com/lars-von-buchholtz/InSituClassification>).

Conflict of interest statement

The authors have no conflicts of interest to declare.

Acknowledgements

The authors are grateful to Dr. Xinzhong Dong for providing *Mrgpra3-Cre* reporter mice, to the NINDS Light Imaging Facility, and to other members of our labs for help and advice. Supported by the Intramural program of the National Institutes of Health, National Institute of Dental and Craniofacial Research (N.J.P.R.) and National Center for Integrative and Complementary Health (A.T.C.) and included funding from Department of Defense in the Center for Neuroscience and Regenerative Medicine (A.T.C.).

Author contributions: study design: L.J. von Buchholtz, A.T. Chesler, and N.J.P. Ryba; experimentation: L.J. von Buchholtz, J.J. Emrick, and R.M. Lam; all software development: L.J. von Buchholtz; data analysis: L.J. von Buchholtz, J.J. Emrick, A.T. Chesler, and N.J.P. Ryba; manuscript draft: L.J. von Buchholtz, A.T. Chesler, and N.J.P. Ryba; final manuscript: L.J. von Buchholtz, J.J. Emrick, R.M. Lam, A.T. Chesler, and N.J.P. Ryba. Fully annotated code is available in Github: <https://github.com/lars-von-buchholtz/InSituClassification>.

Appendix A. Supplemental digital content

Supplemental digital content associated with this article can be found online at <http://links.lww.com/PAIN/B13> and <http://links.lww.com/PAIN/B14>.

Supplemental video content

A video abstract associated with this article can be found at, available at <http://links.lww.com/PAIN/B15>.

Article history:

Received 5 March 2020

Received in revised form 9 April 2020

Accepted 10 April 2020

Available online 4 May 2020

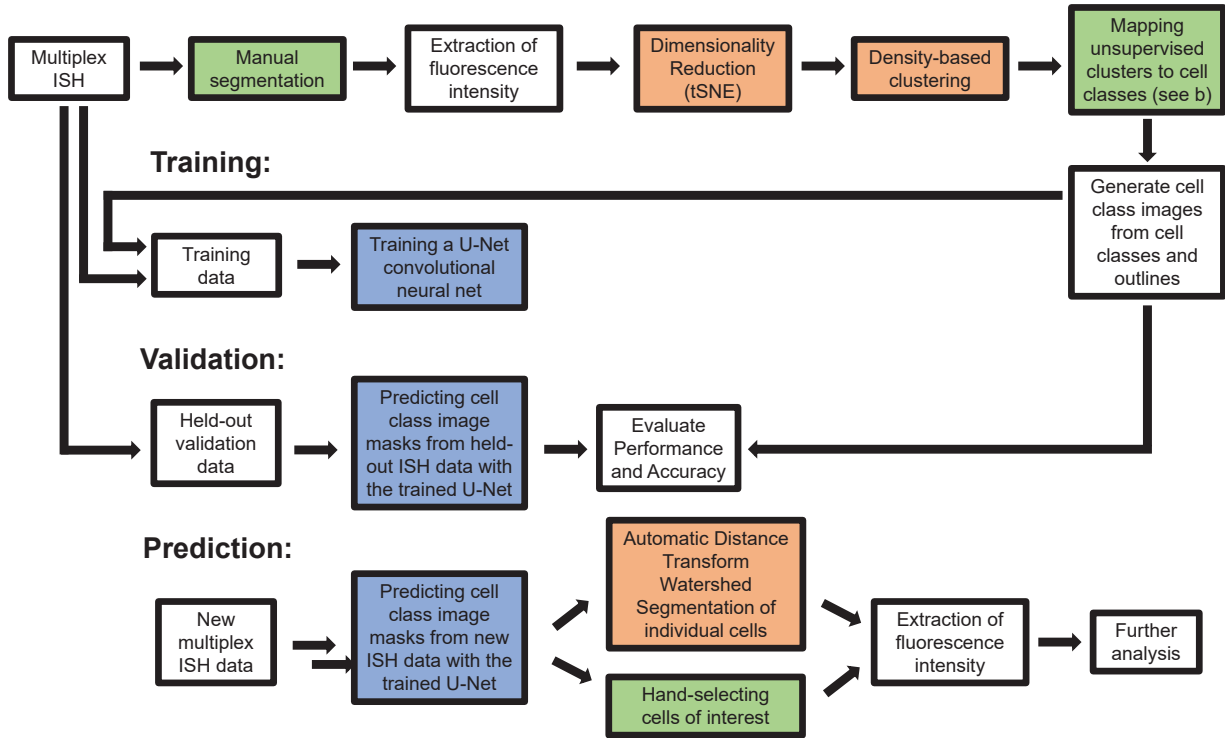
References

- [1] Adelman PC, Baumbauer KM, Friedman R, Shah M, Wright M, Young E, Jankowski MP, Albers KM, Koerber HR. Single-cell q-PCR derived expression profiles of identified sensory neurons. *Mol Pain* 2019;15:174480691988449.
- [2] Arcourt A, Gorham L, Dhandapani R, Prato V, Taberner FJ, Wende H, Gangadharan V, Birchmeier C, Heppenstall PA, Lechner SG. Touch

- receptor-derived sensory information alleviates acute pain signaling and fine-tunes nociceptive reflex coordination. *Neuron* 2017;93:179–93.
- [3] Bautista DM, Siemens J, Glazer JM, Tsuruda PR, Basbaum AI, Stucky CL, Jordt SE, Julius D. The menthol receptor TRPM8 is the principal detector of environmental cold. *Nature* 2007;448:204–8.
- [4] Bautista DM, Wilson SR, Hoon MA. Why we scratch an itch: the molecules, cells and circuits of itch. *Nat Neurosci* 2014;17:175–82.
- [5] Bouharaoua N, Fouquet S, Marcos-Almaraz MT, Karagogeos D, Laroche L, Chedotal A. Genetic analysis of the organization, development, and plasticity of corneal innervation in mice. *J Neurosci* 2019;39:1150–68.
- [6] Chen KH, Boettiger AN, Moffitt JR, Wang S, Zhuang X. RNA imaging. Spatially resolved, highly multiplexed RNA profiling in single cells. *Science* 2015;348:aaa6090.
- [7] Chiu IM, Barrett LB, Williams EK, Strohlic DE, Lee S, Weyer AD, Lou S, Bryman GS, Roberson DP, Ghasemlou N, Piccoli C, Ahat E, Wang V, Cobos EJ, Stucky CL, Ma Q, Liberles SD, Woolf CJ. Transcriptional profiling at whole population and single cell levels reveals somatosensory neuron molecular diversity. *eLife* 2014;3:e04660.
- [8] Choi HMT, Schwarkopf M, Fornace ME, Acharya A, Artavanis G, Stegmaier J, Cunha A, Pierce NA. Third-generation *in situ* hybridization chain reaction: multiplexed, quantitative, sensitive, versatile, robust. *Development* 2018;145:dev165753.
- [9] DeNardo LA, Liu CD, Allen WE, Adams EL, Friedmann D, Fu L, Guenther CJ, Tessier-Lavigne M, Luo L. Temporal evolution of cortical ensembles promoting remote memory retrieval. *Nat Neurosci* 2019;22:460–9.
- [10] Dib-Hajj SD, Black JA, Waxman SG. NaV1.9: a sodium channel linked to human pain. *Nat Rev Neurosci* 2015;16:511–19.
- [11] Dong X, Han S-k, Zylka MJ, Simon MI, Anderson DJ. A diverse family of GPCRs expressed in specific subsets of nociceptive sensory neurons. *Cell* 2001;106:619–32.
- [12] Dussor G, Cao Y-Q. TRPM8 and migraine. *Headache. J Head Face Pain* 2016;56:1406–17.
- [13] Gatto G, Smith KM, Ross SE, Goulding M. Neuronal diversity in the somatosensory system: bridging the gap between cell type and function. *Curr Opin Neurobiol* 2019;56:167–74.
- [14] Ghitani N, Barik A, Szczot M, Thompson JH, Li C, Le Pichon CE, Krashes MJ, Chesler AT. Specialized mechanosensory nociceptors mediating rapid responses to hair pull. *Neuron* 2017;95:944–54.e944.
- [15] Goadsby PJ, Reuter U, Hallstrom Y, Broessner G, Bonner JH, Zhang F, Sapra S, Picard H, Mikol DD, Lenz RA. A controlled trial of erenumab for episodic migraine. *New Engl J Med* 2017;377:2123–32.
- [16] Han L, Limjanyawong N, Ru F, Li Z, Hall OJ, Steele H, Zhu Y, Wilson J, Mitzner W, Kollarik M, Udem BJ, Canning BJ, Dong X. Mrgprs on vagal sensory neurons contribute to bronchoconstriction and airway hyper-responsiveness. *Nat Neurosci* 2018;21:324–8.
- [17] Han L, Ma C, Liu Q, Weng HJ, Cui Y, Tang Z, Kim Y, Nie H, Qu L, Patel KN, Li Z, McNeil B, He S, Guan Y, Xiao B, Lamotte RH, Dong X. A subpopulation of nociceptors specifically linked to itch. *Nat Neurosci* 2013;16:174–82.
- [18] Huang CC, Yang W, Guo C, Jiang H, Li F, Xiao M, Davidson S, Yu G, Duan B, Huang T, Huang AJW, Liu Q. Anatomical and functional dichotomy of ocular itch and pain. *Nat Med* 2018;24:1268–76.
- [19] Julius D. TRP channels and pain. *Annu Rev Cel Dev Biol* 2013;29:355–84.
- [20] Khoutorsky A, Price TJ. Translational control mechanisms in persistent pain. *Trends Neurosci* 2018;41:100–14.
- [21] Kunkler PE, Ballard CJ, Oxford GS, Hurley JH. TRPA1 receptors mediate environmental irritant-induced meningeal vasodilatation. *PAIN* 2011;152:38–44.
- [22] Kunkler PE, Ballard CJ, Pellman JJ, Zhang L, Oxford GS, Hurley JH. Intraganglionic signaling as a novel nasal-meningeal pathway for TRPA1-dependent trigeminovascular activation by inhaled environmental irritants. *PLoS One* 2014;9:e103086.
- [23] LaMotte RH, Dong X, Ringkamp M. Sensory neurons and circuits mediating itch. *Nat Rev Neurosci* 2014;15:19–31.
- [24] Li CL, Li KC, Wu D, Chen Y, Luo H, Zhao JR, Wang SS, Sun MM, Lu YJ, Zhong YQ, Hu XY, Hou R, Zhou BB, Bao L, Xiao HS, Zhang X. Somatosensory neuron types identified by high-coverage single-cell RNA-sequencing and functional heterogeneity. *Cell Res* 2016;26:83–102.
- [25] Lignell A, Kerosuo L, Streichan SJ, Cai L, Bronner ME. Identification of a neural crest stem cell niche by Spatial Genomic Analysis. *Nat Commun* 2017;8:1830.
- [26] Macpherson LJ, Dubin AE, Evans MJ, Marr F, Schultz PG, Cravatt BF, Patapoutian A. Noxious compounds activate TRPA1 ion channels through covalent modification of cysteines. *Nature* 2007;445:541–5.
- [27] Mishra SK, Hoon MA. The cells and circuitry for itch responses in mice. *Science* 2013;340:968–71.

- [28] Mitchell K, Lebovitz EE, Keller JM, Mannes AJ, Nemenov MI, Iadarola MJ. Nociception and inflammatory hyperalgesia evaluated in rodents using infrared laser stimulation after Trpv1 gene knockout or resiniferatoxin lesion. *PAIN* 2014;155:733–45.
- [29] Moeyaert B, Holt G, Madangopal R, Perez-Alvarez A, Fearey BC, Trojanowski NF, Ledderose J, Zolnik TA, Das A, Patel D, Brown TA, Sachdev RNS, Eickholt BJ, Larkum ME, Turrigiano GG, Dana H, Gee CE, Oertner TG, Hope BT, Schreier ER. Improved methods for marking active neuron populations. *Nat Commun* 2018;9:4440.
- [30] Moffitt JR, Bambah-Mukku D, Eichhorn SW, Vaughn E, Shekhar K, Perez JD, Rubinstein ND, Hao J, Regev A, Dulac C, Zhuang X. Molecular, spatial, and functional single-cell profiling of the hypothalamic preoptic region. *Science* 2018;362:eaau5324.
- [31] Nguyen MQ, Le Pichon CE, Ryba N. Stereotyped transcriptomic transformation of somatosensory neurons in response to injury. *eLife* 2019;8:e49679.
- [32] Nguyen MQ, Wu Y, Bonilla LS, von Buchholtz LJ, Ryba NJP. Diversity amongst trigeminal neurons revealed by high throughput single cell sequencing. *PLoS One* 2017;12:e0185543.
- [33] Northcutt AJ, Kick DR, Otopalik AG, Goetz BM, Harris RM, Santin JM, Hofmann HA, Marder E, Schulz DJ. Molecular profiling of single neurons of known identity in two ganglia from the crab *Cancer borealis*. *Proc Natl Acad Sci U S A* 2019;116:26980–90.
- [34] Osteen JD, Herzig V, Gilchrist J, Emrick JJ, Zhang C, Wang X, Castro J, Garcia-Caraballo S, Grundy L, Rychkov GY, Weyer AD, Dekan Z, Undheim EA, Alewood P, Stucky CL, Brierley SM, Basbaum AI, Bosmans F, King GF, Julius D. Selective spider toxins reveal a role for the Nav1.1 channel in mechanical pain. *Nature* 2016;534:494–9.
- [35] Pal NR, Pal SK. A review on image segmentation techniques. *Pattern Recognition* 1993;26:1277–94.
- [36] Parra A, Madrid R, Echevarria D, del Olmo S, Morenilla-Palao C, Acosta MC, Gallar J, Dhaka A, Viana F, Belmonte C. Ocular surface wetness is regulated by TRPM8-dependent cold thermoreceptors of the cornea. *Nat Med* 2010;16:1396–9.
- [37] Pogorzala LA, Mishra SK, Hoon MA. The cellular code for mammalian thermosensation. *J Neurosci* 2013;33:5533–41.
- [38] Ronneberger O, Fischer P, Brox T. U-net: convolutional networks for biomedical image segmentation. In: Navab N, Hornegger J, Wells W, Frangi A (eds). *Medical Image Computing and Computer-Assisted Intervention – MICCAI 2015*. MICCAI 2015. Lecture Notes in Computer Science, vol 9351.
- [39] Sathyamurthy A, Johnson KR, Matson KJE, Dobrott CI, Li L, Ryba AR, Bergman TB, Kelly MC, Kelley MW, Levine AJ. Massively parallel single nucleus transcriptional profiling defines spinal cord neurons and their activity during behavior. *Cell Rep* 2018;22:2216–25.
- [40] Satija R, Farrell JA, Gennert D, Schier AF, Regev A. Spatial reconstruction of single-cell gene expression data. *Nat Biotechnol* 2015;33:495–502.
- [41] Shah S, Lubeck E, Zhou W, Cai L. seqFISH accurately detects transcripts in single cells and reveals robust spatial organization in the hippocampus. *Neuron* 2017;94:752–8.e1.
- [42] Sharma N, Flaherty K, Lezgyyeva K, Wagner DE, Klein AM, Ginty DD. The emergence of transcriptional identity in somatosensory neurons. *Nature* 2020;577:392–8.
- [43] Silberstein SD, Dodick DW, Bigal ME, Yeung PP, Goadsby PJ, Blankenbiller T, Grozinski-Wolff M, Yang R, Ma Y, Aycardi E. Fremanezumab for the preventive treatment of chronic migraine. *New Engl J Med* 2017;377:2113–22.
- [44] Solinski HJ, Kriegbaum MC, Tseng PY, Earnest TW, Gu X, Barik A, Chesler AT, Hoon MA. Nppb neurons are sensors of mast cell-induced itch. *Cell Rep* 2019;26:3561–73.e4.
- [45] Sullivan MN, Gonzales AL, Pires PW, Bruhl A, Leo MD, Li W, Oulidi A, Boop FA, Feng Y, Jaggar JH, Welsh DG, Earley S. Localized TRPA1 channel Ca²⁺ signals stimulated by reactive oxygen species promote cerebral artery dilation. *Sci Signaling* 2015;8:ra2.
- [46] Tasic B, Yao Z, Graybuck LT, Smith KA, Nguyen TN, Bertagnolli D, Gody J, Garren E, Economo MN, Viswanathan S, Penn O, Bakken T, Menon V, Miller J, Fong O, Hirokawa KE, Lathia K, Rimorin C, Tieu M, Larsen R, Casper T, Barkan E, Kroll M, Parry S, Shapovalova NV, Hirschstein D, Pendergraft J, Sullivan HA, Kim TK, Szafer A, Dee N, Groblewski P, Wickersham I, Cetin A, Harris JA, Levi BP, Sunkin SM, Madisen L, Daigle TL, Looger L, Bernard A, Phillips J, Lein E, Hawrylycz M, Svoboda K, Jones AR, Koch C, Zeng H. Shared and distinct transcriptomic cell types across neocortical areas. *Nature* 2018;563:72–8.
- [47] Umans BD, Liberles SD. Neural sensing of organ volume. *Trends Neurosci* 2018;41:911–24.
- [48] Usoskin D, Furlan A, Islam S, Abdo H, Lonnerberg P, Lou D, Hjerling-Leffler J, Haeggstrom J, Kharchenko O, Kharchenko PV, Linnarsson S, Ernfors P. Unbiased classification of sensory neuron types by large-scale single-cell RNA sequencing. *Nat Neurosci* 2015;18:145–53.
- [49] Wang X, Allen WE, Wright MA, Sylwestrak EL, Samusik N, Vesuna S, Evans K, Liu C, Ramakrishnan C, Liu J, Nolan GP, Bava FA, Deisseroth K. Three-dimensional intact-tissue sequencing of single-cell transcriptional states. *Science* 2018;361:eaat5691.
- [50] Winnubst J, Bas E, Ferreira TA, Wu Z, Economo MN, Edson P, Arthur BJ, Bruns C, Rokicki K, Schauder D, Olbris DJ, Murphy SD, Ackerman DG, Arshadi C, Baldwin P, Blake R, Elsayed A, Hasan M, Ramirez D, Dos Santos B, Weldon M, Zafar A, Dudman JT, Gerfen CR, Hantman AW, Korff W, Sternson SM, Spruston N, Svoboda K, Chandrashekar J. Reconstruction of 1,000 projection neurons reveals new cell types and organization of long-range connectivity in the mouse brain. *Cell* 2019;179:268–81.e213.
- [51] Zeisel A, Hochgerner H, Lonnerberg P, Johnsson A, Memic F, van der Zwan J, Haring M, Braun E, Borm LE, La Manno G, Codeluppi S, Furlan A, Lee K, Skene N, Harris KD, Hjerling-Leffler J, Arenas E, Ernfors P, Marklund U, Linnarsson S. Molecular architecture of the mouse nervous system. *Cell* 2018;174:999–1014.e1022.
- [52] Zheng Y, Liu P, Bai L, Trimmer JS, Bean BP, Ginty DD. Deep sequencing of somatosensory neurons reveals molecular determinants of intrinsic physiological properties. *Neuron* 2019;103:598–616.e597.
- [53] Zimmerman A, Bai L, Ginty DD. The gentle touch receptors of mammalian skin. *Science* 2014;346:950–4.
- [54] Zimmermann K, Leffler A, Babes A, Cendan CM, Carr RW, Kobayashi J, Nau C, Wood JN, Reeh PW. Sensory neuron sodium channel Nav1.8 is essential for pain at low temperatures. *Nature* 2007;447:855–8.

a

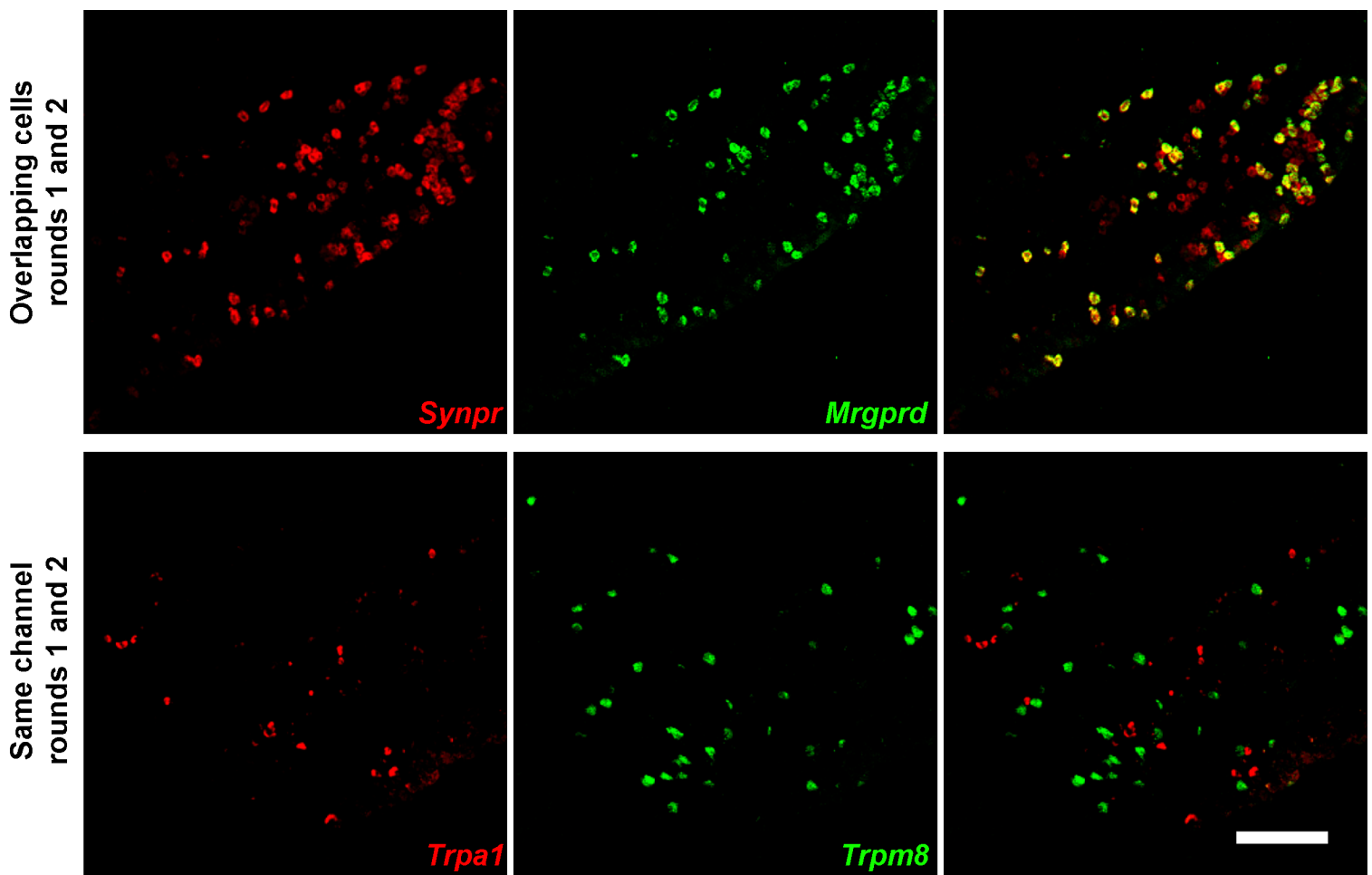


b

Cell class	Criteria for cluster mapping	Expression pattern within 8 probe model
C1	High <i>Trpm8</i>	<i>Trpm8</i> +
C3	High <i>Cd34</i>	<i>Fxyd2</i> +, <i>Tmem233</i> -, <i>S100b</i> -, <i>Nppb</i> -, <i>Mrgprd</i> -
C4	High <i>S100b</i> , low <i>Fxyd2</i> , low <i>Calca</i>	<i>S100b</i> +, <i>Fxyd2</i> -, <i>Calca</i> -
C5	High <i>S100b</i> , high <i>Fxyd2</i>	<i>S100b</i> +, <i>Fxyd2</i> +
C6	High <i>S100b</i> , high <i>Calca</i>	<i>S100b</i> +, <i>Calca</i> +
C7/9/10	High <i>Trpv1</i> , low <i>Trpa1</i>	<i>Calca</i> +, <i>S100b</i> -, <i>Tmem233</i> -, <i>Trpa1</i> -, <i>Fxyd2</i> -, <i>Nppb</i> -
C8	High <i>Trpa1</i>	<i>Trpa1</i> +, <i>Calca</i> +, <i>Tmem233</i> -, <i>Fxyd2</i> -, <i>Mrgprd</i> -
C11	High <i>Nppb</i>	<i>Nppb</i> +
C12	High <i>Etv1</i> , low <i>Nppb</i>	<i>Tmem233</i> +, <i>Mrgprd</i> -, <i>Nppb</i> -, <i>S100b</i> -
C13	High <i>Mrgprd</i>	<i>Mrgprd</i> +

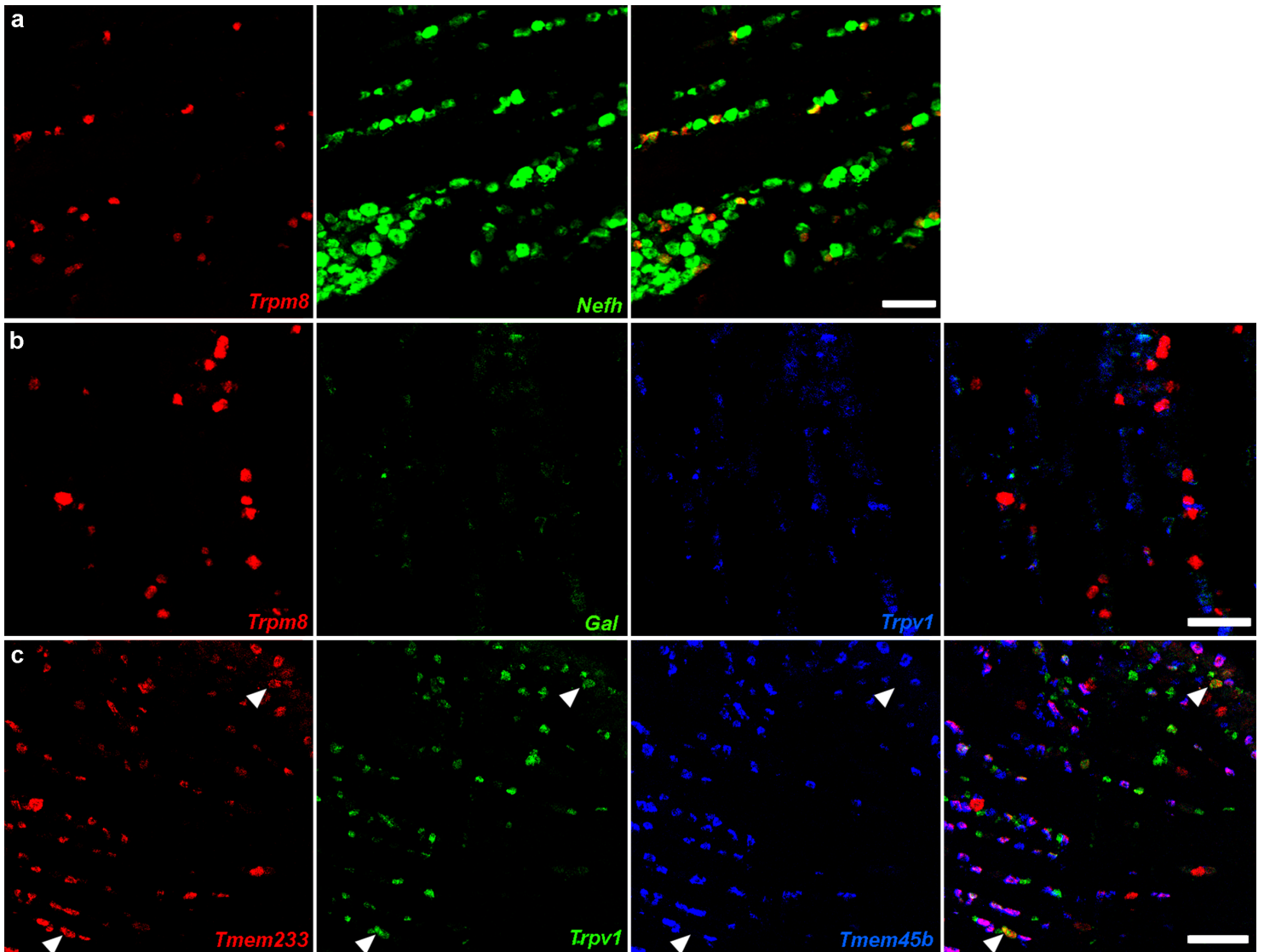
Supplementary Figure 1. Data flow in the semi-supervised machine learning approach

(a) Manually generated, supervised aspects (green) and automatically generated, unsupervised aspects (brown) of the data were used to train the core U-Net Deep Learning model (blue). This model was then validated on a held-out validation data set and ultimately was used to predict cell class images from new multiplex ISH data. (b) Criteria used for cluster / cell class matching and expression patterns observed within the 8-probe model.



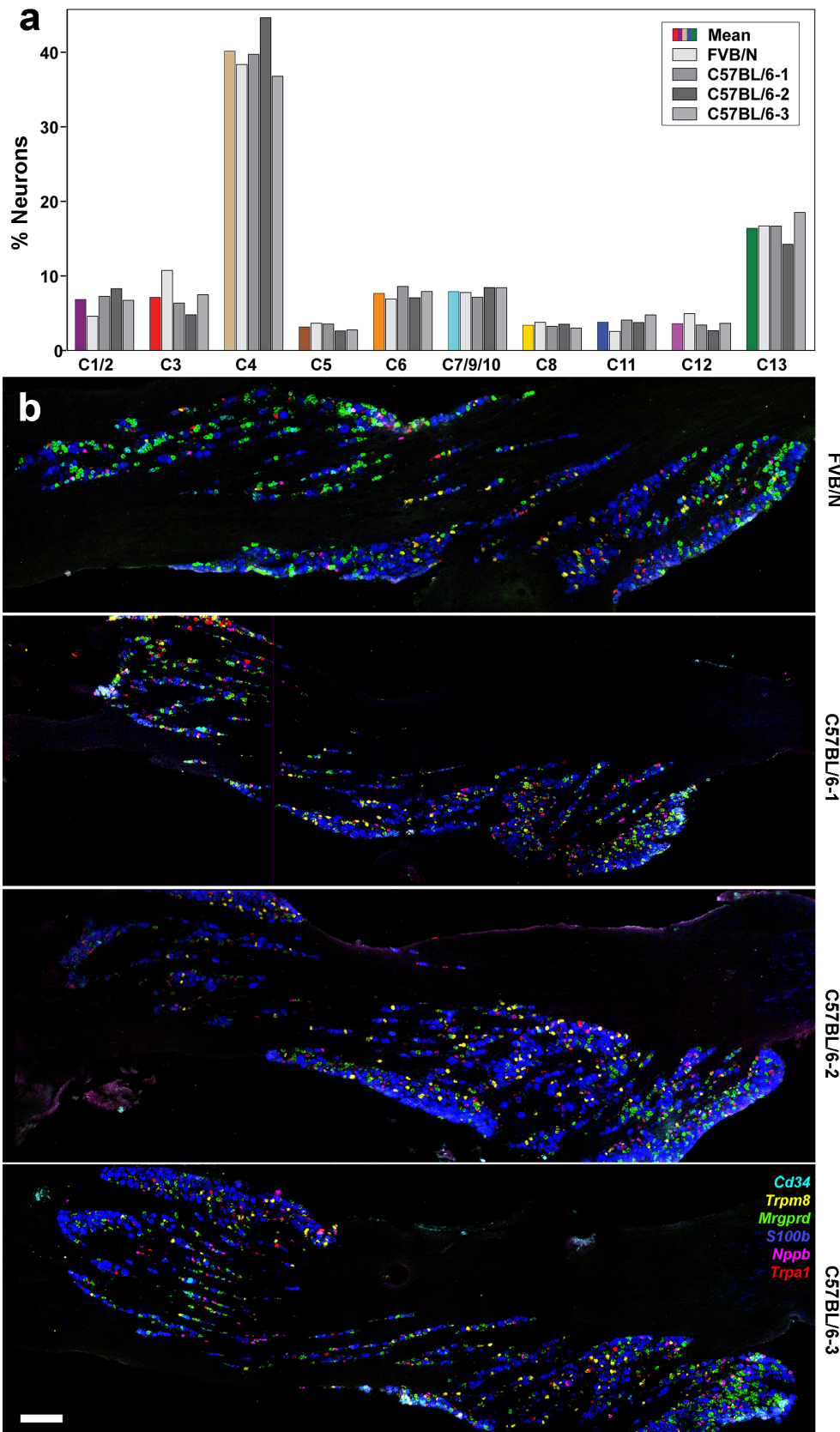
Supplementary Figure 2. Controls for multiplex ISH

Example images from different rounds of ISH on a single section. Top panels: control to show that images can be accurately aligned between rounds using rotation and transposition. A subset of cells labeled in round 1 by *Synpr* were also detected in round 2 using a probe to *Mrgprd*. These cells align perfectly as shown in the combined image. Lower panels: control to demonstrate that stripping probes prevents signal carry over between rounds. *Trpa1* and *Trpm8* are expressed in non-overlapping populations of cells and were detected using the same amplifiers and fluorophores in rounds 1 and 2 respectively. The combined image shows that these two probes detect completely non-overlapping cells confirming that there is no carryover of signal between rounds; scale bar, 100 μm .



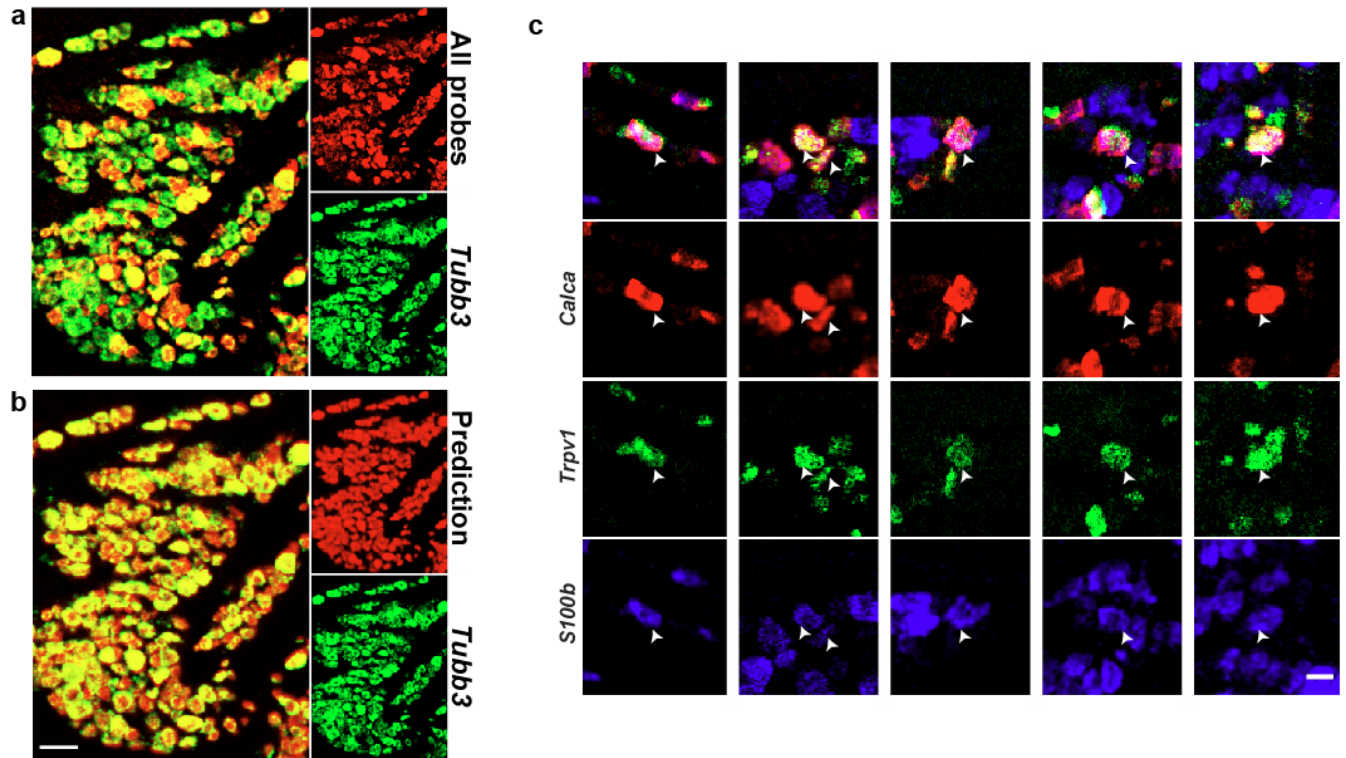
Supplementary Figure 3. Not all predicted neural classes were detected by multiplex ISH

(a) Expression of *Nefh* was predicted to divide *Trpm8* expressing neurons into 2 distinct classes (C1 and C2). However, ISH revealed that all *Trpm8* neurons expressed similar levels of *Nefh*. (b) A second marker predicted to distinguish C1 and C2 neurons was the neuropeptide galanin. ISH revealed low level expression of *Gal* in the ganglion and co-expression with *Trpv1*, rather than *Trpm8* (a marker of C1/2 neurons). Together these data suggest that the division of C1 and C2 classes in the sc-analysis may be a consequence of methodology rather than biology. (c) Single cell data divided *Trpv1*-expressing neurons into several classes. One of these, C7, was distinguished from other classes of *Trpv1* neurons by its co-expression of *Tmem233* but not *Tmem45b*. As illustrated in an example image of multiplexed ISH, a few such cells (arrowheads) could be distinguished but they failed to segregate from classes C9 and C10 in tSNE based cluster analysis (Fig. 3); scale bars, 125 μm .



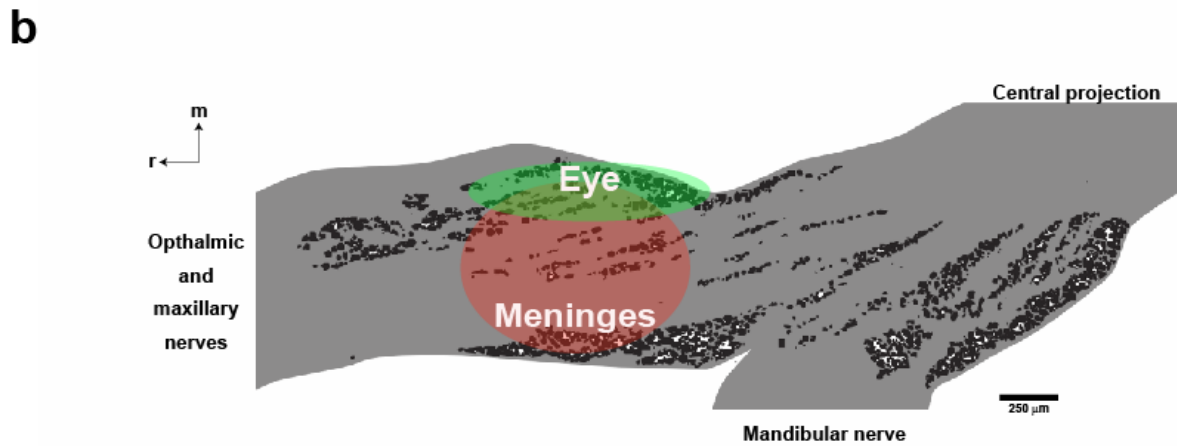
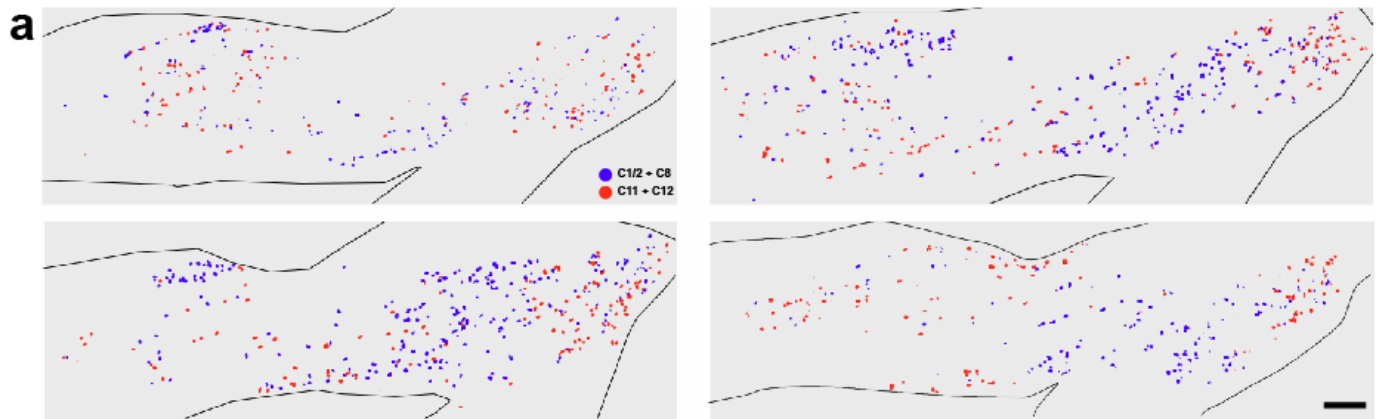
Supplementary Figure 4. High consistency in class assignment between animals and sections

(a) Bar graph showing the classification of trigeminal neurons using multiplex ISH in four animals (grey bars) and the mean values (colored bars). (b) Sections of the trigeminal ganglion from the FVB/N and three C57BL/6 mice; shown are the overlaid ISH images of 6 non-overlapping probes colored as indicated; scale bar, 200 μ m.



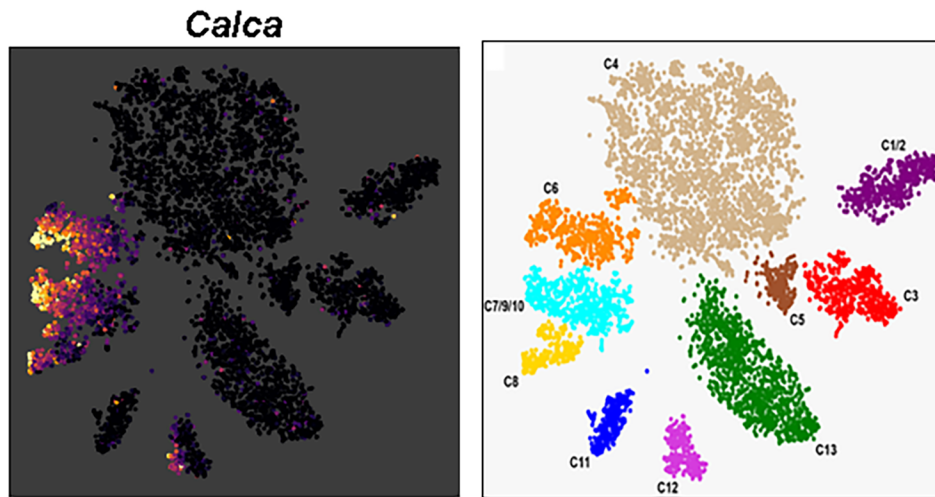
Supplementary Figure 5. ISH probes and U-Net predictions identify all trigeminal neurons

(a) Representative image showing that in combination the 13 ISH probes used in clustering-based classification of trigeminal neurons (colored red) detected all the neurons identified using a pan-neuronal *Tubb3* probe (green) and did not identify non-neuronal cells. Similarly, (b) the U-Net prediction (red) very closely matched the distribution of neurons revealed by *Tubb3* ISH (green). Importantly, predicted neurons were always *Tubb3* positive. Also note the more uniform definition of cell boundaries that can be discerned in the prediction data than in the ISH images; scale bar 100 μ m. (c) Sample images selected to show a subset of C6 neurons defined by co-expression of *Calca* (red) and *S100b* (blue) also express the heat and capsaicin sensitive ion channel *Trpv1* (green); these neurons are arrowed, scale bar 20 μ m.



Supplementary Figure 6. Regional segregation of neural class in the trigeminal ganglion

(a) Anatomical mapping of C1/2 plus C8 neurons (blue) and C11 plus C12 neurons (red) in the sections through the trigeminal ganglion of four mice reveals extensive spatial segregation of these neural classes; differences between the four ganglia likely reflect the sectioning plane but may also include animal to animal variation. (b) WGA-labeling from the eye and meninges labeled distinctive regions of the ganglion (indicated by green and red shading); scale bars, 250 μm ; m, medial; r, rostral.



Supplementary Figure 7. tSNE representations of ISH intensities of *Calca* expression in trigeminal ganglion neurons

(Left panel) Cells were manually segmented and the cellular ISH intensity of *Calca* expression was assessed (see Fig. 2b). The tSNE representation highlights differences in expression between classes and shows that a fraction of C12 neurons express this gene. (Right panel) The distribution of neuronal classes is shown for comparison purposes.

Table S1 Statistical analysis of data in Fig. 5c

208 trigeminal neurons innervating the eye and 239 targeting the meninges were classified. The proportional representations of the different neuronal classes in these populations were compared with their prevalence in the trigeminal ganglion using an unpooled two-tailed z-test for proportions that does not assume common variance between the two populations. The p-values are reported for each class. In addition, where differences were significant, $p < 0.05$, the color coding indicates upregulation (pink) or downregulation (pale blue) in the neurons innervating the target.

Neuronal Class	Eye (p-value)	Meninges (p-value)
C1/2	8.65×10^{-6}	4.08×10^{-7}
C3	8.45×10^{-11}	8.19×10^{-9}
C4	5.41×10^{-8}	4.29×10^{-4}
C5	4.01×10^{-3}	0.381
C6	0.015	4.21×10^{-7}
C7/9/10	0.260	5.53×10^{-5}
C8	3.51×10^{-14}	$< 1 \times 10^{-20}$
C11	$< 1 \times 10^{-20}$	0.062
C12	0.215	7.16×10^{-5}
C13	9.37×10^{-8}	6.66×10^{-16}

Chapter 4

Part 2

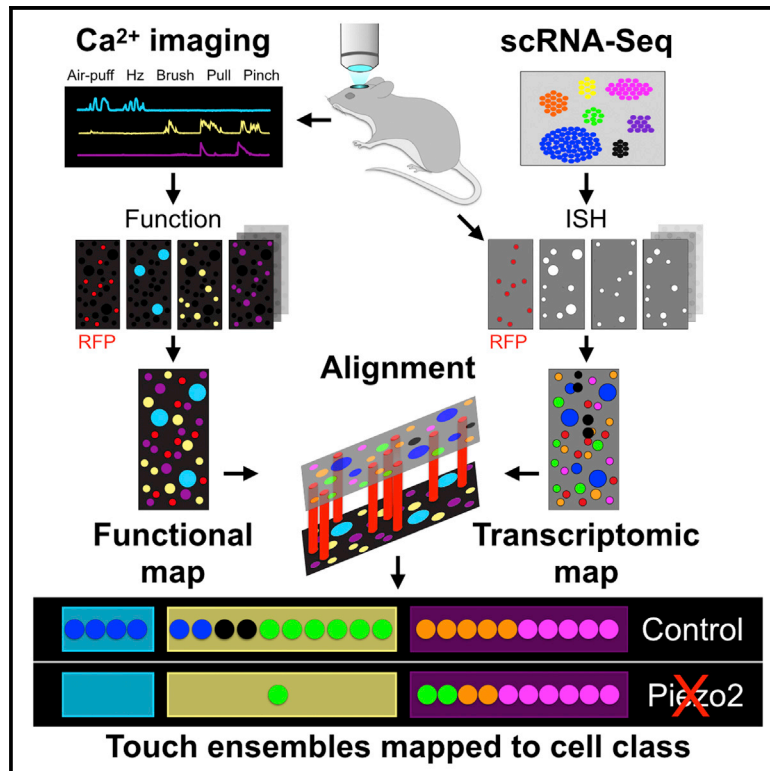
* This section is presented in the form it was published in the journal *Neuron* with the following citation and contributions

“von Buchholtz, Lars J., Nima Ghitani, **Ruby M. Lam**, Julia A. Licholai, Alexander T. Chesler, and Nicholas JP Ryba. "Decoding cellular mechanisms for mechanosensory discrimination." *Neuron* 109, no. 2 (2021): 285-298”

Contributions: R.M.L. collected data, performed analysis and conducted the investigation. Specifically, RML conducted and analyzed functional calcium imaging experiments and preprocessed imaging and insitu data with warping alignments. The results of RML investigations are reported in Figure 6, Figure 7, Supplementary Figure4, Supplementary Figure 7 and Supplementary Table 1. RML created and maintained viral cre induced Piezo2KO:Gcamp:tacrfp animals. She reviewed and edited final versions of the manuscript.

Decoding Cellular Mechanisms for Mechanosensory Discrimination

Graphical Abstract



Authors

Lars J. von Buchholtz, Nima Ghitani,
Ruby M. Lam, Julia A. Licholai,
Alexander T. Chesler,
Nicholas J.P. Ryba

Correspondence

alexander.chesler@nih.gov (A.T.C.),
nick.ryba@nih.gov (N.J.P.R.)

In Brief

von Buchholtz et al. evaluate the representation of naturalistic mechanosensory stimuli by combining functional imaging with multigene *in situ* hybridization to determine gene expression profiles of large ensembles of trigeminal neurons. Their results expose a transcriptomic logic for touch discrimination and cell-class-specific roles for the Piezo2 ion channel.

Highlights

- Naturalistic mechanical stimuli activate large overlapping ensembles of neurons
- *In situ* hybridization after functional imaging maps responses to cell class
- Tuning properties of the classes reveal a transcriptomic basis for specialization
- Mechanotransduction via Piezo2 contributes to almost all aspects of touch



Article

Decoding Cellular Mechanisms for Mechanosensory Discrimination

Lars J. von Buchholtz,^{1,4} Nima Ghitani,^{2,4} Ruby M. Lam,^{2,3} Julia A. Licholai,^{1,3} Alexander T. Chesler,^{2,5,*} and Nicholas J.P. Ryba^{1,*}

¹National Institute of Dental and Craniofacial Research, NIH, Bethesda, MD 20892, USA

²National Center for Complementary and Integrative Health, Bethesda, MD 20892, USA

³Brown-National Institutes of Health Graduate Partnerships Program, Brown University, Providence, RI, USA

⁴These authors contributed equally

⁵Lead Contact

*Correspondence: alexander.chesler@nih.gov (A.T.C.), nick.ryba@nih.gov (N.J.P.R.)

<https://doi.org/10.1016/j.neuron.2020.10.028>

SUMMARY

Single-cell RNA-sequencing and *in vivo* functional imaging provide expansive but disconnected views of neuronal diversity. Here, we developed a strategy for linking these modes of classification to explore molecular and cellular mechanisms responsible for detecting and encoding touch. By broadly mapping function to neuronal class, we uncovered a clear transcriptomic logic responsible for the sensitivity and selectivity of mammalian mechanosensory neurons. Notably, cell types with divergent gene-expression profiles often shared very similar properties, but we also discovered transcriptomically related neurons with specialized and divergent functions. Applying our approach to knockout mice revealed that Piezo2 differentially tunes all types of mechanosensory neurons with marked cell-class dependence. Together, our data demonstrate how mechanical stimuli recruit characteristic ensembles of transcriptomically defined neurons, providing rules to help explain the discriminatory power of touch. We anticipate a similar approach could expose fundamental principles governing representation of information throughout the nervous system.

INTRODUCTION

Sensory neurons innervating the skin provide animals with important details about their environment and induce complex behavioral, motor, and emotional responses to a range of stimuli including temperature and touch. These neurons, localized to the trigeminal and dorsal root ganglia, have been classified using anatomy, genetics, physiology and biochemistry, according to their functional tuning and by the responses they provoke (Abraira and Ginty, 2013; Basbaum et al., 2009; Julius, 2013; Le Pichon and Chesler, 2014). Although some modalities, like cooling (Bautista et al., 2007; Dhaka et al., 2007) or itch (Abraira and Ginty, 2013; Mishra and Hoon, 2013), may be encoded by dedicated neurons that serve as labeled lines, it is believed that most types of mechanical stimuli activate broad and overlapping populations of differentially responsive cells to trigger percepts (Norrzell et al., 1999). Indeed, the human sense of touch exhibits a tremendous range of sensitivity: detecting the bending of a single hair but still discriminating intensity even after a stimulus becomes painful (Hill and Bautista, 2020). At the same time, it provides exquisite positional information and temporal resolution as well as a multitude of qualities (e.g., sharpness, roughness, or compliance). Most naturalistic stimuli are extremely complex, for example a breath of wind may ruffle

hairs, vibrate the skin, and rapidly evolve in terms of direction, speed, and intensity, but both the nature of the stimulus and its features can be instantaneously and unambiguously recognized. How does the activity of the different types of sensory neurons combine to provide us with this remarkable perceptual power?

Recently, single-cell (sc)RNA-sequencing added a new dimension to understanding the diversity of the nervous system by classifying neurons according to the expression of hundreds of genes (Tasic et al., 2018; Zeisel et al., 2018). In the somatosensory system, many of the sc-transcriptomic classes define cell types that had previously been studied using genetic strategies supporting the premise that they encode functional types of cells (Nguyen et al., 2017; Sharma et al., 2020; Usoskin et al., 2015). Moreover, comparison between dorsal root and trigeminal ganglia reveals a set of tightly conserved cell types that provide a minimal framework for classifying these cells (Gatto et al., 2019; von Buchholtz et al., 2020). In parallel, advances in functional imaging have provided a way to characterize large groups of neurons according to their activity (Ghitani et al., 2017; Szczot et al., 2018; Yarmolinsky et al., 2016). One approach for associating function with gene expression relies on restricting expression of genetically encoded calcium indicators (e.g., GCaMP) to select subsets of neurons (Chang et al., 2015; Ghitani et al.,



2017; Williams et al., 2016). Other strategies involve single cell sequencing after functional recordings (Cadwell et al., 2016) or functional tagging (Lee et al., 2019). However, naturalistic stimuli produce highly complex neuronal activity patterns. Thus, in a more ideal scenario, transcriptomic class of all the responding neurons would be determined and directly matched to function at a single cell level. We reasoned that molecular profiling after Ca-imaging should link these different types of classification, broadly map function to transcriptomic class, and reveal how features of mechanical stimuli are detected and represented by the somatosensory system.

The neurons responsible for detecting touch in mice fall into at least 5 broad categories (Abraira and Ginty, 2013; Hill and Bautista, 2020; Zimmerman et al., 2014) reflecting their degree of myelination and conduction velocity (unmyelinated, c; medium, A δ ; and high, A β) and also their sensitivity (high or low threshold mechanoreceptors, HTMRs or LTMRs, respectively). These groups are also distinguished at the transcriptomic level: in the trigeminal ganglion, c-LTMRs have been referred to as C3 cells, A β -LTMRs as C4, A δ -LTMRs as C5, A δ -HTMRs as C6, and c-fiber nociceptors (including HTMRs), a range of classes from C7–C13 (Nguyen et al., 2017). Of these, the C4 A β -LTMRs are known to be physiologically and anatomically variable. For example, they exhibit a range of adaptation rates (e.g., slowly adapting [SA] or rapidly adapting [RA]), diverse terminal specializations (e.g., lanceolate or circumferential endings) as well as distinct receptive tuning profiles (Bai et al., 2015; Ghitani et al., 2017; Rutlin et al., 2014; Zimmerman et al., 2014). Consistent with this heterogeneity, the C4 class (A β -LTMRs) can be divided into many transcriptomic subgroups (Nguyen et al., 2019; Sharma et al., 2020). However, how these different types of somatosensory neurons combine to represent and distinguish a gentle brush or a pinch remains largely unknown.

We recently showed that multiplex *in situ* hybridization (ISH) using just eight genes could be used to distinguish the major classes of trigeminal neurons (von Buchholtz et al., 2020). Based on this approach, we have now developed a platform for assigning transcriptomic class to large ensembles of functionally characterized neurons and use it to reveal important features and mechanistic detail about the sense of touch.

RESULTS

Matching functionally distinct classes of neurons with their molecular expression profile is a fundamental problem throughout neuroscience. Recently, we developed a GCaMP6f-based approach for measuring the sensory responses of trigeminal neurons innervating the cheek (Ghitani et al., 2017; Szczot et al., 2018). Importantly, this type of Ca-imaging allows the functional tuning of hundreds of neurons to be determined simultaneously, is highly reliable with the same neurons responding reproducibly to the same type of stimulation and has single-spike sensitivity. In parallel we developed a multigene ISH methodology for decoding transcriptomic class in tissue sections (von Buchholtz et al., 2020). We reasoned that combining these techniques might provide a powerful strategy for determining not only how complex mechanical stimuli are represented by

ensembles of neurons but also if responding cells are differentially tuned by virtue of their gene expression profiles.

A Robust Approach for Aligning *In Vivo* Functional Imaging to Post Hoc ISH

Neonatal injection of adeno associated virus (AAV)-Cre into Ai95 (*Rosa-LSL-GCaMP6f*) mice provides an effective way of inducing GCaMP-expression in a large and representative subset of trigeminal neurons without excessive neuropil staining (Szczot et al., 2018). *In vivo* epifluorescence GCaMP-imaging of the trigeminal ganglion reveals the functional tuning of neurons at its exposed dorsal surface. After isolating the ganglion, a whole mount ISH preparation should provide information about gene expression in the same set of cells, but tissue distortion confounds accurate alignment of the different images. We reasoned that if a red fluorescent protein marker could be detected during the functional imaging and also by whole mount ISH-imaging, these cells would act as fixed guideposts for image matching. To this end, we expressed a red fluorescent protein (tagRFP) in a subset of sensory neurons. The *Tac1-tagRFP* mouse-line that we chose provided four important features: first, fluorescent signal was readily detectable and resolved from GCaMP fluorescence in live mice; second, expression of this marker was dense enough to allow accurate alignment, but nonetheless sparse enough for resolution of single cells (Figure 1A); third, the endogenous tagRFP fluorescence was destroyed during ISH meaning that it did not interfere with hybridization signal detection; finally, *Tac1* is a useful marker of a subset of nociceptive somatosensory neurons, thus its expression pattern contributes to the molecular characterization of cells.

Images from functional imaging and ISH (Figure 1A) illustrate that the whole mount ISH recapitulated the pattern of tagRFP detected *in vivo* but with significant regional distortions. Even with the tagRFP-guideposts, these differences prevented alignment using automated approaches based on simple transformations. To solve this issue, we manually matched guideposts between the two images (Figure 1B) and implemented an algorithm that splits the images into triangular sections where the guideposts serve as vertices (Figure 1B, Delaunay triangulation). The Delaunay triangles in the ISH image could then be warped into their target counterparts in the live image by affine transformation (Figure 1C). A related strategy is used in face-morphing (Figure S1A), which provided us with a framework for software development. Because *Tac1*-expression is dense and distributed in cells of the trigeminal ganglion, we typically could match large areas containing hundreds of neurons in multiple rounds of ISH imaging to their *in vivo* partners (Figure 1C) with accurate cellular resolution (Figures S1B and S1C) allowing us to map functional responses to GCaMP-expressing cells (Figure 1D). A similar approach could easily be developed to simultaneously determine the gene-expression profiles of ensembles of functionally characterized neurons in many regions of the nervous system.

Decoding the Molecular Signatures of Neurons Activated by Naturalistic Mechanical Stimuli

Naturalistic mechanical stimuli including gentle brush, pinch, hair-pull, air-puff, and vibration applied to a small region of cheek

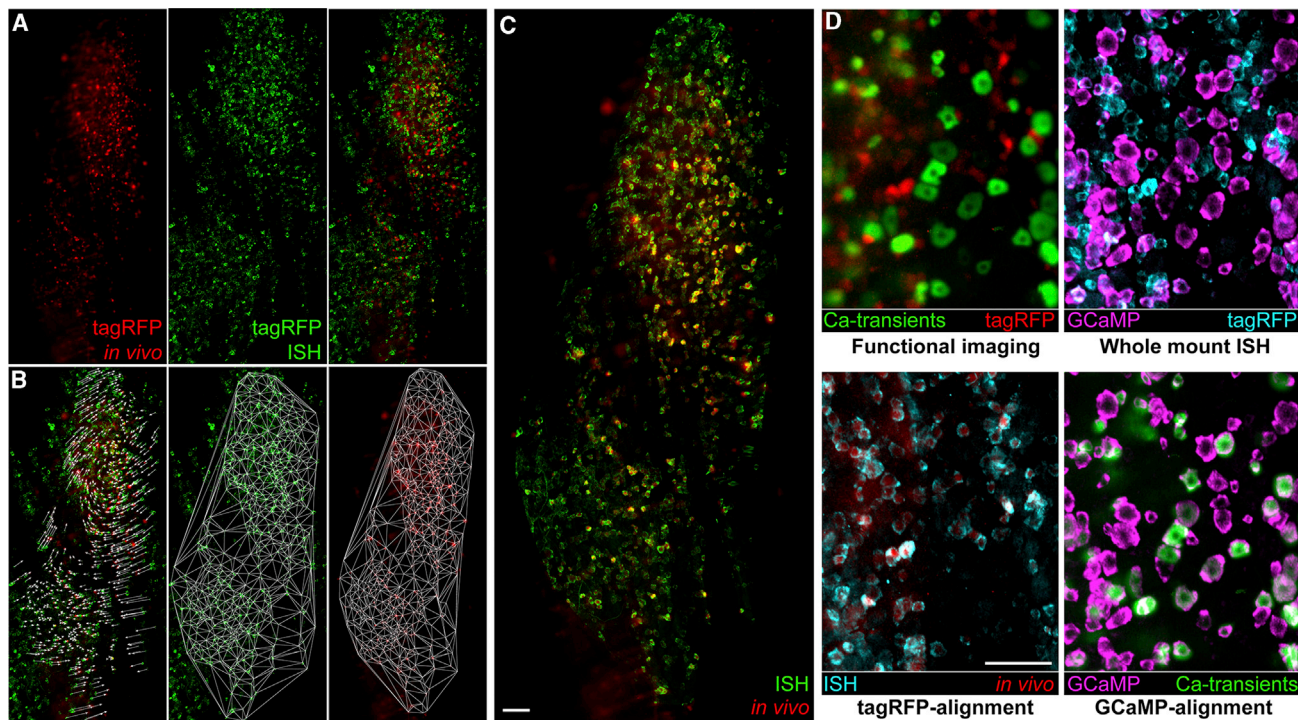


Figure 1. Aligning *In Vivo* Imaging of Large Ensembles of Neurons with Whole Mount ISH

(A) Example images of a dorsal view of the trigeminal ganglion showing red fluorescence in a live *Tac1-tagRFP* mouse (left panel, red) and whole mount *tagRFP* ISH from the excised ganglion (middle panel, green). Images were aligned using scaled rotation (right panel); note that only very few cells overlap but other non-aligned pairs of red and green neurons can be identified.

(B) Images were aligned by manual matching of cell pairs (left panel, arrows) to identify guideposts for Delaunay triangulation of the ISH image (middle panel) and construction of corresponding triangles in the live image (right panel). The aligned region is delimited by the triangles.

(C) Affine transform of Delaunay triangles (see [Figure S1](#)) generates a continuous image where a large area and many neurons are perfectly matched between the live image (red) and ISH (green).

(D) Imaging from a different mouse showing *in vivo* fluorescence of tagRFP (top left, red) and GCaMP6f calcium transients (green, see methods for details). The whole mount ISH counterpart (top right; tagRFP, cyan; GCaMP6f, magenta) was aligned to the live image using tagRFP guideposts (bottom left). As a result, functional activity maps also matched the GCaMP6f expression (bottom right). Note that as expected only a subset of GCaMP6f expressing neurons responded to mechanical stimulation of the cheek. Scale bars, 100 μ m.

See also [Figure S1](#).

located between the whisker pad and the eye activated large sets of trigeminal neurons ([Figure 2](#)). These responses were robust, reliable, and selective allowing neurons to be assigned to one of five categories ([Figure 2A](#)). We defined criteria (see [STAR Methods](#)) based on maximum calcium responses to the stimuli for automatically classifying 1,840 mechanosensory neurons from 23 mice. The heatmap and example traces of responses ([Figure 2](#)) confirm that this approach provides overall consistency while eliminating observer bias. Air-puff cells were rather selectively tuned but often also responded strongly to vibration; vibration cells only detected vibration; brush cells detected gentle brushing, but typically also responded to high threshold stimulation and vibration; high threshold cells (HT-cells) were tuned to noxious stimuli (pinch and/or hair-pull) and showed, at most, very weak responses to brush or air-puff; finally, we identified a group of mixed responders that detected air-puff, brush, and high-threshold stimulation. Approximately 40% of mechanosensors were HT-cells, 35% were brush cells with the other three classes making up the remaining 25% ([Figure 2A](#)). Notably, \sim 80% of the mechanosensory neurons were

engaged by noxious stimuli including all brush cells and mixed responders. The skin is flexible, meaning that hair pull and pinch affect wide areas of the face. Therefore, it would be expected that sensitive brush responsive neurons might be activated by distal noxious stimuli. Indeed, this is exactly what we found ([Figure S2](#)): brush cells respond to pinch at multiple locations on the cheek. By contrast, HT-cells have smaller receptive fields to pinch. Interestingly, although air-puff, vibration, and mixed responder cells appeared rather uniform in their calcium transients, the larger groups of brush cells and HT-cells were more functionally diverse ([Figure 2B](#)). For example, \sim 30% of the brush cells were vibration-insensitive, half responded preferentially to lower frequency vibration, and a smaller fraction were strongly activated by the full spectrum of vibration frequencies ([Figure 2](#)). Similarly, HT-cells exhibited differences in their sensitivity to hair-pull and their response dynamics ([Figure 2B](#)). This type of heterogeneity is consistent with previous results demonstrating the existence of several different classes both of low and high threshold mechanosensors ([Abraira and Ginty, 2013](#); [Ghitani et al., 2017](#); [Hill and Bautista, 2020](#); [Zimmerman et al., 2014](#)).

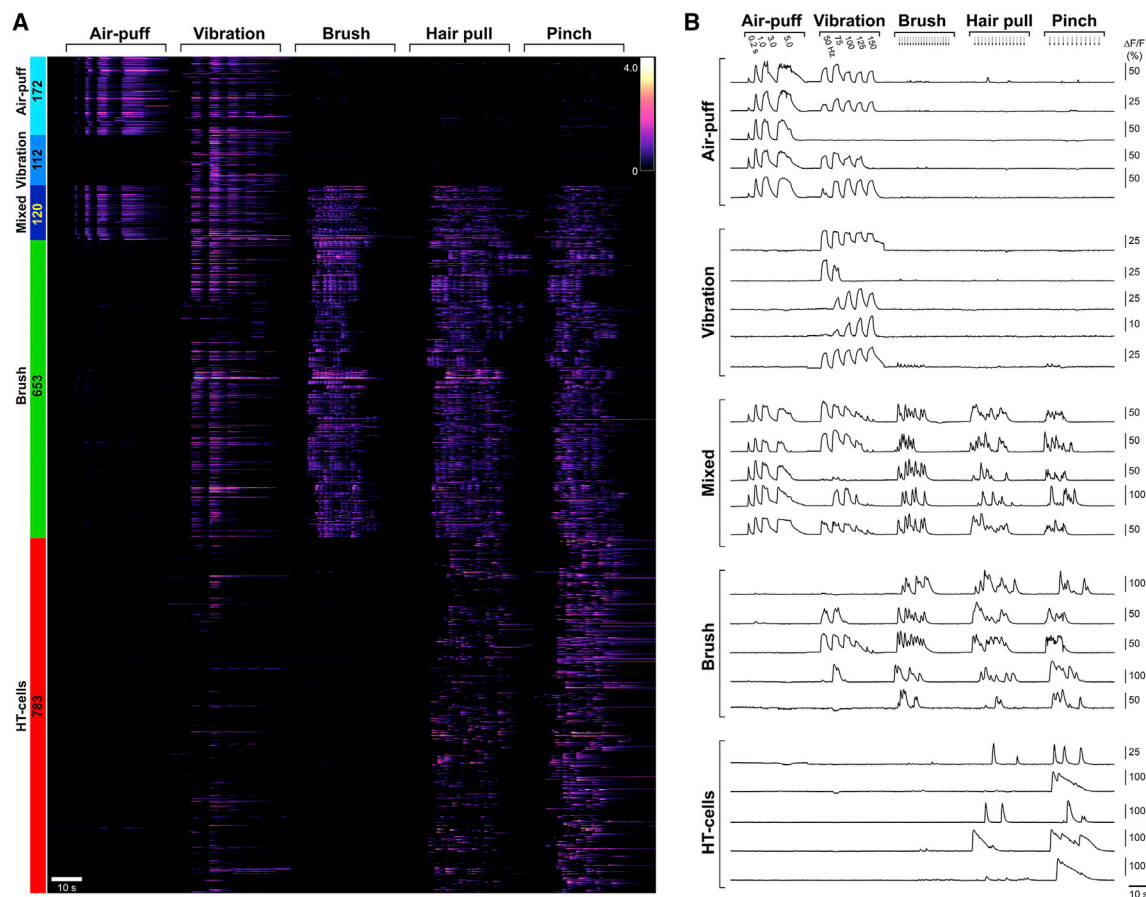


Figure 2. Trigeminal Neuron Responses to Naturalistic Mechanical Stimuli Identify Clear Functional Categories

(A) Heatmap showing the *in vivo* GCaMP6f responses from 1,840 neurons responding to five types of mechanical stimulation as labeled (top) in 23 mice. Calcium transients were first normalized to the median pinch response in that animal and colored as indicated in the scale bar (inset). The five cell-categories (labeled colored boxes, with cell numbers) were assigned using an automated script and a set of thresholding rules. Note sharp boundaries in response profiles demarcate the categories highlighting robust differences in the tuning of these groups of cells.

(B) Representative example GCaMP-transients ($\Delta F/F$ fluorescence changes indicated by scale bars) for each category of cells showing responses of individual neurons to a series of air-puff durations, vibration frequencies, gentle brush strokes, vigorous hair-pulls and pinching (the order, approximate timing, and repetitive nature is schematically represented by number scales or arrows). Note that responses to vibration are somewhat variable in all categories of LTMRs. See also Figure S2.

Taken together, our analysis highlights the value of using functional imaging for analyzing responses to naturalistic stimuli and reveals the existence of a novel class of mechanosensory neurons adapted for selective detection of air-puff.

How are the five categories of mechanosensory neurons specified by the genes they express? To address this issue, we developed sets of robust probes for classifying neurons according to their transcriptomic profiles (see Figure S3 for explanation of diagnostic gene expression patterns) and aligned multiplex ISH images to the functional responses. Our approach and its specificity are illustrated in Figure 3 where a region of a trigeminal ganglion containing 48 responding cells is shown. *In vivo* GCaMP-imaging was used to assign a functional category to each of these cells (Figure 3A). Subsequent whole mount ISH, warped to match the functional imaging (Figure 3B), shows the combined expression of 6 diagnostic markers in this region of the ganglion. The expression profiles of select cells highlighted

in Figures 3A and 3B are enlarged and analyzed in detail (Figure 3C), showing the basis for transcriptomic classification of functionally categorized neurons. For example, the air-puff cell A1 corresponds with GCaMP-expression and also is positive for *S100b* but no other markers, defining it as a C4 cell (see Figure S3). By contrast, the HT-cell H2 again aligns with GCaMP-expression but does not contain *S100b* mRNA and instead expresses all the other markers shown, making it a C13 neuron. In this way, 46 of the 48 responding neurons in this field could be classified (Figures 3D and S4) and their response dynamics analyzed in detail with respect to their cell class (Figure 3E).

Transcriptomic Classes Selectively Encode Distinct Mechanosensory Features

We used the strategy of combining functional imaging and ISH to unambiguously assign transcriptomic class to more than 1,000 of the 1,830 mechanosensory neurons categorized in 23 mice

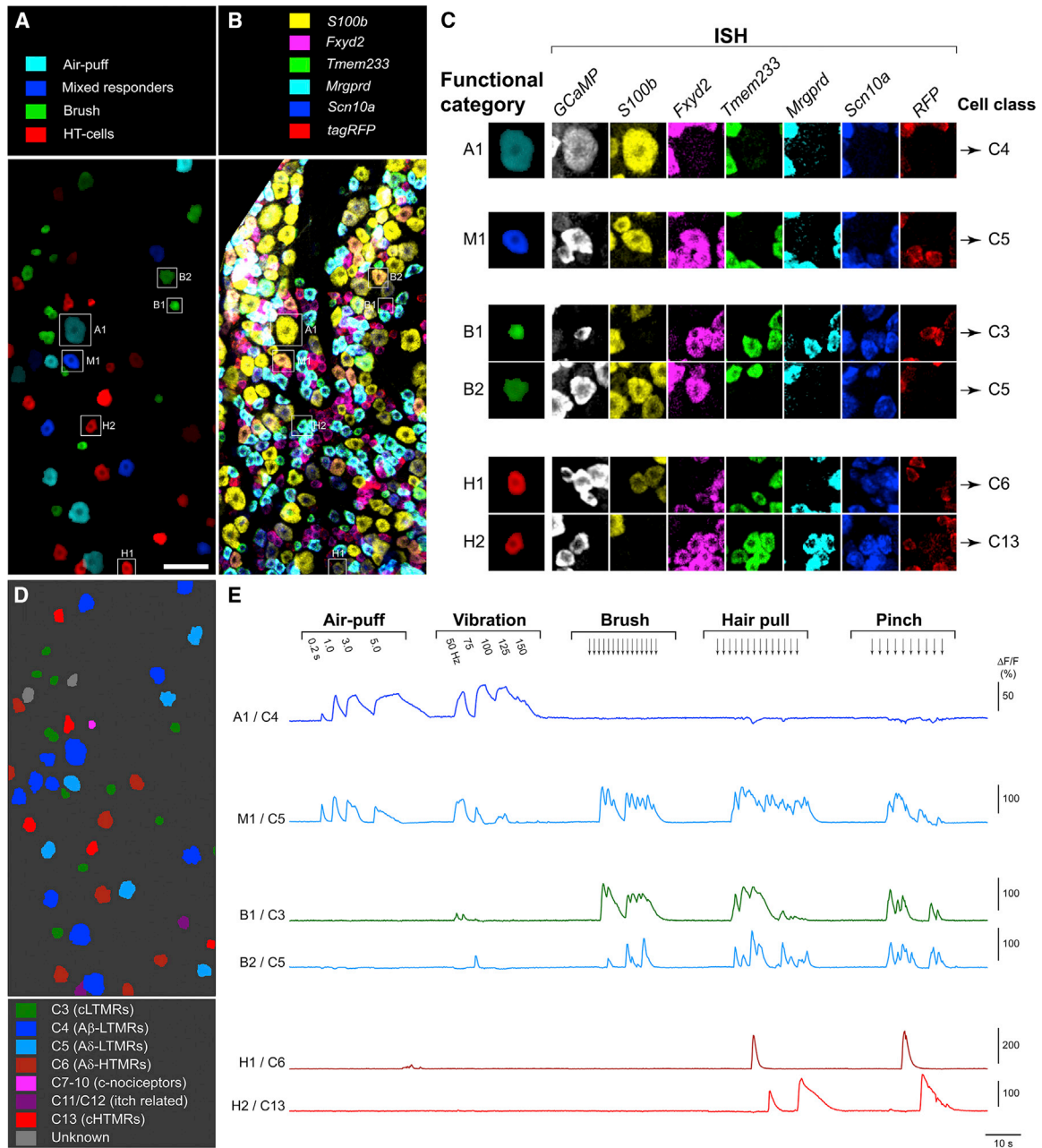


Figure 3. Multiplexed ISH Aligned to Functional Imaging Maps Cellular Responses to Transcriptomic Class

(A) Activity maps for 48 responding neurons in a region of the trigeminal ganglion shown in Figure S1C were color coded to distinguish their functional categories. (B) Multiplex whole-mount ISH was performed and images for 6 probes were aligned to the functional image using tagRFP guideposts; the overlaid 6 images were colored as indicated in the upper panel. Boxes in (A) and (B) depict representative cells with a variety of distinct functional responses (A, air-puff cell; M, mixed responder; B, brush cell; and H, HT-cell) and gene expression patterns. Scale bar, 100 μ m.

(C) Activity map (left column) and detailed gene expression patterns for the cells boxed in (A) and (B) illustrate our strategy for assigning cell class to functionally characterized mechanosensory neurons (see also Figure S3).

(D) Map of transcriptomic classes of the responding cells; note in this imaging field 46 from 48 neurons were classified using this panel of genes (see also Figure S4 for details). The color code for classes is shown in the lower panel.

(E) GCaMP-transients for the cells boxed in (A) and (B) with transcriptomic class indicated. $\Delta F/F$ fluorescence changes are indicated by scale bars and traces are color coded according to transcriptomic class (as specified, D).

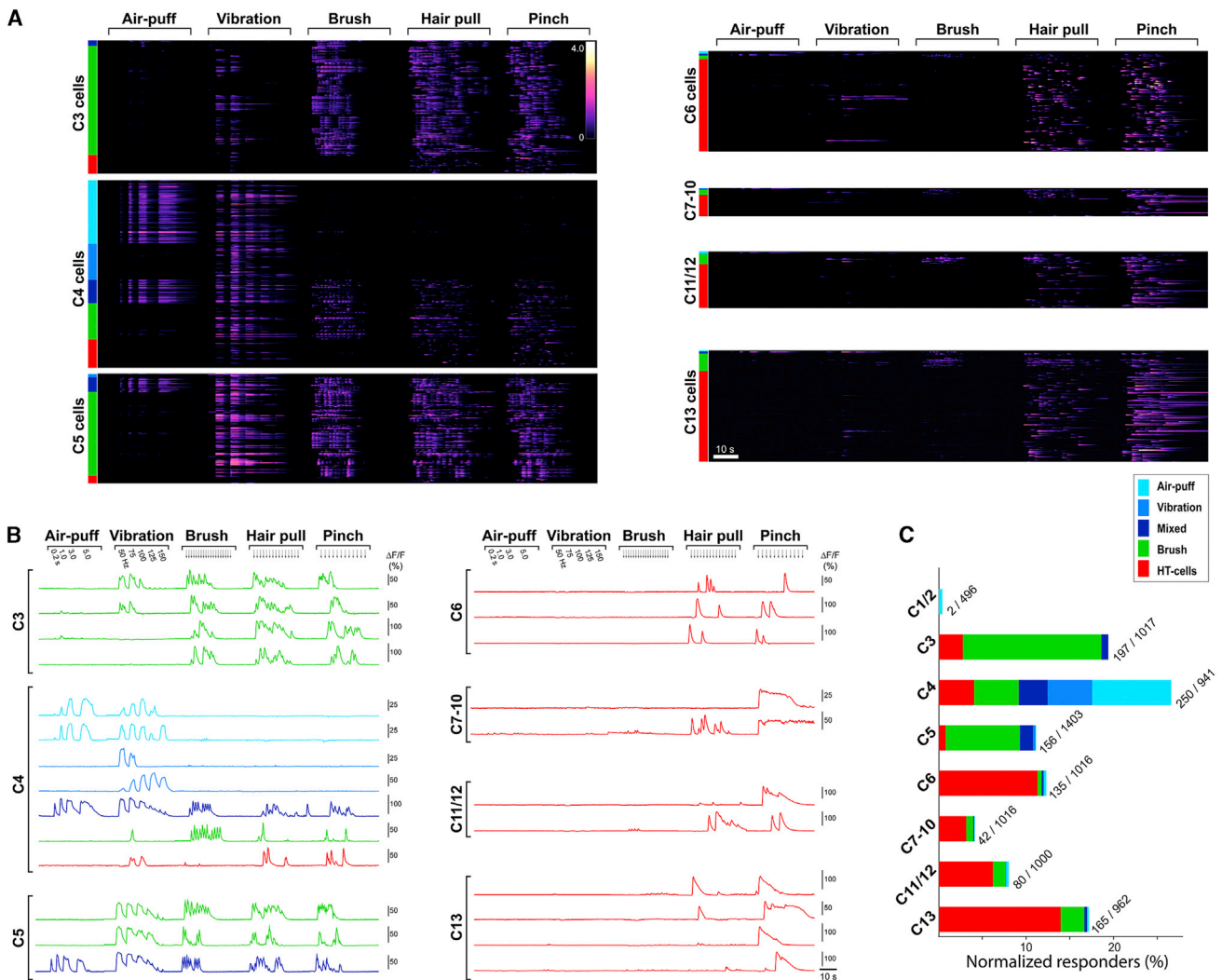


Figure 4. Sweeping Assignment of Transcriptomic Class to Function Reveals a Cellular Basis for the Detection and Coding of Mechanosensation at the Periphery

(A) Heatmaps showing normalized mechanical responses from transcriptomically classified neurons tested with the five stimuli (indicated above the heatmaps) grouped according to transcriptomic class. Data display is as in Figure 2A and functional category color coding is shown in (C); note that mechanical stimuli broadly activate all transcriptomic classes of neurons with the exception of C1/2 cooling sensors (see Figure S5A). Nonetheless, clear functional differences are immediately apparent with most classes selectively tuned to either brush or noxious stimuli. By contrast, C4 A β -LTMRs are diverse and include the vast majority of the specialized air-puff and vibration cells.

(B) Example GCaMP-transients of each cell class ($\Delta F/F$ fluorescence changes indicated by scale bars; traces color coded according to functional category) highlight their different tuning characteristics. Differential vibration sensitivity and calcium transient dynamics are also class dependent (see Figures S5B–S5D).

(C) Quantification of response category across cell-class; data were normalized to the number of responding neurons tested for each class (numbers of class responders/responding cells tested for that class by ISH are also indicated).

using definitive gene expression patterns. This comprehensive survey (Figure 4) exposed six fundamental principles for detection and representation of a range of salient mechanical stimuli at the periphery defining the transcriptomic basis for their discrimination. First, the vast majority of mechanosensors responding to low threshold stimuli (air-puff, vibration, mixed responders, and brush cells) were C3, C4, and C5 neurons (Figures 4 and S5); responses in these neuronal classes were saturated by gentle stimuli. Second, C3 and C5 cells were both quite ho-

mogeneous in their tuning and were predominantly brush cells; despite their markedly different transcriptomic profiles, these two classes appeared very similarly tuned. Third, most (>80%) mechanosensory neurons were activated by stimuli that evoke pain, with all classes of brush cells and mixed responders reliably responding to pinch and hair-pull. Fourth, the C4 class encompassed the only mechanosensor categories (air-puff and vibration) not robustly activated during noxious stimulation. However, this cell class was heterogeneous, including not only air-puff and

vibration cells but also half the mixed responders and a small fraction (12.5%) of the brush cells as well as an equal number of cells activated only by higher intensity stimuli (Figure 4C). Fifth, our data showed that classes C6–C13 (nociceptors) only very rarely responded to air-puff, vibration, or brush (Figures 4 and S5) and represented more than 80% of HT-cells. Finally, C1/2 neurons (*Trpm8*-expressing) were essentially unresponsive to any mechanical stimulus with just 2 cells responding to air-puff (Figure S5).

The overarching conclusion from this broad classification of mechanosensory neurons is one of consistency: class determines function (Figure 4). However, a small fraction of cells showed atypical response profiles: part of this may be experimental as a result of using naturalistic stimuli. For example, differences in stimulation intensity and target are impossible to rule out. Thus, C3 or C5 HT-cells may simply reflect that the area brushed fell outside their receptive fields. Nonetheless, some of these outliers likely have a biological role: a small subgroup of C5 neurons, which are mainly brush cells, also respond to air-puff and are mixed responders in our classification scheme (Figures 4A and 4B). C5 A δ -LTMRs are extremely uniform in their transcriptomic profile (Nguyen et al., 2017; Usoskin et al., 2015) and quite unique in the markers they express. Thus, their unexpected functional diversity further highlights the power of using an unbiased and comprehensive imaging-based approach. Conversely, the response heterogeneity of C4-neurons that we observed likely reflects the transcriptomic diversity of this class in recent scRNA sequencing (Nguyen et al., 2019; Sharma et al., 2020).

Does the classification of cells responding to the different naturalistic stimuli begin to explain how touch stimuli might be distinguished from one another? At the most fundamental level, LTMRs and HTMRs are defined by their genetic profiles (Figure 4). However, the majority of LTMRs respond to a wide range of naturalistic stimuli and indeed often have extended receptive fields for noxious hair-pull and pinch (Figure S2). By contrast, air-puff and vibration cells are unusually selective and do not respond to hair-pull, pinch, or gentle brushing. Our data demonstrate that both these functional categories are narrowly tuned C4 A β -LTMRs (Figure 4) insinuating them as labeled lines that could allow an animal to unambiguously identify these types of stimuli. The high specificity of air-puff cells was particularly unexpected: in the past, air-puff has only been shown to activate a population of rapidly adapting A β -LTMRs that detect a wide range of mechanical deflections of the hair including brushing and make lanceolate endings in the skin (Bai et al., 2015). These RA-A β -LTMRs have functional properties and a genetic profile matching the C4 mixed responder category that we identified here (Figure 4); intriguingly, C5 A δ -LTMRs also make lanceolate endings and, as noted above, a subset of these cells exhibited a similar mixed responder profile.

The other category of LTMRs, the brush cells, were more variable in their gene expression profiles but primarily fell into three transcriptomic classes, C3–C5 (Figure 4). This complex representation of brush is completely consistent with several elegant studies that examined individual responses of select types of cell in the dorsal root ganglia (DRG) (Bai et al., 2015; Rutlin et al., 2014) and nicely demonstrates how single brush strokes simul-

aneously activate tens to hundreds of transcriptomically heterogeneous neurons to provide a peripheral representation of this stimulus. Notably, when brush cells were separated by class, a logic explaining the differences in their response properties began to emerge (Figures 4B and S5). For example, C4-brush cells exhibited staccato calcium transients to brush, hair-pull, and pinch, with each stimulus event resolved (Figure S5). In contrast, responses tended to be more sustained in their C3 and C5 counterparts (Figure S5). Vibration responses were also transcriptomic class dependent and again were largely observed in C3–C5 cells (Figure 4). Notably, unlike for brush, C3-cells were relatively insensitive to vibration and rarely responded to frequencies above 100 Hz (Figures 4A and 4B). Therefore, although C3, C4 and C5 brush cells detect broadly overlapping stimuli these neurons transmit related but distinct information.

High intensity mechanical stimuli provide crucial information for survival by activating nociceptors that trigger protective behavioral responses and evoke acute pain. Most HT-cells were C6 A δ -nociceptors or C13 non-peptidergic c-nociceptors, with C11/C12 (itch-related) neurons (Abraira and Ginty, 2013; Mishra and Hoon, 2013) making up an additional and surprisingly large group. These classes are all strongly positive for the Nav1.8 sodium channel (*Scn10a*) reflecting the key role of this channel in mechanical nociception (Abrahamsen et al., 2008). Interestingly, just as we had observed for C3 and C4 brush cells, the clearest distinction between c- and A-fiber nociceptors was in the dynamics of their responses (Figures 4B and S5B–S5D). Indeed, quantitative analysis demonstrated that responses of C13 neurons decayed significantly more slowly than those of C6 cells (Figures S5C and S5D).

Genetic Identification of a Class of Neurons that Respond Selectively to Air-Puff and Vibration

Air-puff cells represent a new type of mechanosensor with highly specialized properties: strong responses to relatively gentle deflection of hairs by air flow and vibration but not brushing the fur or noxious stimuli like hair-pull and pinch. Previously, directed genetic strategies have revealed important information about the tuning and anatomy of select types of mechanosensory neurons (Abraira and Ginty, 2013; Zimmerman et al., 2014). Just like many of these mechanosensors, the air-puff cells are C4 A β -LTMRs (Figure 4), a large and transcriptomically diverse set of neurons. Therefore, we reasoned that markers defining air-puff cells might be revealed by screening the responding cells for expression of genes mapping to C4-subtypes (Nguyen et al., 2019). Indeed, this approach revealed that a subset of the air-puff cells expressed the calcium binding protein calretinin (*Calb2*) (Figures 5A and 5B). By contrast, this marker very rarely labeled mixed responders, brush, or HT-cells (Figures 5B and 5C).

Using the multiplex ISH approach, we demonstrated that 30% of air-puff cells (23 from 76 responders) expressed the gene *Calb2*; 23% of vibration cells (9/39) were also positive, suggesting that a subset of vibration cells are air-puff cells with receptive fields outside the region that we stimulated. Importantly, the vast majority of the responding *Calb2*-A β -LTMRs (~90%) were activated just by these two stimuli that both cause repetitive

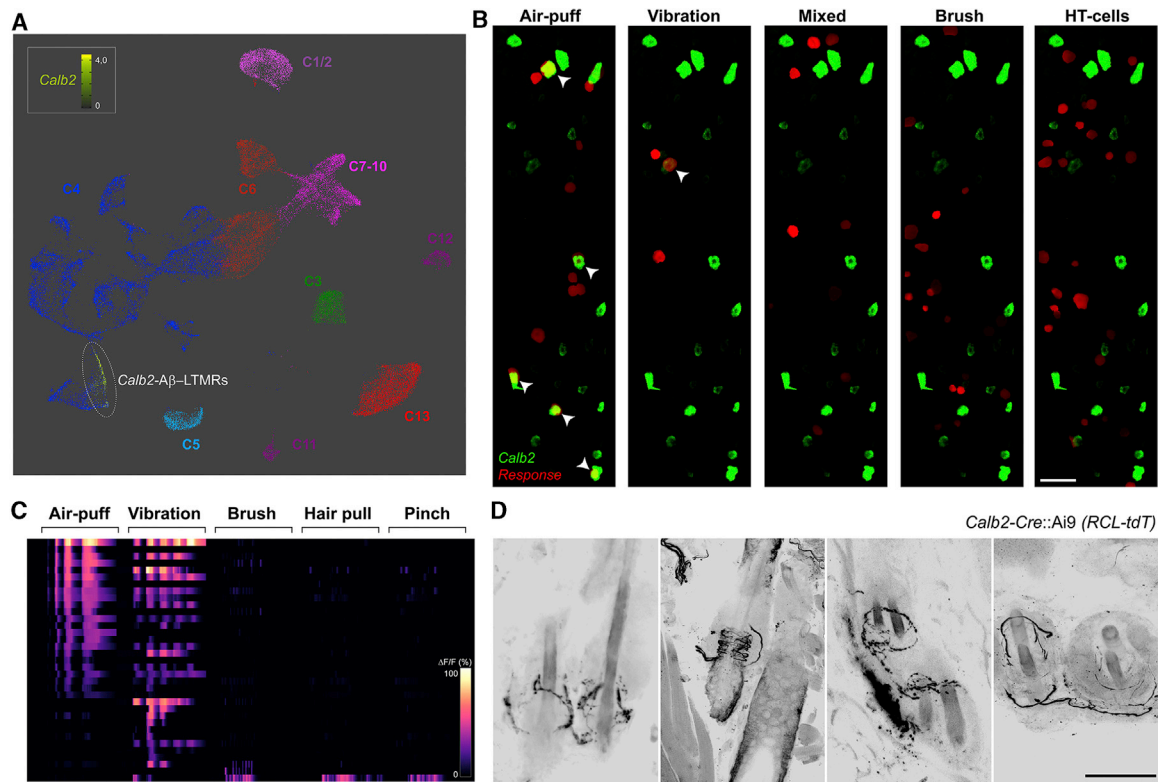


Figure 5. Calretinin (*Calb2*) Expression Defines a Subtype of $A\beta$ -LTMRs Selectively Tuned to Air-Puff and Vibration

(A) UMAP representation of single nucleus (sn)RNA sequence data (Nguyen et al., 2019) showing that *Calb2* expression is restricted to a transcriptomically defined subgroup of C4 $A\beta$ -LTMRs (dark blue); the expression of *Calb2* (yellow) is overlaid on the classified cells; see also Figure S6.

(B and C) *Calb2*- $A\beta$ -LTMRs are highly selective for air-puff and vibration. (B) Sample images showing ISH localization of *Calb2* (green) overlaid on category specific spatial activity maps (red). Arrowheads highlight the *Calb2*-expressing cells with air-puff and vibration response profiles; note only a subset of air-puff or vibration cells express this marker and that many *Calb2* cells are not stimulated, likely reflecting their projections to different areas of the head and neck. (C) Heatmap showing the response profiles of all 37 responding *Calb2*- $A\beta$ -LTMRs identified by ISH after functional imaging in 10 mice.

(D) Representative fluorescence micrographs of *Calb2*- $A\beta$ -LTMR termini in the skin illustrating that these neurons form circumferential endings around small hairs. Neurons were labeled by tdT-expression (*Calb2-Cre*/*Ai9 RCL-tdT* mice with appropriate recombination, see also Figure S6); signal is shown in black and contrasts with the weaker autofluorescence of hairs allowing morphology to be clearly discerned. These neuronal termini are not limited to the cheek (left panel) but are also prominent in the nearby whisker pad (center left) and back skin (right panels). Scale bars, 100 μ m.

fluctuation of hairs (Figure 5C). The specificity and the functional homogeneity of *Calb2*- $A\beta$ -LTMRs fits nicely with *Calb2*, marking a small transcriptomically distinct subgroup of C4 neurons (Figures 5A and S6A).

We next set out to determine if specific anatomic features of *Calb2*- $A\beta$ -LTMRs might account for their unusual response properties. To do this, we used a well-characterized *Calb2-Cre* knockin mouse line (Taniguchi et al., 2011) to genetically target these cells by crossing it into *Rosa-Cre*-reporter backgrounds. We observed markedly variable recombination in the trigeminal ganglion using this line, regardless of breeding strategy. For some mice, recombination and expression of reporter-genes was detected in many sensory neurons with a wide range of diameters. In others, just a few large diameter neurons were labeled in keeping with the *Calb2*-expression profile (Figures S6A and S6B). Variability is a relatively common and well-documented problem, with Cre-based labeling strategies most likely reflecting stochastic expression of Cre during development (Luo et al., 2020). We tested whether mice with sparse recombina-

tion labeled the appropriate cells: only a small subset of *Calb2*-positive cells expressed the reporter (Figure S6B) but all labeled cells (in sections from 5 ganglia) expressed *Calb2* and therefore provided high-specificity for directed functional and anatomical studies.

Genetically targeted expression of GCaMP6f in *Calb2*-neurons confirmed that the labeled neurons selectively responded to air-puff and vibration but are rarely activated by gentle brush or high threshold mechanical stimuli (Figure S6C). Of 61 cells recorded in 4 mice, 51 (83%) were air-puff/vibration cells confirming our initial findings and validating the genetic targeting approach. Notably, the majority of air-puff responding cells responded continuously for the duration of the stimulus (maximum 5-s tested, Figure S6D) without adaptation or inactivation. This suggests that *Calb2*- $A\beta$ -LTMRs are not only specialized to respond selectively to repetitive stimuli but also must be able to sustain this response for extended periods of time.

We then studied the anatomical projections of this class of neuron in hairy skin (Figure 5D) using *Calb2-Cre* to drive

tdTomato (tdT) expression. To our surprise, we only observed distinctive circumferential endings targeting fine hairs in the cheek, whisker pad, and back skin of these mice (Figure 5D). Previous studies have demonstrated that field-LTMRs (Bai et al., 2015) and circ-HTMRs (Ghitani et al., 2017) exhibit this type of terminal specialization around hairs but neither responds to air-puff. Instead, both field-LTMRs and circ-HTMRs are particularly sensitive to hair-pull (Bai et al., 2015; Ghitani et al., 2017), which is not detected by *Calb2*-A β -LTMRs. Given their anatomic specialization, we suspect that *Calb2*-A β -LTMRs selectively respond to high-frequency and distributed deflection of small hairs either caused by airflow or repetitive skin motion. We propose that their selectivity results from rapid adaptation to sustained stimulation, and in keeping with this hypothesis, we detected very brief weak responses to brush, pinch, and hair-pull in a number of cells (Figure S6D). In the future, it will be important to determine if the other C4 air-puff cells not marked by expression of *Calb2* share anatomic, gene expression, or biophysical properties (Zheng et al., 2019) with the *Calb2*-A β -LTMRs and thus help explain their unusual stimulus-response profile.

Class-Specific Functions of Piezo2 in Mechanosensation

We next explored the molecular mechanisms responsible for the differential response properties of the various transcriptomic classes. Recent studies have demonstrated that the tension-gated ion channel Piezo2 is required for detection of gentle touch, vibration, and proprioceptive stimuli by mice and humans (Bai et al., 2015; Chesler et al., 2016; Coste et al., 2010; Ranade et al., 2014). *Piezo2* is broadly expressed in almost all classes of trigeminal neurons including nociceptors (Figure 6A). Knockout of *Piezo2* in nociceptors alters spike frequencies, but these animals still respond to noxious mechanical stimuli (Murthy et al., 2018; Szczot et al., 2018). Similarly, humans with complete loss of PIEZO2 function report normal mechanical pain sensation in response to noxious pinch, pinprick, and pressure (Chesler et al., 2016; Szczot et al., 2018). Therefore Piezo2-independent pathways for detecting stronger mechanical forces must exist. To determine the roles and relative contributions of these sensory mechanisms, we investigated how the representation of touch was changed in each of the transcriptomic classes following *Piezo2*-knockout (Figures 6 and 7).

We recently developed a versatile strategy for imaging the functional responses of neurons lacking *Piezo2*-expression that involves AAV-*Cre*-mediated knockout just in the neurons expressing GCaMP (Szczot et al., 2018). This approach was easily rendered compatible with our platform for ISH after functional recordings by crossing the reporter mice into a conditional *Piezo2*-KO background. As expected, knockout of *Piezo2* dramatically alters mechanosensation by essentially eliminating responses to gentle stimuli (Figures 6B–6E and S7A). In wild-type controls, C4-neurons represented all five functional categories with ~85% being LTMRs. Among these LTMRs, air-puff and vibration cells normally accounted for nearly half of the C4 responsive neurons and only responded to these types of gentle mechanical stimulation (Figure 4). As expected, these cells were almost completely silenced after *Piezo2*-knockout (Figures 6D, 6E,

and S7C). More interestingly, the C4 brush and mixed responder cells, which in control animals are also activated by noxious pinch and hair-pull, were also silenced (i.e., they were not transformed to a corresponding large set of C4-HT-cells) (Figures 6 and S7). Similarly, C5-class (A δ -LTMR) brush and mixed responding cells were also extensively silenced (Figures 6 and S7). Thus, Piezo2 is the essential mechanosensor for touch detection by these myelinated neurons and endows them with sensitivity to a wide range of stimuli including some that are noxious to the animal like hair-pull and pinch.

In wild-type mice, C3 cLTMRs are mainly brush cells and exhibit similar sensitivity and tuning to their myelinated C4 and C5 counterparts. However, many C3 cells remained mechanosensitive after *Piezo2* knockout but, for the most part, now just responded to high threshold stimuli making these neurons a new type of HT-cells (Figures 6D–6G and S7). This indicates that C3 neurons must possess at least two distinct types of transduction pathways. Closer examination of the responses of C3 cells in the knockout reveals that responses to high threshold stimuli show altered dynamics (Figure S7B). In control animals, a series of hair-pulls generally evokes responses that track each event; in marked contrast, the same stimulation paradigm predominantly elicits a single slowly adapting transient in the mutant cells reminiscent of wild-type C13 (cHTMR) responses (compare Figures S5C and S7B). This was also reflected in a profound narrowing of the C3 receptive field to hair pull (Figures 7E–7G). Taken together, these results strongly suggest that Piezo2 not only sets the threshold for mechanosensation in C3 neurons but also contributes to their detection of pinch and hair pull. The unknown mechanosensory transduction pathway exposed in knockout C3 cells is less sensitive and likely endows cLTMRs with an extended dynamic range in wild-type mice.

Piezo2 is prominently expressed in many HTMRs as well as LTMRs (Figures 6A and 7A) raising the question of its importance in mechanical nociception. Our data demonstrate that C13 nociceptors become, by far, the largest class of mechanosensors after *Piezo2*-knockout, doubling their representation among responding neurons (Figures 7 and S7C). Thus, Piezo2 independent mechanisms must play a dominant role for the mechanosensitivity of this cell class. Nonetheless, rare C13-neuron responses to brush in wild-type mice (Figure 4) were eliminated after *Piezo2* knockout, demonstrating that this ion channel plays a role for setting mechanical threshold even in this neuronal class (Figures 6F and 7). Because many LTMRs are silent in the conditional knockout animals, we had expected C6-nociceptors to also become more prevalent among responding neurons. Surprisingly, however, this was not the case; their representation was dramatically reduced compared with the C13 neurons (Figure 7D) or even the itch-related C11 and C12 classes (Figures S7A and S7C). Importantly, in wild-type mice, C6 neurons have all the hallmarks of nociceptors: they express nociceptive markers (e.g., *Scn10a* and *Calca*), do not detect brush or air-puff, and have restricted receptive fields (Figures 7E–7G). Moreover, in contrast to C3-neurons, where Piezo2 knockout decreases a cell's effective receptive field size to noxious stimulation, this was unchanged both in C6 and C13 class nociceptors (Figure 7G). Therefore, Piezo2 plays an unexpectedly important role in transducing rapid responses to painful mechanical stimuli in a large subset of the C6 A δ -HTMRs.

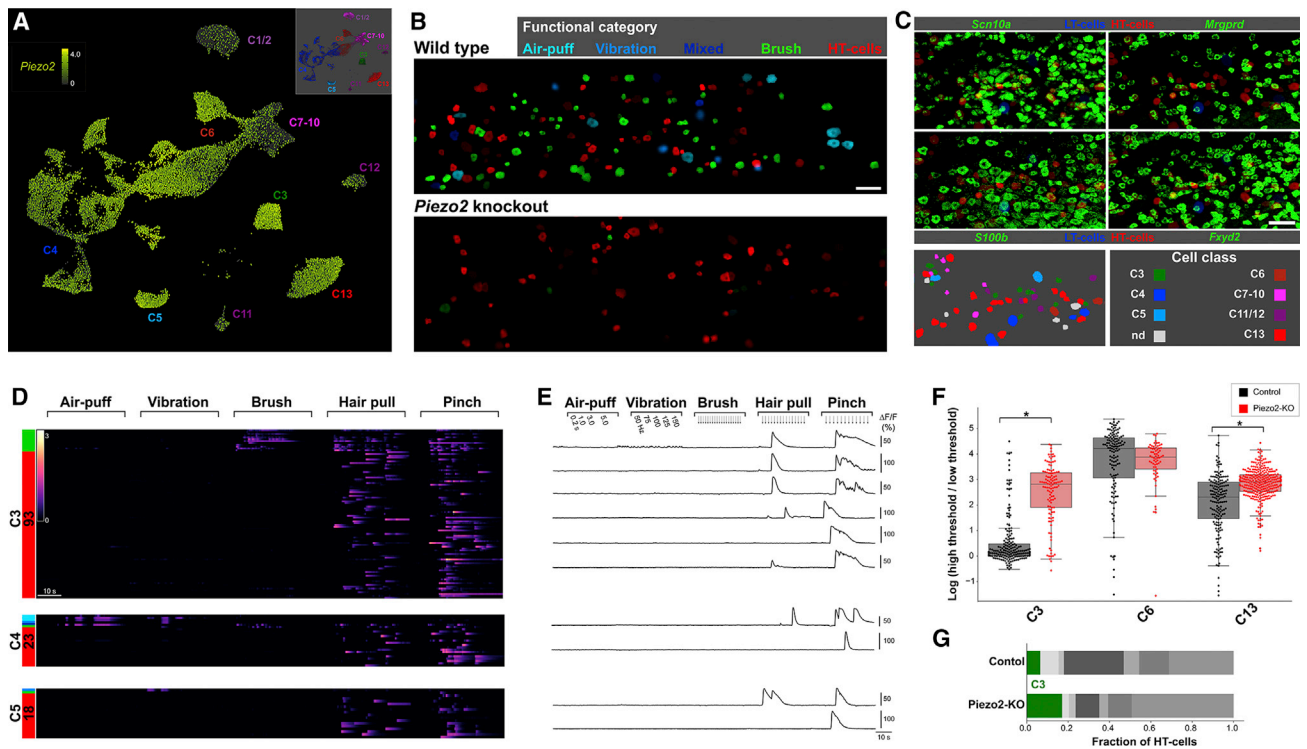


Figure 6. Piezo2 Differentially Confers Mechanosensitivity to LTMR Classes

(A) UMap representation of snRNA sequence data (Nguyen et al., 2019) showing broad expression of *Piezo2* in almost all classes of trigeminal neurons; note that only a limited subset of C1/2 and C7–C12 class neurons express this gene; by contrast it is a prominent marker of C6 and C13 nociceptors.

(B) Representative spatial activity maps showing the functional categories of mechanosensory neurons in equivalent areas of the dorsal trigeminal ganglion in control and *Piezo2*-KO recordings. Cellular response magnitude (see methods) is indicated by brightness and functional category by color; note how the functional response spectrum is narrowed by *Piezo2* knockout.

(C) Example images showing ISH images (green) aligned to activity maps as indicated by color coding (top four panels) as well as the classified cells (lower left) in *Piezo2*-KO.

(D) Heatmaps showing mechanosensory responses for the three classes C3, C4, and C5 that normally encompass LTMRs after *Piezo2*-KO. Functional category (colored bars) and number of cells of a given class are indicated. Note that whereas almost all C4 and most C5 cells are silenced by *Piezo2*-KO many C3 neurons appear transformed from brush cells in control animals (Figure 4) to HT-cells (see Figure S7 for quantitation and detail).

(E) Representative GCaMP-transients illustrating the lack of responses of C3–C5 neurons to gentle mechanical stimuli but robust activation of select neurons by hair-pull and pinch after *Piezo2*-KO.

(F) Box and whisker plot comparing the mechanical tuning of C3-cLTMRs with C6- and C13-HTMRs in control and *Piezo2*-KO recordings. Points represent the ratio for the maximum response of individual cells to pinch or hair-pull to gentle brush or air-puff (plotted on a natural log scale). Note that in control animals (black) C3-responses are generally saturated by low threshold stimuli with $\ln(\text{ratio})$ near 0 and are thus distinct from HT-cells. After *Piezo2*-KO (red) most mechanosensitive C3 neurons are HT-cells; $*p < 10^{-20}$, Welch's t test with Holm-Sidak correction for multiple tests.

(G) As a consequence of this functional transformation, stacked bar graphs show that the proportion of C3 cells (green) among HT-cells nearly triples after *Piezo2*-KO. Scale bars, 100 μm .

DISCUSSION

The sense of touch allows us to distinguish objects, warns of dangers, and underlies our most intimate social interactions. The prevailing view stemming from studies carried out more than 100 years ago is that specialized receptor cells tuned to detect specific features function together to endow touch with its remarkable discriminatory repertoire (Norsell et al., 1999). Subsequent work has revealed the beautiful anatomical specializations responsible for cellular level tuning (Willis, 2007) and more recently has linked this to selective molecular markers (Abraira and Ginty, 2013; Arcourt et al., 2017; Bai et al., 2015;

Ghitani et al., 2017; Rutlin et al., 2014; Zimmerman et al., 2014). However, deciphering how the various classes of specialized neurons combine to provide a physical substrate encoding the rich sensory information of naturalistic stimuli remains challenging. *In vivo* functional imaging studies have begun to provide a view of how somatosensory stimuli may be represented by tens or even hundreds of neurons (Ghitani et al., 2017; Szczot et al., 2018; Yarmolinsky et al., 2016). But how do these rich and complex activity patterns relate to the anatomical and molecular features of the responding cells? Here, we devised an approach to link the molecular and anatomical description of individual neurons to population responses. Using this platform,

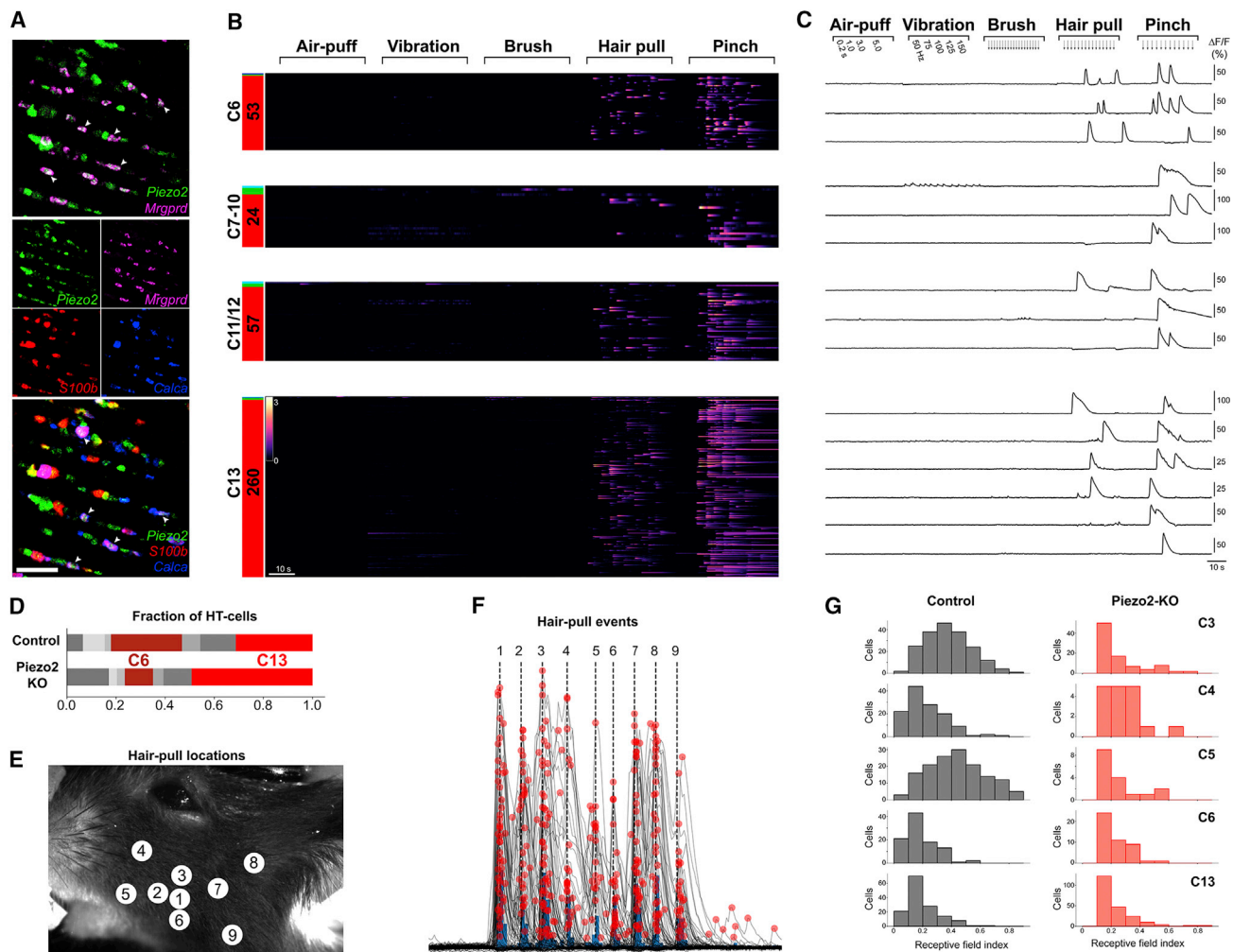


Figure 7. Transcriptomic Class-Dependent Roles for *Piezo2* in Mechanical Nociception

(A) Typical multiplex ISH images from sections of the trigeminal ganglion show robust expression of *Piezo2* in both C13 and C6 neurons that represent mechanonociceptors. Top panel: co-expression of *Piezo2* (green) with *Mrgprd* (magenta) in C13 non-peptidergic nociceptors. Bottom panel: a subset of C6 A δ -HTMRs by their co-expression of *S100b* (red) and *Calca* (blue). Middle panels: the individual images; arrowheads highlight a subset of nociceptors expressing *Piezo2*. Scale bar, 100 μ m.

(B and C) Heatmaps (B) and GCaMP-transients (C) showing mechanosensory responses for mechanonociceptors after *Piezo2*-KO. Note the large proportion of C13 HTMRs and their very homogeneous response profiles.

(D) Indeed, quantitation (stacked bar graph) reveals that after *Piezo2*-KO, C13 neurons are now the dominant class of HT-cells and that unexpectedly the proportional representation of C6 A δ -HTMRs was reduced by a factor of 2.5 relative to the control; see also Figure S7.

(E–G) Individual hair pull responses were analyzed to evaluate the receptive field size of classified neurons to this stimulus both in control cells and after *Piezo2*-KO. (E) Shows the location of hair pulls across the cheek during a typical recording from a control animal and (F) the corresponding hair pull calcium transients of all neurons in that animal (gray overlaid traces). Pink dots represent computer determined maxima and blue bars are the corresponding peristimulus time histograms demonstrating that the different hair pulls can be reliably identified from the data. (G) The number and magnitude of calcium transients in every hair pull responsive neuron was used to calculate its receptive field index (RFI); low RFI indicates a narrow receptive field, see Quantification and Statistical Analysis for details. Shown are the RFI distributions for the major classes of mechanosensor in control (gray bars) and after *Piezo2*-KO (pink bars). Note the receptive fields of brush sensitive C3 and C5 neurons were broader than for C6 and C13 HT-cells in control cells; after *Piezo2*-KO C3 and C5 neurons had lower RFIs ($p = 4.5 \times 10^{-8}$ and 2.2×10^{-4} , respectively) whereas C6 and C13 RFIs were unaffected ($p = 0.22$ and 0.07 , respectively).

we exposed new information about the representation of touch at the periphery, we then identified a transcriptomic subgroup of myelinated neurons that function as selective detectors for air-puff and vibration, and finally, we uncovered mechanistic detail about mechanosensory detection across the full range of neuronal classes.

As a rule, we found that naturalistic stimuli activate many different classes of sensory neurons with most types of LTM also responding to higher intensity stimulation. Because brush responsive neurons detect distal high force stimuli, this means that pinch and hair pull are represented both by specialist C6 and C13 nociceptors (with narrow receptive fields) and an

additional population of C3 and C5 touch neurons. Notably, however, we identified two functional classes of C4 neurons (air-puff and vibration) that were completely dependent on Piezo2 for mechanotransduction and only responded to gentle stimuli. Air-puff cells are particularly interesting, because this type of stimulus was previously thought to be detected primarily by broadly tuned A β -RA-LTMRs (Bai et al., 2015) with properties of mixed responders. Moreover, our data revealed that there are at least 2 distinct transcriptomic types of air-puff cell with one of these marked by expression of calretinin (*Calb2*). These *Calb2*-A β -LTMRs constitute a third class of neurons with circumferential endings that wrap around hair follicles. Remarkably, the two other types of myelinated mechanosensors with this anatomical specialization do not respond to air-puff induced hair deflection but are sensitive to sustained stimuli and higher forces (Bai et al., 2015; Ghitani et al., 2017) demonstrating that anatomy alone does not account for tuning. So how is functional diversity achieved, and how can a neuron detect an air-puff but not respond to brushing or far higher forces? We suspect that the *Calb2*-A β -LTMRs may rapidly inactivate to sustained deflection of a hair and thus preferentially detect repetitive stimuli like vibration or the turbulent effects of air-puff. Indeed, very small and short-lived calcium transients were sometimes observed in response to other types of stimulation, in keeping with this hypothesis. Alternatively, it has been beautifully demonstrated that neurons forming circumferential endings almost always have expansive terminal fields (Wu et al., 2012), thus the distributed nature of air-puff and vibration might also play a role. In the future, targeted electrophysiological recordings will be needed to address these issues and may help explain how other differences arise between anatomically related classes of mechanosensors.

We take our sense of touch for granted despite its fundamental importance for many aspects of our lives including both pleasure and pain. Our identification of a group of individuals who lack PIEZO2 function has highlighted both expected and unexpected impact of losing this mechanosensor on human touch perception (Chesler et al., 2016; Szczot et al., 2018). Notably, despite these individuals' inability to detect vibration, they could still perceive slow brushing on hairy skin but showed atypical fMRI responses (Chesler et al., 2016). Anecdotally, we noted that this type of brushing and other types of touch would often evoke unusual sensations that they described as pricking or itchy. Here, we showed that almost all somatosensory neurons are impacted by Piezo2 knockout and were able to disentangle how each transcriptomic class was differentially affected. For example, whereas A-type LTMRs were essentially silenced, cLTMRs remained mechanosensitive albeit with higher threshold and altered kinetics. Given that these different types of mechanosensor normally respond to brushing, their different reliance on Piezo2 provides a plausible explanation for how human PIEZO2 loss of function subjects still detect this type of relatively gentle stimulation as well as their atypical brush perception.

Recently, other mechanosensitive transduction channels and receptors have been described that are expressed in sensory neurons and may detect painful stimuli (Beaulieu-Laroche et al., 2020; Murthy et al., 2018; Xu et al., 2018; Zhang et al., 2018). Our results suggest that such mechanisms would be

particularly important in C13-cHTMRs consistent with the recent report that one of these, Tacan, is essential for C13-nociception (Beaulieu-Laroche et al., 2020). Nonetheless, Piezo2 also appears important for mechanonociception with a large subset of C6 A δ -HTMRs silenced by its knockout. It remains formally possible that some of these neurons respond to gentle stimulation either outside the area of skin that we tested or of a specialized nature (not brush, air-puff, or vibration). However, both the gene-expression profile and the restricted receptive fields of these cells to hair pull (Figure 7G) make this unlikely. Therefore, it will be important to understand features of these cells, perhaps including splice forms of Piezo2 (Ghitani et al., 2017) or interacting proteins (Poole et al., 2014), that allow a very sensitive channel to provide C6 cells with the ability to specifically detect high-threshold stimuli. In the future, it will also be interesting to address whether people with PIEZO2-deficiency syndrome have selective rapid mechanical pain deficits (e.g., to hair-pull), which in mice strongly activates a subset of C6-neurons (Ghitani et al., 2017).

In this study, we generated a rich dataset examining mechanical responses applied to just a small region of the cheek. Expanding the approach to other stimuli and specialized peripheral targets should help decipher an expanded logic for peripheral somatosensory coding. Interestingly, an analogous approach has just been used to study cellular level function-gene expression profiles in the zebrafish hypothalamus (Lovett-Barron et al., 2020). Thus, phenotyping ensembles of neurons followed by *in situ* hybridization in different brain regions is an attractive approach for matching function to cell identity and will provide a new dimension for understanding of how the nervous system represents and processes complex information.

STAR★METHODS

Detailed methods are provided in the online version of this paper and include the following:

- KEY RESOURCES TABLE
- RESOURCE AVAILABILITY
 - Lead Contact
 - Materials Availability
 - Data and Code Availability
- EXPERIMENTAL MODEL AND SUBJECT DETAILS
- METHOD DETAILS
 - Injection of AAV in mouse pups
 - *In vivo* epifluorescence calcium imaging
 - Spatial activity maps
 - Analysis of fluorescence dynamics
 - Functional categorization of cells
 - Whole-mount ISH of trigeminal ganglia
 - ISH of tissue sections
 - Confocal imaging and signal unmixing
 - Aligning whole mount ISH images to *in vivo* recordings
 - Evaluation of alignment accuracy
 - Analysis of gene expression and transcriptomic classification
 - Skin histology
- QUANTIFICATION AND STATISTICAL ANALYSIS

SUPPLEMENTAL INFORMATION

Supplemental Information can be found online at <https://doi.org/10.1016/j.neuron.2020.10.028>.

ACKNOWLEDGMENTS

We thank Drs. M. Nguyen, A. Barik, and M. Szczot for their help and input; we are also indebted to other members of our groups and Drs. M. Hoon, M. Krashes, C. Le Pichon, and C. Bushnell for their encouragement and advice. NINDS Light Imaging Facility was used for microscopy. This work was supported by the Intramural program of the NIH, the National Institute of Dental and Craniofacial Research (N.J.P.R.), and the National Center for Complementary and Integrative Health (A.T.C.) and included funding from Department of Defense in the Center for Neuroscience and Regenerative Medicine (A.T.C.).

AUTHOR CONTRIBUTIONS

Conceptualization, L.J.v.B., N.G., A.T.C., and N.J.P.R.; Software, L.J.v.B.; Methodology, L.J.v.B. and N.G.; Investigation, L.J.v.B., N.G., R.M.L., and J.A.L.; Formal Analysis, L.J.v.B.; Data Curation, L.J.v.B., N.G., R.M.L., and J.A.L.; Writing – Original Draft, L.J.v.B., A.T.C., and N.J.P.R.; Writing – Review & Editing, L.J.v.B., N.G., R.M.L., J.A.L., A.T.C., and N.J.P.R.; Supervision, A.T.C. and N.J.P.R.

DECLARATION OF INTERESTS

The authors declare no competing interests.

Received: June 26, 2020

Revised: September 27, 2020

Accepted: October 20, 2020

Published: November 12, 2020

REFERENCES

Abrahamsen, B., Zhao, J., Asante, C.O., Cendan, C.M., Marsh, S., Martinez-Barbera, J.P., Nassar, M.A., Dickenson, A.H., and Wood, J.N. (2008). The cell and molecular basis of mechanical, cold, and inflammatory pain. *Science* 321, 702–705.

Abraira, V.E., and Ginty, D.D. (2013). The sensory neurons of touch. *Neuron* 79, 618–639.

Arcourt, A., Gorham, L., Dhandapani, R., Prato, V., Taberner, F.J., Wende, H., Gangadharan, V., Birchmeier, C., Heppenstall, P.A., and Lechner, S.G. (2017). Touch Receptor-Derived Sensory Information Alleviates Acute Pain Signaling and Fine-Tunes Nociceptive Reflex Coordination. *Neuron* 93, 179–193.

Bai, L., Lehnert, B.P., Liu, J., Neubarth, N.L., Dickendesh, T.L., Nwe, P.H., Cassidy, C., Woodbury, C.J., and Ginty, D.D. (2015). Genetic Identification of an Expansive Mechanoreceptor Sensitive to Skin Stroking. *Cell* 163, 1783–1795.

Basbaum, A.I., Bautista, D.M., Scherrer, G., and Julius, D. (2009). Cellular and molecular mechanisms of pain. *Cell* 139, 267–284.

Bautista, D.M., Siemens, J., Glazer, J.M., Tsuruda, P.R., Basbaum, A.I., Stucky, C.L., Jordt, S.E., and Julius, D. (2007). The menthol receptor TRPM8 is the principal detector of environmental cold. *Nature* 448, 204–208.

Beaulieu-Laroche, L., Christin, M., Donoghue, A., Agosti, F., Yousefpour, N., Petitjean, H., Davidova, A., Stanton, C., Khan, U., Dietz, C., et al. (2020). TACAN Is an Ion Channel Involved in Sensing Mechanical Pain. *Cell* 180, 956–967.

Cadwell, C.R., Palasantza, A., Jiang, X., Berens, P., Deng, Q., Yilmaz, M., Reimer, J., Shen, S., Bethge, M., Tolias, K.F., et al. (2016). Electrophysiological, transcriptomic and morphologic profiling of single neurons using Patch-seq. *Nat. Biotechnol.* 34, 199–203.

Chang, R.B., Strohlic, D.E., Williams, E.K., Umans, B.D., and Liberles, S.D. (2015). Vagal Sensory Neuron Subtypes that Differentially Control Breathing. *Cell* 161, 622–633.

Chesler, A.T., Szczot, M., Bharucha-Goebel, D., Āeko, M., Donkervoort, S., Laubacher, C., Hayes, L.H., Alter, K., Zampieri, C., Stanley, C., et al. (2016). The Role of PIEZO2 in Human Mechanosensation. *N. Engl. J. Med.* 375, 1355–1364.

Choi, H.M.T., Schwarzkopf, M., Fornace, M.E., Acharya, A., Artavanis, G., Stegmaier, J., Cunha, A., and Pierce, N.A. (2018). Third-generation *in situ* hybridization chain reaction: multiplexed, quantitative, sensitive, versatile, robust. *Development* 145, dev165753.

Coste, B., Mathur, J., Schmidt, M., Earley, T.J., Ranade, S., Petrus, M.J., Dubin, A.E., and Patapoutian, A. (2010). Piezo1 and Piezo2 are essential components of distinct mechanically activated cation channels. *Science* 330, 55–60.

Delaunay, B. (1934). Sur la sphere vide. *Bull. Acad. Sci. USSR(VII), Classe Sci Mat Nat*, pp. 793–800.

Dhaka, A., Murray, A.N., Mathur, J., Earley, T.J., Petrus, M.J., and Patapoutian, A. (2007). TRPM8 is required for cold sensation in mice. *Neuron* 54, 371–378.

Gatto, G., Smith, K.M., Ross, S.E., and Goulding, M. (2019). Neuronal diversity in the somatosensory system: bridging the gap between cell type and function. *Curr. Opin. Neurobiol.* 56, 167–174.

Ghitani, N., Barik, A., Szczot, M., Thompson, J.H., Li, C., Le Pichon, C.E., Krashes, M.J., and Chesler, A.T. (2017). Specialized Mechanosensory Nociceptors Mediating Rapid Responses to Hair Pull. *Neuron* 95, 944–954.

Hill, R.Z., and Bautista, D.M. (2020). Getting in Touch with Mechanical Pain Mechanisms. *Trends Neurosci.* 43, 311–325.

Julius, D. (2013). TRP channels and pain. *Annu. Rev. Cell Dev. Biol.* 29, 355–384.

Le Pichon, C.E., and Chesler, A.T. (2014). The functional and anatomical dissection of somatosensory subpopulations using mouse genetics. *Front. Neuroanat.* 8, 21.

Lee, D., Kume, M., and Holy, T.E. (2019). Sensory coding mechanisms revealed by optical tagging of physiologically defined neuronal types. *Science* 366, 1384–1389.

Lovett-Barron, M., Chen, R., Bradbury, S., Andalman, A.S., Wagle, M., Guo, S., and Deisseroth, K. (2020). Multiple convergent hypothalamus-brainstem circuits drive defensive behavior. *Nat. Neurosci.* 23, 959–967.

Luo, L., Ambrozkievicz, M.C., Benseler, F., Chen, C., Dumontier, E., Falkner, S., Furlanis, E., Gomez, A.M., Hoshina, N., Huang, W.H., et al. (2020). Optimizing Nervous System-Specific Gene Targeting with Cre Driver Lines: Prevalence of Germline Recombination and Influencing Factors. *Neuron* 106, 37–65.

Madisen, L., Zwingman, T.A., Sunkin, S.M., Oh, S.W., Zariwala, H.A., Gu, H., Ng, L.L., Palmiter, R.D., Hawrylycz, M.J., Jones, A.R., et al. (2010). A robust and high-throughput Cre reporting and characterization system for the whole mouse brain. *Nat. Neurosci.* 13, 133–140.

Madisen, L., Garner, A.R., Shimaoka, D., Chuong, A.S., Klapoetke, N.C., Li, L., van der Bourg, A., Niino, Y., Ego, L., Monetti, C., et al. (2015). Transgenic mice for intersectional targeting of neural sensors and effectors with high specificity and performance. *Neuron* 85, 942–958.

Mishra, S.K., and Hoon, M.A. (2013). The cells and circuitry for itch responses in mice. *Science* 340, 968–971.

Murthy, S.E., Dubin, A.E., Whitwam, T., Jojoa-Cruz, S., Cahalan, S.M., Mousavi, S.A.R., Ward, A.B., and Patapoutian, A. (2018). OSCA/TMEM63 are an evolutionarily conserved family of mechanically activated ion channels. *eLife* 7, e41844.

Nguyen, M.Q., Wu, Y., Bonilla, L.S., von Buchholtz, L.J., and Ryba, N.J.P. (2017). Diversity amongst trigeminal neurons revealed by high throughput single cell sequencing. *PLoS ONE* 12, e0185543.

Nguyen, M.Q., Le Pichon, C.E., and Ryba, N. (2019). Stereotyped transcriptomic transformation of somatosensory neurons in response to injury. *eLife* 8, e49679.

Norsell, U., Finger, S., and Lajonchere, C. (1999). Cutaneous sensory spots and the “law of specific nerve energies”: history and development of ideas. *Brain Res. Bull.* 48, 457–465.

- Poole, K., Herget, R., Lapatsina, L., Ngo, H.-D., and Lewin, G.R. (2014). Tuning Piezo ion channels to detect molecular-scale movements relevant for fine touch. *Nat. Commun.* **5**, 3520.
- Ranade, S.S., Woo, S.H., Dubin, A.E., Moshourab, R.A., Wetzel, C., Petrus, M., Mathur, J., Bégay, V., Coste, B., Mainquist, J., et al. (2014). Piezo2 is the major transducer of mechanical forces for touch sensation in mice. *Nature* **516**, 121–125.
- Rutlin, M., Ho, C.Y., Abaira, V.E., Cassidy, C., Bai, L., Woodbury, C.J., and Ginty, D.D. (2014). The cellular and molecular basis of direction selectivity of A δ -LTMRs. *Cell* **159**, 1640–1651.
- Schindelin, J., Arganda-Carreras, I., Frise, E., Kaynig, V., Longair, M., Pietzsch, T., Preibisch, S., Rueden, C., Saalfeld, S., Schmid, B., et al. (2012). Fiji: an open-source platform for biological-image analysis. *Nature Methods* **9**, 676–682.
- Sharma, N., Flaherty, K., Lezgyjeva, K., Wagner, D.E., Klein, A.M., and Ginty, D.D. (2020). The emergence of transcriptional identity in somatosensory neurons. *Nature* **577**, 392–398.
- Szczot, M., Liljencrantz, J., Ghitani, N., Barik, A., Lam, R., Thompson, J.H., Bharucha-Goebel, D., Saade, D., Neccaise, A., Donkervoort, S., et al. (2018). PIEZO2 mediates injury-induced tactile pain in mice and humans. *Sci. Transl. Med.* **10**, eaat9892.
- Taniguchi, H., He, M., Wu, P., Kim, S., Paik, R., Sugino, K., Kvitsiani, D., Fu, Y., Lu, J., Lin, Y., et al. (2011). A resource of Cre driver lines for genetic targeting of GABAergic neurons in cerebral cortex. *Neuron* **71**, 995–1013.
- Tasic, B., Yao, Z., Graybiel, L.T., Smith, K.A., Nguyen, T.N., Bertagnolli, D., Goldy, J., Garren, E., Economo, M.N., Viswanathan, S., et al. (2018). Shared and distinct transcriptomic cell types across neocortical areas. *Nature* **563**, 72–78.
- Usoskin, D., Furlan, A., Islam, S., Abdo, H., Lönnnerberg, P., Lou, D., Hjerling-Leffler, J., Haeggström, J., Kharchenko, O., Kharchenko, P.V., et al. (2015). Unbiased classification of sensory neuron types by large-scale single-cell RNA sequencing. *Nat. Neurosci.* **18**, 145–153.
- von Buchholtz, L.J., Lam, R.M., Emrick, J.J., Chesler, A.T., and Ryba, N.J.P. (2020). Assigning transcriptomic class in the trigeminal ganglion using multiplex in situ hybridization and machine learning. *Pain*. Published online May 2, 2020. <https://doi.org/10.1097/j.pain.0000000000001911>.
- Williams, E.K., Chang, R.B., Strohlic, D.E., Umans, B.D., Lowell, B.B., and Liberles, S.D. (2016). Sensory Neurons that Detect Stretch and Nutrients in the Digestive System. *Cell* **166**, 209–221.
- Willis, W.D., Jr. (2007). The somatosensory system, with emphasis on structures important for pain. *Brain Res. Brain Res. Rev.* **55**, 297–313.
- Wu, H., Williams, J., and Nathans, J. (2012). Morphologic diversity of cutaneous sensory afferents revealed by genetically directed sparse labeling. *eLife* **1**, e00181.
- Wu, Y., Luna, M.J., Bonilla, L.S., Ryba, N.J.P., and Pickel, J.M. (2018). Characterization of knockin mice at the *Rosa26*, *Tac1* and *Plekha1* loci generated by homologous recombination in oocytes. *PLoS ONE* **13**, e0193129.
- Xu, J., Mathur, J., Vessières, E., Hammack, S., Nonomura, K., Favre, J., Grimaud, L., Petrus, M., Francisco, A., Li, J., et al. (2018). GPR68 Senses Flow and Is Essential for Vascular Physiology. *Cell* **173**, 762–775.
- Yarmolinsky, D.A., Peng, Y., Pogorzala, L.A., Rutlin, M., Hoon, M.A., and Zuker, C.S. (2016). Coding and Plasticity in the Mammalian Thermosensory System. *Neuron* **92**, 1079–1092.
- Zeisel, A., Hochgerner, H., Lönnnerberg, P., Johnsson, A., Memic, F., van der Zwan, J., Häring, M., Braun, E., Borm, L.E., La Manno, G., et al. (2018). Molecular Architecture of the Mouse Nervous System. *Cell* **174**, 999–1014.
- Zhang, M., Wang, D., Kang, Y., Wu, J.-X., Yao, F., Pan, C., Yan, Z., Song, C., and Chen, L. (2018). Structure of the mechanosensitive OSCA channels. *Nat. Struct. Mol. Biol.* **25**, 850–858.
- Zheng, Y., Liu, P., Bai, L., Trimmer, J.S., Bean, B.P., and Ginty, D.D. (2019). Deep Sequencing of Somatosensory Neurons Reveals Molecular Determinants of Intrinsic Physiological Properties. *Neuron* **103**, 598–616.
- Zimmerman, A., Bai, L., and Ginty, D.D. (2014). The gentle touch receptors of mammalian skin. *Science* **346**, 950–954.

STAR★METHODS

KEY RESOURCES TABLE

REAGENT or RESOURCE	SOURCE	IDENTIFIER
Bacterial and Virus Strains		
AAV9-CAG-Cre	Vigene	CV17187-AV9
Critical Commercial Assays		
Hybridization Chain Reaction (HCR) version 3 kit	Molecular Instruments	N/A
RNAscope Fluorescent Multiplex	ACD	N/A
Deposited Data		
Calcium traces, ISH annotation and cell classifications	This paper	https://dx.doi.org/10.17632/hct95nx3t8.1
Experimental Models: Organisms/Strains		
Mouse: B6;129S-Gt(ROSA) ^{26Sortm95.1(CAG-GCaMP6f)Hze/J} (Ai95)	The Jackson Laboratory	Stock No: 024105
Mouse: B6.Cg-Gt(ROSA) ^{26Sor^{tm9(CAG-tdTomato)Hze/J}} (Ai9)	The Jackson Laboratory	Stock No: 007909
Mouse: B6(Cg)-Calb2 ^{tm1(cre)Zjh/J}	The Jackson Laboratory	Stock No: 010774
Mouse: Tac1-tagRFP-2a-TVA	Wu et al., 2018	N/A
Mouse: Piezo2 ^{lox/lox}	Szczot et al., 2018	N/A
Mouse: C57BL/6N	Harlan	N/A
Software and Algorithms		
Python 3.6	N/A	https://www.python.org
OpenCV 3	N/A	https://www.opencv.org
Fiji/ImageJ	Schindelin et al., 2012	https://imagej.net/Fiji
ZEN	Zeiss	https://www.zeiss.com/microscopy/us/products/microscope-software.html
Custom ImageJ macros and Python scripts	This paper	https://github.com/lars-von-buchholtz/warping ; https://doi.org/10.5281/zenodo.4088771

RESOURCE AVAILABILITY

Lead Contact

Further information and requests for resources and reagents should be directed and will be fulfilled by the Lead Contact, Alexander Chesler (alexander.chesler@nih.gov).

Materials Availability

This study did not generate new unique materials.

Data and Code Availability

Calcium traces, gene expression annotation, and cell classification data have been deposited at Mendeley (<https://dx.doi.org/10.17632/hct95nx3t8.1>). ImageJ macros and Python scripts for morphing/aligning images are available on Github (<https://github.com/lars-von-buchholtz/warping>).

EXPERIMENTAL MODEL AND SUBJECT DETAILS

All experiments using animals strictly followed National Institutes of Health (NIH) guidelines and were approved by the National Institute of Neurological Disorders and Stroke (NINDS) or the National Institute of Dental and Craniofacial Research (NIDCR) Animal Care and Use Committees and used male and female mice. Ai95(*RCL-GCaMP6f*)-D (#024105), Ai9(*RCL-tdT*) (#007909) and *Calb2-Cre* (#010774) mice were purchased from the Jackson laboratory. *Tac1-tagRFP-2a-TVA* and *Piezo2^{lox/lox}* lines have been described previously ([Szczot et al., 2018](#); [Wu et al., 2018](#)). For the main body of this study, *Tac1-tagRFP-2a-TVA::Ai95(RCL-GCaMP6f)-D* double transgenic mice were bred and GCaMP6f expression was induced by AAV-Cre injection. *Piezo2* knockout effects were investigated in mice that additionally were homozygous for the *Piezo2^{lox}* allele.

Calb2-expressing cells were investigated in *Calb2-Cre::Ai95(RCL-GCaMP6f)*-D double heterozygous transgenic mice (Madisen et al., 2015; Taniguchi et al., 2011) and their peripheral projections were visualized in *Calb2-Cre::Ai9(RCL-tdT)* double heterozygous transgenic mice (Madisen et al., 2010). C57BL/6N mice were purchased from Harlan.

METHOD DETAILS

Injection of AAV in mouse pups

Trigeminal ganglion neurons were targeted by intracerebroventricular, intrajugular and intraperitoneal injections (either singly or in combination) of AAV9-Cre in postnatal day 1-3 mouse pups. Mouse pups were briefly anesthetized by placing the animals in a plastic weighing tray on ice. An infusion syringe pump (KDS230, KD Scientific) setup with a 0.3 mL insulin syringe (BD) or a Hamilton syringe (Hamilton Robotics, Reno, USA) was used to inject 1-3 μL of AAV9-CAG-Cre virus (2×10^{12} to 2×10^{13} virions/ml, catalog # CV17187-AV9, Vigene, Rockville, USA).

In vivo epifluorescence calcium imaging

The surgical preparation to gain optical access to the trigeminal ganglion was performed as previously described (Ghitani et al., 2017). Calcium imaging used a custom-built epifluorescence Cerna microscope (Thorlabs) with a 4x, 0.16 NA objective (Olympus) using a 480nm fluorescence LED to image GCaMP6f, and a 561nm LED to image tagRFP (Lambda, Sutter Instruments). Excitation and emission light passed through a standard green fluorescent protein (GFP) filter cube for GCaMP6f, and an mCherry filter cube for tagRFP (Olympus). Images were acquired at 5 Hz using a PCO Panda 4.2bi scientific CMOS camera, using the provided PCO acquisition software. For each trigeminal ganglion, *Tac1-tag-RFP* expressing neurons were imaged in the red channel, then GCaMP6f transients were recorded in the green channel, without moving the specimen. A series of air-puffs of increasing durations (0.2, 1, 3 and 5 s) was delivered to the face using a Picospritzer III (Parker). This device delivered pressurized air at 25psi through a 1mm inner diameter Teflon tubing that ejected air at a distance of 3 cm from the face to achieve visible hair deflection. Vibration was delivered using a custom-built latex- Pasteur-pipette bulb tipped applicator that was applied by just touching the hairs over the center of the cheek. Sinusoidal waveforms at 50, 75, 100, 125, and 150 Hz, lasting 3 s for each, were generated using a Digidata 1550 (Molecular Devices) to control a solenoid (SolidDrive SD1sm, Induction Dynamics) and were amplified by a 70W subwoofer plate amplifier (SA70, Dayton Audio). Manual gentle stroking of a large area of the cheek was performed repeatedly using a cotton tipped applicator with the grain (i.e., in a rostral to caudal direction). Hair-pull and pinch were performed manually using forceps at multiple locations covering the whole cheek between the eye and whisker pad in each stimulation epoch. The Digidata 1550 was also used to control image acquisition, timing of air-puff pulses and vibration. GCaMP6f fluorescence was recorded during stimulation episodes (40 s at 5Hz for each stimulus) and concatenated to a single image stack in ImageJ. Individual frames were registered to the first frame using a custom ImageJ macro based on the 'Linear Stack Alignment With SIFT' plugin to correct for motion artifacts.

Spatial activity maps

To generate spatial maps of activity, the standard deviation for each pixel over a stimulation episode was calculated in FIJI/ImageJ. Silent cells show a very low standard deviation from their mean fluorescence whereas stimulus-induced calcium transients result in high standard deviations. To compound activity across multiple stimuli, a maximum intensity projection over the individual episodes was used.

Regions of interest (ROIs) were manually extracted from these images using the 'Cell Magic Wand' plugin in ImageJ. Overlapping cell ROIs that were contaminated by each other's responses as well as out of focus or spontaneously active cells were excluded from the analysis. These choices were made while blind to transcriptomic information.

Functional category specific maps were generated for air-puff cells, vibration cells, brush cells, mixed responders and HT-cells. To do this, the standard deviation images for the preferred stimulus of a category were multiplied with binary masks that outline the cell ROIs belonging to that category (see below). These maps are specific for a functional category of cells and provide an estimate of the response magnitude as well as the shape and location of a cell.

Analysis of fluorescence dynamics

For each cell ROI, relative change in GCaMP6f fluorescence was calculated as percent $\Delta F/F$ and potential contaminant signal from the underlying out-of-focus tissue and neighboring cells was removed by subtracting the fluorescence of a donut-shaped area surrounding each cell using a custom MATLAB script (Szcot et al., 2018). Responses to each stimulus were recorded as individual 40 s episodes and concatenated for display as traces or activity heatmaps.

For the heatmaps in Figures 2, 4, 6, and 7, GCaMP6f fluorescence changes were normalized to the median of the pinch response peaks in the respective mouse to standardize data between animals.

Functional categorization of cells

Each cell's background fluorescence noise was calculated as the standard deviation of the bottom 50% of all data points. A transient rise in fluorescence was considered significant if its peak exceeded 10 times this value. A cell was assigned a functional category according to a set of numerical rules to allow automation and eliminate observer bias. Air-puff cells had significant air-puff responses

and ratios of air-puff response to brush response exceeding 2. Vibration cells had significant vibration responses and a ratio of vibration responses to all other responses greater than 3. Brush cells had a significant brush response and a ratio of brush to air-puff response greater than 2 and a ratio of pinch and hair-pull responses to brush greater than 3. Mixed responders had significant air-puff and brush responses with ratio between 0.5 and 2 and ratios of pinch and hair-pull responses to brush responses larger than 3. HT-cells were defined as cells that had a significant response to pinch and/or hair-pull and had a ratio of high threshold to low threshold peak responses of at least 3.

In order to compare the effective receptive field sizes of brush and HT neurons, a separate set of 4 ganglia was stimulated with 4 pinches in a straight line across the cheek at ~1mm intervals and gentle brushing of the cheek. A total of 580 neurons were identified in these experiments. They were functionally classified into brush / mixed responder and HT cells as described above and their calcium transients were normalized to their maximal response to better visualize the effective receptive field of these neurons.

Whole-mount ISH of trigeminal ganglia

Immediately after *in vivo* calcium imaging, trigeminal ganglia were immersed in ice-cold 4% PFA (Electron Microscopy Sciences) in phosphate-buffered saline (PBS) for 90 min. They were then washed 3 times in PBS and attached (ventral surface, super-glue) to plastic strips (10 × 2mm) to facilitate handling and then were rinsed again using PBS. ISH was performed using hybridization chain reaction (HCR) version 3 (Choi et al., 2018): pre-hybridization, 30 min, 35°C in HCR hybridization solution (Molecular Instruments); hybridization, 48 - 72 h, 35°C using combinations of five of the following probes: *Trpm8* (GenBank NM_134252, full-length), *Cd34* (NM_001111059, full-length), *S100b* (NM_009115, full-length), *Fxyd2* (NM_007503, full-length), *Scn10a* (NM_001205321, CDS), *Calca* (NM_007587, full-length), *Trpv1* (NM_001001445, full-length), *Etv1* (NM_007960, full-length), *Tmem233* (NM_001101546, full-length), *Mrgprd* (NM_203490, full-length), *Calb2* (NM_007586, CDS), *tagRFP-TVA* and *EGFP* (which detects *GCaMP6f*-expression). Ganglia were then washed 2 times, 15 min in wash buffer (Molecular Instruments) at 37°C followed by 4 times, 30 min in 2xSSC / 30% formamide, 37°C. Ganglia were rinsed twice in 2xSSC and incubated overnight at room temperature with amplifier hairpins for adapters B1 - B5 conjugated to Alexa488, Alexa514, Alexa561, Alexa594 and Alexa647 that were prepared as described by the manufacturer. Ganglia were then washed 4 times, 20 min in 5xSSC/0.1% Tween-20 and embedded in 2% low-melt agarose in the top half of a CoverWell imaging chamber (Grace Biolabs). The rest of the chamber was filled with Imaging Buffer (3 U / ml pyranose oxidase, 0.8% D-glucose, 2 x SSC, 10 mM Tris HCl pH 7.4). After imaging, ganglia were rinsed in 2xSSC and DNA probes and amplifiers were removed by incubation in 250 U / ml RNase-free DNase (Roche Diagnostics), 60 min at room temperature. Ganglia were washed 6 times, 5 min in 2xSSC and pre-hybridized for the next round of hybridization with the next 5 probes. For some ganglia, this procedure was repeated a third time to increase the number of aligned probes but deterioration both of signal to noise ratio and ganglion integrity meant this additional round rarely added useful information.

ISH of tissue sections

Trigeminal ganglia dissected from 2-4 months old C57BL/6 and *Calb2-Cre::Ai9 (RCL-tdT)* mice were embedded in OCT medium and frozen at -80°C. 20 μm sections were prepared for RNAscope (ACD Inc.) ISH or for HCR probing as described previously (Nguyen et al., 2017; von Buchholtz et al., 2020). RNAscope probes were to *Calb2* (313641-C3), *Cre* (474001), *S100b* (431731-C2) and *tdT* (317041); HCR probes to mouse *Piezo2* (GenBank NM_001039485, full-length), *Mrgprd*, *S100b* and *Calca*.

Confocal imaging and signal unmixing

HCR ISH imaging was carried out using a Zeiss LSM 880 confocal microscope with spectral detector using a 10x/0.45NA air objective. Alexa647 was stimulated with a 633 laser and emission was collected from 644-752 nm. Alexa546 and Alexa594 were stimulated with 561 and 594 lasers respectively and wavelength scans with 9nm windows were collected to allow unmixing signals from different fluorophores. Similarly, Alexa488 and Alexa514 were stimulated with a 488 nm laser and 9nm wavelength scans allowed unmixing of these fluorophores. For detection of single transcripts of weakly expressed genes, imaging was performed with a 40x/1.1NA long working distance water immersion objective (Zeiss LD C-Apochromat). Spectral unmixing was performed using Zeiss ZEN software. Dorsal views of whole-mount ganglia were imaged as Z stacks with 10 μm intervals to capture the convex surface of the ganglion. Since the ganglion is opaque and our confocal imaging only penetrates ~20-30 μm into the tissue the convex surface of the ganglion captured in the Z stack can be collapsed by maximum intensity projection into a 2D dorsal view comparable to the *in vivo* image. This almost exclusively is a single cell layer both in functional imaging experiments and for ISH images. Imaging of sections was as previously described (Nguyen et al., 2017; von Buchholtz et al., 2020).

Aligning whole mount ISH images to *in vivo* recordings

As a first step, multi-channel 2D ISH images were crudely aligned to *in vivo* fluorescence by scaled rotation using the TurboReg plugin and a custom-written macro in ImageJ/FIJI. *tagRFP* mRNA positive guidepost cells were then manually matched to their *in vivo* red fluorescent counterparts using a custom-written ImageJ macro that identified coordinate pairs for each guidepost. The ISH image was then morphed to match its *in vivo* counterpart using these coordinates with a custom Python script that builds on the OpenCV library and was adapted from face morphing software (<https://www.learnopencv.com/face-morph-using-opencv-cpp-python/>).

In brief, Delaunay triangulation (Delaunay, 1934) was used to connect the guidepost points to obtain the most even set of triangles in the source image. The corresponding triangles for the target (*in vivo*) guideposts were calculated; then each source triangle was

transformed into its target shape by affine transformation. This approach allows each triangular patch to be transformed independently from the rest of the image. As a result, the whole area of the ISH image spanned by the guidepost cells is morphed smoothly and continuously to fit the matching *in vivo* pair (Figure 1, see also Figure S1 for illustration). Similarly, multiple rounds of ISH were aligned to each other using a shared probe (or probes labeling similar sets of cells) in both rounds to provide guideposts for morphing.

Evaluation of alignment accuracy

In order to evaluate the alignment accuracy between subsequent rounds of ISH, 3 trigeminal ganglia were stained with probes for *Trpm8*, *Mrgprd*, *S100b* and *Tac1* which cover > 90% of trigeminal ganglion neurons. In a second round, ganglia were re-stained with the same set of probes. ISH images were aligned using *Trpm8* cells as guideposts and correct recovery of *Mrgprd* cells (which are not overlapping with *Trpm8* cells) was assessed in a blinded fashion: 3000 cell outlines and their *Mrgprd* expression were determined by an annotator based on first round ISH data and *Mrgprd* status of each cell outline in the second round was determined by a second annotator based solely on ISH data from the second round. Similarly, accuracy of alignment between *in vivo* functional imaging and ISH images was assessed by comparing spatial activity maps to their corresponding GCaMP ISH in two representative ganglia. A first annotator outlined responsive cells and discarded cells that were not suitable for functional analysis (spatially overlapping, out-of-focus and spontaneously active cells). The same annotator generated an equal number of decoy ROIs interspersed in the area of alignment. After alignment using tagRFP guidepost cells, a second annotator who was blind to the *in vivo* imaging then determined the GCaMP status of functional and decoy ROIs based solely on GCaMP ISH data. Relative cell displacement was measured in ImageJ.

Analysis of gene expression and transcriptomic classification

Cell ROIs based on the functional imaging (i.e., responding cells) were manually analyzed for the cellular expression (positive or negative) of every gene with high-quality (diagnostic) ISH data. ROIs that were located outside the alignment area or could not be matched unambiguously to the ISH data were discarded from the analysis. At the time of analysis, the annotator was blind to the response profile of the ROI cells. Binary expression patterns were decoded into transcriptomic cell classes by the set of rules explained in Figure S3; rare cells (< 2%) with conflicting expression patterns (unclassified or nd) were excluded from subsequent analysis.

Skin histology

Skin from the back, cheek and whisker pad of *Calb2-Cre::Ai9(RCL-tdT)*-D mice with appropriate expression of tdT-fluorescence in a small subset of large diameter trigeminal neurons was fixed in 4% PFA in PBS for 5 days at 4°C. Tissue samples were washed in PBS and embedded in OCT medium (Tissue Tek) for cryosectioning. Thick sections (60–80 μm) were collected, washed in PBS and mounted in Vectashield with DAPI (Vector Labs) for imaging. Z stack images were acquired using a 40x oil objective on a laser scanning confocal system (Olympus Fluoview FV1000) and collapsed by maximum intensity projection using FIJI/ImageJ software.

QUANTIFICATION AND STATISTICAL ANALYSIS

The number of control (*Tac1-tagRFP-2A-TVA::Ai95(RCL-GCaMP6f)*-D, *Piezo2^{+/+}*) and *Piezo2-KO* (*Tac1-tagRFP-2A-TVA*, *Ai95(RCL-GCaMP6f)*-D, *Piezo2^{lox/lox}*) animals that were tested for each transcriptomic class and functional category is shown in the Table S1.

In order to calculate receptive field indices (RFI), individual response peaks to multiple pinches or hair pulls distributed across the cheek were determined using the `find_peaks` function of the `scipy.signal` package and normalized to the neuron's maximal response. Stimulation time points were identified by pooling response peaks from all neurons in an experiment and finding maxima in the histogram of response time points. Peaks that did not occur within a 2.4 s window around a stimulation-time point were excluded from the analysis. The RFI was calculated as the sum of all (normalized) response peaks divided by the number of stimulations. A wide receptive field will result in robust responses from many stimulations across the cheek and therefore a high RFI whereas a narrow field neuron will only respond to one or a few stimulations. In experiments using 4 pinches in a straight line (Figure S2), a stringent cutoff for wide field neurons was set at an RFI of 0.35.

Percentages of transcriptomic cell classes contributing to a functional cell category were calculated by dividing the number of responding cells positive for a given class by the number of responding cells that were tested with ISH probes for that class. Since not all classes were tested in any individual animal, the summed percentages do not exactly add up to 100%; (98.59% for control and 98.61% for *Piezo2-KO*). To display proportions in stacked bar graphs (Figures 6G and 7D), percentages were further normalized to total 100% in these graphs.

Relative abundance of functional cell categories in control animals and after *Piezo2* knockout (Figure S7A) was calculated as the number of cells belonging to a specific category divided by the total number of responding cells.

The log ratio of high threshold to low threshold responses per cell (Figure 6F) was calculated by dividing the response peak to hair-pull and pinch by the response peak to air-puff and brush and taking the natural logarithm.

Mean lifetime of GCaMP transients was calculated by fitting logarithmic decay from maximum to 10% this value using linear regression. The mean lifetime τ is the negative inverse of the coefficient. Values in Figure S5D are the means \pm s.e.m. of τ values of the individual cells.

Data were plotted as either bar graphs or as box and whisker plots with the medians and quartiles indicated by the box and the whiskers extending to the most extreme data point within 1.5 times the interquartile range. Individual data points (animals or cells) are superimposed as dots on these graphs. Since our data compared different sample sizes with potentially different variances, we chose a two-sided Welch's unequal variances t test to assess the significance of differences. Holm-Šidák correction was applied to all statistical tests to adjust for multiple comparisons.

Neuron, Volume 109

Supplemental Information

**Decoding Cellular Mechanisms
for Mechanosensory Discrimination**

Lars J. von Buchholtz, Nima Ghitani, Ruby M. Lam, Julia A. Licholai, Alexander T. Chesler, and Nicholas J.P. Ryba

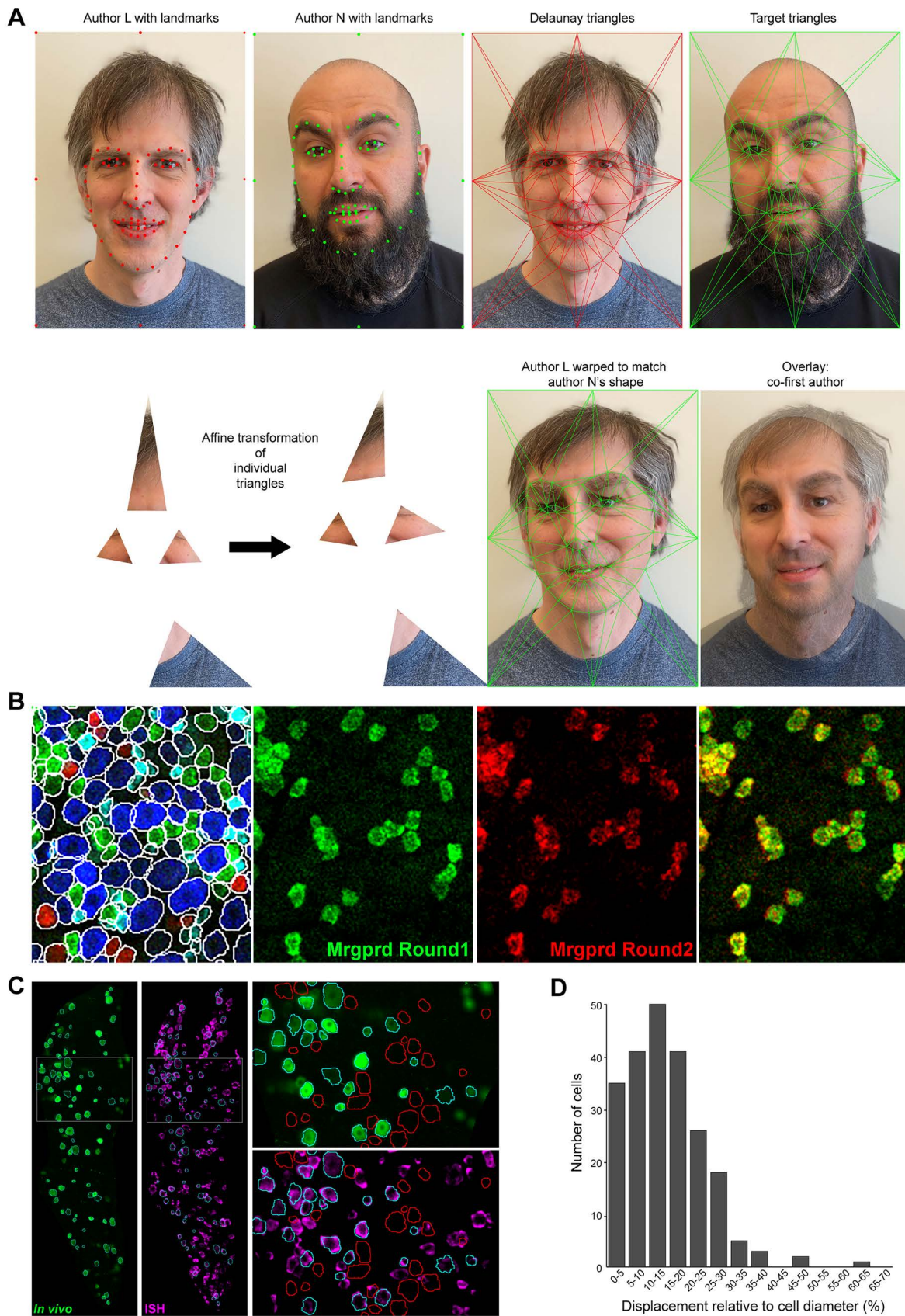


Figure S1. A simplified illustration of the strategy used for aligning images, Related to Figure 1

(A) (Top row) Face landmarks (equivalent to RFP guideposts) were automatically selected for photos of the two co-first authors and used for Delaunay triangulation. (Bottom, left) Illustration of how the vertices of four individual triangles in the author L

image were matched to the corresponding triangle in the author N image; note that each triangle uses its own affine transformation to generate the image of author L warped to match author N's shape. This allowed images to be merged to generate the composite co-first author (Bottom, right). **B**) Control to evaluate the accuracy of aligning successive whole mount ISH rounds to each other. Left panel: first round four color ISH image showing a region of a trigeminal ganglion and the dense packing of neurons; *Mrgprd*, green; *Trpm8*, red; *S100b*, blue; *Tac1*, cyan. ROIs were drawn by one author for cells identified by any probe (white outlines). Middle panels show successive rounds of ISH for *Mrgprd* that were aligned using *Trpm8* guideposts. Note the high-fidelity overlap (right panel). A second author, blind to the first-round data scored all the ROIs for *Mrgprd* signal in the second round of ISH. 3000 ROIs from 3 different ganglia were scored with 97% accuracy (correct/all), 93% recall (true positive/[true positive + false negative], 96% precision (true positive/[true positive + false positive]) and 98% specificity (true negative/[true negative + false negative]). **C**) Control to determine the accuracy of matching functional imaging to ISH data. Left two panels show GCaMP6f calcium transients (green) and aligned ISH image for *GCaMP* (magenta) with ROIs chosen for functional analysis indicated by cyan outlines. Signals outside the aligned region (outside the triangles used in alignment) have been blacked out; note that not all GCaMP positive neurons responded to mechanical stimulation of the cheek and that not all cells with detectable signal in functional imaging were chosen for analysis (see Star Methods for details). Boxed regions of the two rounds of imaging are shown enlarged to the right. Note that most ROIs selected for analysis (cyan) match the *GCaMP* ISH signal in terms of position, size and shape. An equal number of decoy ROIs (colored red) were generated by one author to allow accuracy to be scored. A second author, blind to the functional imaging data, scored the true and the decoy ROIs for *GCaMP* ISH signal. 231 ROIs chosen for functional analysis and the same number of decoy ROIs from two ganglia were scored yielding 96% accuracy, 94% recall, 97% precision and 97% specificity. **D**) The displacement of cells between functional and ISH imaging was also determined (see Star Methods for details). The distribution of displacement of cell centers relative to cell diameter is shown; < 5% of cells were displaced by more than 30% of their diameter.

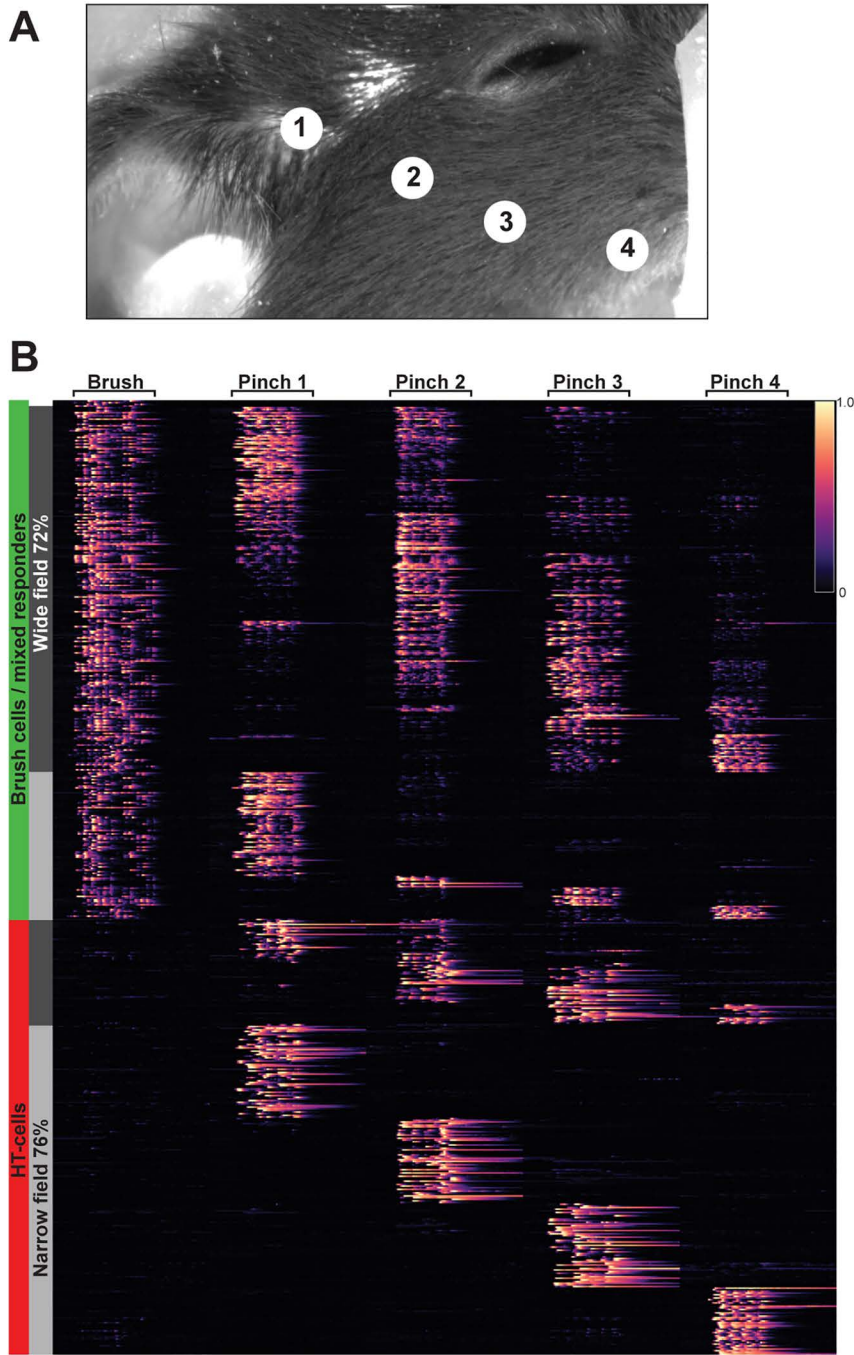


Figure S2. Brush cells have very large receptive fields for pinch, related to Figure 2

Naturalistic stimuli like brush, air puff and vibration are not localized making it impossible to functionally map the receptive field of neurons responding to these stimuli. By contrast, pinch and hair pull events were localized to specific sites. Nonetheless, the force of these stimuli and the flexibility of the cheek mean that large areas of skin are affected by these stimuli with distal sites likely experiencing low mechanical forces. Brush responsive neurons were typically engaged by multiple pinch and hair pull events. Since these neurons are sensitive to gentle stimuli, it is possible that they are activated by distal noxious stimuli and would thus have much broader receptive fields to e.g. pinch than HT-cells that only detect noxious stimuli. To test this hypothesis, we recorded brush responses from the cheek and then applied a series of pinches at four locations each approximately 1 mm apart across the cheek. **A**) A frame from the synchronized videography showing the locations of the four pinches. **B**) Heatmap showing the *in vivo* GCaMP6f responses of neurons from four trigeminal ganglia, tested for responses to brush and 4 pinches in a line. Calcium transients were scaled to the maximum response in that cell and colored as indicated in the scale bar (inset). Cells were sorted first by presence of a brush response, then by presence of a pinch response, then by classification as a wide field neuron based on a receptive field index (see Star Methods for details) and finally by order of their pinch response. The cell-categories are indicated by labelled colored boxes with dark grey indicating wide field neurons and light grey, narrow field cells. Note that more than 70% of brush responsive cells also detected pinch from at least 2 sites; whereas >75% of HT-cells only responded to pinch at a single site. Since the receptive fields of some HT-cells are known to be extensive (Ghitani et al., 2017) with linear dimensions of approx. 1 mm, it is not surprising that some HT-cells were activated by pinch at two sites.

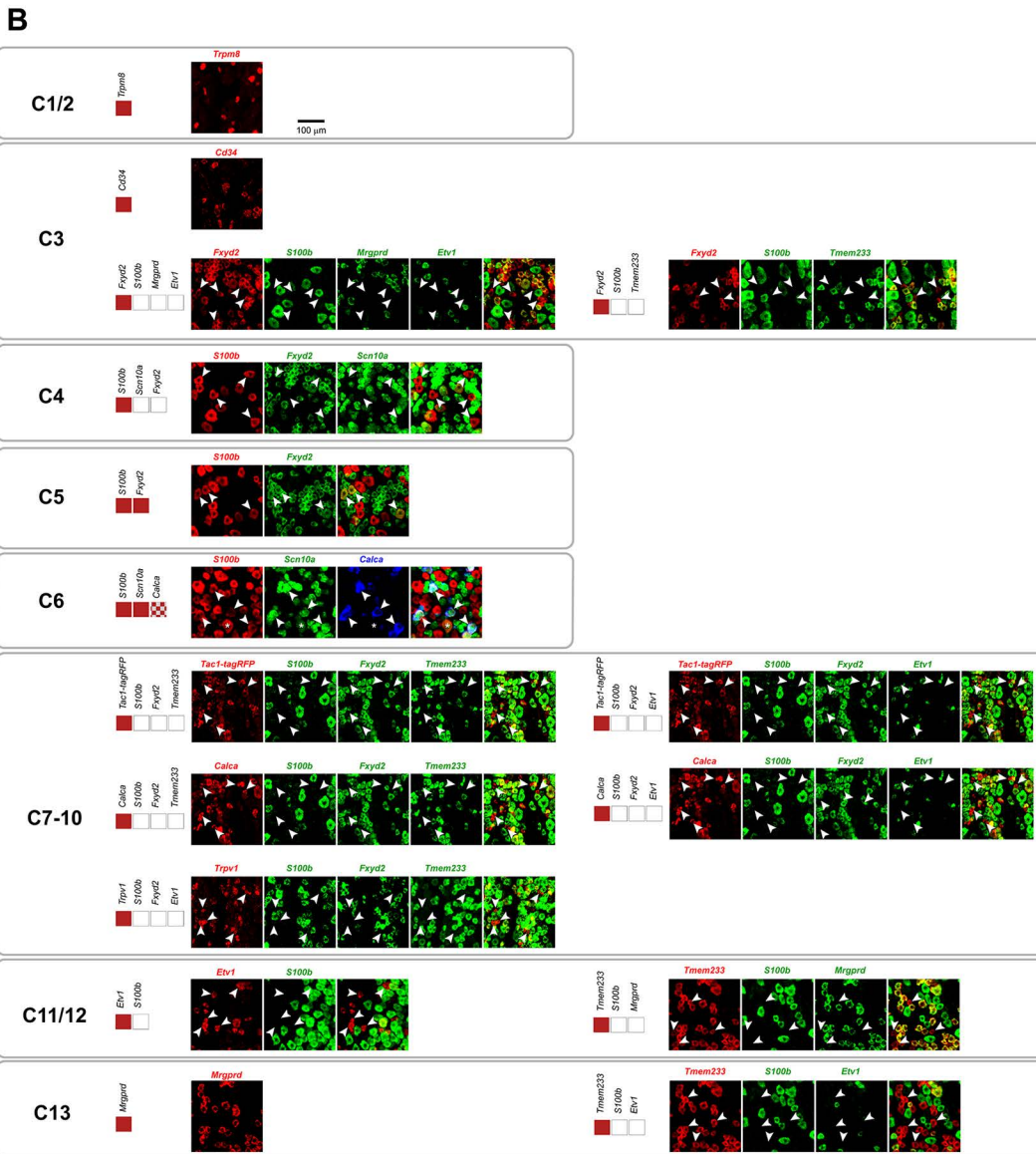
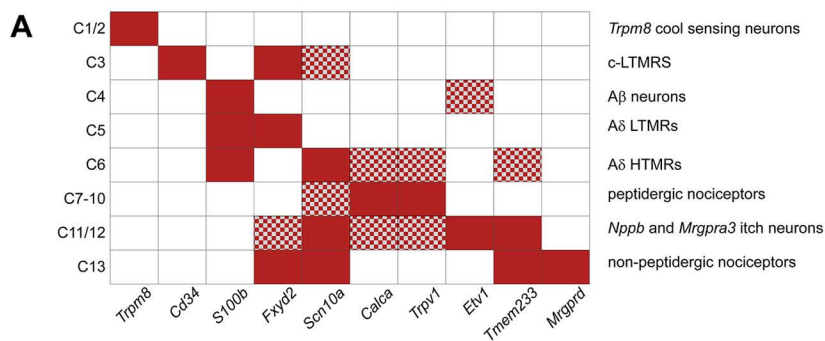


Figure S3. Strategies for decoding trigeminal transcriptomic class using multiplexed ISH, related to Figure 3 and Figure S4

A) Schematic representation of cell class specific expression patterns of the panel of genes that was used to classify trigeminal neurons in whole-mount ISH following *in vivo* functional imaging. Filled red boxes indicate diagnostic expression and empty boxes indicate diagnostic absence; checked-fill highlights probes that are expressed in a subset of cells of that class. Classes are labeled C1-C13 (Nguyen et al., 2017) and by their corresponding characteristics. **B**) ISH probing strategies used to decode indicated cell classes; shown are the defining gene expression patterns (presence and absence) for that class and example ISH images. Arrowheads indicate a subset of example cells of the indicated class. Some classes were detected using a single probe (or probe combination) while others could be identified by several strategies. Probe combinations were adjusted to optimize classification of mechanosensitive neurons using two rounds of multiplexed ISH. C6 neurons were originally defined by co-expression of *S100b* and *Calca* (Nguyen et al., 2017; von Buchholtz et al., 2020); however, more recent sequencing data suggest that *Scn10a* is a more diagnostic marker (Nguyen et al., 2019). A C6 neuron expressing *S100b* (red) and *Scn10a* (green) but not *Calca* (blue) is indicated by an asterisk.

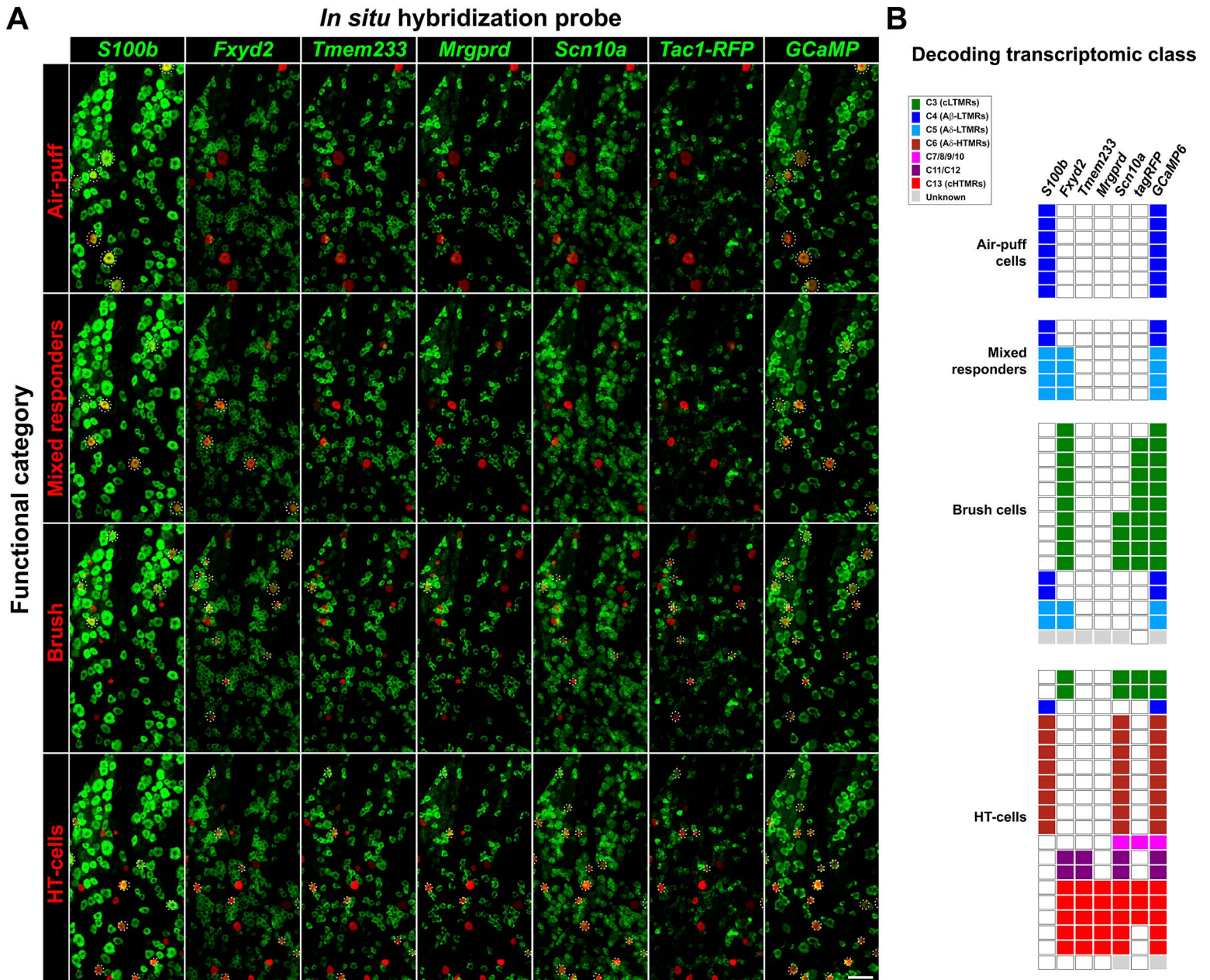


Figure S4. Transcriptomic classification of mechanosensory neurons in the trigeminal field shown in Figure 3, related to Figure 3

A) Representative images of ISH (green) aligned to category specific activity maps (red; see methods). Each row represents a single functional category of cells and each column a single ISH probe. All images are from the same area of the trigeminal ganglion dorsal surface. Responding cells that are ISH positive are highlighted by dotted circles to emphasize their expression profiles shown schematically in **(B)**; scale bar = 100 μ m. **B**) Decoding gene expression patterns for every active cell in **(A)**: each column represents a responding cell with filled boxes color coded according to cell class indicating ISH positives. Note that in this example 46 from 48 responding cells could be classified (see Figure S3 for more details).

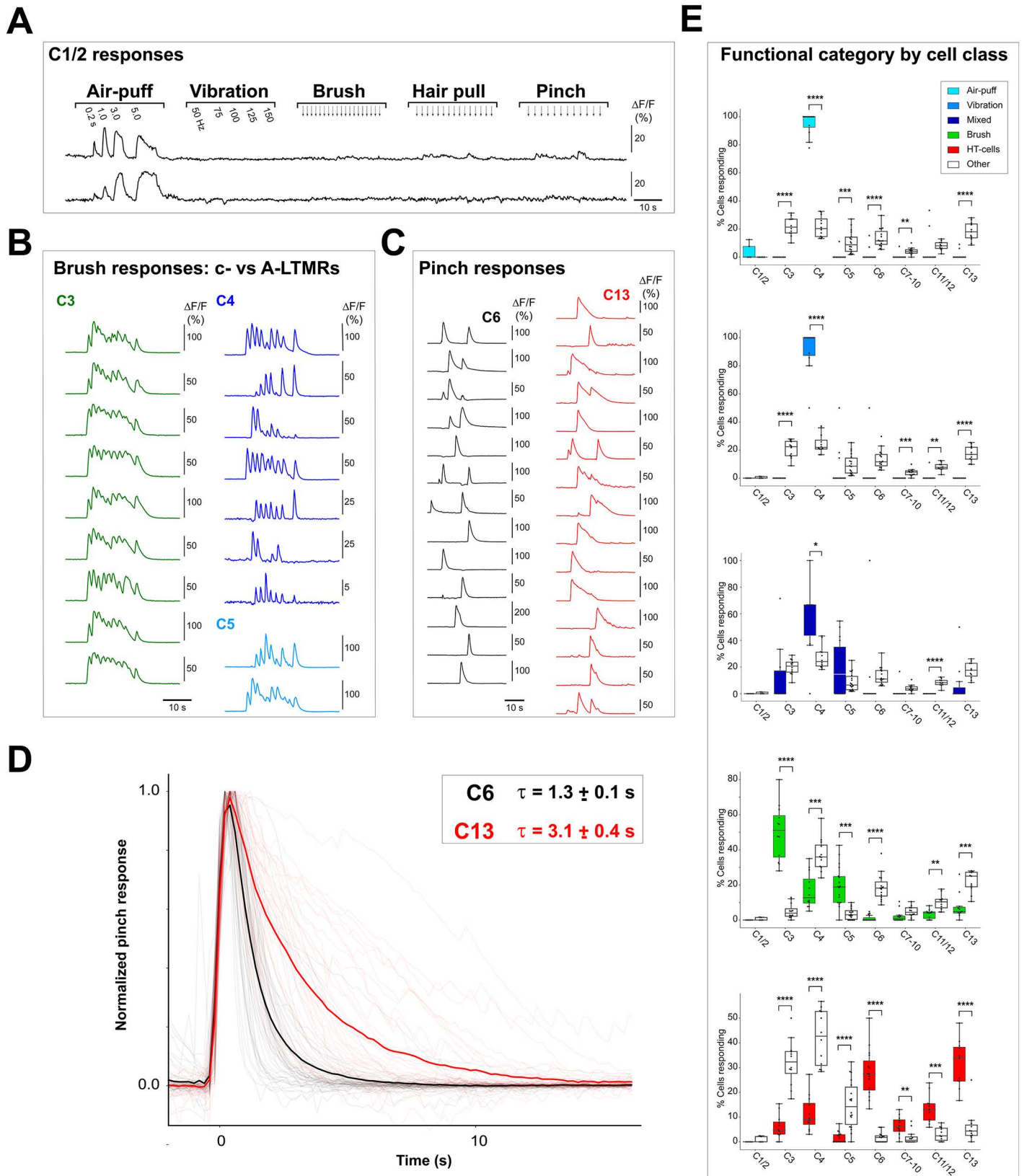


Figure S5. Function and response dynamic differences between transcriptomic classes of trigeminal neurons, related to Figure 4

A) Only two C1/2 neurons responded to any mechanical stimuli (496 mechanoreceptors probed for *Trpm8* expression, Figure 4C). Shown are GCaMP-transients of these cells demonstrating that although they detected air-puff, they did not respond to any other stimulus including vibration, which typically also activated the other air-puff cells (Figure 4). C1/2 neurons are known to be exquisitely sensitive to small changes in temperature. Thus, their response to air-puff but not vibration likely results from cooling, perhaps

caused by evaporation. Given that the cheek is covered by a thick layer of fur, we suspect that these cells may target the nearby cornea. B-D) The GCaMP-transient dynamics of A- and c-type mechanosensory neurons to several stimuli were markedly different. For example, **(B)** the decay of C3 cLTMR responses to single brush strokes was slower than those of C4 or C5 A-LTMRs; note traces do not return to baseline between strokes for the C3 cells, whereas they do for C4 A β -LTMRs and approach baseline in the C5 A δ -LTMRs. All the responding C3-C5 neurons from a single animal are shown; equivalent results were observed in all other mice (see Figure 4). Similarly **(C)** illustrates pinch responses of HT-cells from a single mouse showing faster decay for C6 A δ -HTMRs than for C13 non-peptidergic HTMRs. **(D)** The peak final pinch response recorded across multiple animals was aligned for 29 C6 and 75 C13 neurons (faint black and red traces, respectively); responses were averaged for each class of cells to generate the mean response curves (bold lines). Also indicated are the mean lifetime and s.e.m. derived from the individual responses; differences were significant (Welch's two-sided t-test, $p = 0.00012$). **(E)** The transcriptomic class dependency of functional category was analyzed on a mouse by mouse basis. Shown are five box plots (see Methods): where air-puff, vibration, mixed responders, brush and HT-cells are each compared to the four other functional categories (Other); dots show data from individual mice; p-values are indicated by * <0.05 , ** <0.01 , *** <0.001 , **** <0.0001 , Welch's two-tailed t-test with Holm-Šídák correction for multiple tests. Percentage of cells within each functional category were calculated by dividing the number of cells positive for a specific transcriptomic class by the total number of cells tested for that class.

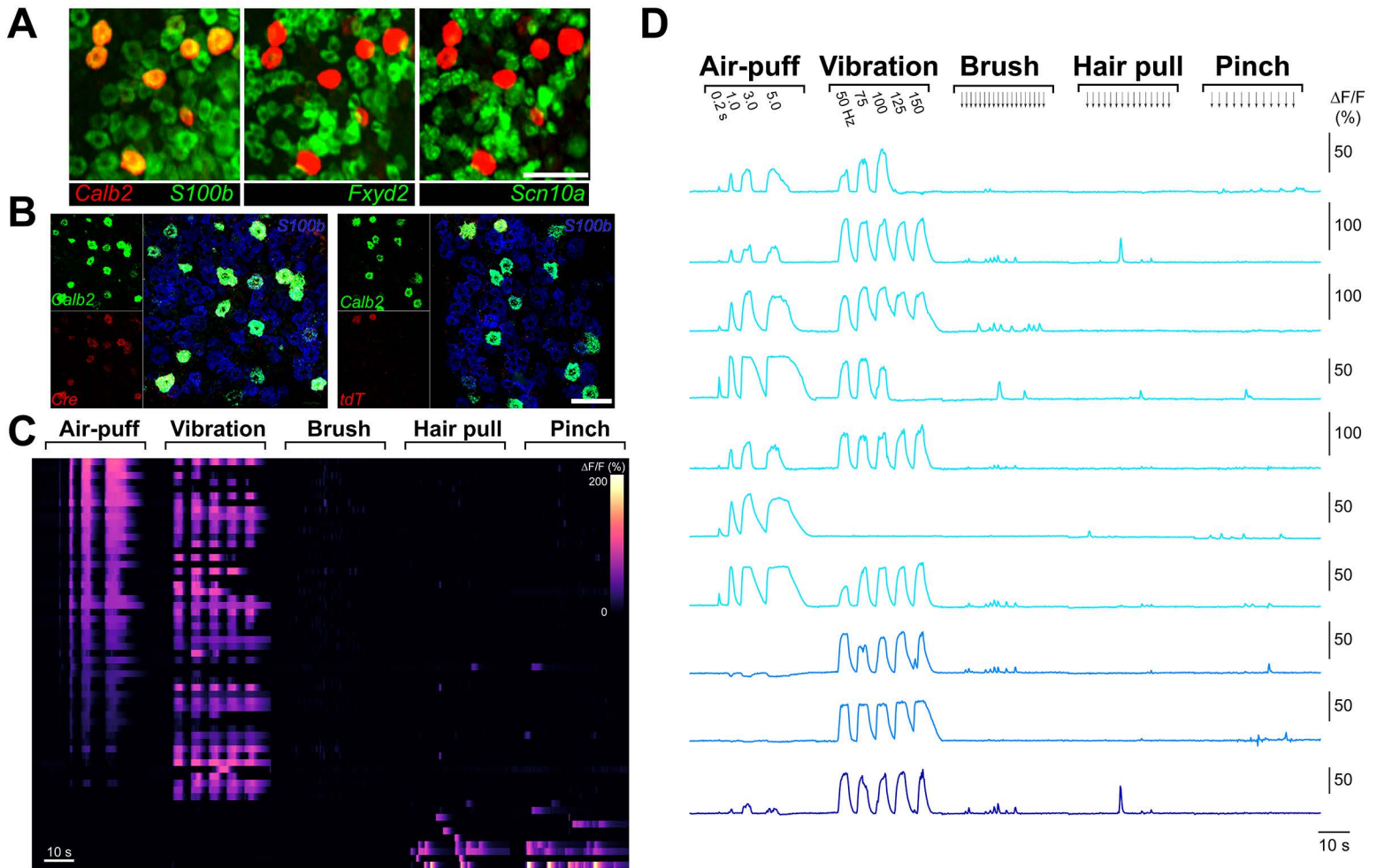


Figure S6. Expression of *Calb2* marks a subset of C4 neurons and fidelity of *Calb2-Cre* for targeting these cells, related to Figure 5

A) Example whole mount ISH images demonstrating that *Calb2* (red) is selectively expressed in a subset of *S100b* positive neurons but shows no overlap with *Fxyd2* or *Scn10a* (green) defining *Calb2*-expressing neurons as C4 cells. **B)** ISH analysis demonstrates overlapping expression of *Calb2* and *Cre* in the trigeminal ganglion of *Calb2-Cre/Ai9 RCL-tdT* mice with restricted *tdT* in a subset of these neurons. Left, example image showing that *Cre*-expression (red) corresponds to *Calb2*-expression (green) in a subset of *S100b*-positive (blue) trigeminal neurons. Right, image showing that recombination and *tdT*-expression (red) was only observed in a subset of *Calb2*-expressing (green) neurons; the merged image includes *S100b*-labeling (blue). **C)** Heatmaps and **(D)** GCaMP-transients showing mechanosensory responses from 61 trigeminal neurons in 4 *Calb2-Cre/Ai95(RCL-GCaMP6f)-D* double transgenic mice that exhibited restricted *GCaMP*-expression. Note the similarity of responses to those identified using ISH after imaging (Figure 5C) with 84% selectively tuned to air-puff and/or vibration. Small short duration responses to brush, hair-pull and pinch seen in some of these neurons **(D)** support the idea that although capable of sensing sustained stimuli, rapid adaptation may dampen responses of this class of cells. The small number of HT-cells **(C)** likely reflect a small degree of inappropriate recombination in these animals (see Figure 5); scale bars = 100 μ m.

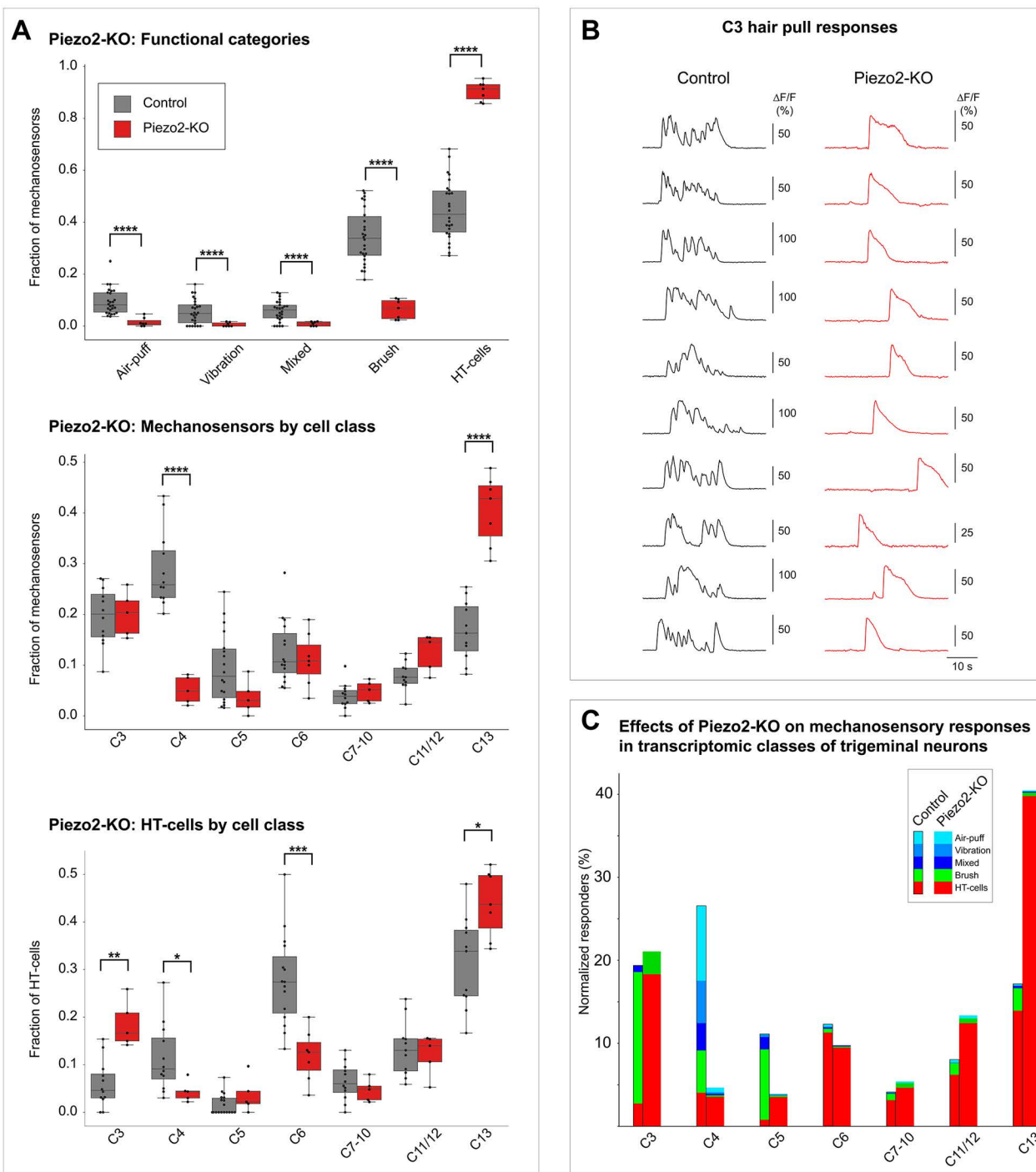


Figure S7. Analysis of effects of Piezo2-KO on mechanosensory responses of trigeminal neurons, related to Figure 6 and Figure 7

A) Quantitation of how Piezo2-KO differentially affects functional categories of mechanosensory neurons and the responses of transcriptomic classes. Box and whisker plots showing: Upper panel, the fraction of mechanosensory neurons assigned to a specific functional category in 26 control (grey boxes) and 7 Piezo2-KO mice (red boxes). Piezo2-KO resulted in statistically significant changes in all categories. The fraction of mechanosensory neurons (middle panel) and HT-cells (lower panel) assigned to a specific transcriptomic class in control (grey boxes) and Piezo2-KO mice (red boxes); the individual mice tested for that class are shown as dots (see also supplemental Data Table 1); p-values are indicated by * <math><0.05</math>, ** <math><0.01</math>, *** <math><0.001</math>, **** <math><0.0001</math>, Welch's two-tailed t-test with Holm-Šídák correction for multiple tests. **B)** Sample GCaMP-transients from C3 neurons responding to pinch showing large differences in activation frequency and response dynamics between control (black) and Piezo2-KO (red) cells. Note the responses to individual hair-pulls in the different C3 neurons of the control and the greatly reduced frequency of responses after Piezo2-KO. **C)** Stacked bar graph showing quantification of response category across cell-class in control (left, slender bar, data as in Figure 4C) and Piezo2-KO (right, thicker bar); data were normalized to the number of responding neurons tested for each class.

Supplemental Data Table 1. Number of mice and cells used for testing cell classes by ISH after functional imaging, related to [Figure 4](#), [Figure 6](#), [Figure 7](#), [Figure S5](#) and [Figure S7](#)

Cell class	Control		Piezo2-KO	
	Animals tested	Cells tested	Animals tested	Cells tested
C1/2	5	496	0	0
C3	12	1017	5	546
C4	12	941	5	536
C5	18	1403	5	539
C6	15	1098	7	707
C7-10	12	1016	5	537
C11/12	11	1000	5	539
C13	11	962	7	724

Chapter 5

Discussion and end of thesis

“Every animal can only tap into a small fraction of reality’s fullness...there is a wonderful word for this sensory bubble–Umwelt.” -Ed Young

Jakob von Uexküll was a Baltic-German zoologist who popularized the term Umwelt. He compared an animal’s Umwelten to a house with different types of windows. There are light windows, sound windows, olfactory windows, tasting windows and a whole lot of tactile windows. The animal’s perception of the outside world depends on what types of windows they have¹. The cells and molecules underlying mechanosensation are fundamental building blocks for creating our brain’s window into the physical world. These sensory neurons are responsible for converting mechanical interactions we experience, both internally and externally into useful information that are vital to many bodily functions.

In the second chapter of this thesis, I used mice to demonstrate that mechanical touch applied to certain body locations like the skin of the perineum is more salient than other body locations like the hindpaw. I then showed that altering touch in these hyper-salient body locations by removing a key touch molecule, *Piezo2*, can dramatically affect the sensory experience and change important behaviors in sexual reproduction. Finally I found a specific sensory neuron class, the C3 C-LTMRs, which relies heavily on the expression of *Piezo2* for producing successful copulation, mating and reproductive behaviors. While these experiments clearly highlight the circumstances that are necessary for successful reproduction, it will be exciting to see in follow-up work if activating C-LTMRs can sufficiently induce erection responses on its own. Nonetheless, it is remarkable how the expression of *Piezo2* in a specific class of sensory neuron, is required for such fundamental survival and reproductive behaviors.

In the third chapter of this thesis, we demonstrated the importance of cells and molecules underlying mechanotransduction for interoception. Internal mechanical sensation

regulates the transit of luminal contents throughout the gastrointestinal tract and is critical to ensure proper digestion, nutrient absorption, and waste removal. We show that sensory neurons in DRG that innervate the gastrointestinal tract influences stool sizes, peristaltic movement and bowel motility needed for normal transit of GI contents. Furthermore, I recorded from sensory neurons innervating the lower colon to demonstrate that *Piezo2* is directly required to detect mechanical distension. As for sexual functions, sensory neurons expressing *Piezo2* that innervate the gastrointestinal tract, transduce mechanical information necessary for gastrointestinal health.

In both of these studies, altering the expression of a molecule from specific populations of neurons innervating anatomical locations like gastrointestinal tract or perigenital area dramatically impacts their bowel motility and sexual reproduction. Excitingly, human subjects with hereditary *PIEZO2* loss of function have largely validated our mouse models of *Piezo2* knock out. In clinical evaluations and surveys, human subjects report both sexual and gastrointestinal symptoms that largely recapitulates the results of our experiments performed in mice.

Having demonstrated with these two examples that specific cells expressing *Piezo2*, have specific functions, in the fourth chapter, I revisited the age-old quest of many scientists to organize and classify primary sensory neurons. By surveying all sensory neurons using modern tools like sequencing, transcriptome analysis, and functional imaging, I connected the cells, the molecules they express, with their functional roles in detecting mechanical stimuli. We verified the existence of about a dozen distinct molecular classes on sensory neurons with sequencing experiments. We discovered that neurons in each of these classes have predictable functional roles. Furthermore, we found that altering the expression of *Piezo2* affects neurons in different classes in different but predictable ways. Some classes suffered a loss of transcriptomic identity whereas others kept their transcriptomic identity but shifted their functional identity from LTMRs to HTMR-like neurons. Organizational rules that apply differently to each class of sensory

neurons support the idea that functional roles should be considered in addition to the molecular transcriptomes, and all the classical anatomical, neurochemical, electrophysiological, and tuning features, when classifying sensory neurons in the future.

While we were able to elucidate some interesting patterns that emerged from these studies, there are still exciting avenues for future exploration and refinement of classes. One promising avenue of exploration is tracking the molecular expression of sensory neurons throughout development. In a recently published dataset, force direction projection of sensory neurons highlight the fact that sensory neuron classes are undifferentiated early in development and specialize into the dozen or so defined classes as animals develop into adults². This data set shows different classes have divergent trajectories, for example some classes differentiate earlier, while others partially differentiate together and split into more classes later in development. It will be interesting to match the different classes of sensory neurons with their developmental stages, and learn about the appearance of different somatosensory percepts coming online as the animal grows and experiences the world.

Another ongoing mystery touched on in the work from this thesis is the identity of a mechanosensory mechanism besides *Piezo2*, responsible for high-threshold mechanosensation. *Hoxb8cre:piezo2^{fl/fl}* cre animals with no *Piezo2* expression in the caudal portion of their body still readily withdraw in response to noxious stimuli like pinprick to the paw and perineum. Whole cell patch recordings while poking *Piezo2*-deficient sensory neurons *in vitro* shows the complete loss of all types of mechanically-evoked currents³. However, functional calcium imaging of neurons without *Piezo2*, revealed persistent calcium responses to noxious stimuli like hair pull and pinch. Our experiments assigning functional roles to molecular profiles, revealed that this mysterious mechanism is definitely present in LTMRs of C3 neurons. This mechanism may contribute to the C3 neuron's ability to keep their molecular identity in the absence of *Piezo2*. These results revealed that there is a mysterious mechanism that transduces high threshold nociceptive mechanical sensations. Mining the transcriptomic dataset

from the fourth chapter of this thesis may reveal new candidate molecules, or perhaps orphan receptors which could be the elusive high threshold mechanosensory mechanism.

The studies in this thesis largely neglects the range of the somatosensory system. In focusing on mechanotransduction, I have left out the contributions of other sensations which are integral components of creating somatosensory percepts. Since most creatures, almost always experience tactile stimuli simultaneously accompanied by proprioception, temperature and chemical sensations, studying the associated molecules will allow us to better understand how more complex somatosensory percepts such as stickiness, viscosity, slippery wetness, evaporation, suction or chemical damage are built. Using the data sets and expertise generated for the studies mentioned throughout this thesis may also predict other examples of label line-like circuits. It will be exciting to find new circuits with functional roles for specific classes of sensory neurons, expressing specific molecules, with particular innervations that produce specific sensory percepts and behaviors. Perhaps we could learn of circuits for different types of headaches, sensory processing disorders like touch synesthesia, how cross modal illusions such as temperature-weight heaviness are generated.

Finally, all of this work focused predominantly on peripheral sensory neurons. I've glazed over the contributions of the central nervous system. The central processing of sensory information is a major role of the somatosensory system. Primary afferent information is relayed into various areas including the spinal cord, the brainstem, the thalamus, and ultimately representing somatosensation in cortical areas. As I have shown that the saliency of the genitalia is not entirely encoded by the primary sensory neurons, it is therefore likely that amplification happens in the central nervous system. Further work characterizing the neuronal circuitries involved in building the sensory percept will be fascinating.

Acknowledgements Take Two and Behind the Scenes

If you have made it this far, you may have noticed that several chapters of this thesis have already been disseminated in several journals, however, the dimensionless author lists really don't do justice to how these humans contributed to the interweaving of ideas and how these projects really began. This seemed like a good place to rectify that by documenting the environment and context which made these projects possible, the many failures and deadends along the way, and generally to properly thank the many awesome humans who have contributed to the environment which made these projects possible. For preservation... or whatever.

The introductory chapter about Piezo2 incorporates figures I generated for a review I helped write with Marcin Szczot and Alex Nickolls. We had collectively neglected the deadline until the world shut down because of a global pandemic, writing this review was one of the silver linings. It was great fun and gave me purpose. I would also like to thank the members of NIH Media Arts for helping convert my hand drawn powerpoint concept diagrams into spatially accurate ribbon diagrams. Also thank you Jennifer Osborne for all the proofreading.

The seeds for the conceptualization of a project focused around genital sensation, which eventually became Chapter 2 was planted good naturedly during conversations over beers and coffee with Marcin Szczot, Nima Ghitani and Eleni Frangos. It was during Arnab Barik's farewell party, sitting 6ft apart poolside, that Alex enthusiastically approved this supposed "side quest". While various experimentation avenues didn't make it into the final manuscript, the dedicated efforts of Minh Nguyen, Lars von Buchholtz, Max Nagel, Monesha Jayabalan, and Jennifer Osborne should be acknowledged. These ill-fated experiments included sequencing DRGS from hundreds of mice, tracing sensory neurons innervating the genitalia, fos-trap labeling fluffed neurons, sectioning, staining, and imagining thousands of sections of tissue. I would also like to acknowledge the contributions of all the other members of the Cheslerlab who engaged in many insightful discussions throughout this process. In putting the "sex" manuscript together, Alex and

Nick spun gold out of a stack of hay, it was science bootcamp in the best way. Thank you for the invaluable masterclasses.

The majority of the experiments and data for Chapter 2-"Sex" and Chapter 3-"Gut" were collected after the global pandemic began and as such made having a collaborator on the other side of the country equidistant to other members of the lab. I credit both Alex and Ardem for their incredible foresight to put together a gut team that met regularly over Zoom. Rocio Servin, thank you for being an awesome collaborator, working on the gut project whenever my sex project stagnated kept me sane. Absolutely enjoyed juggling two projects with parallel timelines with you.

The final chapters includes experiments I have done in collaboration with Nima Ghitani and members of the Ryba lab, Lars von Buchholtz and Minh Nguyen. While I contributed to these projects only by performing experiments, I consider these projects to be the greatest contributions towards the field during the course of my PhD. Thanks for having me on the team.

I would also like to acknowledge the animal care and Veterinary staff of building 35 and 49 for their tireless work and vigilant care of our animals.

To the Wednesday evening 5pm Journal Club. Thanks for getting me out of the lab and sharpening my critical thinking skills. It was some of the most intellectually stimulating and fun times of my PhD.

Thank you to all the Chesler lab members for proofing every talk, poster and manuscript. Y'all are awesome.

Special acknowledgements to Nima, Melanie, Erin and Nadira for their truly heroic efforts in helping proofread and format this thesis in the final hours.

Chapter 5 References

1. Yong, E. (2022). *An Immense World: How Animal Senses Reveal the Hidden Realms Around Us* (Random House Publishing Group).
2. Meltzer, S., Santiago, C., Sharma, N., and Ginty, D.D. (2021). The cellular and molecular basis of somatosensory neuron development. *Neuron* 109, 3736-3757.

3. Szczot, M., Liljencrantz, J., Ghitani, N., Barik, A., Lam, R., Thompson, J.H., Bharucha-Goebel, D., Saade, D., Necaise, A., and Donkervoort, S. (2018). PIEZO2 mediates injury-induced tactile pain in mice and humans. *Science translational medicine* *10*, eaat9892.

The End